Rare-Earth Based Fullerides: tuning the onset of valency transitions

Takeshi Nakagawa

Rare-Earth Based Fullerides:

Tuning the onset of Valency Transitions

By

Takeshi Nakagawa

Submitted in part of fulfilment of the requirements for the degree of Doctor of Philosophy

Durham University

July 2009

I hereby declare that the work described in this thesis was carried out in the Department of Chemistry at Durham University and the European Synchrotron Radiation Facility (Grenoble, France), between April 2004 and September 2007 under the supervision of Prof. K. Prassides. All the work is my own, unless otherwise stated, and has not been submitted previously either in the same or different form, to this or any other University for a degree.

Takeshi NAKAGAWA
Durham, July 2009

Signature:

Durham University

Takeshi Nakagawa Degree: D. Phil

Rare-earth based Fullerides: Tuning the onset of valancy transitions

Summary

In this thesis, the recent advances in studies on rare-earth metal intercalated fullerene solids with emphasis on their structural, electronic, and magnetic properties. The investigations on the rare-earth based fullerides have been concentrated on their structural, electronic, and magnetic properties.

Intercalation of C_{60} with rare-earth metals results in interesting compounds not only for the appearance of superconductivity but also for the magnetic properties and mixed valence phenomena related to the localised 4f electrons. Of particular interest, I discuss the results obtained from various experiments on rare-earth based mixed valence fullerides, of which displays a remarkable sensitivity of rare-earth valency to external stimuli, such as temperature and pressure. Among the family of rare-earth fullerides, $Sm_{2.75}C_{60}$ was the first known molecular-based material to show valence fluctuation associated with the highly-correlated narrow-band behaviour of the 4f electrons in Sm ions. Improvement in the synthetic technique to produce single-phase rare-earth doped fullerides have opened the way to carry out detailed and systematic study of the structural properties of the $RE_{2.75}C_{60}$ (RE = Sm, Eu, and Yb) as a function of temperature and pressure, which were carried out using the synchrotron X-ray powder diffraction technique. The obtained results have lead us to find a rich variety of temperature- and pressure-driven abrupt or continuous valence transitions. In addition, we have observed that by taking precise control on the nature of dopants, the tuning of the onset temperature and pressure of this valence transition were possible.

Direct measurements on the valence states of the rare-earth ions in the fulleride salts as a function of temperature were carried out using X-ray absorption spectroscopy using the alkaline-earth and rare-earth mixed compound, $(Sm_{2/3}Ca_{1/3})_{2.75}C_{60}$. The obtained spectra have provided clear evidence to confirm the electronic nature of the low-temperature first-order valence transition.

Table of Contents

List of Tables

List of Figures

Acknowledgements

When I first stepped inside the laboratory, I immediately realised how tough it can be to get through the three years of Ph.D work. The fullerenes, a new molecular form of pure carbon displaying fascinating properties and attracting huge interest from many researchers, was just a black powder to me and caused lots of trouble handling before I can do any of scientific work on them. However, as I see one of my precious samples displayed clean single-phase diffraction patterns at ESRF, I started to see the interesting part of fullerene and it turned out that handling of this black powder became one of my specialities during the course of Ph.D. For all this period as Ph.D student, I would like to thank my supervisor, Professor Kosmas Prassides, who offered me this wonderful opportunity to work in his research group and for his support. He showed me a path to grow up as a scientist with independent mind and taught me how to look at the science behind various phenomena.

My gratitude also goes to all the great people in the group who had given me lots of help throughout my project work, especially Yiannis Arvanitidis, who showed me the entrance and bright future, Yasuhiro Takabayashi, who was a perfect guide when I just started Ph.D., Dionisis and Martin who made my life in Durham more enjoyable.

Finally, special thanks to my family and friends who supported me from different part of the world.

Takeshi Nakagawa

July 1, 2009

CHAPTER 1

INTRODUCTION

1.1 Introduction

The discovery of the fullerene family, the third allotropic form of pure carbon after graphite and diamond, has attracted a great interest for both its chemical and physical properties. Following the isolation and production of bulk crystalline samples of fullerenes, a set of hollow, closed-cage molecules consisting purely of carbon, research on the solid-state properties of fullerene-based materials proceeded at a remarkable pace. The structure and dynamical properties of pristine fullerene solids posed many challenging questions to modern day experimental and theoretical science.

In September 1985, Kroto *et al.* [1] discovered the remarkably stable molecule formed by 60 carbon atoms, now known as Buckminsterfullerene, C_{60}. These laboratory experiments were initially aimed to simulate the physicochemical conditions in a cool red giant star. A pulsed laser was focused onto the surface of graphite leading to the vapourisation of the carbon species into a high density helium flow. The resulting carbon clusters were freely expanded in a supersonic molecular beam, being ionised, and an exceptionally strong signal was detected by mass spectrometry for the C_{60}^+ ion. From the spectra obtained and considering the remarkable stability of the produced clusters, Kroto and co-workers proposed that the molecule has a closed-cage structure consisting of 12 pentagons and 20 hexagons with the icosahedral symmetry of a soccer ball. This was confirmed five years later when macroscopic quantities of C_{60} were first isolated. All fullerenes have an even number of carbon atoms arranged over the surface of a closed hollow cage consisting of 12 pentagons and n hexagons, where n, according to Euler's theorem for polyhedra, can be any number other than one (including zero).

The smallest possible fullerene is, therefore, C_{20} with 12 pentagonal faces and no hexagonal faces. However, theoretical work pointed out that carbon cage structures are more stable or energetically more-favoured when these pentagons are isolated, which is known as the "isolated pentagon" rule. Using this rule together with symmetry principles, a family of closed carbon cages with (20+2n) atoms, where $n = 0, 2, 3, 4$, and so on, is predicted to exist, where the smallest fullerene satisfying this rule is the C_{60} molecule. Several members of the family that includes chiral and achiral molecules have been isolated, including C_{70}, C_{76}, C_{78}, C_{82}, C_{84},..., some in several isomeric forms.

1.2 The molecular and solid state structures of C_{60}

The C_{60} molecule is the parent member of the fullerene family and consists of sixty symmetry-equivalent carbon atoms located at each vertex adopting the familiar shape of a truncated icosahedron (Fig. 1.1). Each carbon atom is bonded to three of its neighbours in the sp^2 σ bonding configuration on a curved surface leading to the formation of a closed shell of 32 faces, 12 of which are pentagonal and 20 hexagonal, while remaining p electrons of each carbon are delocalised in π-molecular orbitals which cover the outside (exo) and inside (endo) surface of the molecule. The C_{60} has molecular point group symmetry, $m\bar{3}5$ (I_h) which is the highest symmetry of any known molecule [2]. There are two types of carbon-carbon (C-C) bonds in C_{60}; two "single bonds" which are located along a pentagonal edge that fuse a hexagon to a pentagon (6:5) and the "double bond" is located between two hexagons.

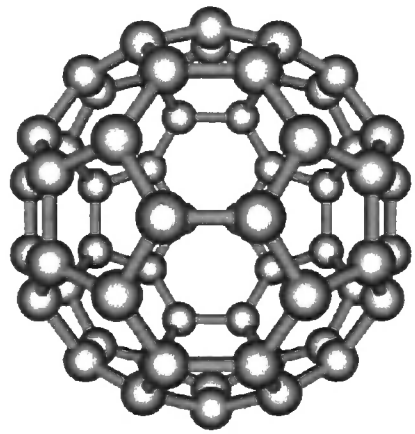

Fig. 1.1. The C_{60} molecule.

The nuclear magnetic resonance (NMR) spectrum has indicated that these bonds have different bond lengths (r): 60 "single bonds" have bond length of, r_1 = 1.46 Å, and 30 short "double bonds" with a bond length, r_2 = 1.40 Å [3]. Pseudo-hexagonal faces are centres of three-fold rotational symmetry, pentagonal faces are centres of five-fold rotational symmetry, edges between two hexagons are centres of two-fold rotational symmetry, and the entire molecule is symmetric under inversion. Periodic translational symmetry is incompatible with five-fold rotational symmetry and the maximal subgroup consistent with crystalline symmetry is $m\bar{3}$.

The simplest model developed for the electronic structure of the fullerene molecule is based on Hückel theory. In this model, each carbon atom forms σ bonds with its neighbours, leaving 30 filled $p\pi$-orbital to hold 60 electrons, i.e. one π electron per carbon atom, near the Fermi surface [4]. Thus, the electronic properties of C_{60} molecule are determined by the π orbitals. The figure below shows the $p\pi$-orbital levels for an isolated C_{60} molecule from a Hückel calculation (Fig. 1.2).

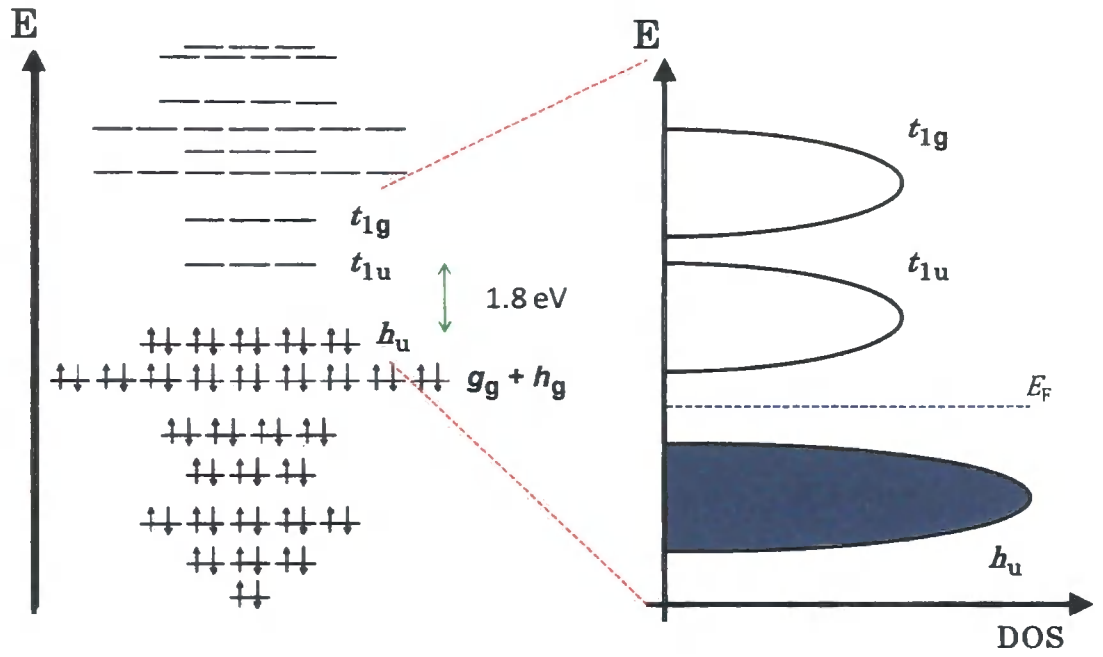

Fig. 1.2. Schematic diagrams of the molecular orbital levels scheme for C_{60} molecules and of the electronic density of states of the HOMO, LUMO and LUMO+1 derived bands for solid C_{60}.

C_{60} has just enough electrons to fully fill the lowest energy level of the l = 5 state (five-fold h_u level). This filled level forms the highest occupied molecular orbital (HOMO) for C_{60}, whereas the empty three-fold t_{1u} level of the l = 5 state is the lowest unoccupied molecular orbital (LUMO). The HOMO and LUMO levels are separated by a gap (ΔE = E(HOMO) – E(LUMO) of ~1.8 eV [5]. The ionisation potential for the C_{60} molecule is 7.6 eV, whereas its electron affinity is 2.65 eV. The large ionisation potential prevents C_{60} from behaving as an electron donor.

In the solid state, C_{60} crystallises into a cubic structure via van der Waals interactions between neighbouring molecules. X-ray diffraction work [6, 7] revealed that at room temperature, the C_{60} crystalline powder consisted of spherical molecules of diameter ~7.1 Å, forming a random mixture of

hexagonal close-packed (*hcp*) and face-centred cubic (*fcc*) arrays. Elimination of solvent molecules trapped in interstitial cavities by sublimation leads only to a *fcc* crystal structure in which each C_{60} molecule is orientationally disordered [8]. This implies that when a static C_{60} molecule is placed in a cubic crystalline lattice, the icosahedral symmetry is broken leading to increasing the number of inequivalent carbon atoms to three and the number of positional parameters required to describe the molecule to eight. In the simplest possible crystalline structure, all molecules in the lattice have the same "standard orientation" with respect to a cubic crystal lattice. For this case, the relative orientation of a truncated icosahedron placed at the origin of a cubic lattice is such that the [100] axes pass through three orthogonal two-fold molecular axes (6:6 edges), and the four [111] axes pass through hexagonal faces. There are two such standard orientations of the molecule, related by a 90° rotation about [100] axes. In a *fcc* lattice, four C_{60} molecules are placed at the corners and at the midpoints of the faces of the cubic cell and if all of them have the same standard orientation, the crystal symmetry will be $Fm\bar{3}$. If, on the other hand, the molecules are orientationally disordered, then the crystal symmetry is raised to $Fm\bar{3}m$. This was proven by powder neutron [9] and X-ray [7] diffraction measurements – at room temperature, the lattice constant is 14.17 Å and the nearest-neighbour C_{60}-C_{60} distance is 10.02 Å (Fig. 1.3).

Synchrotron X-ray powder diffraction measurements of solid C_{60} showed the appearance of new reflection peaks on cooling. This is consistent with the occurrence of a first-order transition from the *fcc* phase to an orientationally ordered simple-cubic (*sc*) phase with an onset temperature at 249 K [10].

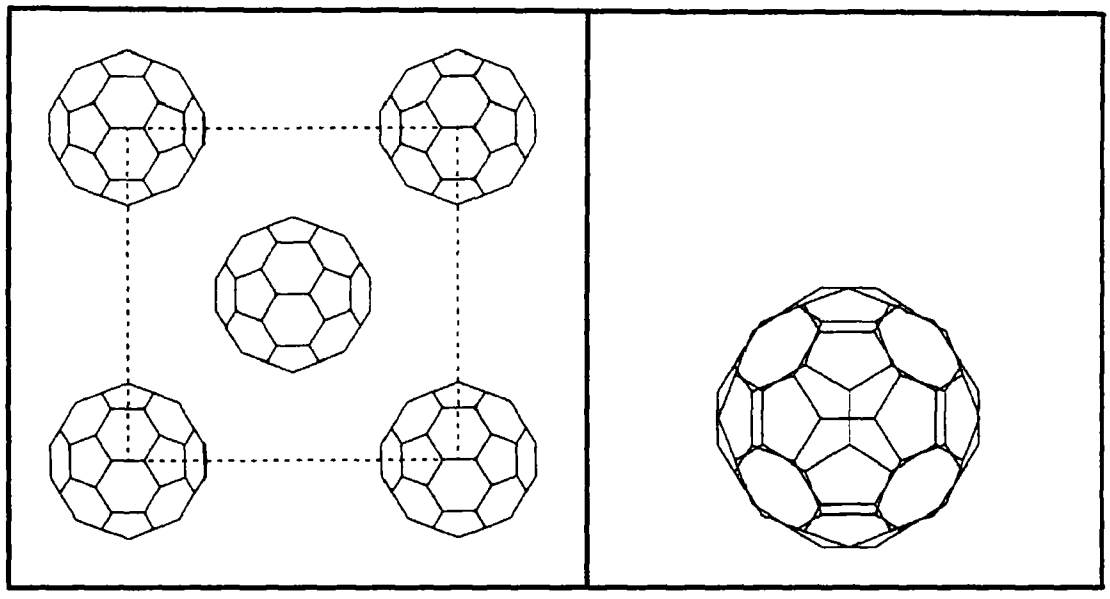

Fig. 1.3. Basal plane projection of the crystal structures of solid C_{60} for orientationally disordered face-centred cubic (*fcc*) structure (space group $Fm\bar{3}m$) at room temperature. The C_{60} in dark colours are shown to have the same orientation for simplicity. In the right panel, the two standard orientations of the C_{60}, which are related by 90° rotation, and give rise to merohedral disorder in the solid are also shown.

The reason for the orientational order has been discussed in terms of van der Waals bonding and electrostatic repulsion that results in the facing of the most electron-poor regions (the pentagonal faces) and the most electron-rich regions (the higher bond-order inter-pentagon bonds) of adjacent molecules [11]. The orientationally ordered *sc* structure has been discussed in detail by Sachidanandam and Harris [12], proposing the cubic $Pa\bar{3}$ space group. Here, starting from an ideal $Fm\bar{3}$ space group with the molecules in their standard orientation, and then, in $Pa\bar{3}$ structure, the molecules at (000), (½0½), (½½0), and (0½½) are rotated anticlockwise by an angle φ about the [111], [$\bar{1}\,\bar{1}$1], [1$\bar{1}\,\bar{1}$], and [$\bar{1}$1$\bar{1}$] axes, respectively [13]. The molecular rotation angle was found to be $\varphi \approx 98°$ [11, 12, 14] (Fig. 1.4).

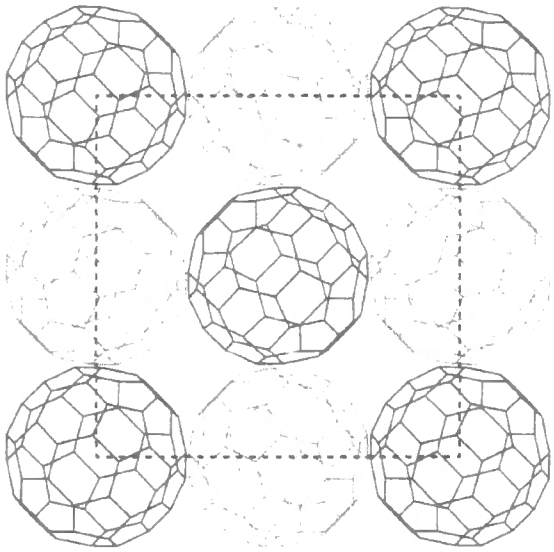

Fig. 1.4. Basal plane projection of the crystal structure of solid C_{60} for the orientationally ordered primitive-cubic structure (space group $Pa\bar{3}$) below 249 K.

1.3 Intercalated Fullerides

The doped derivatives of fullerene solids, known as fullerides, can be prepared by several different ways and exhibit interesting properties depending on the doping level and the nature of the dopant ions. The most widely used method for fulleride preparation is by intercalation of the fullerite solid. Intercalation of fullerite is successful because of two specific properties of C_{60}: a) the six low-lying empty orbitals and the high electronegativity of C_{60} allow C_{60} to accept electrons readily and b) the weak intermolecular van der Waals forces between the C_{60} molecules in the crystal.

The structure of pristine *fcc* C_{60} is characterised by the presence of two types of unoccupied interstitial holes with high symmetry, the smaller tetrahedral, T_d site (two per C_{60} unit with a radius of 1.12 Å) and the larger octahedral, O_h site (one per C_{60} unit with a radius of 2.06 Å). The crystalline

structures of intercalated fullerides can be classified into four types depending on the relative occupancy of the T_d and O_h sites: (i) a rock-salt type, in which one metal ion is accommodated in every O_h site, (ii) an antifluorite type, in which both T_d sites are occupied, (iii) a cryolite type, in which all T_d and O_h sites are fully occupied, and (iv) a zinc-blende type, in which the metal ions occupy half of the available T_d sites. The properties of the resulting fulleride salts are determined and can be modified by the number and nature of the intercalants.

When an ion occupies the tetrahedral site, it is important to consider its size as this influences sensitively the structural properties. This is because the size of the T_d site is larger than Na^+, but smaller than K^+, while the size of the O_h site is large enough to accommodate all alkali metal ions. This implies that when the T_d sites are occupied by the smaller ions, such as Na^+ or Li^+, there is enough space for the C_{60} molecules to rotate and adopt an orientationally ordered primitive cubic structure just below room temperature. However, different structural behaviour is observed when the T_d sites are occupied by the larger metals, as these cannot be accommodated without substantial expansion of the lattice. In this case, the C_{60} molecules are no longer free to rotate, and adopt a merohedrally disordered structure.

Upon doping, charge transfer between the guest donor atoms and the host C_{60} acceptor molecules takes place, where the transferred electrons are delocalised over the molecular cage. Intercalation of solid C_{60} with electron donors, such as the alkali-metals, results in a wealth of intercalated fulleride salts with stoichiometries A_xC_{60}, where A represents an alkali-metal and x can be as low as 1 (Cs_1C_{60}) or as high as 12 ($Li_{12}C_{60}$). This reflects the ease of reduction of C_{60}, especially to oxidation states ranging from -1 to -6.

In 1991, it was discovered that the alkali-metal fullerides, A_xC_{60}, are conducting [15]. Soon afterwards, it was also observed that among these fullerides, potassium-doped C_{60} becomes superconducting with an onset temperature of 18 K [16]. The discovery of superconductivity with relatively high transition temperature in alkali-metal fullerides initiated intensive scientific research in the intercalated fullerene solids area.

1.3.1 Alkali-metal doped Fullerides

Prominent among the alkali-metal fulleride salts are those with composition A_3C_{60}, as it is the only composition that exhibits superconductivity. The first evidence for superconductivity in alkali-metal doped C_{60} was observed in K_3C_{60} ($T_c \sim 18$ K). Within a short period of time, superconductivity in other alkali-metal fullerides at even higher temperatures was observed ($T_c \approx 28$ K for Rb_3C_{60}) [17].

The structure of A_3C_{60} fullerides is *fcc* and is based on the cryolite structure type. However, different structural behaviour is observed between alkali fullerides containing larger alkali ions (Cs, Rb, K) and those containing smaller alkali ions (Na, Li). In the first case, the structure is best described in the space group $Fm\bar{3}m$ with an expanded unit cell size caused by the addition of alkali ions (Fig. 1.5). The fulleride ions are no longer free to rotate due to steric effects associated with the dopants in the T_d sites. Instead, they are characterised by merohedral disorder and occur in two equally populated orientations which are the two standard orientations already described for C_{60}. No phase transitions driven by changes in the reorientational behaviour

occur at low temperatures, while C_{60}^{3-} ions perform small-amplitude librational motion whose amplitude increases and energy decreases with increasing temperature.

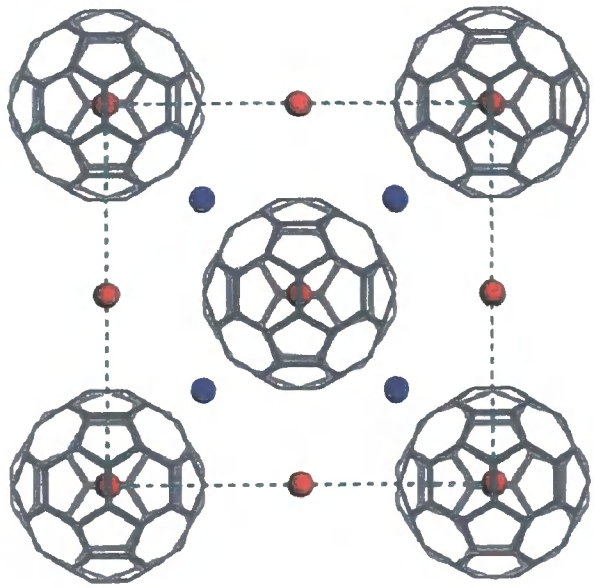

Fig. 1.5. The cryolite structural type adopted by A_3C_{60} (A = K, Rb) fullerides. The grey spheres represent the C_{60}^{3-} ions, while red and blue spheres represent alkali-metal ions residing in the O_h and T_d sites, respectively. The structure is *fcc* (space group $Fm\bar{3}m$) with the C_{60}^{3-} ions adopting two different molecular orientations related by a 90° rotation about the [001] or equivalently by 44°23' about the [111] crystal axis.

Different behaviour is observed when the T_d sites are occupied by smaller alkali-metals, Na^+ or Li^+ in systems like Na_xC_{60} and Li_xC_{60}. Unlike the case of K^+ and Rb^+, Na^+ and Li^+ ions are too small to stabilise the A_3C_{60} *fcc* structure [18, 19]. While many attempted to prepare Na_3C_{60}, it has been reported that Na_3C_{60} shows phase separation on cooling into Na_2C_{60}, where the dopants fill the T_d sites, leaving the O_h sites unoccupied and Na_6C_{60}, where two Na^+ ions occupy T_d sites and four Na^+ ions occupy O_h sites

preserving the *fcc* structure [20-22]. No superconductivity is observed in this system. Superconducting compounds containing smaller alkali metals can be found in $A_2A'C_{60}$, where A = Na or Li and A' = Rb or Cs [23, 24]. In these cases, the smaller Na^+ or Li^+ ions are placed in T_d sites and the larger Rb^+ or Cs^+ ions are placed in O_h sites. As orientational ordering is sensitive to the dopant occupying the T_d sites, the fulleride ions are no longer confined to the two standard orientations described earlier; instead, there is enough space for them to rotate in such a way as to optimise both the attractive A^+-C_{60}^{3-} and the C_{60}^{3-}-C_{60}^{3-} interactions. As a consequence, the $Na_2A'C_{60}$ systems adopt an orientationally ordered primitive cubic (space group $Pa\bar{3}$) structure, in which the majority of fulleride ions are rotated counter-clockwise by ~98° about [111] cube diagonal, with remaining ions adopting minor orientations (Fig. 1.6a).

When Li^+ ions are introduced as dopants to afford fullerides such as Li_2CsC_{60}, structural studies reveal that the systems adopt *fcc* structures (space group $Fm\bar{3}m$) but they contain quasi-spherical C_{60}^{3-} ions [25]. Detailed analysis has shown that there is a substantial excess of carbon atom density in the $\langle 111 \rangle$ directions, indicating strong bonding Li^+-C interactions. This is consistent with Raman spectroscopic measurements, which show that the number of electrons transferred from each Li atom to C_{60} is n~0.75 [26]. This implies a t_{1u} band filling level of less than three (~2.5), consistent with the absence of superconductivity.

It should be noted that it has been very difficult to isolate by standard solid state preparative routes a stable fulleride phase with stoichiometry

Cs_3C_{60} in the *fcc* structure, as this readily disproportionates into Cs_4C_{60} and Cs_1C_{60}. However, solution-based synthetic protocols have recently led to the isolation of Cs_3C_{60} with a body-centred-cubic-derived (*bcc*) structure. Cs_3C_{60} adopts the so-called A15-type structure, which has primitive cubic symmetry as the fulleride anions at the body centre are rotated by 90° about the [100] direction relative to the anion at the origin. A15-structured Cs_3C_{60} is an insulator at ambient pressure but becomes a bulk superconductor with $T_c(P)$ passing through a maximum at 38 K [27] (Fig. 1.6b).

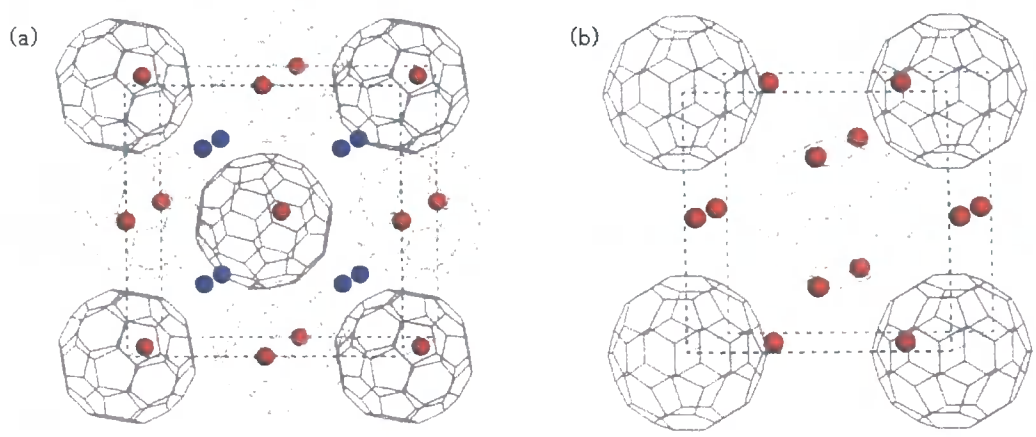

Fig. 1.6. Crystal structures of alkali fulleride phases, $A_2A'C_{60}$ and Cs_3C_{60}. (a) orientationally ordered primitive cubic (space group $Pa\bar{3}$) for A = Na and A' = Rb, Cs, and (b) A15-type (space group $Pm\bar{3}n$) for Cs_3C_{60}.

In all superconducting compounds adopting the *fcc* structure, T_c increases with increasing lattice constant (Fig. 1.7) reaching the highest value of T_c = 33 K for $RbCs_2C_{60}$ [28]. The relationship between lattice dimensions and superconducting transition temperatures in A_3C_{60} both at ambient and high pressures is consistent with T_c being modulated by the density-of-states at the Fermi level, $N(E_F)$ [17]. As the interfullerene separation increases, the overlap between the molecules decreases; this leads

to a reduced bandwidth and, for a fixed band filling, to an increased N(E_F). From a BCS type relationship:

$$T_c \propto (\hbar\omega_{ph})\exp[-1/N(E_F)V] = (\hbar\omega_{ph})\exp(-1/\lambda) \qquad \text{(Eqn. 1.3)}$$

where V is the electron-phonon coupling strength and ω_{ph} is the average intramolecular phonon energy. This implies that the observed T_c may be understood in terms of: (i) a high average phonon frequency resulting from the light carbon mass and the large force constants associated with the intramolecular modes, (ii) a moderately large V with contribution from both radial and tangential C_{60} vibrational modes and (iii) a high DOS at E_F, resulting from the weak intermolecular interactions.

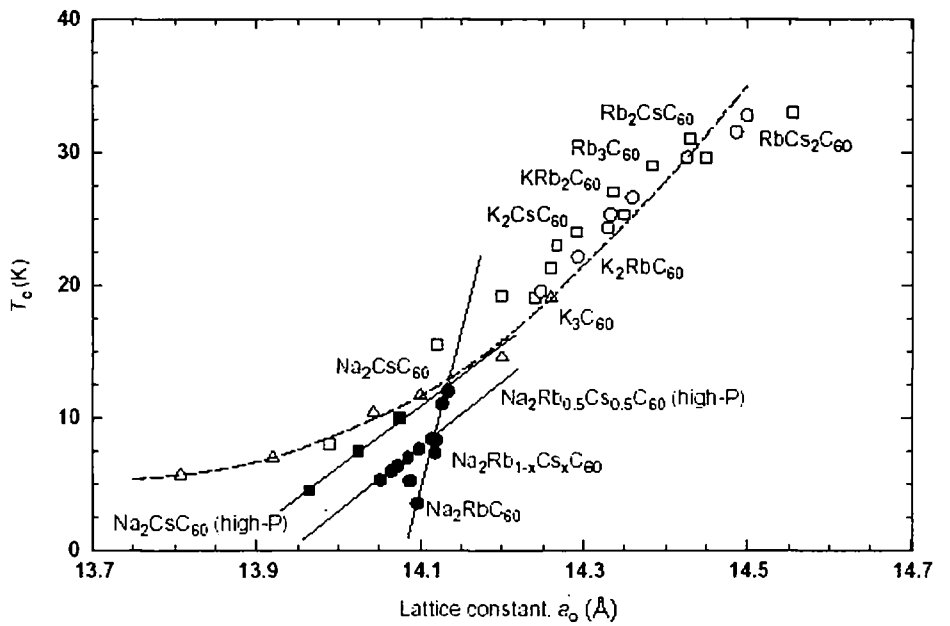

Fig. 1.7. Dependence of T_c on the cubic lattice constant, a_0, for various A_3C_{60}.

In alkali-metal doping, charge transfer of one electron per dopant atom to the C_{60} molecule occurs, leading to C_{60}^{n-} molecular anions and gradual

filling of the (LUMO) of t_{1u} orbital. A metallic state is achieved when this level is half filled, corresponding to the stoichiometry A_3C_{60} (or $A_xA'_{3-x}C_{60}$ for a binary alloy) and an insulating state is achieved when it is fully occupied, corresponding to A_6C_{60} fullerides. This assumption depends on the electronic kinetic energy, defined by the t_{1u} bandwidth W, being the dominant energy scale. However, the validity of this assumption is tested when the magnitudes of the on-site Coulomb repulsion, U, and W of these materials are compared [29]. The Hubbard U, which is defined as the difference between the ionisation energy and the electron affinity, acts to oppose the tendency of the electrons to delocalise and reduce their kinetic energy. This competes with the energy gained by delocalising the outer electrons in the solid, given by W, and if the repulsion energy is larger than that gained on delocalisation, then the electrons become localised and a metal-insulator transition takes place [30].

The estimate of U for the free C_{60} molecule is on the order of 3 eV, while in the solid, U is reduced due to the polarisation of surrounding molecules to give ~1 eV. The typical values of W for A_3C_{60} is ~0.5 eV. The single-band Hubbard model gives the critical (U/W) ratio to produce insulating behaviour as between 1 and 1.5 [31], and thus the A_3C_{60} systems are expected to be in the Mott-Hubbard insulating state. However, metallic behaviour survives with the triple orbital degeneracy of the t_{1u} LUMO state being the key difference between the actual electronic structure of the fullerides and theoretical models. Theoretical work indicates that the critical U/W ratio for electron localisation is influenced by the orbital degeneracy N at each site, which reduces the gap from $U-W$ to $U-\sqrt{N}W$, and shifts the boundary of the metal-insulator transition to a critical value of $(U/W)_c \approx 2.5$ [32]. As a result,

the metallic fulleride phases can be considered as archetypal highly-correlated molecular systems with electron correlations playing a crucial role in determining the normal and superconducting state properties of stoichiometric A_3C_{60}.

1.3.2 Alkaline-earth-metal doped Fullerides

The solid-state chemistry of alkaline-earth-metal intercalated fullerides is not as widely established as that of the alkali-metals. Still a broad range of compositions has gradually become available, exhibiting interesting structural and electronic properties. Highly doped states of C_{60}^{n-} (n > 6) can be achieved when alkaline-earth-metals are used as intercalants, in which the conduction band is derived from the next unoccupied triply degenerate t_{1g}, (LUMO+1), state of C_{60}. For instance, mixed alkali and alkaline-earth fullerides have been synthesised for higher doping concentrations, resulting in doping levels as high as n = 9 which correspond to half-filling of the t_{1g} state. Among these, stable superconducting phases were observed in the $A_3Ba_3C_{60}$ (A = K, Rb) family, which can be thought as the direct analogue of the t_{1u} superconductors.

Among the alkaline-earth salts, the $A_3Ba_3C_{60}$ (A = K, Rb, Cs) family is of particular interest. Bulk superconductivity is observed for $K_3Ba_3C_{60}$ (T_c = 5.4 K) and $Rb_3Ba_3C_{60}$ (T_c = 2.0 K), while $Cs_3Ba_3C_{60}$ is not a superconductor down to 0.5 K [33, 34]. $K_3Ba_3C_{60}$ adopts a *bcc* structure [17], isostructural with the non-superconducting A_6C_{60} fullerides. Due to the similar ionic radii of the two cations, the occupation of the interstitial sites by K^+ or Ba^{2+} is random and the structure can be regarded as a 1:1 solid solution of the isostructural

fullerides, K_6C_{60} and Ba_6C_{60}. A notable feature here is that susceptibility measurements showed that $N(E_F)$ decreases with increasing cell size in sharp contrast with the A_3C_{60} superconductors [18]. A combined high-resolution synchrotron X-ray and neutron diffraction study revealed the existence of short Ba-C and K-C contacts, implying hybridisation between the K, Ba, and C_{60} states [35]. The orbital mixing strongly modifies the shape of the conduction band, leading to a larger bandwidth and a smaller $N(E_F)$ value than those in t_{1u} superconductors, despite the similar band filling.

Superconductivity was also encountered for binary alkaline-earth fullerides with different compositions, namely, Ca_5C_{60}, Sr_4C_{60}, and Ba_4C_{60}. In the case of barium and strontium metals, it was reported that they form stable compositions AE_xC_{60} for x = 3, 4, and 6 (Fig. 1.8). AE_3C_{60} (AE = Ba, Sr) are insulating and adopt the A15 structure type (space group $Pm\bar{3}n$) with lattice constants of 11.34 and 11.14 Å, respectively [36, 37]. Early works suggested that a superconducting phase was observed for AE_6C_{60} (AE = Ba, Sr) ($Im\ \bar{3}\ bcc$) with transition temperatures of 6.5 K for Ba_6C_{60} and 4 K for Sr_6C_{60} [37, 38]. Subsequently, it was unambiguously established that both Ba_6C_{60} and Sr_6C_{60} are metallic despite the formally full t_{1g}-derived band, but not superconducting [39]. Their density-of-states at the Fermi level is found to increase with decreasing interfullerene separation, which was rationalised both theoretically and experimentally in terms of strong hybridisation between the alkaline-earth *d* and *s* orbitals and C_{60} $p\pi$-orbital which leads to a modified and much broader conduction band [40, 41].

Bulk superconducting phases in the Ba-C_{60} and Sr-C_{60} systems have been established to have stoichiometries Ba_4C_{60} and Sr_4C_{60} with T_c of 6.7 and 4.4 K, respectively adopting highly anisotropic orthorhombic structures

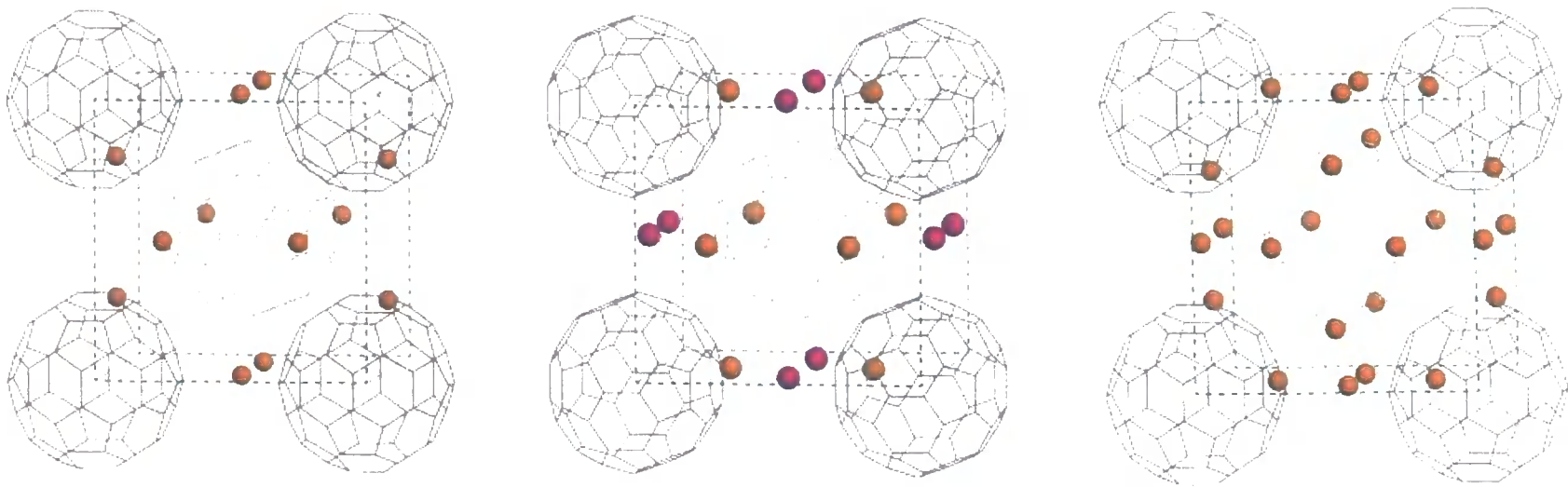

Fig. 1.8. Crystal structures of AE_xC_{60} (AE = Ba, Sr), (a) $x = 3$, A15-type structure (space group $Pm\bar{3}n$), (b) $x = 4$, orthorhombic structure (space group *Immm*); the two sets of crystallographically distinct barium ions, Ba(1) (*m*2*m* site) and Ba(2) (2*mm* site) are shown by yellow and purple spheres, and (c) $x = 6$, *bcc* structure (space group $Im\bar{3}$).

(space group *Immm*). These systems are the first examples reported so far of non-cubic superconductors. High resolution X-ray diffraction has revealed the existence of very short Ba-C contacts which imply strong hybridisation between the $5d$ orbitals of Ba and the $2p$ orbitals of carbon [42]. Such a strong orbital mixing was confirmed by local-density approximation (LDA) calculations [43]. In sharp contrast to superconducting Ba_4C_{60} and Sr_4C_{60}, the alkali fullerides, A_4C_{60} are non-metallic despite the similar (A = K, Rb) or identical (A = Cs) structures. This is due to the narrow band nature of the t_{1u}-originated conduction band with the metallic state being easily destroyed by various instabilities.

1.3.3 Rare-earth-metal doped Fullerides

Recent progress in rare-earth intercalated fullerides has resulted in preparation of some interesting compounds, although in this area much less is still known when compared to the chemistry of alkali and alkaline-earth fullerides. This has been mainly due to the difficulties in devising reliable protocols for preparation of single-phase RE_xC_{60} materials. Reaction of rare-earth- metals with fullerenes requires high temperature annealing; however, this competes with the formation of rare-earth carbide phases [44]. The first successful intercalation of C_{60} with a rare-earth-metal has been reported for ytterbium, leading to the $Yb_{2.75}C_{60}$ composition [45]. Following this result, various research groups reported that single-phase materials can be obtained for compositions, RE_xC_{60} (RE = Sm, Eu, and Yb) with $x = 2.75$ and 6 [46-49]. Some of these compounds were reported to be superconducting, while others to exhibit interesting magnetic properties related to the

introduction of electronically active cations in the void spaces of the C_{60} lattice, which may result in coupling of the two electronically active sublattices. For instance, given that the rare-earth dopants may carry a magnetic moment, rare-earth fullerides can be good candidates for the synthesis of molecular magnetic materials. Such examples have been recently provided by work on the Eu-C_{60} phase diagram, leading to the isolation of highly-doped Eu_6C_{60} and Eu_9C_{70} phases which display transitions to ferromagnetic states with Curie temperatures of 14 and 40 K, respectively [50, 51]. The ferromagnetic interaction in these systems develops either through direct exchange interactions between the Eu^{2+} ($4f^7$) ions or through *p-d, f* interactions mediated by the fulleride units.

i) Possible superconductivity in $RE_{2.75}C_{60}$ (RE = Yb, Sm)

Early work has claimed that $Yb_{2.75}C_{60}$ was superconducting below 6 K with a shielding fraction of ~8% [45]. Powder X-ray diffraction was used for a quantitative structural determination of $Yb_{2.75}C_{60}$, which showed that Yb cations are located in both T_d and O_h interstitial sites and X-ray absorption near-edge structure (XANES) measurements showed that they are divalent Yb^{2+} ions. The crystal structure of $Yb_{2.75}C_{60}$ was found to be orthorhombic with a space group *Pcab* ($b \geq a \geq c$, no. 61, option 2), a direct subgroup of $Pa\bar{3}$. The Yb^{2+} cations occupy all O_h sites but leave one out of every eight tetrahedral sites unoccupied. In addition, this structural model is characterised by large displacements of the cations from the centres of the O_h sites ($\approx$ 2.3 Å) and smaller displacements from the centres of the T_d sites ($\approx$ 0.4 Å) where these displacements are directed towards the nearest T_d defects

and the mid-pont of two neighbouring C_{60} molecules, respectively. These T_d vacancies and associated off-centre displacements of the O_h cations, due to a strong, short-range interaction between C_{60} and the divalent Yb cations, are thought to be responsible for the long-range ordering of the T_d defects, which results in a unit cell with dimensions twice as large as those of the commonly encountered *fcc* structure of the alkali fullerides (unit cell volume: $V_{ortho} \approx 8\,V_{fcc}$) [52], known as the cation-vacancy ordered superstructure (Fig. 1.9).

Similar measurements have been carried out for $Sm_{2.75}C_{60}$ and $Eu_{2.75}C_{60}$, where X-ray diffraction profiles obtained were almost identical to each other, indicating that all $RE_{2.75}C_{60}$ (RE = Sm, Eu, Yb) have the same crystal structure. Magnetic measurements showed that superconductivity was also observed for $Sm_{2.75}C_{60}$ with a transition temperature of 8 K and a shielding fraction of 10% in a field of 20 Oe [46].

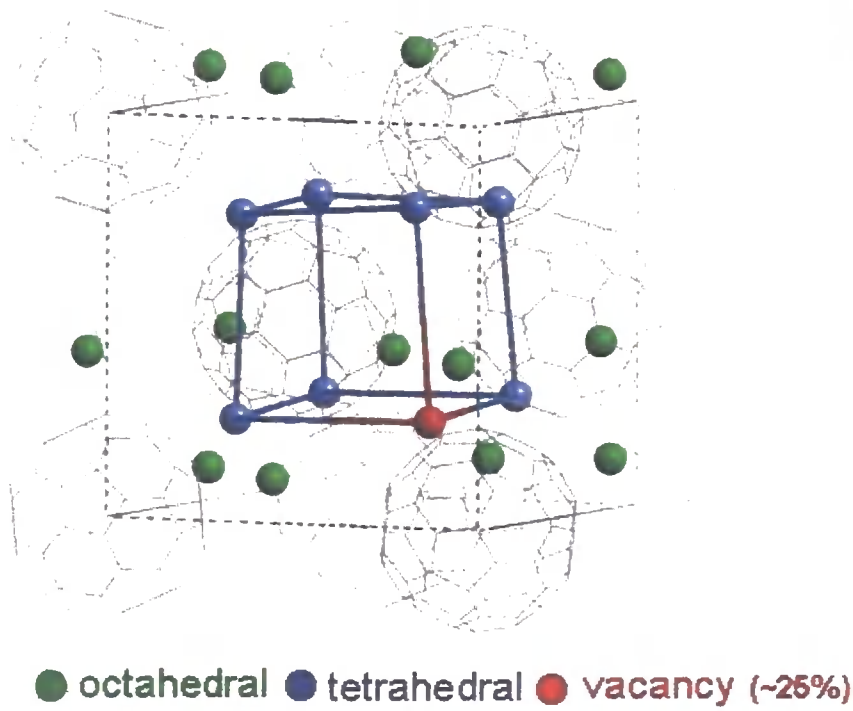

Fig. 1.9. Building block of the orthorhombic superstructure of $RE_{2.75}C_{60}$ that

Fig. 1.9. (continued) can be obtained by doubling the sub-cell along all three lattice directions. Distorted octahedral and tetrahedral rare-earth cations are represented by green and blue spheres, respectively. The tetrahedral defect is shown as red sphere.

On the other hand, the highly-doped rare-earth fullerides, RE_6C_{60}, are isostructural with the A_6C_{60} alkali fullerides adopting the *bcc* structure and no superconducting phase was observed [47, 50]. This is suggesting that cation-vacancy ordering and the cation displacements disappear with further addition of RE dopants into the C_{60} solid. The preparation of RE_xC_{60} samples of nominal concentration $x \neq 2.75$ and 6 have been tried by several groups. It has been reported that when the concentration of RE is less than 2.75, no stable crystal phases were detected, and phase separation into pristine C_{60} and $RE_{2.75}C_{60}$ was observed [51, 53, 54]. On the other hand, for intermediate phases between $RE_{2.75}C_{60}$ and RE_6C_{60}, only the appearance of Bragg reflections from RE_6C_{60} [53-56] was found, and thus it was concluded that the mixture is under non-equilibrium conditions and that $RE_{\sim 3}C_{60}$ is in a metastable state which could represent a transition state towards RE_6C_{60}.

ii) Magnetic properties of Eu_6C_{60}

As previously mentioned, superconductivity was not observed in $Eu_{2.75}C_{60}$; instead, the magnetic properties of $Eu_{\sim 3}C_{60}$ and Eu_6C_{60} investigated by Ksari-Habiles *et al.* showed some magnetic anomalies [48]. In this report, it was claimed that a mixed valence state of Eu exists for Eu_xC_{60}, where $Eu^{2+}/Eu^{3+} = 2$ for $x \sim 3$ and a transition to a ferromagnetic state near $T_C = 16$ K, while $Eu^{2+}/Eu^{3+} \approx 1 - 4$ depending on sample for $x = 6$

and three successive magnetic anomalies at 65, 12 and 8 K. The results obtained from recent work on Eu-C_{60} systems are different from what was claimed in this early report. For $Eu_{\sim 3}C_{60}$ compounds, detailed studies have been carried out in the current project and will be discussed in a later Chapter. In the case of Eu_6C_{60}, the ferromagnetic transition occurs near 14 K, and unlike the early report no evidence for three anomalies was found [57]. Rietveld refinement of neutron diffraction data at 1.7 K resulted in a magnetic moment of 7.1(3) μ_B per Eu atom, which is in agreement with field-dependent magnetisation measurements at 2 K [50]. This result is also consistent with the magnetic moment of Eu^{2+}, where the Eu atom has a magnetic moment of 7 μ_B (S = 7/2, L = 0, and J = 7/2) in the divalent state, while it is non-magnetic (S = 3, L = 3, and J = 0) in the trivalent state. This indicates that the Eu sites in Eu_6C_{60} are in the divalent state, not a mixed valence state claimed before. The origin of the ferromagnetic exchange interactions between Eu^{2+} can be interpreted in the same manner as in the case for AE_6C_{60} (AE = Sr, Ba). Here, due to the short lattice constant for Eu_6C_{60}, the Eu-C contacts are also short implying the existence of hybridisation between 5d and 6s orbitals of Eu and the t_{1g} orbital of C_{60}. This strong interaction affects the magnetic interaction of 4f electrons, thus leading the observed magnetic and conducting properties of the material.

iii) Recent advances in Rare-earth based fullerides

Following the report on the appearance of superconductivity in $RE_{2.75}C_{60}$ (RE = Yb, Sm), intensive research on these compounds was initiated. However, recent magnetisation studies on numerous samples [53,

58] showed that the reports of bulk superconductivity have been erroneous. Only a trace superconducting fraction (less than 0.8%) was ever observed on $Yb_{2.75}C_{60}$ and it was found to increase as the nominal Yb concentration was increased. The maximum superconducting diamagnetic susceptibility was reached for the nominal Yb_4C_{60} phase and starts to decrease as Yb is added further towards Yb_6C_{60}, while the T_c did not vary with the nominal Yb concentrations [53]. This implies, in analogy with the chemistry of alkaline-earth fullerides where the superconducting phase was found to be AE_4C_{60} (AE = Ba, Sr), that Yb_4C_{60} phase might be the true bulk superconducting phase.

In the case of $Sm_{2.75}C_{60}$, the results of low-field magnetisation measurements showed no evidence for a transition to an (even trace) superconducting state down to 2 K in contrast to ref. 46. However, very interestingly, the temperature evolution of the structural properties of the same compound obtained by high resolution synchrotron X-ray diffraction at various temperatures between 4 and 295 K revealed that $Sm_{2.75}C_{60}$ exhibits isotropic negative thermal expansion (NTE) in the temperature range 4 to 32 K [59] (Fig.1.10a). The origin of this feature in this temperature region was interpreted by implicating a temperature-induced valence transition of Sm from +2 to an intermediate valence of +(2+ε) state. Soon afterwards, the compression behaviour of $Sm_{2.75}C_{60}$ was also studied at elevated pressures ranging from 0 to 6 GPa at room temperature using the powder synchrotron X-ray diffraction technique [60]. Here, an abrupt hysteretic phase transition was also observed at ~4 GPa; the transition was accompanied by a large lattice collapse induced by a Sm valence transition from +(2+ε) state towards +3 (Fig. 1.10b). The pressure-induced phase transition is also accompanied

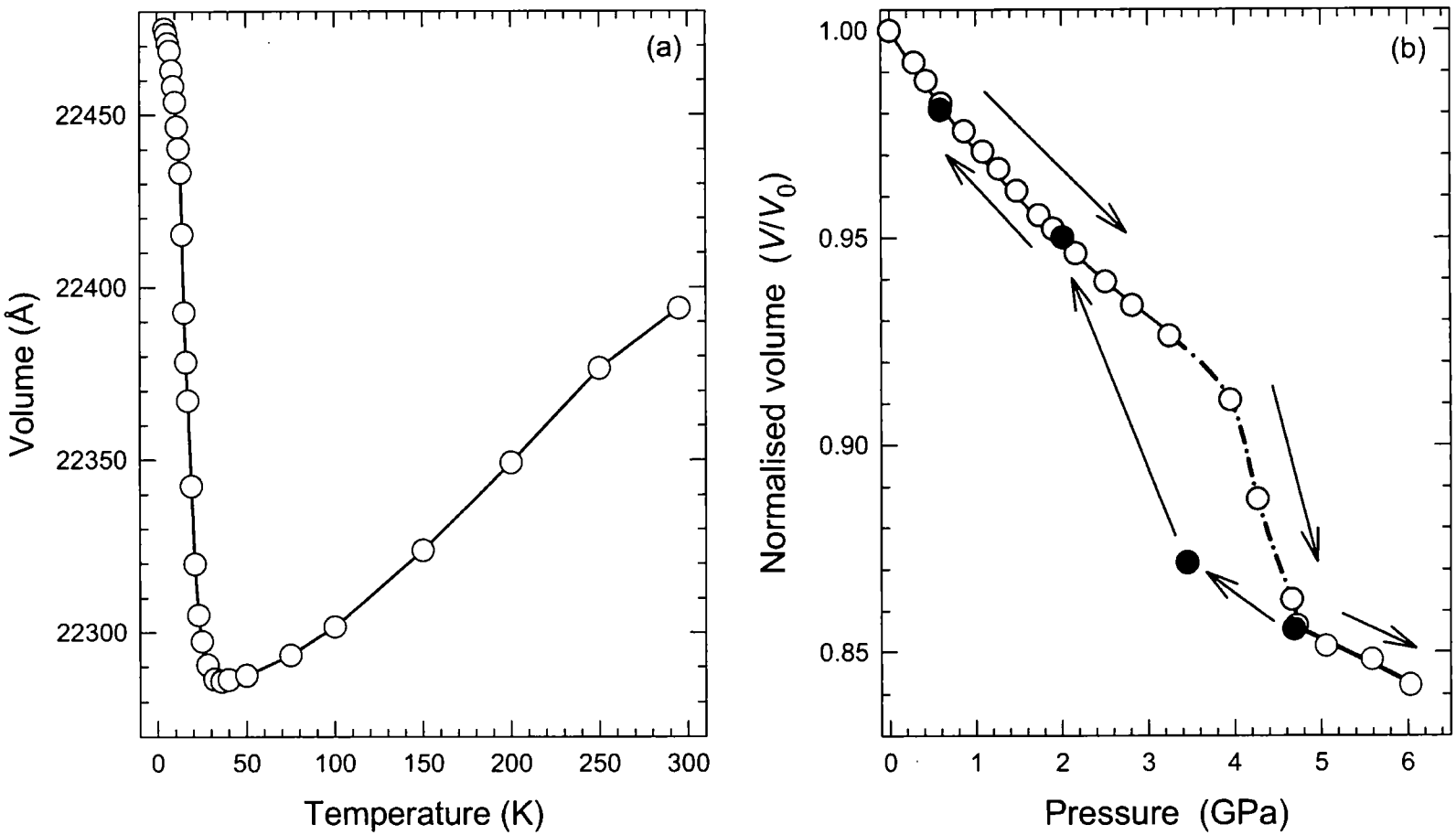

Fig. 1.10. (a) Temperature and (b) pressure evolution of the unit cell volume in $Sm_{2.75}C_{60}$.

by a reversible colour change of the material from black to golden, implying the occurrence of an insulator- to-metal transition upon pressurisation.

The properties of this mixed valence rare-earth fulleride, which undergoes an electronically-driven valence transition from one electronic state to another caused by changing some external stimulus, are determined by the coupling of the strongly correlated rare-earth $4f$ and $5d$ bands with the narrow C_{60} t_{1u} band. The tendency of Sm to exhibit mixed valence states and valence transitions with changes in external parameters is due to the small energy difference between the divalent and trivalent states as shown in the figure below (Fig. 1.11) [61].

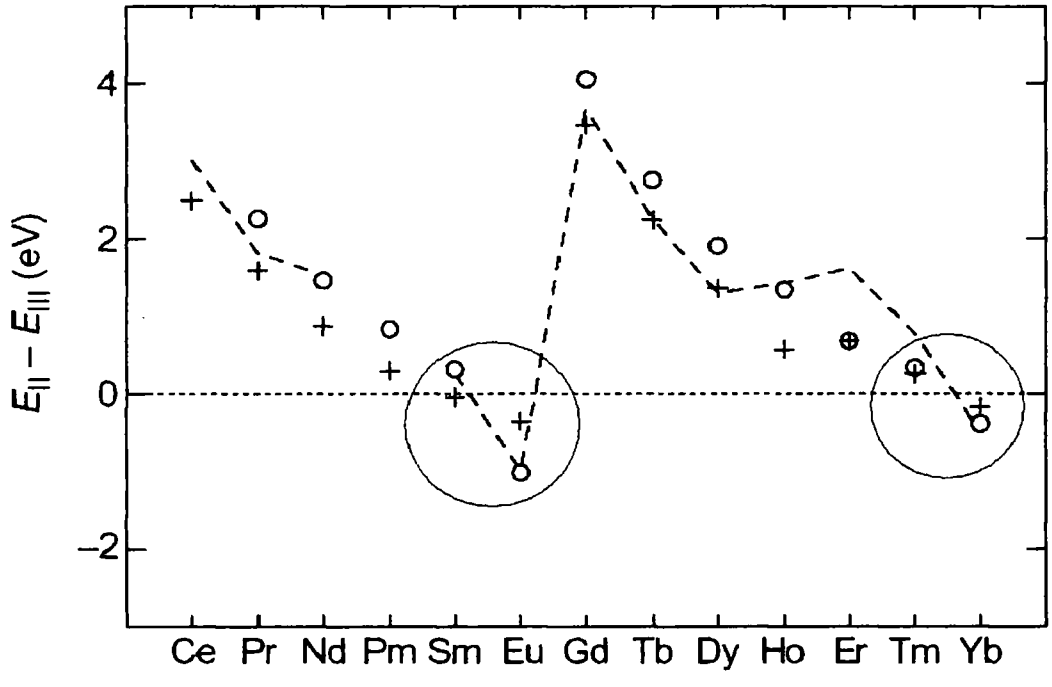

Fig. 1.11. The energy difference between divalent and trivalent states of rare-earth-metals. Open circles and crosses show the calculated values for rare-earth metals and that for rare-earth sulfides, respectively. The blue circles indicate the metals we attempted to intercalate the C_{60} solid in the present work.

We note here that this leads to the prediction of encountering analogous electronic and structural instabilities in other isostructural rare-earth fullerides such as $Yb_{2.75}C_{60}$, $Eu_{2.75}C_{60}$ and $Tm_{2.75}C_{60}$. At the same, the possible synthesis of mixed compositions, $(Sm_{1-x}Eu_x)_{2.75}C_{60}$ and $(Sm_{1-x}Ca_x)_{2.75}C_{60}$ ($0 \leq x \leq 1$), could allow to follow the effect on the anomalous lattice responses by diluting the rare-earth cation sublattice. The properties of such fulleride phases will be discussed in later Chapters of this thesis.

1.4 Outline of the Thesis

The aim of the present thesis is to carry out systematic investigations on the structural and electronic properties of selected rare-earth-metal based fullerides using synchrotron X-ray diffraction, X-ray absorption spectroscopy, Rutherford Backscattering spectroscopy, and SQUID magnetisation. The investigation was initiated following the exciting results obtained on $Sm_{2.75}C_{60}$. A variety of temperature- and pressure-driven abrupt or continuous valence transitions were expected by substituting Sm by other rare-earth and alkaline-earth metals. Difficulties in the preparation of single-phase rare-earth based fullerides had prevented before such investigations. Thus, establishing reliable and reproducible synthetic protocols for intercalation of both rare-earth and alkaline-earth metals was required. The details for the synthetic techniques that have been employed during this project are presented in Chapter 2. This chapter also includes the description of the experimental instrumentation and the background to the techniques employed together with theoretical and practical aspects related to data analysis.

Chapter 3 deals with the structural properties of the $Yb_{2.75}C_{60}$ fulleride, where the evolution of the unit cell dimensions were followed by using the synchrotron X-ray powder diffraction method. The diffraction profiles were collected both as a function of temperature and pressure in order to find out what is happening in this compound at the microscopic level. Extraction of the unit cell volumes was performed using both Rietveld and LeBail refinement methods. The temperature-dependent measurements revealed the occurrence of NTE at low temperatures on heating but with somewhat higher onset temperatures compared to those in $Sm_{2.75}C_{60}$. Results obtained on application of pressure are discussed towards the end of chapter.

Chapter 4 presents an investigation of the effect of Eu substitution on the Sm sites in samples with stoichiometry, $(Sm_{1-x}Eu_x)_{2.75}C_{60}$ $(0 \leq x \leq 1)$. Here, surprisingly, the observed unit cell metrics become larger as the Eu concentration increases, in contrast to what is expected from the simple lanthanide contraction effect. The temperature evolution of the lattice parameters for various Eu concentrations was closely followed. The results of the pressure evolution of both $Eu_{2.75}C_{60}$ and Eu and Sm solid solutions showed the occurrence of valence transitions above some critical pressure, accompanied by both reversible lattice collapse and insulator-to-metal transitions.

In Chapter 5, the results obtained on Ca-substituted compounds with the stoichiometry $(Sm_{1-x}Ca_x)_{2.75}C_{60}$ $(0 \leq x \leq 1)$ are discussed. In a similar fashion to the behaviour of Yb- and Eu-substituted compounds, anomalous responses of the lattice size upon cooling were observed, except for the case of the alkaline-earth parent compound, $Ca_{2.75}C_{60}$. This is consistent with the direct relationship between the observed physical effects and the presence of

selected rare-earth ions in these systems. Direct experimental information about the valence states of the rare-earth ions in the $(Sm_{2/3}Ca_{1/3})_{2.75}C_{60}$ fulleride was obtained by using partial fluorescence yield (PFY) X-ray absorption spectroscopy and resonant inelastic X-ray scattering (RIXS) measurements. Both PFY-XAS and RIXS have revealed the electronic origin of the first-order transition in the low temperature region, which was rationalised in terms of the average RE oxidation state approaching +2 upon cooling below some critical temperature. The complementary results from RBS and SQUID measurements will also be presented in detail.

Finally, Chapter 6 summarises the results of the present work, its contribution to our understanding of the properties of fullerene-based materials, and the future directions.

1.5 References

[1] Kroto, H. W., Heath, J. R., O'Brien, S. C., Curl, R. F., Smalley, R. E., *Nature* **318**, 162 (1985).

[2] Dresselhaus, G., Dresselhaus, M. S., Eklund, P. C., *Phys. Rev. B* **45**, 6923 (1992).

[3] Birkett, P. R., Hitchcock, P. B., Kroto, H. W., Taylor, R., Walton, D. R. M., *Nature* **357**, 478 (1992).

[4] Fischer, J. E., Heiney, P. A., McGhie, A. R., Romanow, W. J., Denenstein, A. M., McCauley, J. P., Smith, A. B., *Science* **252**, 1288 (1991).

[5] Haddon, R. C., Brus, L. E., Raghavacari, K., *Chem. Phys. Lett.* **125**, 459

(1986).

[6] Krätschmer, W., Lamb, L. D., Fostiropoulos, K., Huffman, D. R., *Nature* **347**, 356 (1990).

[7] Heiney, P. A., Fischer, J. E., McGhie, A. R., Romanow, W. J., Denenstein, A. M., McCauley, J. P., Smith, A. B., Cox, D. E., *Phys. Rev. Lett.* **66**, 2911 (1991).

[8] Fleming, R., Hessen, B., Siegrist, T., Kortan, A. R., Marsh, P., Tycko, R., Dabbagh, G., Haddon, R. C., *Synthesis Properties and Chemistry of large Carbon Clusters*, American Chemical Society Symposium Series Vol. **481**, p. 25 (1991).

[9] David, W. I. F., Ibberson, R. M., Dennis, T. J. S., Hare, J. P., Prassides, K., *Europhys. Lett.* **18**, 225 (1992).

[10] Heiney, P. A., Vaughan, G. B. M., Fishcer, J. E., Coustel, N., Cox, D. E., Copley, J. R. D., Neumann, D. A., Kamitakahara, W. A., Creegan, K. M., Cox, D. M., McCauley, J. P., Smith, A. B., *Phys. Rev. B* **45**, 4544 (1992).

[11] David, W. I. F., Ibberson, R. M., Matthewman, J. C., Prassides, K., Dennis, T. J. S., Hare, J. P., Kroto, H. W., Taylor, R., Walton, D. R. M., *Nature* **353**, 147 (1991).

[12] Sachidanandam, R., Harris, A. B., *Phys. Rev. Lett.* **67**, 1467 (1991).

[13] Heiney, P. A., *J. Phys. Chem. Solds* **53**, 1333 (1992).

[14] Copley, J. R. D., Neumann, D. A., Cappelletti, R. L., Kamitakahara, W. A., Prince, E., Coustel, N., McCauley, J. P., Maliszewskyj, N. C., Fishcer, J. E., Smith, A. B., Creegan, K. M., Cox, D. M., *Physica B* **180 & 181**, 706 (1992).

[15] Haddon, R. C., Hebard, A. F., Rosseinsky, M. J., Murphy, D. W., Duclos, S. J., Lyons, K. B., Miller, B., Rosamilla, J. M., Fleming, R. M., Kortan, A.

R., Glarum, S. H., Makhija, A. V., Muller, A. J., Eick, R. H., Zahurak, S. M., Tycko, R., Dabbagh, G., Thiel, F. A., *Nature* **350**, 320 (1991).

[16] Hebard, A. F., Rosseinsky, M. J., Haddon, R. C., Murphy, D. W., Glarum, S. H., Palstra, T. T. M., Ramirez, A. P., Kortan, A. R., *Nature* **350**, 600 (1991).

[17] Fleming, R. M., Ramirez, A. P., Rosseinsky, M. J., Murphy, D. W., Haddon, R. C., Zahurak, S. M., Makhija, A. V., *Nature* **352**, 787 (1991).

[18] Gu, C., Stepniak, F., Poirier, D. M., Jost, M. B., Benning, P. J., Chen, Y., Ohno, T. R., Martins, J. L., Weaver J. H., Fure, J., Smalley, R. E., *Phys. Rev. B* **45**, 6348 (1992).

[19] Prassides, K., Christides, C., Thomas, I. M., Mizuki, J., Tanigaki, K., Hirosawa, I., Ebbesen, T. W., *Science* **263**, 950 (1994).

[20] Rosseinsky, M. J., Murphy, D. W., Fleming, R. M., Tycko, R., Ramirez, A. P., Siegrist, T., Dabbagh, G., Barrett, S. E., *Nature* **356**, 416 (1992).

[21] Tanigaki, K., Hirosawa, I., Ebbesen, T. W., Mizuki, J., Tsai, J. S., *J. Phys. Chem. Solids* **54**, 1645 (1993).

[22] Yildirim, T., Zhou, O., Fischer, J. E., Strongin, R. A., Cichy, M. A., Smith III, A. B., Lin, C. L., Jelinek, R., *Nature* **360**, 568 (1992).

[23] Tanigaki, K., Hirosawa, I., Ebbesen, T. W., Mizuki, J., Kuroshim, S., *Chem. Phys. Lett.* **203**, 33 (1993).

[24] Tanigaki, K., Hirosawa, I., Ebbesen, T. W., Mizuki, J., Shimakawa, Y., Kubo, Y., Tsai, J. S., Kuroshim, S., *Nature* **356**, 419 (1992).

[25] Hirosawa, I., Prassides, K., Mizuki, J., Tanigaki, K., Gevaert, M., Lappas, A., Cockcroft, J.K., *Science* **264**, 1294 (1994).

[26] Kosaka, M., Tanigaki, K., Prassides, K., Margadonna, S., Lappas, A., Brown, C.M., Fitch, A.N., *Phys. Rev. B* **59**, R6628 (1999).

[27] Ganin., A. Y., Takabayashi, Y., Khimyak, Y. Z., Margadonna, S., Tamai, A., Rosseinsky, M. J., Prassides, K., *Nature Mater.* **7**, 367 (2008).

[28] Tanigaki, K., Kuroshim, S., Fujita, J., Ebbesen, T. W., *Appl. Phys. Lett.* **63**, 2351 (1993).

[29] Margadonna, S., Prassides, K., *J. Solid State Chem.* **168**, 639 (2002).

[30] Durand, P., Darling, G. R., Dubitsky, Y., Zaopo, A., Rosseinsky, M. J., *Nat. Mater.* **2**, 605 (2003).

[31] Georges, A., Kotliar, G., Krauth, W., Rozenberg, M. J., *Rev. Mod. Phys.* **68**, 13 (1996).

[32] Koch, E., Gunnarson, O., Martin, R. M., *Phys. Rev. Lett.* **83**, 620 (1999).

[33] Iwasa, Y., Hayashi, H., Furudate, T., Mitani, T., *Phys. Rev. B* **54**, 14960 (1996).

[34] Iwasa, Y., Kawaguchi, M., Iwasaki, H., Mitani, T., Wada, N., Hasegawa, T., *Phys. Rev. B* **57**, 13395 (1998).

[35] Margadonna, S., Aslanis, E., Li, W. Z., Prassides, K., Fitch, A. N., Hansen, T. C., *Chem. Mater.* **12**, 2736 (2000).

[36] Kortan, A. R., Kopylov, N., Fleming, R. M., Zhou, O., Thiel, F. A., Haddon, R. C., Rabe, K. M., *Phys. Rev. B* **47**, 13070 (1993).

[37] Kortan, A. R., Kopylov, N., Özdas, E., Ramirez, A. P., Fleming, R. M., Haddon, R. C., *Chem. Phys. Lett.* **223**, 501 (1994).

[38] Kortan, A. R., Kopylov, N., Glarum, S., Gyorgy, E. M., Ramirez, A. P., Fleming, R. M., Zhou, O., Thiel, F. A., Trevor, P. L., Haddon, R. C., *Nature* **360**, 566 (1992).

[39] Gogia, B., Kordatos, K., Suematsu, H., Tanigaki, K., Prassides, K., *Phys. Rev. B* **58**, 1077 (1998).

[40] Erwin, S. C., Pederson, M. R., *Phys. Rev. B* **47**, 14657 (1993).

[41] Saito, S., Oshiyama, A., *Phys. Rev. Lett.* **71**, 121 (1993).

[42] Brown, C. M., Taga, S., Gogia, B., Kordatos, K., Margadonna, S., Prassides, K., Iwasa, Y., Tanigaki, K., Fitch, A. N., Pattison, P., *Phys. Rev. Lett.* **83**, 2258 (1999).

[43] Umemoto, K., Saito, S., *Phys. Rev. B* **61**, 14204 (2000).

[44] Margadonna, S., Iwasa, Y., Takenobu, T., Prassides, K., *Fullerene-Based Materials: Structures and Properties Structure and Bonding* **109**, 127 (2004).

[45] Özdaş, E., Kortan, A. R., Kopylov, N., Ramirez, A. P., Siegrist, T., Rabe, K. M., Bair, H. E., Schuppler, S., Citrin, P. H., *Nature* **375**, 126 (1995).

[46] Chen, X. H., Roth, G., *Phys. Rev. B* **52**, 15534 (1995).

[47] Chen, X. H., Liu, Z. S., Li, S. Y., Chi, D. H., Iwasa, Y., *Phys. Rev. B* **60**, 6183 (1999).

[48] Ksari-Habiles, Y., Claves, D., Chouteau, G., Touzain, P., Jeandey, C., Oddoou, J. L., Stepanov, A., *J. Phys. Chem. Solids* **58**, 1771 (1997).

[49] Cao, X. W., Hao, J. M., Wu, X. S., Wang, Y. F., Wu, Y., Liu, J. J., Hu, S. F., Lan, G. X., *Appl. Phys. A* **70**, 223 (2000).

[50] Margiolaki, I., Margadonna, S., Prassides, K., Hansen, T., Ishii, K., Suematsu, H., *J. Am. Chem. Soc.* **124**, 11288 (2002).

[51] Takenobu, T., Chi, D. H., Margadonna, S., Prassides, K., Kubozono, Y., Fitch, A. N., Kato, K., Iwasa, Y., *J. Am. Chem. Soc.* **125**, 1897 (2003).

[52] Sun, Z., Chen, X. H., Takenobu, T., Iwasa, Y., *J. Phys. Condens. Matter.* **12**, 8919 (2000).

[53] Takeuchi, J., Tanigaki, K., Gogia, B., In *Nanonetwork Materials*, AIP Conference Proceedings **590**, 361 (2001).

[54] Claves, D., Ksari-Habiles, Y., Chouteau, G., Collomb, A., Touzain, P.,

Solid State Commun. **99**, 359 (1996).

[55] Claves, D., Ksari-Habiles, Y., Chouteau, G., Touzain, P., *Solid State Commun.* **106**, 431 (1998).

[56] Claves, D., Hamwi, A., *Solid State Commun.* **113**, 357 (2000).

[57] Ishii, K., Fujiwara, A., Suematsu, H., Kubozono, Y., *Phys. Rev. B* **65**, 134431 (2002).

[58] Akada, M., Hirai, T., Takeuchi, J., Yamamoto, R., Kumashiro, R., Tanigaki, K., *Phys. Rev. B* **73**, 0945091 (2006).

[59] Arvanitidis, J., Papagelis, K., Margadonna, S., Prassides, K., Fitch, A. N., *Nature* **425**, 599 (2003).

[60] Arvanitidis, J., Papagelis, K., Margadonna, S., Prassides, K., *Dalton Trans.* 3144 (2004).

[61] Strange, P., Svane, A., Temmerman, W. M., Szotek, Z., Winter, H., *Nature* **399**, 756 (1999).

CHAPTER 2

EXPERIMENTAL TECHNIQUES

2.1 Introduction

In order to carry out the extensive investigation on the structural, electronic and magnetic properties of the rare-earth based fullerides in the solid state, a series of different experimental techniques have been employed. In particular, the use of synchrotron radiation facility was essential for studying their properties while having precise control of external stimuli such as a temperature and pressure. The SQUID measurements using the Magnetic Property Measurement System (MPMS XL, Quantum design) were carried out to study the magnetic properties of the samples. Finally, careful analysis of the experimental data reveals many unusual and interesting features.

In this chapter, a brief description of the synthesis and experimental techniques and the theoretical aspects used in the experimental data analysis is presented. The description of the synthetic technique, in Section 2.2, includes how the samples have been prepared for the different type of instruments and measurements, such as X-ray diffraction and SQUID measurements. It is then followed by a brief overview of Magnetic measurements and Rutherford Backscattering Spectrometry (RBS). In section 2.5, basic theory and methodology for the determination of structural properties of the materials using powder diffraction techniques will be introduced. Then theoretical aspects of Rietveld and LeBail method used to determine the lattice dimension of the powder diffraction data will be presented. The descriptions of X-ray absorption spectroscopy technique will be introduced towards the end of this chapter.

2.2 Synthetic Techniques and Sample Preparation

2.2.1 Preparation for synthesis

All the samples prepared during the period of the project were related to the metal intercalated fullerides, such as, the alkali-metal-doped fullerides (A_xC_{60}), the alkaline-earth-doped fullerides (AE_xC_{60}), the rare-earth-doped fullerides (RE_xC_{60}), and the mixture of alkaline-earth and rare-earth-doped fullerides ($AE_xRE_yC_{60}$). The intercalation of solid C_{60} with different electron donors requires different methods and some found to be more difficult compared to the other.

One of the most important aspects for obtaining reliable data sets from the experiments is not only to produce good samples but also to establish the method to reproduce the sample with same quality and enough quantity to obtain as many experimental data as possible under different conditions. To make this possible, all tools have to be handled carefully, take control of the working environment, and most importantly, one have to precisely be aware of what is happening at each stage of synthesis.

As all metal intercalated fullerides are extremely sensitive to oxygen and moisture, the sample handlings were therefore carried out in a controlled argon atmosphere glove-box, where the oxygen and water vapour levels are maintained below 0.1 parts per million (ppm). In order to keep the glovebox free from oxygen and moisture, the purifier attached to the glove-box was regenerated regularly using a hydrogen and nitrogen gas.

2.2.2 Starting materials

The fullerene C_{60}, super gold grade of purity >99.9%, was purchased from MER corporation. As C_{60} itself is not as sensitive to oxygen and moisture as other metals or intercalated fullerenes, it does not require any special storage environment. However, to ensure any trace of solvents, moisture and oxygen do not react with intercalating metals, it requires degassing process before used for synthesis. The degassing of the C_{60} was carried out using glass tube, vacuum line, and furnace set up as shown in the figure below (Fig. 2.1).

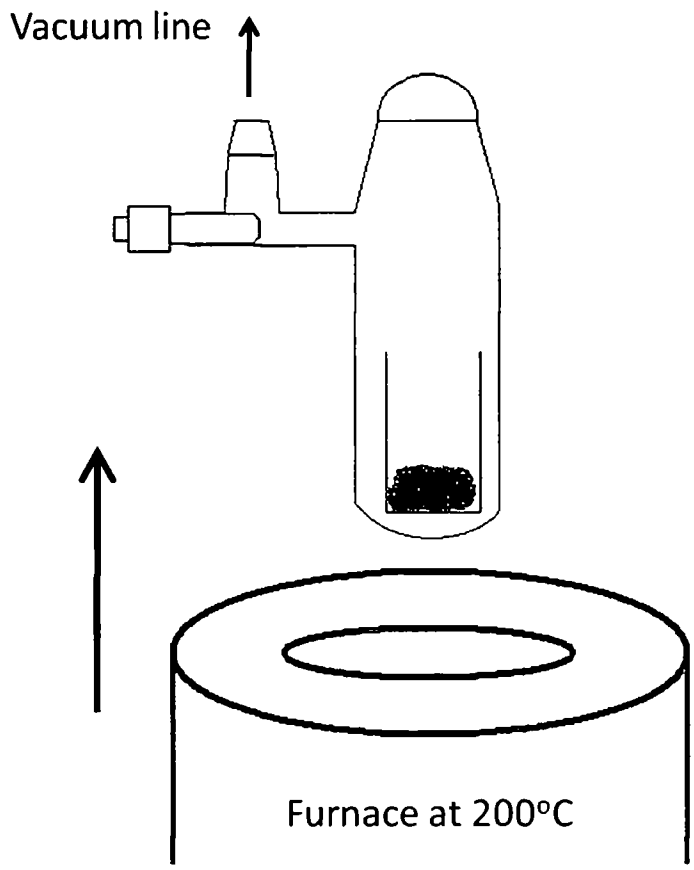

Fig. 2.1. Set up for the degassing C_{60}. C_{60} is placed inside glass container, which is attached to vacuum line, and heated at 200°C for 12 hours.

The glass tube was first attached onto a vacuum line, which is connected to a rotary and turbomolecular pump to obtain high vacuum of 10^{-5} mbar. Then the tube was slowly warmed up to 200°C and kept heating for 12 hours under vacuum. Switch off the furnace and let it cool down to room temperature, then remove the glass tube from the vacuum line carefully and take it into the glove-box. The degassed C_{60} was then removed from the glass tube and ready to be used for synthesis once they were ground into powder.

Almost all the metals used for the intercalation of C_{60} were purchased from Aldrich except for Europium powder which was purchased from ChemPur. All these metals are graded 99.9+% purity, so that they do not require further purification before using. As these metals are sensitive to a moisture and oxygen, and some are very easily oxidised, they were opened and stored in the glovebox all the time.

The purchased alkali-metals, such as, sodium, potassium, and rubidium usually come in a soft silver ingot, which can be easily cut using a scalpel and weighed for the stoichiometric quantities for further synthesis. While cesium has relatively low melting point at 28.4°C and therefore requires cooling system to handle in the solid state.

The alkaline-earth-metals, such as calcium, strontium, and barium used were in pieces when purchased, and therefore have to be ground into a powder using a diamond coated file. Here, it is important not use the same files for a different metals in order to avoid mixing unwanted metals for synthesis. For the case of calcium, the fine powder can also be obtained by dissolving the metal using liquid ammonia. In this way, sufficient amount

of fine and pure Ca powder for the intercalation can be efficiently obtained.

Finally, the rare-earth-metals, such as samarium, europium, ytterbium, and thulium usually come in a powder form, which can be directly used in the synthesis.

2.2.3 Intercalation of Alkali-metals

Although alkali-metal-doped fullerenes are sensitive to oxygen and moisture, which limits the choice of sample preparation methods, a variety of synthetic techniques have been established [1] since the discovery of superconductivity in K_3C_{60} [2]. The technique employed to synthesize the alkali-metal-doped fullerides, A_xC_{60}, depends on the type of metal, A, and how much metal doped, x [3 - 5], among these, the frequently used technique is to prepare compounds by direct reaction of alkali metal vapour and C_{60}.

The alkali-metal-doped fullerides samples were synthesised by reacting stoichiometric amounts of C_{60} powder, which was degassed prior to synthesis, and the relevant alkali-metals. All the materials were combined within specially designed, open at one end and closed at the other, tantalum cells. The tantalum cell, containing the C_{60} powder and alkali-metal, was then placed in a tantalum tube, of which both ends can be closed, before placed into a pyrex tube as shown below (Fig. 2.2). The tantalum cell and the tube were used to prevent any unwanted reaction between metals and the pyrex tube when the material was annealed.

The pyrex tube was then carefully removed from the glovebox and attached to the vacuum line to evacuate the inert atmosphere and filled with a high purity helium gas before sealed. The helium gas can be heat

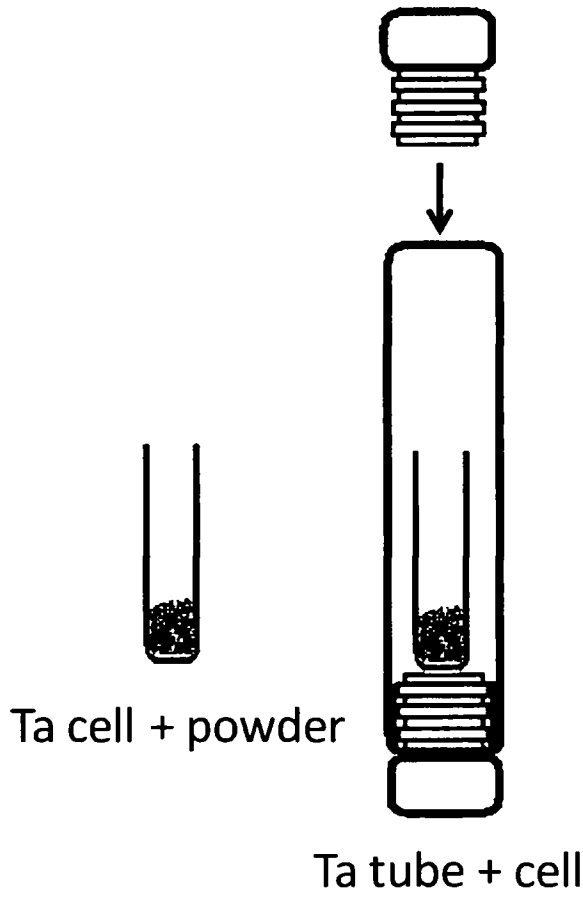

Fig. 2.2. Set up for the intercalation of alkali-metal-doped C_{60}. Stoichiometric amount of C_{60} powder and alkali-metal are put together in the Ta cell and then Ta tube.

conductor to ensure the temperature derivative to be as small as possible along the tube. The pressure of the helium gas inside the tube was calculated to be less than 1 atmospheric (atm) pressure with the maximum annealing temperature used ($PV = nRT$), this is to avoid any possibility for the glass tube getting crack with increasing pressure inside the tube. The sample was then placed in a pre-heated furnace and annealing processes were carried out for a half day to maximum of 2 weeks at a temperature between 200 to 450°C depending on the composition of the sample.

The samples were then placed back into the glovebox and ground into a

fine powder to ensure a homogeneity within the sample and a small amount from each sample was introduced into glass capillaries (diameter of 0.5 mm) for the X-ray diffraction measurements to monitor the progress of reactions. Further annealing process was performed if necessary under the same set up while the annealing conditions can be varied depending on the state of the reaction. After the final stage of annealing, the two capillaries were prepared for the detailed X-ray diffraction measurements and some were weighed and placed in a quartz tube for the SQUID measurements. The remaining samples were carefully stored inside the pyrex tube under high vacuum.

2.2.4 Intercalation of Alkaline-earth-metals

The first successful intercalation of alkaline-earth-metals with C_{60} has been reported for calcium, leading to the Ca_xC_{60} fullerides where x varies from 1.5 to 8 [6]. This was then followed by the report of barium doped C_{60} [7], and strontium doped C_{60} [8]. However, little systematic investigation of the properties has been undertaken compared to those done for the alkali-metal fullerides. This is mainly due to the difficulty associated with obtaining phase-pure samples, which requires relatively high annealing temperature compared to that for the alkali-metal intercalation.

The most reliable way to synthesize AE_xC_{60} (AE = Ca, Ba, Sr) is direct reaction between the alkaline-earth metals and C_{60}. The AE_xC_{60} samples were prepared by reaction of stoichiometric quantities of high-purity (99.9% pure) AE metal powder and C_{60}. As AE metals are not soft metals, but not sticky compared to alkali-metals, thus, the barium and strontium powder

can be obtained by grinding the metal using a diamond coated files. While calcium metal is stickier than Ba or Sr, thus it is easier to obtain Ca powder by dissolving Ca metal in liquid ammonia at -60°C and then removing the ammonia by heating them at 150°C on vacuum line under a high vacuum of 10^{-5} mbar [9] rather than grinding them by files. Those powders were weighed and mixed with C_{60} and then pressed into pellets using metal die set before placed inside the tantalum tubes as shown below (Fig. 2.3).

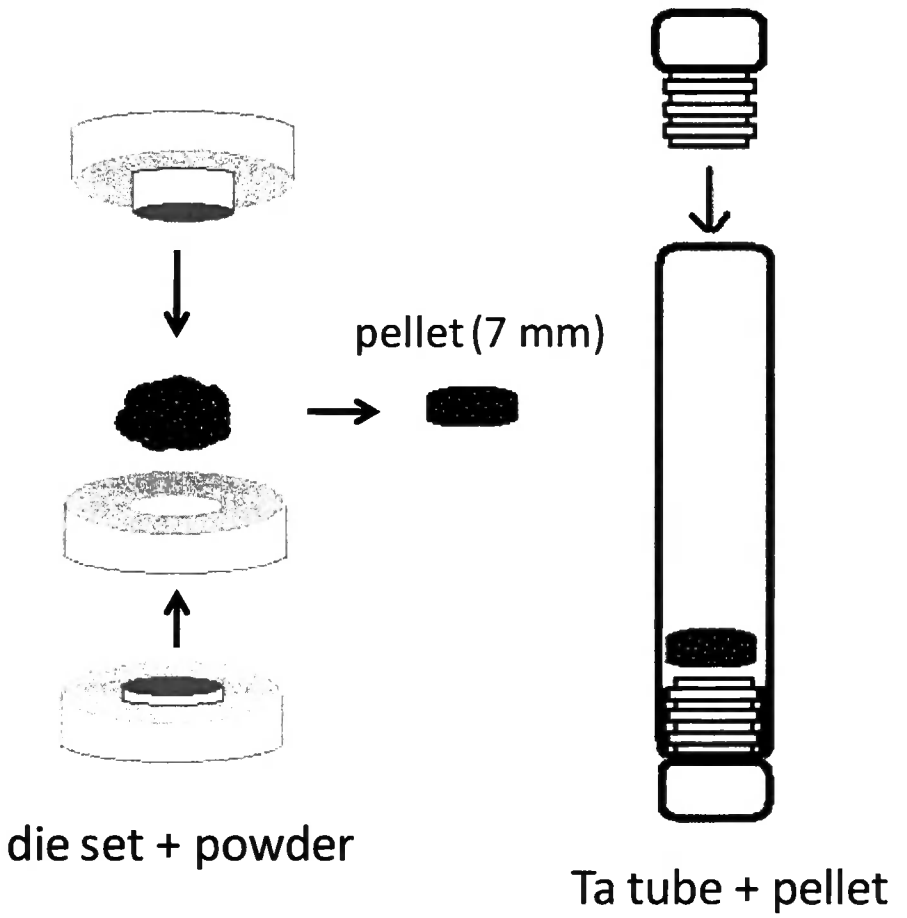

Fig. 2.3. Set up for the intercalation of alkali-earth-metals. Mixed AE metal and C_{60} powder was pelletized and placed inside Ta tube for annealing.

As higher temperature is required for annealing, the tantalum tubes were loaded into quartz tubes. This is due to the alkaline-earth-metals are very reactive with glass, hence direct contact must be avoided and the temperature used here is very close to the melting point of the glass tubes which requires the quartz tubes that has higher melting point. The quartz tube was then carefully removed from the glove-box and attached to the vacuum line to evacuate the inert atmosphere and filled with a high purity helium gas before sealed. The tube was placed inside the pre-heated furnace and the annealing was carried out at the temperature ranging from 500°C to 650°C for 12 days with intermittent grindings. Phase purity was monitored by powder X-ray diffraction and SQUID magnetometry.

When synthesising a mixture of alkali-metal and alkaline-earth-metal fullerides, $A_xAE_yC_{60}$, the techniques introduced in the previous and current sections have to be combined. For example, in order to synthesise $NaBa_3C_{60}$, first barium is intercalated to C_{60} to obtain Ba_3C_{60} using the technique explained in this section, and then reaction of appropriate amounts of Na can be done using the technique introduced in the previous section. This technique can also be used for a mixture of rare-earth and alkaline-earth-metal fullerides, $RE_xAE_yC_{60}$, synthesis.

2.2.5 Intercalation of Rare-earth-metals

Recent observation showed that the rare-earth doped fullerides do form stable intercalation compounds for RE_xC_{60} (RE = Yb, Sm, and Eu, x = 2.75, and 6) which offers wide range of interesting, both electronic and magnetic, behaviour [10–12]. For instance, the first successful intercalation of C_{60}

with a rare-earth metal has been reported for ytterbium, leading to the $Yb_{2.75}C_{60}$ fullerides, which showed superconducting phase below 6 K [10]. However, systematic investigations on the family of rare-earth fullerides have been limited due to the difficulties in devising reliable protocols for preparation of single-phase materials. The reactions of rare-earth metals with C_{60} require high temperature which competes with the formation of rare-earth carbides with the formation of fullerides [13].

The rare-earth-metal-doped fullerides samples were synthesised in a controlled argon atmosphere glove-box by reacting stoichiometric amounts of C_{60} powder and relevant amount of rare-earth-metals. This mixed powder was pressed into a pellet, using 7 mm die set, and placed into a closed tantalum tube before loading them into a quartz tube. The tubes were then connected to the vacuum line to evacuate the inert gas and obtain high vacuum of 10^{-5} mbar. Then sealed under a helium gas of half the atmospheric pressure, and placed in a pre-heated furnace and carried out annealing processes for a minimum of 2 hours to a maximum of 2 weeks at high temperature between 500°C and 625°C depending on the composition of the sample.

In order to find the optimum reaction temperatures and annealing times, several samples having same composition were placed in the different furnace at various temperatures for different annealing times. The samples were placed back into the glovebox for intermediate grindings to ensure the homogeneity of the powder and a small amount from each sample was introduced into glass capillaries for the X-ray diffraction measurements to monitor the progress of reactions.

Another difficulty that has to be encountered here is that the X-ray produced by a copper target is not sufficient to carry out diffraction measurements for rare-earth-doped fullerides especially for the samples containing samarium and europium. This is due to the wavelength of X-ray produced by the copper atom is very close to the L_1-absorption edge of samarium and europium giving resulting diffraction profiles with very poor intensities (Fig. 2.4).

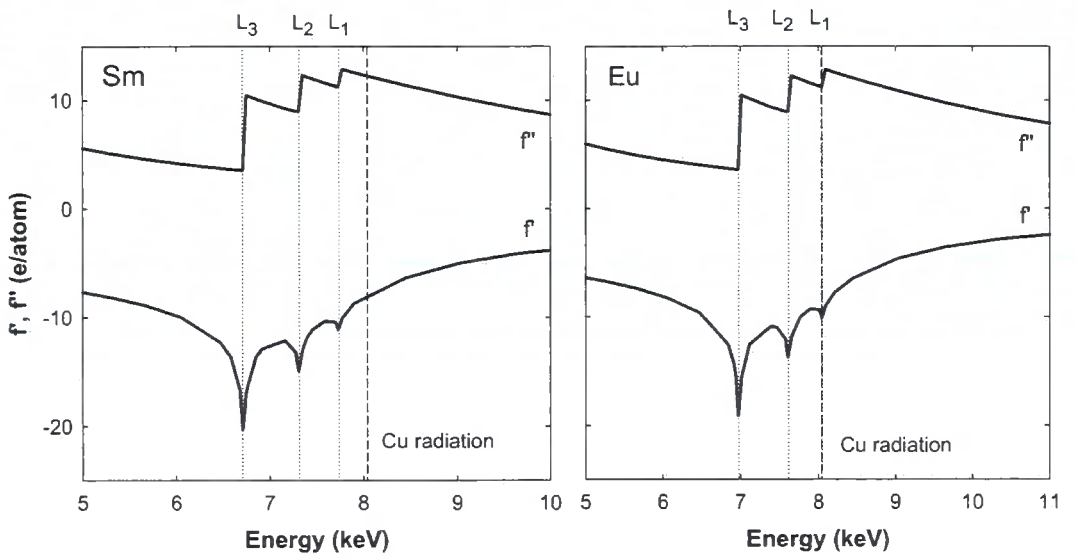

Fig. 2.4. The X-ray form factor as a function of energy. Three X-ray edges: L_1, L_2, and L_3 (dotted lines) and the copper K_α radiation (dashed line) are shown for samarium (left) and europium atoms (right).

On top of this, the angular accuracy and energy resolution obtained from the laboratory diffractometer is only good enough to monitor the progress of reactions and hence requires high-resolution synchrotron radiation to study the structural properties of interesting but very complicated compounds.

At the end of the annealing process, two glass capillaries from each samples containing sufficient amount of powder were prepared and sealed not longer than 3 cm for X-ray diffraction measurements. The remaining part of samples were weighed and stored safely until it is required for different experiments.

This techniques has been employed to synthesize a mixture of two different rare-earth-metal doped C_{60}, namely, samarium and europium leading to the sample composition of $(Sm_{1-x}Eu_x)_{2.75}C_{60}$ and mixture of alkaline-earth and rare-earth-metal doped C_{60}, in this case $(Sm_{1-x}Ca_x)_{2.75}C_{60}$.

2.3 Magnetic Measurements

2.3.1 The MPMS SQUID Magnetometre

The Magnetic Property Measurement System (MPMS) was designed for measuring the magnetic moments of a material with high accuracy under a broad range of applied magnetic fields (up to 5 Tesla) and precise low temperature control (LTC) system. The MPMS (Fig. 2.5) is composed of several different systems. Among these components, the Superconducting Quantum Interference Device (SQUID) detector is the heart of the magnetic moment detection system. Recent improvements in the MPMS control software can provide various sample temperatures ranging from 1.9 to 400 K using the internal heater, liquid helium and nitrogen. Another important feature of the MPMS is that a large magnetic field from zero to both positive and negative 5 Tesla is generated with the use of a superconducting solenoid, and the desired value can be obtained by the magnet control system.

Fig. 2.5. The picture of whole MPMS components (left), schematic diagram of MPMS probe with blow up of superconducting solenoid detector coil (right).

The sample chamber is located inside the superconducting detection coils and is maintained at a low pressure with static helium gas. The sample is attached to an end of a rigid sample rod that enters this sample space and it is controlled by the Sample Handling System. A measurement is performed by moving a sample in a series of discrete steps through the detection coils, which are connected to the SQUID input coil with superconducting wires, forming a closed superconducting loop (Fig. 2.6).

As a sample is moving through this loop, it causes a change in the magnetic flux within the detection coils. This change modifies the current in the superconducting circuit and the SQUID produces an output voltage, which is proportional to the current flowing in the SQUID input coil. In other words, the SQUID is a device that can function as a highly linear and sensitive current-to-voltage converter.

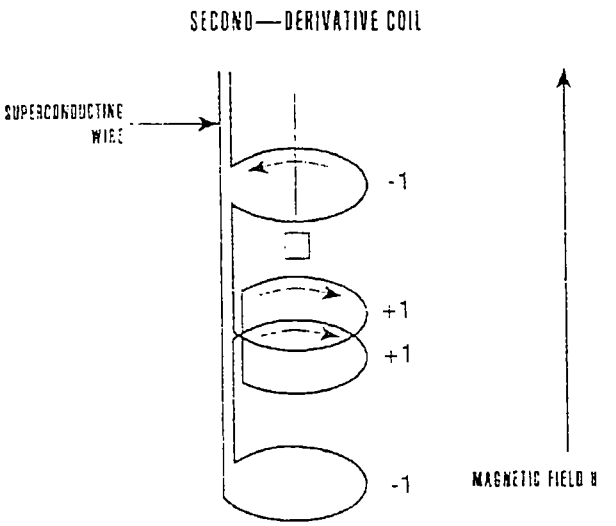

Fig. 2.6. Configuration of the Second-derivative coil.

The measurements of the voltage variations are stored in a computer and the integration of the area under the voltage *vs* position gives a highly accurate measurement of the magnetic moment of the sample. The determination of the magnetic moment as a function of temperature and/or magnetic field can provide information about the magnetic properties and the electronic structure of a studied material.

2.3.2 Introduction to Magnetism

All the material can be classified into different types of magnetic behaviour, such as paramagnetic, diamagnetic or ferromagnetic, depending on the behaviour of its magnetic moments in the presence of an external field. The characterisation of the magnetism exhibited by a material can be determined by measuring how magnetisation changes with respect to temperature or the strength of an applied magnetic field using the SQUID magnetometer.

When a material placed in a magnetic field, the magnetic flux density, B, will either increase if the materials are paramagnetic or decrease if the materials are diamagnetic. The magnetic flux density in a material is given by:

$$B = \mu_0 (H + M) \qquad \text{(Eqn. 2.1)}$$

where M is the magnetisation of the material, μ_0 is the permeability of free space, and H is the magnetic field intensity.

The MPMS provides the value of the magnetisation of the material and hence the magnetic susceptibility, χ, which is the ratio of the magnetisation of the material with respect to the applied magnetic field. The magnetic susceptibility per unit volume is defined as:

$$\chi = \frac{M}{H} \qquad \text{(Eqn. 2.2)}$$

and hence χ is dimensionless. In the *cgs* system, the unit of the magnetisation is *emu* (electromagnetic unit) and the units of the susceptibility are given in emu/cm^3. The susceptibility is also defined referred to unit mass or to a number of moles in the material, which gives the units in emu/g or emu/mol respectively.

The two principal magnetic measurements that are usually performed are the magnetisation as a function of temperature, *M(T)*, and the magnetisation as a function of an applied magnetic field, *M(H)*. The *M(T)* measurements are made by fixing the applied field H and measuring M at a different temperatures, while *M(H)* measurements are performed by fixing

the temperature and measuring M at a series of H values. These measurements of magnetisation, *M(T)* and *M(H)* are then plotted against applied temperature, T, and field, H, respectively, and these graphs can be used to determine the magnetic properties of the measured samples. A typical *M(T)* plot for different types of magnetism is shown in the figure below (Fig. 2.7), indicating that the type of magnetism exhibited can be classified depending on how the material is affected by the applied magnetic field.

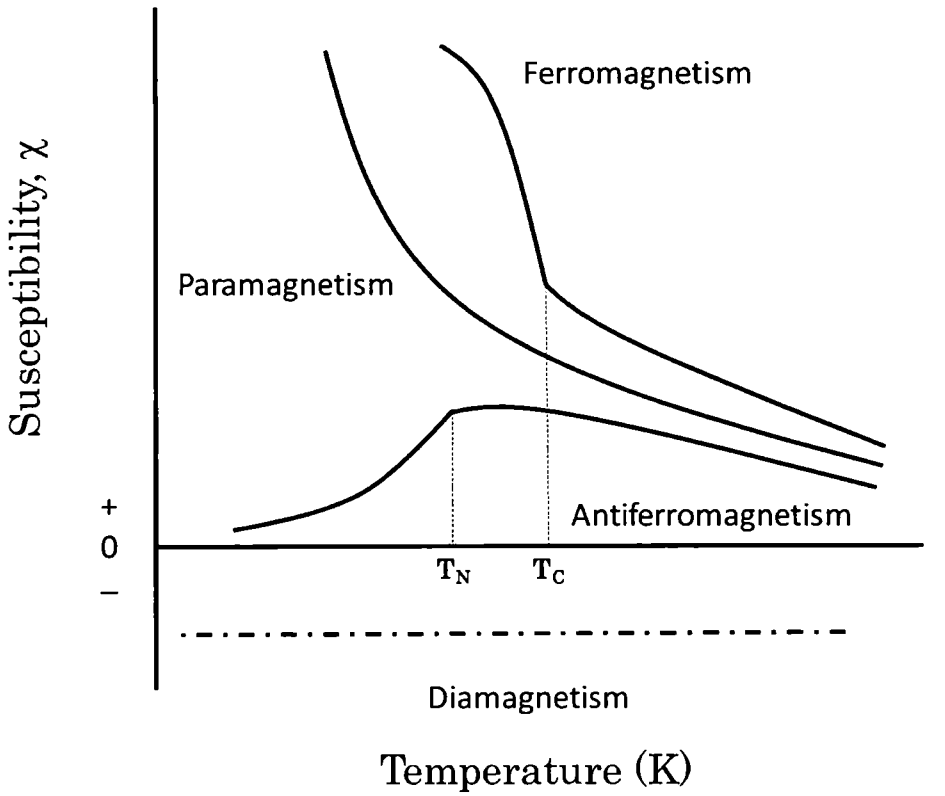

Fig. 2.7. χ vs T curves of the different types of magnetism.

In the case of the *M(T)* measurements, the applied magnetic field can either be as high as 5 T depending on the material measured to determine the type of magnetism exhibited over wide range of temperature as shown in the Figure 2.8, or as low as 10 Oe over relatively narrow temperature range

to observe histeresis behaviour. The latter measurements are known as zero-field-cooled (ZFC) and field-cooled (FC) sets of measurements. In ZFC measurement, the material is cooled down to the lowest measurement temperature with no applied field, then a weak magnetic field is turned on and the magnetisation is measured as a function of temperature. In FC measurement, the material is cooled under a magnetic field to the lowest temperature and measurements are also collected as a function of temperature. This measurements are useful to determine the temperature range over which the magnetic changes in a system are irreversible.

i) Curie-type Paramagnetism

Probably the simplest type of magnetic behaviour is known as Curie-type paramagnetism, which arises from the partial alignment of the unpaired electron spins within a material by an applied magnetic field in the direction of the field. Within an applied magnetic field, for a non-interacting isolated spins, the magnetic moment tends to align, however, these effects are encountered by a randomisation of the spins due to thermal energy. This paramagnetic behaviour can be explained by the Curie law, which describes a temperature dependence of the susceptibility, given by:

$$\chi(T) = \frac{C}{T} \qquad \text{(Eqn. 2.3)}$$

where C is the Curie constant, which plays an important role in determining the origin of the paramagnetism. This suggests that when the material is paramagnetic, a plot of $1/\chi$ versus T will be a straight line through the origin,

and the Curie constant can be determined from its slope.

The molar Curie constant can give information on the effective magnetic moment of an atom and the number of magnetic atoms in the material as it is defined as:

$$\chi_m = \frac{C_m}{T} = \frac{N_A p_{eff}^2 \mu_B^2}{3k_B T} \qquad \text{(Eqn. 2.4)}$$

where
N_A = Avogadro's number,
p_{eff} = Effective magnetic moment,
μ_B = Bohr magneton,
k_B = Boltzmann's constant.

Temperature dependence of the magnetic susceptibility in paramagnetic material is shown in figure below (Fig. 2.8).

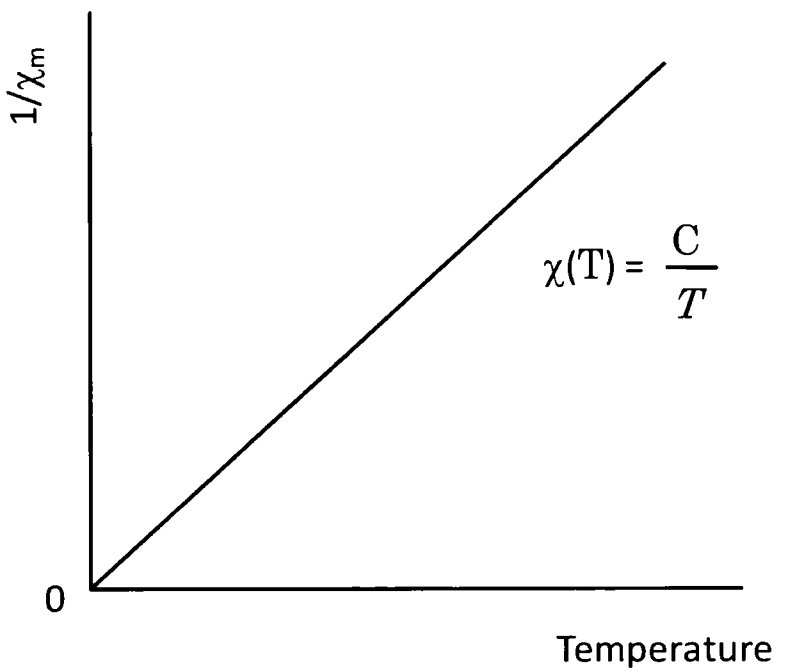

Fig. 2.8. Schematic plot of $1/\chi$ *vs* T for a paramagnetic material.

It was observed for some compounds deviates from the Curie law and in such a cases, the modification to the above formula (Eqn. 2.3) is required to describe the variation of susceptibility. The prominent example was reported for compounds containing rare-earth-metal, such as samarium (Sm) and europium (Eu), whose energy intervals between the ground state and the excited state become much greater than $k_B T$ at sufficiently low temperatures [14, 15]. The behaviour of the susceptibility in these regions is best described by:

$$\chi(T) = \frac{C}{T} + \alpha \qquad \text{(Eqn. 2.5)}$$

where α is the temperature independent susceptibility and this is known the van Vleck temperature independent paramagnetism. The figure below shows the temperature-dependent magnetic susceptibilities of the free Sm^{2+} and Sm^{3+} ions between 4.2 K and 300 K.

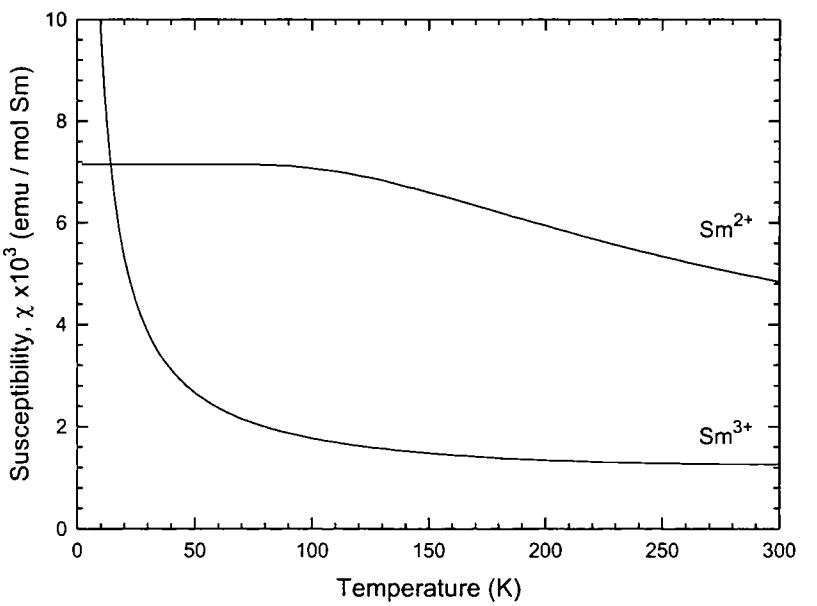

Fig. 2.9. The magnetic susceptibilities of the free Sm^{2+} and Sm^{3+} ions.

For the Sm^{3+} ion, because of the relatively small spacing (348 K) between the ground state ($^6H_{5/2}$) and the first excited state ($^6H_{7/2}$), the susceptibility is obtained by summing the corresponding Curie and van Vleck contributions. While for Sm^{2+} ion, at low temperatures, only the non-magnetic ground state ($^7F_0$) is populated and thus the Curie contribution to the magnetic susceptibility is zero and there is only a van Vleck temperature independent term arising through the mixing of the ground state and the first excited state (energy separation between these states is 420 K).

ii) Ferromagnetism and Antiferromagnetism

Certain materials exhibit a spontaneous magnetic moment due to strong interaction between the magnetic moments of neighbouring atoms or molecules and formation of magnetically ordered states. These interactions results in a high degree of alignment of the electron spins and magnetic moments in a parallel or anti-parallel to one another, which are known as ferromagnetism and antiferromagnetism. When such interactions between magnetic atoms are considered, the Curie-Weiss susceptibility formula becomes important, which is known as Curie-Weiss law:

$$\chi(T) = \frac{C}{T - \theta} \qquad \text{(Eqn. 2.6)}$$

where θ is called the Curie-Weiss temperature, which can be obtained graphically from the intercept of a plot of $1/\chi$ *vs* T with the x-axis (Fig. 2.10). When θ is positive, the moments are aligned in a parallel fashion to each

other and hence the material is ferromagnetic below T_C (= θ), the Curie temperature. On the other hand, when θ is negative, the moments are aligned in an anti-parallel way and hence the material is antiferromagnetic below T_N (= |θ|), the Néel temperature.

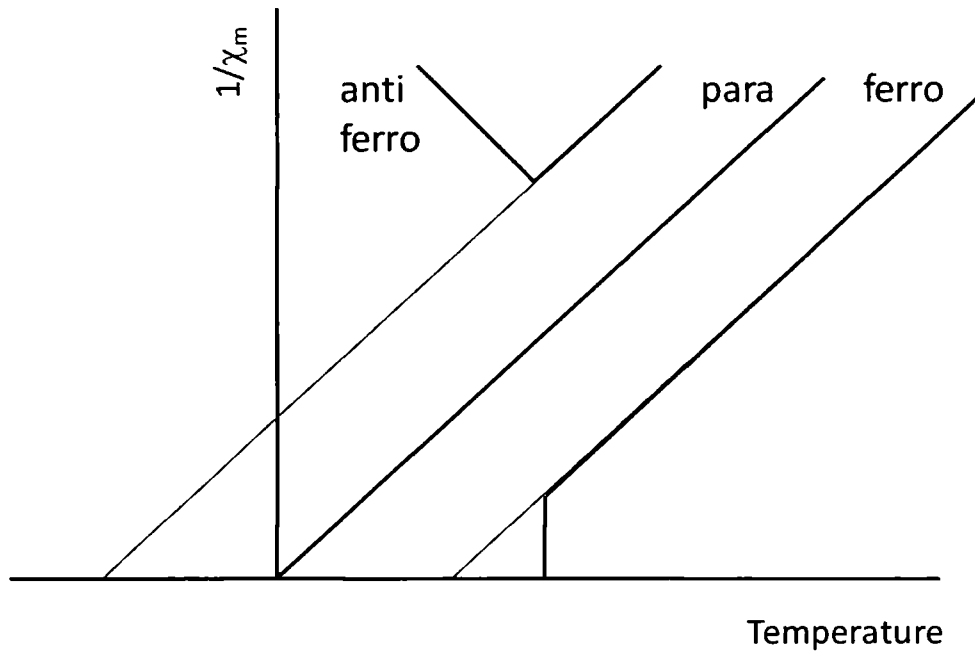

Fig. 2.10. Schematic plots of 1/ χ *vs* *T* for various magnetic systems.

Above the Curie or Néel point, the alignment is broken down and the material becomes paramagnetic. In this region, the observed susceptibility variation is best described using above expression (Eqn. 2.6), which should be rewritten depending on the behaviour below T_C and T_N as following:

$$\chi(T) = \frac{C}{T - T_C} \qquad \text{(Ferromagnetism)} \qquad \text{(Eqn. 2.7)}$$

$$\chi(T) = \frac{C}{T + T_N} \qquad \text{(Antiferromagnetism)} \qquad \text{(Eqn. 2.8)}$$

These are two basic types of phenomena which the susceptibility above certain temperatures follow the Curie-Weiss law in the mean field approximation. A third type is a ferrimagnetism, which can be described as an anti-parallel alignment of two spin lattices having the magnetic moment of one is larger than that of the other.

It should be noted here that a plot of *M(H)* curve for ferromagnetic materials are not linear, the magnetisations are not reversible, and the magnetisation reaches a saturation value as the intensity of applied field is increased. This is due to the fact that the ferromagnets are composed of small regions called domain. As the directions of magnetisation of different domains not necessarily to be parallel, the net magnetisation of a ferromagnet can be less than the saturation moment. Furthermore, the increase in the gross magnetic moment in an applied magnetic field takes place by different processes which results in displaying hysteresis in M vs H plots.

iii) Diamagnetism due to Superconductivity

The two properties that all superconductors have in common are zero resistance and perfect diamagnetism. The most well known property of superconductors is that they have zero resistance, that is, the current created in a superconducting ring will flow without being lost as long as the superconducting state is kept. The other property of a superconductor is known as perfect diamagnetism or the Meissner effect, that is, the current near the surface completely screens the inner part of the material from an applied magnetic field.

Superconductors are classified as one of two types depending on their behaviour within an applied magnetic field. In a type-I superconductor, below critical temperature, T_c, the plot of $M(H)$ at a fixed temperature has a large negative slope up to a certain critical field, H_c. A good type-I superconducting material is placed below T_c and H_c, the surface current on the material prevents the penetration of a magnetic field, thus, the lines of induction are ejected from the material, until superconductivity is destroyed suddenly. In a type-II superconductor, the $M(H)$ plot shows a linear response to an applied magnetic field up to a certain field known as the lower critical field, H_{c1}. As the applied field is increased, the magnetisation initially drops rapidly and then decreases with constant slope until the upper critical field, H_{c2}, is reached, where it becomes zero. Above this point the field penetrates the material completely and it is in the normal state.

Diamgnetisation is mainly associated with type-I superconductor, whereby the electrical charges partially to shield the inner part of a material from an applied magnetic field results in having negative magnetic susceptibility as shown in Fig. 2.7. The superconductor is said to be a perfect diamagnet if the magnetic field of the induced current inside the material is equal and opposite to the external magnetic field. Here, the ZFC and FC measurement is useful in determining the transition temperature, T_c, at which the material goes from the superconducting state to the normal state. Namely, the fact that below T_c the magnetic field is expelled from the inside of the material, leads to a rapid drop in $M(T)$ to negative values and the onset in this curve is used to estimate the transition temperature.

2.4 Rutherford Backscattering Spectrometry

Rutherford Backscattering Spectrometry (RBS), which sometimes referred to as High-Energy Ion Scattering (HEIS) spectroscopy, is a well-known analytical technique that has been used in materials research for many years. RBS is used in order to determine the stoichiometry of the material very accurately and is based on the study of the energy of ions scattered by atoms situated at various depths in a solid. Its strong point compared to other common analytical techniques such as Auger Electron Spectrometry (AES), Secondary Ion Mass Spectrometry (SIMS), X-ray Photoelectron Spectroscopy (XPS) etc. is its ability to provide absolute elemental concentration as a function of depth, without the use of standards. The results obtained from this technique can therefore be very useful to construct or improve a model that is used for Rietveld refinements of diffraction profile.

RBS technique is based on the effect of single elastic collisions between the probe ions and nuclei in the material. As soon as the ions penetrate the solid, they begin to be slowed by inelastic collisions (ionisation, excitation, etc.) with electrons in the solid, which continues until the ion collides with a target nucleus and suffers an elastic collision. When the collision is purely elastic, that is, the incoming particle does not have sufficient energy to penetrate the Coulomb barrier surrounding the nucleus, the scattering process obeys simple classical laws and the final energy of the scattered ion will depend on the kinematic factor, K, determined by the masses of the incident and sample nuclei and the stopping power of the matrix for the

probe ion at all energies from the incident energy down to that at which it leaves the material (Fig. 2.11) [16].

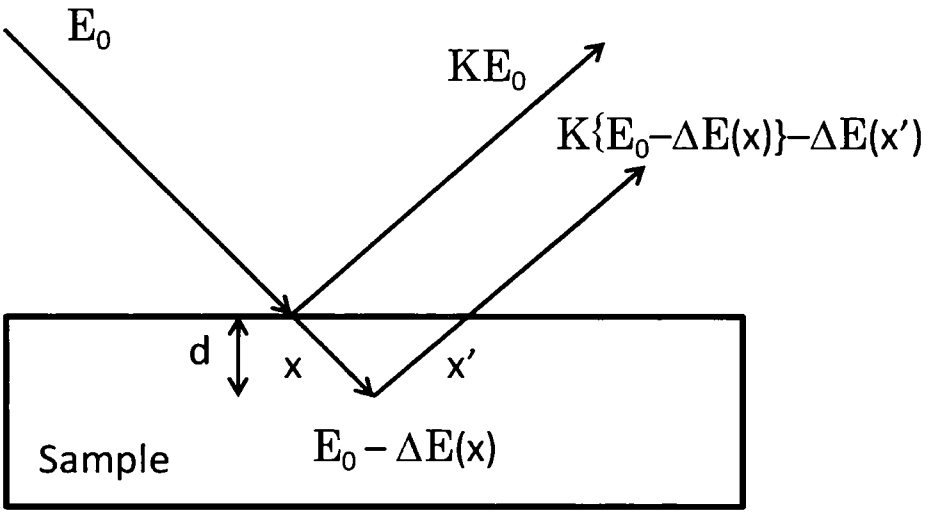

Fig. 2.11. The kinematics of Rutherford scattering.

In this case, both the final energy of the backscattered particle at an angle θ and the probability for the scattering to occur per unit solid angle can be described by the simple Rutherford scattering equations, thus, in turn, the kinematic factor, the ratio of the kinetic energy detected to that just before the collision, is given by:

$$K = \left[\frac{\left(M^2 - m^2 \sin^2 \theta\right)^{1/2} + m\cos\theta}{M+m} \right]^2 \qquad \text{(Eqn. 2.9)}$$

where m and M are the masses of the incident and target atoms respectively, and θ is the laboratory angle through which the incident ion is scattered. The yield, dN (in counts per second), for a given material can be related to its atomic concentration, n (atoms/cm^2), is given by:

$$dN = In\frac{d\sigma}{d\Omega}d\Omega \qquad \text{(Eqn. 2.10)}$$

where I is the beam intensity (ions per second), and dΩ is the solid acceptance angle of the detector. The probability for the scattering to occur per unit solid angle is given by:

$$\frac{d\sigma}{d\Omega} = \left(\frac{1}{4\pi\varepsilon_0}\right)^2\left(\frac{zZe^2}{4E_0}\right)^2 \frac{1}{\sin^4(\theta/2)} \qquad \text{(Eqn. 2.11)}$$

where z and Z are the atomic numbers of the incident and target atoms respectively, E_0 is the kinetic energy of the incident ion just before the collision. Since the parameters m, E_0, and θ are usually known, an energy spectrum of the backscattered ions will provide a profile of the mass and depth distribution of atoms within the material.

The criterion for elastic scattering is met when α particles are used at energies of up to 2 MeV, for this reason helium ions are extensively used for carrying out the vast majority of RBS analyses. The principal limitation of this technique is that it is not good for trace-element analysis. RBS is useful for depth profiling heavy atoms in a material composed of lighter ones, while in the case of light atoms imbedded in a heavy-atom, another approach is required. To account for this problem, the use of the combination of Particle Induced X-ray Emission (PIXE) spectrometry and RBS using protons has been employed. Here, RBS is used for the matrix determination and depth profiling and PIXE is used as it is more sensitive to all elements with $Z > 12$. For this technique, a 2-3 MeV proton is used instead of 2 MeV He^+ beams, since the reduction in cross section for X-ray

production when using α particles makes it useful only for specific cases of low-mass elements.

The RBS/PIXE combined analyses were carried out with the ion beam analysis service located in the chemistry department, Durham University. There are three types of beams available, namely, $1H^{+}$, $4He^{+/++}$, and $3He^{+/++}$, for different purposes, where recent modification to the ion source enabled rapid switching between the available beam species. The ion beams used for RBS/PIXE analysis are produced in a 1.7 MV Tandem accelerator, which is capable of accelerating incident ions in the electrostatic field to required energy range of 1-4 MeV. The ion beam emerging from the accelerator, with energy fixed at 3.0 MeV, first passes through an analyzing magnet, which sorts out the ions of the correct mass and velocity, followed by focussing of the beam, which is then collimated just before entering to the irradiation chamber. A sample material is mounted on a high-precision goniometer together with a thin layer of known areal density, for example Fe, to calibrate the combined detector solid angle and integrated beam charge.

A high-resolution solid state detector was set at 170° to the incident beam to measure energy of backscattered protons. As the spectral intensity in RBS/PIXE is proportional to the number of incident particles, the measurements are generally carried out for a preset charge of protons. The charge is measured by an external counter, and the ratio of the metal concentration was determined unambiguously by fitting simulated spectra to the experimental spectra using RUMP RBS analysis software. Simultaneous PIXE measurements were carried out alongside the RBS measurements and PIXE data were analysed using GUPIX software. PIXE

measurements were not used to determine stoichiometry since this technique is less quantitative than RBS. The PIXE spectra obtained did nevertheless confirms the identity of metals present in each material as well as the absences of impurities.

2.5 Powder diffraction

Structural studies of the materials are usually based on diffraction of photons, neutrons and electrons, where powder diffraction measurements are most commonly used in solid state chemistry when single crystal is not available. The diffraction patterns depend on the crystal structure and the wavelength of the radiation used. For this reason, the powder diffraction analysis can be used as a one of fundamental tools to observe whether the samples form a solid solution and to determine their structure if they were not known.

For an ideal powder X-ray diffraction measurement, the sample should consist of a large number of small crystallites randomly oriented with respect to each other to satisfy the orientation necessary for scattering. For accurate measurements of X-ray diffraction intensities, the sample should have small grain size of 10 μm or less.

Carefully prepared samples were loaded to a diffractometer to collect the powder X-ray diffraction patterns, which were done using two different instruments, a Siemens D5000 diffractometer and a beam line at Synchrotron Radiation at European Synchrotron Radiation Facility (ESRF) in Grenoble, France. These profiles are one of the most useful data sets to

determine the structural parameters and to study the physical properties of compounds.

2.5.1 X-ray diffraction from crystals

In a crystal structure, the atoms, the group of atoms, molecules, etc are arranged in a periodic array in 3-dimensional space, which can be classified into 7 different crystal systems and/or 14 Bravais Lattice (Table 2.1). The X-ray diffraction pattern can be observed when the incident radiations interact elastically with the electrons of the constituent atoms and due to their periodicity, the diffraction peaks can be observed at specific angle.

From a powder diffraction pattern, the position, intensities, and profile of the diffraction peaks can be obtained. These parameters are unique in the sense that different compounds will have different diffraction patterns, depending on the size and the symmetry of the unit cell and the atomic positions within the cell.

The peaks in an X-ray measurement occur as a result of the diffraction from the crystal planes oriented at a specific angle θ, to the incident beam. This angle is known as the Bragg angle, which is only obtained when the angle of incident is appropriate for the wavelength and for the distance between two adjacent planes (Fig. 2.12).

The difference in path between the waves scattered at D and B is equal to AB + BC = $2d \sin \theta$. When this is satisfied, the diffracted beams are in phase and interfere constructively, and hence, precise indexing of the crystal planes is possible and the distance between two parallel planes, known as d-spacing, can be accurately measured. This condition is known as the

Table 2.1. Seven crystal systems and the corresponding characteristic parameters.

System	Restriction on conventional cell axes and angles	Number of lattices	Relation between lattice constants and d-spacing
Cubic	a=b=c, $\alpha=\beta=\gamma=90°$	3	$\frac{1}{d^2}=\frac{h^2+k^2+l^2}{a^2}$
Tetragonal	a=b≠c, $\alpha=\beta=\gamma=90°$	2	$\frac{1}{d^2}=\frac{h^2+k^2}{a^2}+\frac{l^2}{c^2}$
Orthorhombic	a≠b≠c, $\alpha=\beta=\gamma=90°$	4	$\frac{1}{d^2}=\frac{h^2}{a^2}+\frac{k^2}{b^2}+\frac{l^2}{c^2}$
Hexagonal	a=b≠c, $\alpha=\beta=90°, \gamma=120°$	1	$\frac{1}{d^2}=\frac{4}{3}\left(\frac{h^2+hk+k^2}{a^2}\right)+\frac{l^2}{c^2}$
Trigonal	a=b=c, $\alpha=\beta=\gamma<120°, \neq 90°$	1	$\frac{1}{d^2}=\frac{(h^2+k^2+l^2)\sin\alpha+2(hk+kl+lh)(\cos^2\alpha-\cos\alpha)}{a^2(1-3\cos^2\alpha+2\cos^3\alpha)}$
Monoclinic	a≠b≠c, $\alpha=\gamma=90°\neq\beta$	2	$\frac{1}{d^2}=\frac{1}{\sin^2\beta}\left(\frac{h^2}{a^2}+\frac{k^2\sin^2\beta}{b^2}+\frac{l^2}{c^2}-\frac{2hl\cos\beta}{ac}\right)$
Triclinic	a≠b≠c, $\alpha\neq\beta\neq\gamma$	1	$\frac{1}{d^2}=\frac{1}{V^2}\left(S_{11}h^2+S_{22}k^2+S_{33}l^2+2S_{12}hk+2S_{23}kl+2S_{13}lh\right)$ *

* $V=abc\sqrt{(1-\cos^2\alpha-\cos^2\beta-\cos^2\gamma+2\cos\alpha\cos\beta\cos\gamma}$

Table 2.1 (continued)

$S_{11} = b^2c^2\sin^2\alpha$, $S_{22} = a^2c^2\sin^2\beta$, $S_{33} = a^2b^2\sin^2\gamma$, $S_{12} = abc^2(\cos\alpha\cos\beta - \cos\gamma)$,

$S_{23} = a^2bc(\cos\beta\cos\gamma - \cos\alpha)$, $S_{13} = ab^2c(\cos\gamma\cos\alpha - \cos\beta)$

Bragg's Law, which can be illustrated by the Bragg equation:

$$2d_{hkl}\sin\theta = n\lambda \qquad \text{(Eqn. 2.12)}$$

where d_{hkl}, θ, n, and λ represents the d-spacing between the (*hkl*) planes, the Bragg angle, an integer, and the wavelength, respectively.

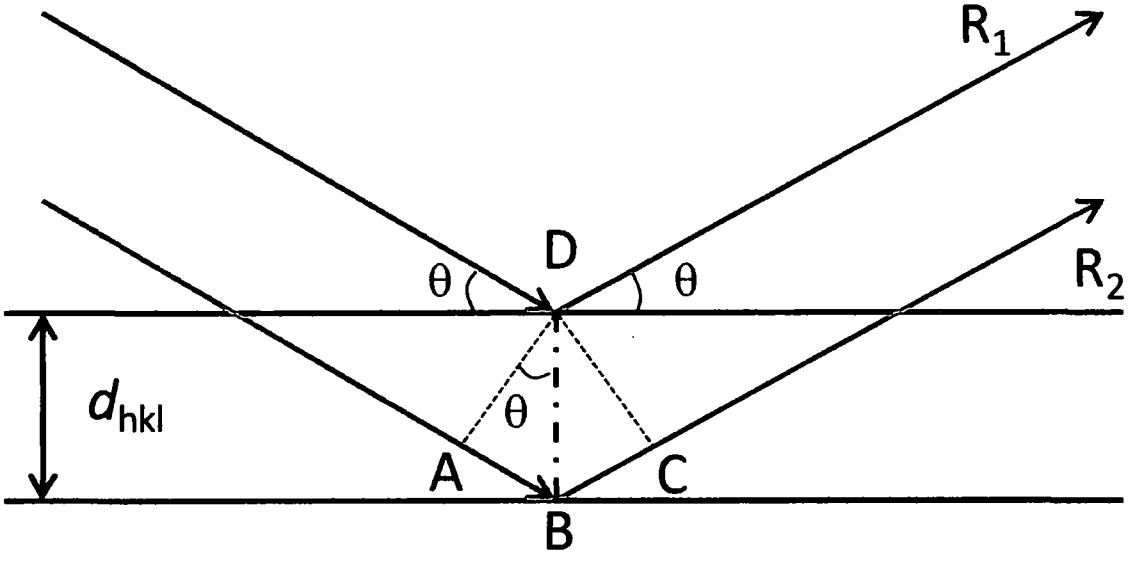

Fig. 2.12. Schematic representation of the Bragg equation, where reflection of X-rays from two lattice planes belonging to the family of lattice planes with indices *h*, *k*, *l*. *d* is the interplanar spacing.

It should be noted that the Bragg's law does not refer to the composition of the basis of atoms associated with every lattice point, but it is a

consequence of the periodicity of the lattice. However, from the above equation, it is clear that the Bragg angle depends on the d-spacing, d_{hkl}, of (hkl) crystal planes, in such a way that larger unit cells with larger spacing give small angles of diffraction and hence produce more reflections compared to the smaller unit cell. If the crystal structure and the lattice constants are known for the sample, using appropriate equation shown in table 2.1 to calculate d-spacing, and hence it can be concluded that the peak positions 2θ depend on the lattice constants of the material.

The other information that can be obtained from the X-ray diffraction profile is that the atomic coordinates of the material determined from the relative intensity of the various orders of diffraction from a given set of parallel planes.

The amplitude of the wave that results from the constructive interference of the waves R_1 and R_2 (Fig. 2.12) can be expressed as:

$$F(hkl) = |F(hkl)| \cdot e^{i\varphi} \qquad \text{(Eqn. 2.13)}$$

where $|F(hkl)|$ is the amplitude, $\varphi = 2\pi \mathbf{r}^*.\mathbf{r}$ is the phase of the diffracted ray and F(hkl) is known as the structural factor.

The intensities of the reflection from hkl planes are related to this structure factor, which depends on the contribution of all scatterers within the unit cell, in such a way that the amplitude is proportional to the square root of the scatter intensity, I(hkl) which is written as:

$$|F(hkl)|^2 = sI(hkl) \qquad \text{(Eqn. 2.14)}$$

where s is the constant factors grouped together, which are the scale factor common to all the reflection and the other parameters that depends on a given sample and set experimental conditions, expressed as:

$$s = \frac{I_0 \lambda^3 l_s}{8\pi r} K_R K_G \frac{j_h}{V_c^2} L_p \qquad \text{(Eqn. 2.15)}$$

where I_0 = intensity of the incident beam, λ = wavelength of the radiation source, I_s = height of the detector slit, r = sample to detector distance, j_h = multiplicity for reflection (h, k, l), V_c = unit cell volume, L_p = the combination of the Lorentz and polarization factors for the diffractometer geometry, K_R = $(e^2/m_e c^2)^2$ where e and m_e are the charge and mass of an electron and c the speed of light, K_G = (1/8)μ for X-ray Bragg-Brentano geometry, $V/4$ for X-ray Debye-Scherrer geometry, where μ is the linear absorption coefficient of the sample and V is the volume of the sample irradiated by the beam.

The structure factor, F(hkl), can also be written as a sum in which each term describe diffraction by one atom in the unit cell. As there is more than one electron around every atom, the scattered radiation from a single atom must take account of interference effects within the atom. This quantity, which is known a measure of the scattering power of the j^{th} atom in the unit cell, is called the atomic structure factor, f_j.

The value of f involves the number and distribution of atomic electrons, and the wavelength and angle of scattering of the radiation, which is expressed as:

$$f_j^2 = (f_0 + \Delta f')^2 + (\Delta f'')^2 \qquad \text{(Eqn. 2.16)}$$

here $\Delta f'$ and $\Delta f''$ are the anomalous dispersion terms.

The scattering factor is different for each element, which depends on the atomic number (Z). The function increases as a number of electron in the atom is increased, hence larger atomic number implies larger scattering power. This also implies that when there is small number of electrons, contribution to the diffraction intensity is also small, and hence it is difficult to determine the atomic coordinates of those atoms with small atomic number, such as helium. When $\theta = 0°$, the value of f is same as the atomic number of the scatterers, and the value decreases as the angle, 2θ increases. This is the one of the reasons for the intensity of diffraction peaks weakens at higher angles.

The structure factor equation, hence, can be written as a Fourier series that describes the sum of diffraction from each N atoms having scattering power factor f_j and atomic coordinates (x_j, y_j, z_j) of the j^{th} atom.

$$F(hkl) = \sum_{j=1..N} f_j (e^{-B_j \sin^2\theta/\lambda^2})(e^{2\pi i(hx_j+ky_j+lz_j)}) \qquad \text{(Eqn. 2.17)}$$

where (h, k, l) is the Miller indices for the reflection, and B_j is the Debye-Waller displacement factor for atom j (in Å^2).

The term, $e^{-B_j \sin^2\theta/\lambda^2}$ takes into account the effect of thermal vibration has on the electron cloud, making it more diffuse and thus reducing the scattering efficiency at higher angles. It should be also mentioned that the structure factor F(hkl) can also be written as the sum of contribution from each volume element of electron density in the unit cell. The electron density of a volume element centred at (x, y, z) is roughly the average value

of ρ(x, y, z) at all points. Considering extremely small volume elements, the structure factor equation can be rewritten as:

$$F(hkl) = \int_V \rho(x,y,z)(e^{-B\sin^2\theta/\lambda^2})(e^{2\pi i(hk+ky+lz}) dV \qquad \text{(Eqn. 2.18)}$$

This equation shows that the structure factor is the Fourier transform of the electron density on the set of the lattice planes (hkl), hence if the value for F(hkl) is obtained, the electron density can be calculated from above using following equation:

$$\rho(x,y,z) = \frac{1}{V} \sum_h \sum_k \sum_l F(hkl) e^{-2\pi i(hx+ky+lz)} \qquad \text{(Eqn. 2.19)}$$

where V is the volume of the unit cell.

These equations demonstrate that the number and positions of reflections are determined by the unit-cell dimensions and the wavelength of the diffracted beam, and the intensity of reflection depends on the electron density of hkl planes. The crystal structure of the samples can be determined either by comparing the diffraction pattern of the sample with that of already know material and use the equations to obtain lattice constants and atomic coordinates. From precisely measured reflection intensity, I(hkl), using equation 2.3 the structure amplitude, $|F(hkl)|$ can be calculated, and obtain the structure factor, F(hkl), from the direct methods, heavy-atom method, anomalous scattering or molecular replacement to

calculate the electron density, ρ(x, y, z), using equation 2.19. The obtained electron density peaks determines the atomic coordinates of the sample and the lattice constants can be obtained using equation 2.12 and using appropriate formula shown in table 2.1.

Once the basic information about the crystal structure of the sample is known, it is possible to simulate the diffraction pattern and using rietveld method to determine parameters related to the crystal structure to obtain more information from the diffraction pattern. The theoretical aspects of the Rietveld method will be presented later this chapter.

2.5.2 Siemens D5000 Diffractometer

The Siemens D5000 diffractometer is used to monitor the progress of reactions of the samples synthesised and to provide data for structural refinement. In the Siemens D5000 diffractometer, X-ray radiation is generated by a beam of electrons is allowed to strike a copper target within a sealed tube that is located inside a high-vacuum chamber. More specifically, an accelerated electron by applied high voltage of 40 kV hits the target metal to allow a $1s$ electron of the copper atom to become ionised. The X-ray photon is emitted when a higher energy electron decays to the empty $1s$ state. The best result from a diffraction measurement can be obtained by using the most intense monochromatic X-ray beam filtering out all other wavelengths. The lowest-frequency line, which is the most intense line, corresponds to the K_α transition, having a wavelength of 1.5418 Å. The K_α wavelength is the averaged wavelength of the two slightly different transitions $K_{\alpha 1}$ and $K_{\alpha 2}$, related to the two possible spin states of a $2p$ electron. A monochromatic

K_α radiation can be obtained by using Ni foil as a filter, which absorbs the unwanted radiation, such as K_β and the white radiation.

This diffractometer used for recent study was optimised for capillary measurement, which allows; easier alignment of X-ray and the sample, rotate the capillary, and obtain better resolution with less background noise. The samples were, hence, sealed in a glass capillary of 0.5 mm diameter and scans were carried out at room temperature in the 2θ range from 8 to 50 degrees with a step size of 0.016 degrees. The different scanning speeds were used for different samples, where longer time per scan is used for more accurate measurements. A schematic diagram of the diffractometer is shown in the figure below (Fig. 2.13).

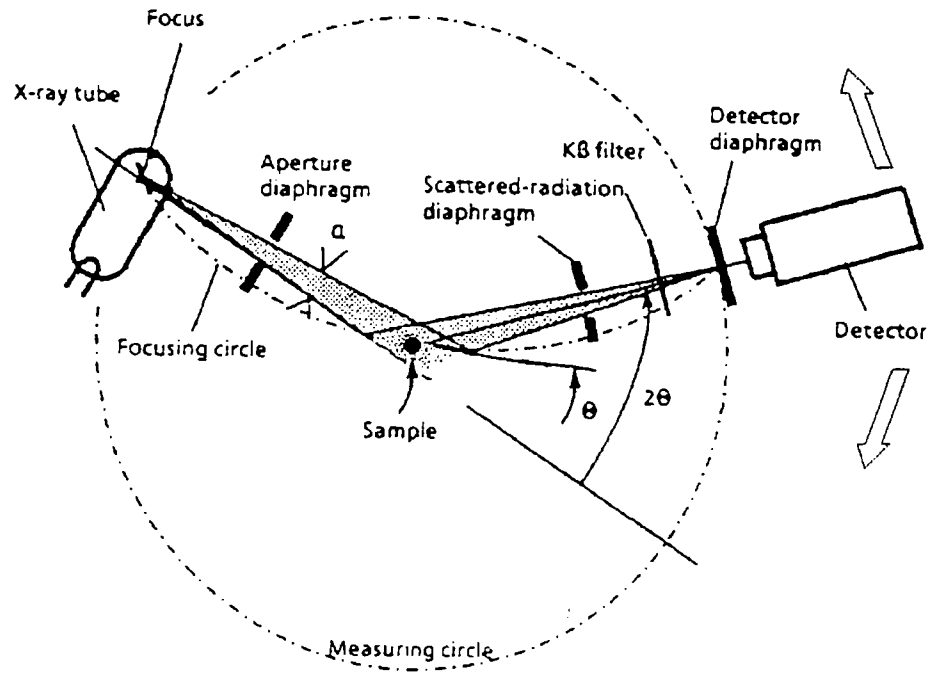

Fig. 2.13. Schematic diagram of the D5000 X-ray diffractometer.

2.5.3 High Resolution Powder Diffraction beamline

The powder diffraction experiments described in this thesis were all performed using synchrotron radiation in the European Synchrotron Radiation Facility (ESRF), Grenoble, France. The ESRF operates the most powerful synchrotron radiation source in Europe, which can reveal variety of information in numerous fields of research, and thus, it is important to understand the property of radiation source and the individual characteristics of each beamline and instruments used to carry out the measurements.

i) Synchrotron X-ray radiation

The synchrotron X-ray radiation of the ESRF is generated with high current, a low emittance electron beam and the use of long undulators allows a number of beamlines to be run with high flux. These electrons are emitted by an electron gun and then accelerated in a linear accelerator (linac) until their energy reaches 200 MeV using pulsed electric fields. Then they are transferred to a circular accelerator (the synchrotron) to be accelerated to close to the speed of light generating the electron beam energy on 6 GeV, and these electrons are kept to travel in a storage ring of 844 m circumference by a series of magnets. The external magnets around the storage ring keep the electrons circulating, accelerating inwards, and also provide a focusing effect that groups the electron into bunches. This will provide a maximum current of 200 mA, different possible frequencies, and a beam lifetime of ~50 hours.

The radiation produced in this way is extremely brilliant, achieving one thousand times more of the number of photons emitted per second, per unit source size, per unit space angle and for a bandwidth of 1/1000 of the photon energy compared with previous synchrotron sources. The other important radiation emitters are specially designed magnetic systems called insertion devices which are placed in the straight sections of the storage ring to generate X-ray beam with specific characteristics. These systems are consisted of two different types of insertion devices, wigglers and undulators, which are both made up of a succession of small magnets with alternating polarity. The wigglers cause sharper bends in the electron path so as to shift the wavelength distribution to higher energies and increase intensity, while the undulators create a series of small deviations such that the emissions produced at each turn are subject to interference from all other turns. This results in a radiation distribution that has an intense characteristic wavelength and harmonic related frequencies with reduced horizontal divergence of the beam. The insertion devices in the ESRF storage ring deliver X-ray beams to the scientific instruments on the 40 different beamlines, where they can provide data sets that can reveal the structural properties of the material at different temperature, pressure, and various wavelengths allowing the determination of parts of the structural phase diagram.

During this project, most of the X-ray powder diffraction data were collected at two beamlines, namely, ID31 and ID09A for different purpose of experiments.

ii) ID31

ID31 is a beamline designed for powder diffraction studies with very high angular accuracy and energy resolution with fast data acquisition times. The beamline is built on an insertion device and operates in the energy range 5-60 keV [17]. The diffraction patterns were measured using high incident flux radiation in the range 0.3-0.9 Å and operated in the simplest optical configuration using capillaries with diameter in the range 0.3-1.5 mm.

The incident white X-ray radiation is first introduced into the beamline from the synchrotron ring in a horizontal fan measuring 4mrad, with a source size of 0.3 × 0.3 mm^2. The radiation is then collimated vertically with a curved mirror that is specifically set at an angle relative to the incident beam to obtain the high resolution. The beam is then focused towards a double-crystal monochromator, of which the first crystal is water-cooled and the second crystal can optionally be bent to focus sagitally the horizontal fan onto the sample. A 1:1 horizontal focusing arrangement is adopted, i.e. the source-to-crystal distance is approximately equal to the crystal-to-sample distance, as this does not greatly perturb the vertical divergence of the beam, and hence maintains the well-collimated beam essential for high angular resolution. A second mirror follows after the monochromator to provide the option to focus the X-ray vertically onto the sample, gaining intensity at the expense of lower angular resolution, however, this option is rarely used on this beamline.

The diffractometer is constructed from two high-precision, heavy-duty rotary tables aligned coaxially on a base plate. A bank of nine detectors

with each preceded by a Ge (111) analyser crystal equally separated by ~2° intervals moves as a unit to collect nine high resolution diffraction patterns in parallel. The diffractometer setup is such that the capillary sample can be rotated on an independent spinner to achieve a better spatial average and reduce preferred orientation. Data are collected in a continuous scanning mode, which eliminates the dead time of a conventional step scan.

The combination of the nine-crystal analyser and the high quality mechanical integrity of the diffractometer results in significant improvement in the peak shape description and the precise definition of the peak position in the diffraction profile. The beamline also allows experiments to be carried out under a wide range of conditions using, for example, liquid-helium-cooled cryostat can cool the sample inside the capillary down to ~5 K or lower with pumping, and using cryostream cold-nitrogen-gas blower the temperature can be varied in the range 80-500 K.

The collected data from the nine detectors are rebinned and normalised to give the equivalent normalised step scan.

iii) ID09A

To obtain a pressure of several million atmospheres in the laboratory and carry out the diffraction analysis under such conditions require the large variety of techniques, equipment, and beam characteristics. ID09A, also known as "white beam station", is equipped with dedicated high-pressure facilities, which provides both the high energy X-ray beams with very small size, and low angular divergence and the technique to perform the diffraction

studies at elevated pressures.

The beamline is built on an in-vacuum U17 insertion device with a 70 mm period hybrid wiggler and two phased undulators on a high-β section. The insertion devices close the magnetic gaps down to 16 mm and thus generate extremely bright beams of high energy radiation. The white radiation is vertically focused by a spherical mirror and horizontally by a bent Si (111) monochromator. The working energy for typical high-pressure experiments is between 25-40 keV with a flux of 10^{11} photons/s at 200 mA. The beam size on the sample can be varied as small as 10 × 10 μm^2 depending on the size of the sample.

The scattered radiation is collected with a versatile high-precision three-circle diffractometer using angle-dispersive, energy-dispersive, and conical geometries. Two-dimensional images of Debye-Scherrer cones are recorded on phosphor Molecular Dynamics image plates.

In high-pressure experiments, the sample is loaded in a diamond anvil cell (DAC) [18]. The DAC consists of two opposed diamond anvils with full parallel surfaces between which the sample is compressed as the diamond surface are driven together. An aluminium gasket with a hole between 70-300 μm is used to keep the sample in position. The sample is loaded in the centre of the diamond anvil along with ruby particles and the pressure medium, typically silicone oil, argon, or nitrogen. The pressure can be measured with the ruby fluorescene technique, where the pressure is calibrated from the observed λ, using the formula [19]:

$$P = \frac{B_0}{B'}\left(\left(\frac{\lambda}{\lambda_0}\right)^{B'} - 1\right) \qquad \text{(Eqn. 2.20)}$$

where B_0 = 1904 GPa, B'= 7.665 and λ_0 is a function of the ruby quality and is calibrated at beginning of each experiment (usually ~694 nm). The sample can be pressurised from atmospheric pressure up to 40 GPa using several membrane-type diamond anvil. This beamline is also equipped with a cryostat to perform high-pressure experiments at low temperature down to 50 K, and external resistive heating equipment for high temperatures up to 600 K.

The obtained 2D diffraction images are collected for spatial distortions of the Debye-Scherer rings are treated using the software package FIT2D [20]. The FIT2D program allow to fix the centre of the 2D pattern by fitting circles to a chosen number of rings after defining the sample-to-detector distance, the tilt axis and angle, and wavelength used, then mask unwanted features and integrate around the rings to obtain the 1D pattern. A standard silicon calibration is performed to refine the wavelength, sample-to-detector distance and tilts of the image plate.

2.6 Rietveld Method

X-ray Powder diffraction profiles obtained from synchrotron radiation experiments provides vast amount of information for identification and characterisation of materials. For example, lattice constants, unit cell volume, atomic coordinates, fractional occupancies, temperature factors can be determined from the peak positions and the peak intensities, and structural disorder can be obtained from peak profiles. However, until recently, for complex structures with lower symmetry, the X-ray powder

diffraction data were not suitable for determining crystal structure. This was due to the difficulty of decomposing the pattern into its Bragg reflections accurately from the patterns consisted of severe peak overlap. To partially solve this peak overlap problem, the Rietveld refinement method was developed by Dr. Rietveld between 1964 and 1969 [21]. This method was initially developed for neutron diffraction, which was then extended its application to X-ray powder diffraction data to allow the maximum amount of information to be extracted from the pattern.

A limitation of this method is that the refinement must be started with a model that is reasonable approximation of the actual structure, as it is primarily a structure refinement. This implies that unless the material possess the structure with high symmetry, it is difficult to determine the crystal structure of unknown materials. However, by conceiving a starting model by using, for example, analogy to similar structures, direct methods, or high-resolution transmission electron microscope images, Rietveld refinements can yield very precise and accurate unit-cell parameters. Rietveld refinements are also well suited for studying phase transformation, heating or cooling experiments, and pressure studies.

2.6.1 Calculating peak intensity

The Rietveld method is an optimised method that compares the observed data points at each 2θ and the calculated powder diffraction pattern based on adjustment of the structural parameters, background coefficients, and profile parameters using a non-linear least-squares fitting

until the calculated powder profile best matches the observed pattern. In the refinement procedure, it is not required to separate the data into a set of integrated intensities for individual Bragg peaks, as was in the profile-fitting procedure, but employs the entire powder diffraction patter to overcome the problem of peak overlap. Instead, the intensity is treated as a sum of the contributions of overlapping reflections at each point of the diffraction pattern, where the number of overlapping reflections at point i in the diffraction pattern is determined from the peak positions, $2\theta_k$, and corresponding widths, H_k, and hence, the intensity y_i can be calculated using following equation:

$$y_{ic} = y_{ib} + sS_R AA_S D \sum_k m_k |F_k|^2 P_k L_k \Phi_k(\Delta 2\theta_{ik}) \qquad \text{(Eqn. 2.21)}$$

where

y_{ib} = background intensity,

s = scale factor,

S_R = surface roughness correction factor,

A = transmission coefficient,

A_S = asymmetry correction factor,

D = polarisation factors,

m_k = multiplicity factor,

F_k = structure factor

P_k = preferred orientation correction,

L_k = Lorentz factor,

$\Phi_k(\Delta 2\theta_{ik}) = \Phi_k(2\theta_i - 2\theta_k)$ = profile function.

During the Rietveld refinement, the least-squares procedure is employed to minimise the difference between the observed diffraction pattern intensity y_{io} and the calculated diffraction pattern intensity y_{ic} for all i steps which results in minimising the function:

$$M = \sum_i w_i (y_{io} - y_{ic})^2 \qquad \text{(Eqn. 2.22)}$$

where the summation is over all points in the pattern and ω_i is a statistical weighting factor, which takes the form:

$$w_i = \frac{1}{y_{io}^t} \qquad \text{(Eqn. 2.23)}$$

where y_{io}^t is the total intensity, which is sum of the observed intensity, y_{io}, and the background intensity, y_{ib}, at position $2\theta_i$.

2.6.2 Background determination

As mentioned in previous section, the total observed intensity at each step i in a diffraction profile is consisted of contributions from Bragg reflections and the background at that step, $y_{io}^t = y_{io} + y_{ib}$. The background can arise from several factors, including fluorescence from the material, detector noise, thermal diffuse scattering from the material, disordered or amorphous phases in the material, incoherent scattering as well as scattering of X-rays from air, diffractometer slits, and sample holder. For the materials which provide relatively simple patterns that have several,

well-spaced intervals between Bragg peaks, the background intensities can be measured accurately. In this case, the most straightforward approach is to select several points in the pattern that are away from Bragg peaks and then model the background by linear interpolation between these points. For more complex diffraction patterns, the background coefficients must be included as variables in the refinements, which can be represented by a polynomial function of the form:

$$y_{ib} = \sum_n b_n [2\theta_i]^n \qquad \text{(Eqn. 2.24)}$$

where b_n are refinable background parameters and $2\theta_i$ is expressed in radians. The background can be refined even for complex patterns if the peak shape is well defined, however, if the pattern is poorly resolved, the background parameters tend to correlate with other parameters, particularly temperature factors. This can result in systematic underestimates of the standard deviations of these other parameters if the background is not included in the refinement.

2.6.3 Determining peak shape

In theory, X-ray powder diffraction pattern is a projection of the weighted crystal reciprocal lattice, where the integrated intensities as distributed by a peak shape function. However, in practice, the observed pattern can be affected by convolution of many factors such as the characteristics of the material and the data collection geometry. For

instance, the intensities can be affected by factors such as absorption, extinction, and preferred orientation of particle in the sample, whereas, the peak shape can be affected by, for example, misalignment of the diffractometer, axial divergence of the X-ray beam, displacement of the material, and transparency of material. As a result, the peak shape deviates from simple the Gaussian or Lorentzian functions, thus more complex peak shape function is required to fit their profiles accurately.

For constant wavelength X-ray diffraction, Young and Wiles proposed a combined Gaussian and Lorentzian peak shape function known as the pseudo-Voigt as most appropriate and now widely used function for describing complex profiles [22]. The pseudo-Voigt function, $\Phi_k(2\theta_i - 2\theta_k)$, is the normalised addition of 2θ-dependent Gaussian (G) and Lorentzian (L) peaks [23]:

$$\Phi(\Delta 2\theta_{ik}) = \eta \bullet L(\Delta 2\theta_{ik}, H_{kL}) + (1-\eta) \bullet G(\Delta 2\theta_{ik}, H_{kG}) \qquad \text{(Eqn. 2.25)}$$

$$G(\Delta 2\theta_{ik}) = \frac{2}{H_G}\left[\frac{\ln 2}{\pi}\right]^{\frac{1}{2}} \exp\left(-4\ln 2\left(\frac{\Delta 2\theta_{ik}}{H_G^2}\right)^2\right) \qquad \text{(Eqn. 2.26)}$$

$$L(\Delta 2\theta_{ik}) = \frac{2}{\pi H_L}\left[1 + 4(\sqrt{2}-1)\left(\frac{\Delta 2\theta_{ik}}{H_L}\right)^2\right]^{-1} \qquad \text{(Eqn. 2.27)}$$

where η is the mixing parameter, which defines the shape of the peak between the limiting Gaussian (when η = 0) and Lorentzian (when η = 1) forms, and H is the full width at half of the maximum peak height (FWHM). Here, η and H are known as a primary profile parameter (PPP). The FWHM of the Gaussian, H_G, and the Lorentzian, H_L, components of the peak profile have an angular dependence [24] which is given by:

$$H_G^2 = U\tan^2\theta + V\tan\theta + W \qquad \text{(Eqn. 2.28)}$$

$$H_L^2 = X\tan\theta + \frac{Y}{\cos\theta} \qquad \text{(Eqn. 2.29)}$$

where U, V, W, X, and Y are known as secondary profile parameter (SPP). The normal procedure in a Rietveld refinement is to define the peak shape through the refinement of the SPP in the equations 2.28 and 2.29, not the PPP.

It is important to note that the basic pseudo-Voigt function is symmetrical about the nominal Bragg peak positions, however, obtained profiles, especially at the lower diffraction angle, the peak shape is not symmetric due a variety of instrumental and sample effects. The fundamental cause of the asymmetry is usually the axial divergence of the X-ray beam, which most Rietveld refinement programs include as a variable semiempirical asymmetry correction term. The one approach to model this asymmetry with formalism based on the optics of the diffractometer, which involves three parameters: the distance between the sample and the detector, L, the horizontal width of the detector slit, 2H, and the horizontal size of the beam on the sample, 2S [25-27]. For the case of GSAS suite for Rietveld refinements (PC version), two refinable parameters, S/L and H/L, have been incorporates into profile function [28]. Both S/L and H/L have to be refined to take additional effects into account in this formalism, such as sample dependent peak broadening. However, as this factor is only concerned with the axial divergence, in some cases the quality of fitting in lower diffraction angles might not be improved. If this was the case, the low angle peaks can be excluded and use only higher angle data to improve the fitting.

In some cases, the peak shape can also be affected by the specimen characteristics. In this case, usually, two more coefficients, *stec* and *ptec*, have to be taken into account for the precise description of the peak shape. The *stec* is an anisotropy coefficient involved in the Lorentzian Scherrer broadening of the peaks while the *ptec*, which is also an anisotropy coefficient but involved in the strain broadening effects.

2.6.4 The reliability of Rietveld refinement

After, or even during, the Rietveld refinement of a particular structural model, the agreement between observed and calculated profile is judged by careful examination of the R-factors, which are listed below:

Weighted Profile R-Factor:
$$R_{wp} = \left(\frac{\sum_i w_i |y_{io} - y_{ic}|^2}{\sum_i y_{io}} \right)^{\frac{1}{2}} \quad \text{(Eqn. 2.30)}$$

Profile R-Factor:
$$R_P = \left(\frac{\sum_i |y_{io} - y_{ic}|^2}{\sum_i y_{io}} \right) \quad \text{(Eqn. 2.31)}$$

Integrated Intensity R-Factor:
$$R_I = \left(\frac{\sum_{ki} |I_{ko} - I_{kc}|}{\sum_k I_{ko}} \right) \quad \text{(Eqn. 2.32)}$$

Expected Weighted Profile R-Factor:
$$R_{\exp} = \left(\frac{N - P + C}{\sum_i w_i y_{io}^2} \right)^{\frac{1}{2}} \quad \text{(Eqn. 2.33)}$$

Goodness-of-fit indicator:
$$S = \frac{R_{wp}}{R_{\exp}} \quad \text{(Eqn. 2.34)}$$

Reduced χ^2:
$$\chi^2 = \left(\frac{R_{wp}}{R_{\exp}} \right)^2 = \frac{\sum_i |y_{io} - y_{ic}|^2}{N - P + C} \quad \text{(Eqn. 2.35)}$$

where N is the number of observations, P is the number of parameters refined, and C is the number of constraints applied to the model. The experimental points in excluded regions are always excluded from the calculation of all agreement factors.

One of the mathematically more meaningful *R*-factors that best reflect how well the refinement is proceeding is the *weighted profile*, R_{wp}, *R*-factor that reflects how well the structural refinement accounts for both large and small Bragg peaks across the pattern. The other reliable factors are: the *profile*, R_p, *R*-factor, which is not weighted, the Bragg '*Integrated Intensity*', R_I, *R*-factor, which is closest to those used in single crystal work, and the *expected*, R_{exp}, *R*-factor that takes into account the statistical quality of the data and the number of variables used in the refinement. However, as the denominator for both R_{wp} and R_p are defined as the sum of observed intensities of the patterns, their values are strongly affected by the diffraction intensities and the background intensities, and thus, use the value of *S*, the goodness-of-fit indicator, or the reduced χ^2 factor to monitor if the agreement between observed and calculated profiles is satisfactory. When a value of $\chi^2 = 1$ the fit is perfect, when $\chi^2 < 1$ is an indication that there are more parameters in the model than justified by the quality of the data, and if $\chi^2 < 1.3$, the fit is said to be satisfactory.

2.6.5 LeBail method

The basic requirements for any Rietveld refinement for structural determination from a diffraction profile are: an indexing of Bragg peaks, a

starting model that is reasonably close to the actual crystal structure, and a model that accurately describes shapes, widths and any systematic errors in the positions of the Bragg peaks in the powder pattern.

The two prototype approaches for powder-pattern decomposition methods are the Pawley technique [29] and the LeBail algorithm [30] which analyses the whole diffraction profile without using any structural model. These methods are useful to approximate the set of lattice constants and the cell symmetry if an initial model for the material is not known. Pawley's approach involves a least-square fitting of the diffraction by adjusting the background parameters, cell parameters, peak-shape parameters and integrated intensities. In the LeBail method, which was used for the analysis of all the data presented in this thesis, no structural information is required, except approximation unit cell and resolution parameters. The calculated intensity y_{ic} at every point *i* of the profile is given by the equation:

$$y_{ic} = B_i + \sum I_k \cdot \Omega_{ik} \qquad \text{(Eqn. 2.36)}$$

where B_i is the background intensity at point *i*, Ω_{ik} is the peak shape, and I_k is the integrated intensity of line k at point *i*. The calculated intensities, here, are initially assigned arbitrarily to all peaks in the diffraction pattern and then by a least-squares minimisation, the first set of integrated intensities is extracted. This procedure is used in order to determine the correct unit cell size, symmetry, and peak shape function without providing any structural information, which can then be directly imported in the Rietveld method. The drawback for the both Pawley technique and the

LeBail method are that none of the two methods are not efficient enough to provide reliable results in the case of severe peak overlap in the diffraction profile.

2.7 X-ray Absorption Spectroscopy

Recent development in the intense synchrotron X-ray sources, X-ray absorption spectroscopy (XAS) became very important and widely used technique. The information which can be obtained from XAS depends on how X-rays are absorbed by an atom at energies near and above the core-level binding energies of that atom. More specifically, XAS spectra are sensitive to the formal oxidation state, coordination chemistry, and the distance, coordination number and species of the atoms surrounding the selected element. Thus, XAS can provide a practical way to determine the chemical and physical state of the selected atom.

2.7.1 Total Fluorescence Yield

The information which can be obtained from XAS includes detailed local atomic structure and electronic and vibrational properties of the material. XAS measures the absorption of X-rays as a function of X-ray energy, $E = \hbar\omega$, where the X-ray absorption coefficient is determined from the decay in the X-ray beam intensity I with distance x (Fig. 2.14). In this process, X-ray photon is absorbed by an electron in a tightly bound quantum core level, such as the $1s$ or $2p$ level, of an atom. When the incident X-ray

with the energy larger than that of the binding energy of the electron, the bound electron will be perturbed from the well-defined quantum state and the atom is said to be in an excited state with one of the core electron levels left empty. Since every atom has core-level electrons with well-defined binding energies, appropriate selection of the element is possible by tuning the X-ray energy to their absorption edge.

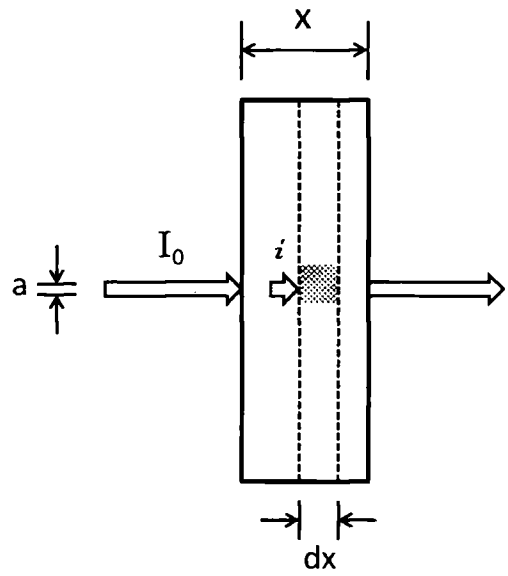

Fig. 2.14. Schematic diagram of how is the X-ray transmitted through the sample.

Inside the absorbing material (of total depth x), the intensity i, and there is a loss of intensity dI in each infinitesimal slab of the material dx. After the X-ray has traversed a distance x into the slab, the intensity has been reduced to:

$$I = I_0 e^{-\mu t} \qquad \text{(Eqn. 2.37)}$$

where I_0 is the intensity of the incoming X-ray beam having a cross-sectional

dimension (width) a, and μ is the absorption coefficient, defined as:

$$\mu(E) = -\frac{d \ln I}{dx} \qquad \text{(Eqn. 2.38)}$$

If the absorption coefficient is plotted as a function of E, the experimental data show three distinctive energy regions: 1) a sharp rise at certain energies called edge region, 2) the region just above the edge position known as the X-ray absorption near-edge structure, XANES (typically lies within 30 eV of the edge position), and 3) the region beyond XANES, which are referred to as extended X-ray absorption fine structure, EXAFS. These regions above the edges show an oscillatory structure in the X-ray absorption coefficient that modulate the absorption, where this feature is known as X-ray absorption fine structure (XAFS), which indicates the sum of XANES and EXAFS spectrum (Fig. 2.15).

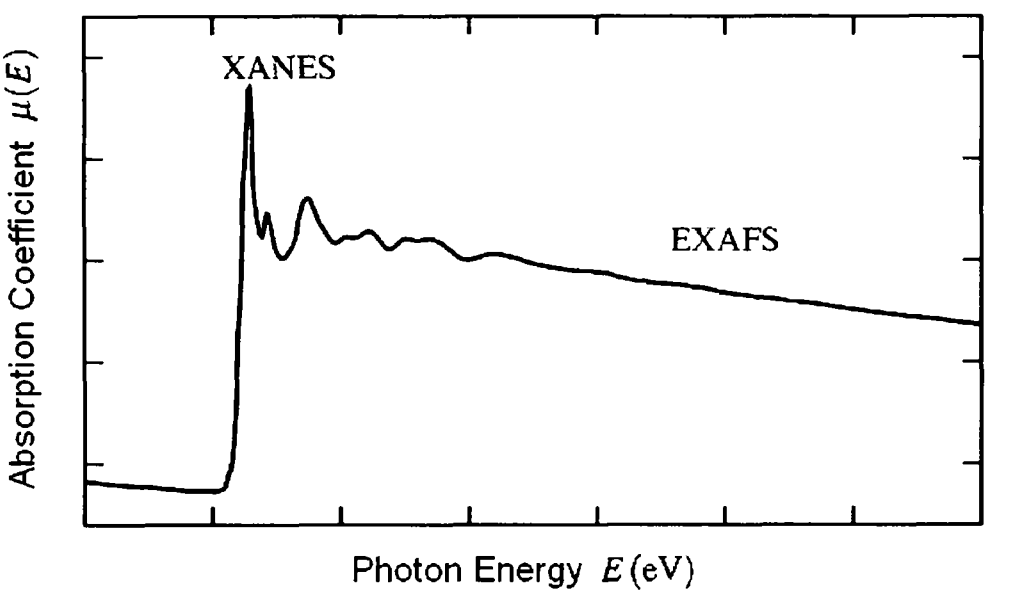

Fig. 2.15. The X-ray absorption spectrum with XANES and EXAFS regions identified.

The first region, absorption edge region, is related to a specific atom present in the material and to an ionisation of the core orbital. For example, K edges refer to transitions that excite the innermost $1s$ electron to unoccupied states, which leaves behind a core hole. The resulting excited electron is often referred to as a photoelectron. The ionisation energies, thus energies of the edges, are unique to the type of atom that absorbs the X-ray, and hence themselves are signatures of the atomic species present in a material [31]. Following an absorption event, the decay of the excited atomic state is observed, in which a higher energy electron fills the deeper core hole resulting in an ejection of X-ray, also known as X-ray fluorescence. The fluorescence energies emitted in this way are also unique and can be used to identify the atoms in a system. This is also known as the total fluorescence yield X-ray absorption (TFY-XAS) spectra.

The XAFS spectrum χ is defined as the normalised oscillatory part of the X-ray absorption above a given absorption edge as given by:

$$\chi(E) = \frac{[\mu(E) - \mu_0(E)]}{\Delta\mu_0} \qquad \text{(Eqn. 2.39)}$$

where $\mu_0(E)$ is the smoothly varying atomic-like background absorption of an embedded atom in the absence of neighbouring scatterers, and $\Delta\mu_0$ is a normalisation factor that arises from the net increase in the total atomic background absorption at the edge, which, in practice, can be approximated by the magnitude of the jump in absorption at the edge (edge-jump normalisation). The generally weak oscillatory structure beyond about 30 eV above the absorption edge, EXAFS region, is used to determine the

distances, coordination number, and species of the neighbours of the absorbing atom, while the XANES region is strongly sensitive to formal oxidation state and coordination chemistry of the absorbing atom. For the EXAFS, a quantitative parametrisation is now established based on a single scattering short range order theory and is best understood in terms of the wave behaviour of the photoelectron created in the absorption process. Thus, it is common to define $\chi(k)$ rather than $\chi(E)$ on an absolute energy scale, where k is the wave number of the photoelectron, leading to the standard EXAFS equation [32]:

$$\chi(k) = \sum_R S_0^2 N_R \frac{|f(k)|}{kR^2} \sin(2kR + 2\delta_c + \Phi) \exp(-2R/\lambda(k)) \exp(-2\sigma^2 k^2) \qquad \text{(Eqn.2.40)}$$

where $f(k)$ is the backscattering amplitude, δc is phase shift, λ(k) is the energy dependent mean free path, Φ is the phase factor, and S_0^2 is the overall amplitude factor. The structure parameters, R, the interatomic distances, N_R, the coordination number, and σ, the bond length which also include effects due to structural disorder, can be determined by knowing the scattering amplitude and phase shift. The exponential terms, $exp(-2R/\lambda)$ is the decay of the wave due to the mean free path of the photoelectron, and $exp(-2\sigma^2k^2)$ is the Debye-Waller factor.

The representation of EXAFS given by Eqn. 2.40 provide a convenient parametrisation for fitting the local atomic structure around the absorbing atom to the experimental EXAFS data, thus allows the determination of the local structure of each individual atomic species.

In contrast, the XANES portion of the spectrum is considerably harder

to fully interpret than EXAFS. The EXAFS equation breaks down at low-k, due to the $1/k$ term and the increase in the mean-free-path at very low-k, which makes precise and accurate calculations of XANES spectral features difficult, time-consuming, and not always reliable. Even though there is not a useful XANES equation available, there is much chemical information from the XANES region. The XANES spectra can be divided into three regions, namely, pre-edge, edge, and post-edge. The first feature is caused by electronic transitions to empty bound states, which gives information on local geometry around absorbing atom and shows dependence on oxidation state and bonding characteristics. In the edge region, the position and shape of the edge provide information on valence state, ligand type, and coordination environment. The third feature is dominated by multiple scattering resonances of the photoelectrons ejected at low kinetic energy, which can give information about atomic position of neighbours: interatomic distances and bond angles. These interpretations can be used as a fingerprint to identify phases. An important and common application of XANES is to use the height and shift of the edge region to determine the valence state of the compounds. With good model spectra, the ratio of different valence states can be determined with very good precision and reliability.

2.7.2 Partial Fluorescence Yield

XANES spectroscopy is a useful and powerful technique to understand the property of metal complex in various forms, such as crystalline or in

solutions. However, these spectroscopic measurements become extremely difficult in some cases, for instance, investigation of intermediate valence compounds under various temperature and/or pressure. This is due to the energy broadening originating from the short lifetime of the deep core hole, resulting in poor energy resolution and preventing detailed analysis of the intermediate valence behaviour. While in the case of high pressure measurements, the problem arise from technical point of view, in which the strong intensity losses through the pressure cell making the XANES measurements under applied pressure less attractive.

Breakthrough to the limitation of the intrinsitc lifetime broadening have been made by using the now available synchrotron radiation fluxes to integrate the photons from the fluorescent radiative decay from TFY-XAS final state as a function of incident energy, which is known as the partial fluorescence yield (PFY-XAS) measurements [33]. The overall broadening due to the finite lifetime of core hole is less seen in the spectral features obtained from PFY mode, which can reveal fine details that was lost in the TFY mode [34].

In the case of intermediate valence rare-earth based compounds, the excitation at the L_3 edge involves the perturbation of a $2p$ core electron, with excitation energy that is much larger than the core electron binding energy, primarily into unoccupied $5d$ states. In the intermediate state, two features corresponding to the transitions $4f$ states, which are partially split by the strong Coulomb interaction energy between the $2p$ core hole, providing a direct measure of the average rare-earth valence in the compound. In the de-excitation phase, the $2p$ hole is filled by a $3d$ core electron, where the

emitted photons (i.e. the fluorescence energy $h\nu_0$) are recorded as function of $h\nu_{in}$. The improved resolution from the PFY-XAS spectral features are sharp enough to estimate the average valence state of the RE ion as a function of temperature.

Recently, resonant inelastic X-ray scattering (RIXS) has been developed and became useful technique to obtain lifetime-broadening-suppressed spectra for the complex intermediate valence behaviour and valence changes driven by temperature and pressure. One of the advantages of RIXS is its bulk sensitivity, making it applicable to the study of samples even when they are in the high pressure cells. The difference between RIXS and a normal fluorescence X-ray emission process is that the core electron is resonantly excited at the absorption threshold [35]. The RIXS experiment involves, similar to the energy analysis of the PFY-XAS, resonant excitation of the $2p$ electrons followed by the decay of 3d levels, where the emitted photons ($h\nu_{out}$) are scanned at fixed $h\nu_{in}$. RIXS spectra are measured for each value of $h\nu_{in}$ to obtain bi-dimensional energy distribution over a broad ($h\nu_{in}$, $h\nu_{out}$) parameter space and plotted as a function of the transferred energy, $h\nu_T = h\nu_{in} - h\nu_{out}$. The signal from RE^{2+} and RE^{3+} configurations are selectively and resonantly enhanced as excitation energy approaches the threshold energy and their contributions appears in the emitted spectrum at constant transferred energy [36]. The maximum intensity occurs in correspondence with each feature observed in the XAS spectrum and thus the integrated fluorescent intensity can closely reproduces the XAS profile.

2.7.3 XAS using Synchrotron radiation

X-ray absorption measurements were performed using a synchrotron radiation at ESRF, where an intense and energy-tunable source of X-ray is available. These measurements were carried out at BM29 and ID16 beamlines, which was designed to perform experiments in the area of conventional X-ray absorption spectroscopy.

i) BM29

BM29 is the general purpose XAS beamline operates on the intrinsic properties of the ESRF synchrotron, as described in previous section, coupled with a bending magnet source and the high quality performance of the beamline's principle optical element, monochromator. This beamline can provide a very large operational energy range, 4 keV to 74 keV, with reasonable X-ray flux and high energy resolution at any K or L absorption edge. The standard ESRF primary slits are used to define the white-beam profile that is incident on the monochromator crystals, which are set to provide a typical beam profile of 10 mm to 20 mm in the horizontal plane and 0.2 mm to 1mm in the vertical plane. The primary slits vertical aperture is a particularly important parameter, as it largely defines the energy resolution of the instrument for a given set of monochromator crystals.

The monochromator is composed of a double crystal having a choice of Si(111), Si(220), Si(311) and Si(511) crystal pairs, depending upon the requirements of user for X-ray flux and operational energy range. The

principle pairs of crystals used are Si(111) and Si(311), which have corresponding operational energy ranges of 4.5 keV to 24 keV and 5 keV to 50 keV, respectively, while use of Si(511) crystals allow operational energy range of 10 keV to 74 keV. The operating geometry is in the vertical plane with the first crystal mounted so as to be able to rotate and translate along a mechanical cam, and directing the Bragg reflected beam upwards, while the second crystal is free to rotate about a single axis, and thus in combination with the translation and rotation of the first crystal, Bragg diffracts the beam through a fixed exit point.

BM29 provides various types of beam intensity monitor for different purpose of experiments and different type of measurements, for example, photodiodes for transmission experiments or fluorescene not requiring energy resolution, NaI scintillator detector for combined XRD, Total electron yield detection in the cryostat, Gas filled position sensitive detector, and so on. Using Ionisation chambers, detection efficiency is controlled by the gas species, gas pressure, and applied voltage of the chamber. The beamline is also equipped with a cryostat to allow the measurements for temperature dependence of X-ray absorption spectroscopy to be carried out.

ii) ID16

ID16 is an undulator beamline dedicated to high resolution inelastic X-ray scattering (IXS), which allows the energy and the momentum transfer to be controlled in wide regions. In this beamline, the incident photon energy can be varied between 5 and 21 keV. Mainly, two different type of

experimental method is offered depending on the incoming photon energy used; resonant IXS (RIXS), if the energy is close to an absorption edge, or non-resonant IXS, if the energy is away from any absorption edge.

Radiation from the undulator source is pre-monochromatized by a cryogenically cooled Si(111) double crystal monochromator, which then impinges on another silicon. One of the key element of this beamline is this, so called, backscattering geometry that can provide an X-ray beam with sub-meV energy resolution by using a utilized Si(*nnn*) reflection as a backscattering monochromator [37]. The scattered photons by the sample was analysed by a Rowland spherical spectrometer, which is equipped with a spherically bent silicon crystal having the same reflection as the monochromator. This spherical perfect crystal spectrometer, which was constructed at ESRF by gluing around 7500 silicon crystal cubes, also plays important role to keep the high energy resolution. The beamline is also equipped by the cryostat, oven, and high pressure cell, which can allow the measurements to carry out under variety of conditions. Temperature can be varied between 2.8 K and 350 K using cryostat, and from room temperature to 1700 K using oven. Pressure can be increased to a maximum of 400 kbar using a diamond anvil cell, and temperature can also varied at the same time by combining the cell with cryostat between 25 K and 350 K.

These set-ups allow us to perform two different types of measurements: high-resolution XAS in the partial fluorescence yield (PFY-XAS) mode and resonant inelastic X-ray scattering (RIXS) measurements as a function of temperature between 4 and 300 K.

2.8 References

[1] Murphy D. W., Rosseinsky M. J., Fleming R. M., Tycko R., Ramirez A. P., Haddon R. C., Siegrist T., Dabbagh G., Tully J. C., Walstedt R. E., *J. Phys. Chem. Solids* **53**, 1321 (1992).

[2] Hebard A. F., Rosseinsky M. J., Haddon R. C., Murphy D. W., Glarum S. H., Palstra T.T. M., Ramirez A. P., Kortan A. R., *Nature* **350**, 600 (1991).

[3] Rosseinsky M. J., Murphy D. W., Fleming R. M., Tycko R., Ramirez A. P., Siegrist T., Dabbagh G., Barrett S. E., *Nature* **356**, 416 (1992).

[4] Zhou O., Fischer J. E., Coustel N., Kycia S., Zhu Q., McGhie A. R., Romanow W. J., McCauley Jr., J. P., Smith A. B. III, Cox D. E., *Nature* **351**, 462 (1991).

[5] McCauley Jr., J. P., Zhu Q., Coustel N., Zhou O., Vaughan G., Idziak S. H. J., Fischer J. E., Tozer S. W., Groski D. M., Bykovetz N., Lin C. L., McGhie A. R., Allen B. H., Romanow W. J., Denenstein A. M., Smith A. B. III, *J. Am. Chem. Soc.* **113**, 8537 (1991).

[6] Kortan A. R., Kopylov N., Glarum S., Gyorgy M., Ramirez A. P., Fleming R. M., Thiel F. A., Haddon R. C., *Nature* **355**, 529 (1992).

[7] Kortan A. R., Kopylov N., Glarum S., Gyorgy M., Ramirez A. P., Fleming R. M., Zhou O., Thiel F. A., Trevor P. L., Haddon R. C., *Nature* **360**, 566 (1992).

[8] Kortan A. R., Kopylov N., Özdas E., Ramirez A. P., Fleming R. M., Haddon R. C., *Chemical Physics Letters* **233**, 501 (1994).

[9] Claridge J. B., Kubozono Y., Rosseinsky M. J., *Chem. Mater.* **15**, 1830

(2003).

[10] Özdas E., Kortan A. R., Kopylov N., Ramirez A. P., Siegrist T., Rabe K. M., Bair H. E., Schuppler S., Citrin P. H., *Nature* **375**, 126 (1995).

[11] Chen X. H., Roth G., *Phys. Rev B* **52**, 15534 (1995).

[12] Margiolaki I., Margadonna S., Prassides K., Hansen T., Ishii K., Suematsu H., *J. Am. Chem. Soc.* **124**, 11288 (2002).

[13] Margadonna S., Iwasa Y., Takenobu T., Prassides K., *Structure and Bonding* **109**, 127 (2004).

[14] Earney, J. J., Finn, C. B. P., Najafabadi, B. M., *J. Phys. C: Solid St. Phys.* **4**, 1013 (1971).

[15] Tover, M., Rao, D., Barnett, J., Oseroff, S. B., Thompson, J. D., Cheong, S. W., Fisk, Z., Vier, D. C., Schultz, S., *Phys. Rev. B.* **39**, 2661 (1989).

[16] Chu, W. K., Mayer, J. W., Nicolet, M. A., Backscattering Spectrometry, Academic Press, NY (1978)

[17] Masson, O., Dooryhée, E., Cheary, R. W., Fitch, A. N., *Mater. Sci. Forum* **378-381**, 300 (2001).

[18] Merrill, L., Basset, W. A., *Rev. Sci. Intrum.* **45**, 290 (1975).

[19] Mao, H. K., Xu, J., Bell, P. M., *J. Geophys. Res.* **91**, 4673 (1986).

[20] Hammersley, A., *FIT2D* Program, ESRF.

[21] Rietveld, H. M., *J. Appl. Cryst.* **2**, 65 (1969).

[22] Young, R. A., Wiles, D. B., *J. Appl. Cryst.* **15**, 430 (1982).

[23] Werthem, G. K., Butler, M. A., Wert, K. W., Buchanan, D. N. E., *Rev. Scient. Instrum.* **45**, 1369 (1974).

[24] Cagliotti, G., Paoletti, A., Ricci, F. P., *Nucl. Instrum.* **3**, 223 (1958).

[25] Laar, B. van., Yelon, W. B., *J. Appl. Cryst.* **17**, 47 (1984).

[26] Finger, L. W., Cox, D. E., Jephcoat, A. P., *J. Appl. Cryst.* **27**, 892 (1994).

[27] Aranda, M. A. G., Losilla, E. R., Cabeza, A., Bruque, S., *J. Appl. Cryst.* **31**, 16 (1998).

[28] Larsen, A. C., Von Dreele, R. B., *GSAS* software, Los Alamos National Laboratory Report No. LAUR 86-748.

[29] Pawley, G. S., *J. Appl. Cryst.* **14**, 357 (1981).

[30] Le Bail, A., Duroy, H., Fourquet, J. L., *Mat. Res. Bull.* **23**, 447 (1988).

[31] Rehr, J. J., Albers, R. C., *Rev. Mod. Phys.* **72**, 621 (2000).

[32] Sayers, D. E., Stern, E. A., Lytle, F. W., *Phys. Rev. Lett.* **27**, 1204 (1971).

[33] Hämäläinen, K., Siddons, D. P., Hastings, J. B., Berman, L. E., *Phys. Rev. Lett.*, **67**, 2850 (1991).

[34] Hayashi, H., Matsuo, S., Kurisaki, T., Kawamura, N., *X-Ray Spectrom.*, **37**, 232 (2008).

[35] Dallera, C., Annese, E., Rueff, J-P., Palenzona, A., Vankó, G., Braicovich, L, Shukla, A., Grioni, M., *Phys. Rev. B.* **68**, 245114 (2003).

[36] Dallera, C., Annese, E., Rueff, J-P., Grioni, M., Braicovich, L, Barla, A., Sanchez, J-P., Gusmeroli, R., Palenzona, A., Degiorgi, L, Lapertot, G., *J. Phys.: Condens. Matter.* **17**, S849 (2005).

[37] Sette, F., Ruocco, G., Krisch, M., Bergmann, U., Masciovecchio, C., Mazzacurati, V., Signorelli, G., Verbeni, R., *Phys. Rev. Lett.* **75**, 850 (1995).

CHAPTER 3

Mixed Valence transitions in Ytterbium intercalated Fullerides

3.1 Introduction

Intercalation of solid C_{60} with electron donors, such as the alkali, alkaline-earth and rare-earth metals can results in a various intercalated fulleride salts with stoichiometries M_xC_{60}, where the dopant level, x can be as low as 1 or as high as 12. This is due to the high electron affinity of the C_{60} molecule and the weak intermolecular van der Waals forces in its crystalline form. The results from intense efforts on these intercalated fullerides revealed that by changing the size and nature of the dopants affects sensitively the structural and electronic properties of the materials [1-3]. One of the most well known examples of this has been seen with alkali-metal doped fullerides of stoichiometry A_3C_{60} (and $A_2A'C_{60}$, A, A' = alkali-metal), at which these salts become superconducting from their metallic state at critical temperatures, T_c, as high as 33 K at ambient pressure [4, 5] and at 38 K under the applied pressure [6]. Experimentally derived relationship between interfullerened spacing and T_c in A_3C_{60} indicated that the superconducting transition temperatures can be controlled by the ion occupying the tetrahedral sites, T_d [7]. In the case of alkaline-earth-metal doped fullerides, which exhibit a hybridisation between alkaline-earth and C orbitals affecting their electronic properties and leads to metallic and superconducting compositions for various levels of band filling [8-10].

The introduction of the rare-earth-metal in the C_{60} lattice can offer wide range of possibilities that could result in the interesting electronic and magnetic behaviour. The chemistry of the rare-earth elements is typically dominated by the +3 oxidation state. However, for certain rare-earth elements such as Sm, Eu and Yb, the valence state can vary between

energetically close RE^{2+} and RE^{3+} electronic configurations. As a result, such rare-earth based compounds may exhibit the phenomenon of mixed (or intermediate) valence, which can be quantified by the number of $4f$ holes, n_h in the RE^{2+} electronic configuration as $n = 2 + n_h$ ($0 \leq n_h \leq 1$). This situation has been encountered in solids like SmS, SmB_6, and YbB_{12} in which the ground state electronic configuration has been interpreted in terms of the valence fluctuation model [11-13]. In this model, two different valence states, namely +3 and +2, of the rare-earth element coexist in the system and the $4f^n$ and $4f^{n-1}5d^1$ configurations, which lie close to the Fermi level, E_F, are nearly degenerate. The existence of the mixed valence state has been observed using various techniques, such as magnetic susceptibility [14], Mössbauer spectroscopy [15], and L_3-edge X-ray absorption measurements [16].

The study of mixed valence compounds such as SmS using powder X-ray diffraction techniques under high pressure at room temperature was first reported by Jayaraman *et al.* [11]. It was shown that with increasing pressure, a discontinuous $4f \rightarrow 5d$ electron delocalization accompanied by an abrupt decrease in volume ($\Delta V/V \sim 16\%$) occurred at ~6.5 kbar. This first-order pressure-induced valence transition without a change in crystal structure was attributed to the electronic transition of the Sm ion from Sm^{2+} ($4f^6$) to Sm^{3+} ($4f^5 5d^1$) and is consistent with the size of the ionic radii ($r(4f^6) > r(4f^5 5d^1)$). Furthermore, complementary resistivity data under pressure also showed an abrupt decrease in resistance at 6.5 kbar reflecting the pressure-induced semiconductor-to-metal transition due the strong hybridisation between the localised $4f$ and the conduction 5d electrons. Soon afterwards, it was shown that the Sm valence change in SmS can be brought to ambient pressure in ternary sulfides such as $Sm_{1-x}Y_xS$ [17]; these were

shown to undergo an abrupt decrease in the lattice parameters on cooling at atmospheric pressure. This suggests that the hybridisation strength between the $4f$ and $5d$ orbitals can be tuned both by the application of pressure and by chemical substitution.

More recent studies in this field revealed that the mixed valence can also arise from the simultaneous presence of electronically active cation and anion sublattices where the anion sublattice can act as an electron reservoir which can accept electrons from or donate electrons to the rare-earth $4f$ bands with changes in external stimuli, such as pressure and temperature. For instance, the $YbGa_{1+x}Ge_{1-x}$ intermetallic exhibits both continuous and abrupt temperature-induced $Yb^{(2+\varepsilon)+} \rightarrow Yb^{2+}$ valence changes. Single- crystal X-ray diffraction data for YbGaGe shows an overall zero thermal expansion (ZTE) between 100 and 400 K, as a result of a temperature-induced continuous valence transition from Yb^{2+} towards the smaller Yb^{3+} on heating [18]. In addition, high-resolution synchrotron powder X-ray diffraction data on the Ga-rich composition, $YbGa_{1.05}Ge_{0.95}$, showed that it exhibits positive thermal expansion between 723 and 15 K, but further cooling to 5 K resulted in an abrupt isosymmetric phase transition which was accompanied by a large volume increase, known as negative thermal expansion (NTE) [19]. This was interpreted as resulting from the sudden change in valence state of Yb ion from Yb^{3+} towards the larger Yb^{2+}. The temperature-induced valence transitions observed in both cases are controlled by the spilling over of the Ga $4p$ electronic density into the Yb $4f$ band.

When the family of rare-earth fullerides are considered, the availability of the narrow C_{60} t_{1u} band with its strongly correlated character in close proximity to the rare-earth $4f$ and $5d$ bands offers particularly intriguing

possibilities of novel electronic behaviour when compared with the other known mixed valence solids described above. In fact, $Sm_{2.75}C_{60}$ displays both temperature- and pressure-induced valence transitions accompanied by isosymmetric lattice responses – NTE and lattice collapse, respectively. $Sm_{2.75}C_{60}$ showed NTE at low temperatures without accompanying change in crystal symmetry; an overall volume decrease of 0.84% occurs on heating between 4.2 and 32 K [20]. The sign of the thermal expansivity then changes and the lattice expands on heating to 295 K, but still not by large enough to produce a cell volume at room temperature comparable to that at 4.2 K. The pressure-response of $Sm_{2.75}C_{60}$ is also intriguing. Upon pressurisation, the unit cell volume contracts monotonically to 3.95 GPa. However, above this pressure, a sudden increase in the volume contraction rate was observed, resulting in a ~6.8% volume collapse which is accompanied by an insulator-to-metal transition. The transformation is complete and the contraction rate becomes much smaller with further increase in pressure. This transformation is found to be both reversible and to be characterised by a large hysteresis as the original low-pressure phase does not recover until a pressure well below 3.45 GPa is reached [21].

An estimate of the average Sm valence at ambient pressure was obtained from variable temperature magnetic susceptibility measurements. The room temperature value of the magnetic susceptibility of $Sm_{2.75}C_{60}$ can be calculated from a linear combination of the free Sm^{2+} and Sm^{3+} ion contributions, giving a value of the average Sm valence approximately equal to +2.2-2.3. This value directly corresponds to full occupation of the LUMO t_{1u} band of the C_{60} and a formal charge of -6 for the fulleride sublattice. The behaviour of $Sm_{2.75}C_{60}$ with changing external stimuli can be rationalised in

the same manner as in the other mixed valence compounds mentioned above. The temperature and pressure evolution of the lattice size is directly related to a temperature- and pressure-induced valence transition where the average Sm oxidation state approaches +2 upon cooling below a critical temperature and increases towards +3 above a critical pressure, respectively.

In order to search for additional examples of mixed valence rare-earth fullerides, the effect of Eu, Tm, Yb, and Ca substitution for Sm in $Sm_{2.75}C_{60}$, as well as the effect of temperature and pressure on the properties of these compounds have been investigated. The choice of the substituent was made by the following considerations: the energy difference between the divalent and trivalent states of Sm, Eu, Tm, and Yb are all similar and very close to zero as shown in Fig. 1.11, circled in blue [22]. According to the lanthanide contraction, the ionic radii of Sm and Eu are almost the same, while those of Tm and Yb are substantially smaller. As all these rare-earth elements have electronically active $4f$ sublattices (Sm^{2+} $4f^6$, Eu^{2+} $4f^7$, Tm^{2+} $4f^{13}$, and Yb^{2+} $4f^{14}$), dilution of the influence of the $4f$ electrons could be studied in the case of the alkaline-earth element, Ca.

In this chapter, the results of the studies on the structural and magnetic properties of the rare-earth fulleride, $Yb_{2.75}C_{60}$ will be presented. The temperature evolution of the structural properties of $Yb_{2.75}C_{60}$ (sample Z) on heating from 5 to 295 K has been reported earlier [23]. These results will be also mentioned briefly, as they are related to those obtained on the same sample on stepwise slow cooling from 295 to 5 K and those of $Yb_{2.75}C_{60}$ (sample C), which will be introduced in the following sections.

3.2 Temperature-induced valence transition

In order to explore the existence of temperature-dependent valence transitions in Yb intercalated fullerides, synchrotron X-ray powder diffraction measurements were performed on $Yb_{2.75}C_{60}$ (samples named C and Z) as a function of temperature. $Yb_{2.75}C_{60}$ and $Sm_{2.75}C_{60}$ are isostructural rare-earth fullerides but changing the nature of the rare-earth cation sublattice from Sm to Yb is found to affect the NTE behaviour.

3.2.1 Experimental Details

As $Yb_{2.75}C_{60}$ is extremely sensitive to air, preparation and sample handling was performed inside an Ar-atmosphere glove-box (O_2 < 0.1 ppm, H_2O < 0.9 ppm). Prior to synthesis, 99.9% purity C_{60} was degassed overnight at 200°C under a dynamic vacuum of 10^{-5} mbar. The samples were prepared by reaction of stoichiometric quantities of well-ground C_{60} and ytterbium powder pressed into pellets and contained in a sealed tantalum tube, which were then placed inside a quartz tube filled with helium gas at 300 mbar. The tube containing sample C was placed in the pre-heated furnace at a temperature of 630°C for 6 hours with two intermediate grindings (2hr + 2hr + 2hr), while the tube containing sample Z was placed in another furnace with a temperature set at 620°C for 6.5 hours with two intermediate grindings (2hr + 2hr + 2.5hr). The pellets were then slowly cooled down to room temperature in ~6 hours. Few milligrams of the samples were sealed in thin-wall glass capillaries of diameter 0.5 mm for the synchrotron X-ray powder diffraction measurements. Phase purity was checked using the

laboratory D5000 X-ray diffractometer prior to the synchrotron X-ray measurements (Fig 3.1).

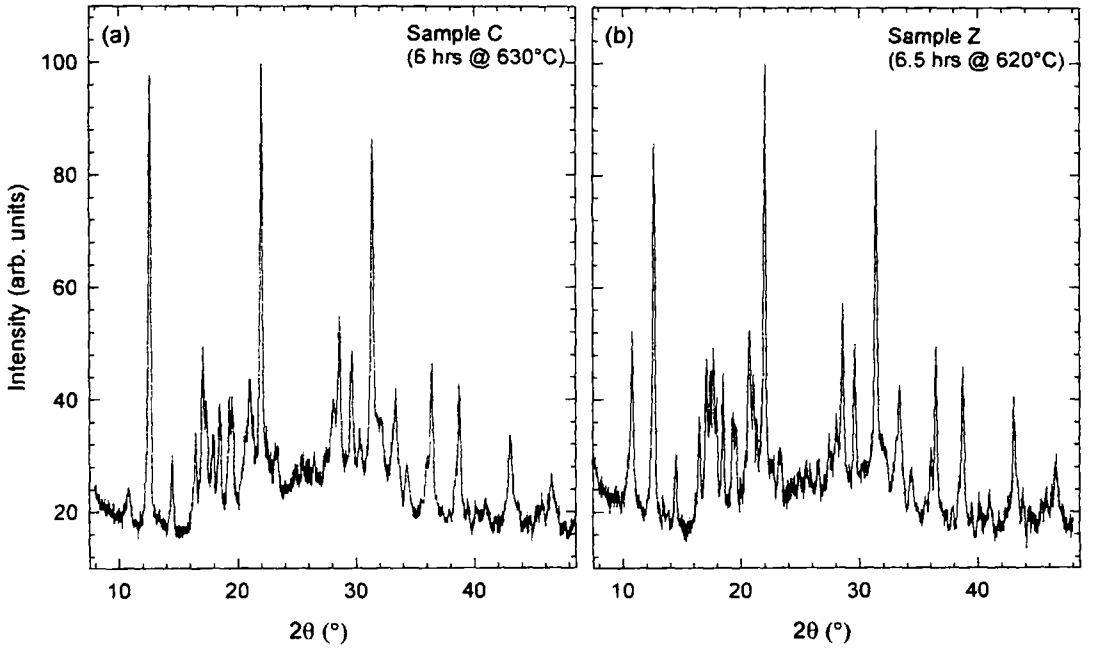

Fig. 3.1. X-ray diffraction profiles of $Yb_{2.75}C_{60}$ (a) sample C and (b) sample Z collected with the Siemens D5000 powder diffractometer (Cu-K_α radiation) at room temperature.

Yb_xC_{60} samples with varying nominal concentrations of x (x = 2.75, 3, 3.5, 4, 4.5, 5, and 6) were also prepared (Table 3.1) and characterised by SQUID magnetisation measurements where about 120 mg of the sample was sealed in a SQUID quartz tube. Low-field measurements in a field of 5 Oe were carried out under ZFC and FC conditions to search for bulk superconductivity, and total susceptibilities were measured between 2 and 300 K in a field of 1 T with a Quantum Design MPMS5 SQUID susceptometer.

Synchrotron X-ray diffraction data on $Yb_{2.75}C_{60}$ (sample C) at various temperatures on heating were collected between 5 and 295 K using a liquid-

Table 3.1. Quantities of reactants used for synthesising Yb_xC_{60} and the final mass of the product obtained after the annealing protocols. The error of the weight was ±1 mg.

Yb_xC_{60} Nominal x	Yb (173.04 g/mol)	C_{60} (720.66 g/mol)	Product (mg)
2.75	66.0 mg 3.816×10^{-4} mol	100 mg 1.388×10^{-4} mol	161 mg
3.0	72.0 mg 4.162×10^{-4} mol	100 mg 1.388×10^{-4} mol	165 mg
3.5	84.0 mg 4.856×10^{-4} mol	100 mg 1.388×10^{-4} mol	176mg
4.0	96.0 mg 5.550×10^{-4} mol	100 mg 1.388×10^{-4} mol	190 mg
4.5	108 mg 6.241×10^{-4} mol	100 mg 1.388×10^{-4} mol	203 mg
5.0	60 mg 3.467×10^{-4} mol	50 mg 0.694×10^{-4} mol	105 mg
6.0	72mg 4.161×10^{-4} mol	50 mg 0.694×10^{-4} mol	115 mg

helium-cryostat in continuous scanning mode with the high-resolution powder diffractometer on beamline ID31 at the ESRF, Grenoble. This sample was first cooled straight down to 5 K at a rate of 5 K/min, then, it was slowly heated using a stepwise warming-up protocol (0.1 K/min between 5 and 60 K, 0.4 K/min up to 295 K), while diffraction data were collected at intermediate temperatures. The diffraction data were collected using a monochromatic X-ray beam of wavelength, λ = 0.799985 Å and the collected data were rebinned to a step of 0.005° in the 2θ range 3.1° - 29° for data analysis.

Similarly, the diffraction profiles of $Yb_{2.75}C_{60}$ (samples Z) were collected using the same experimental setup, first, on heating between 5 and 295 K and then on cooling from 295 down to 4 K. This sample was first cooled straight down to 5 K at a cooling rate of 4 K/min, then it was heated slowly at a rate of 0.2 K/min and data were collected at each step when the

temperature was stabilised. Sample Z was also cooled down using a stepwise cooling protocol while data were collected at various temperatures between 295 and 4 K to investigate the existence of hysteretic effects associated with the transition. These experiments were carried out using a monochromatic X-ray beam of wavelength, λ = 0.85066 Å (heating up) and 0.80098 Å (cooling down), and the collected data were rebinned to a step of 0.005° in the 2θ range 3.2° - 27°. Data analysis was performed with the GSAS suite of Rietveld analysis programs.

3.2.2 Magnetisation Measurements

In an attempt to investigate the presence of bulk superconductivity in $Yb_{2.75}C_{60}$ reported earlier [24], low field (5 Oe) ZFC and FC magnetisation measurements were carried out on many different batches prepared in our laboratory for which powder X-ray diffraction patterns were essentially identical. The results obtained from these measurements showed no support for the appearance of bulk superconductivity, except that, in some cases, a very small diamagnetic response with an onset temperature of 6 K was observed [23]. The plot of magnetisation (emu/g) as a function of temperature for the sample (sample Z) showing the maximum field expulsion is shown in Fig. 3.2, where the calculated maximum shielding fraction obtained data was less than 1%. Perfect diamagnetism (100% shielding fraction) is calculated using the following equation:

$$\chi_{s.f.} = -4\pi \frac{M\rho}{Hm} \qquad \text{(Eqn. 3.1)}$$

where M is the longitudinal moment measured at 2 K, ρ is the density, H is

the magnetic field, and m is the mass of the sample.

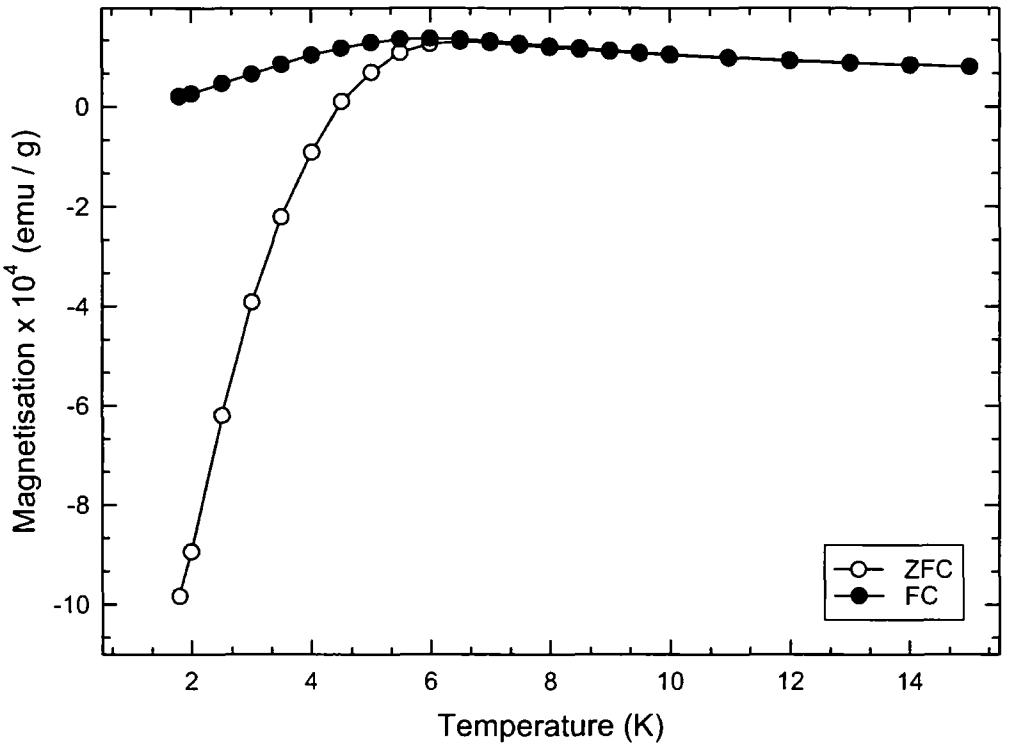

Fig. 3.2. Temperature dependence of the ZFC (open circle) and FC (full circle) magnetisation in a field of 5 Oe for $Yb_{2.75}C_{60}$. The superconducting fraction obtained from these data was ~0.8%.

Given that our analogous measurements on $Sm_{2.75}C_{60}$ never showed any trace of superconductivity for the numerous samples studied, the observed trace superconductivity present in the Yb-C_{60} phase field quite possibly originates from a phase with composition other than $Yb_{2.75}C_{60}$. Comparable measurements were performed on Yb_xC_{60} samples with nominal compositions, x = 3, 3.5, 4, and 4.5 (Fig. 3.3). These provided slightly higher superconducting fractions (~2%) when "Yb_4C_{60}" was measured. The obtained results are in agreement with those mentioned in another early report [25], but at present the superconducting Yb_4C_{60} phase (if it exists) remains unidentified.

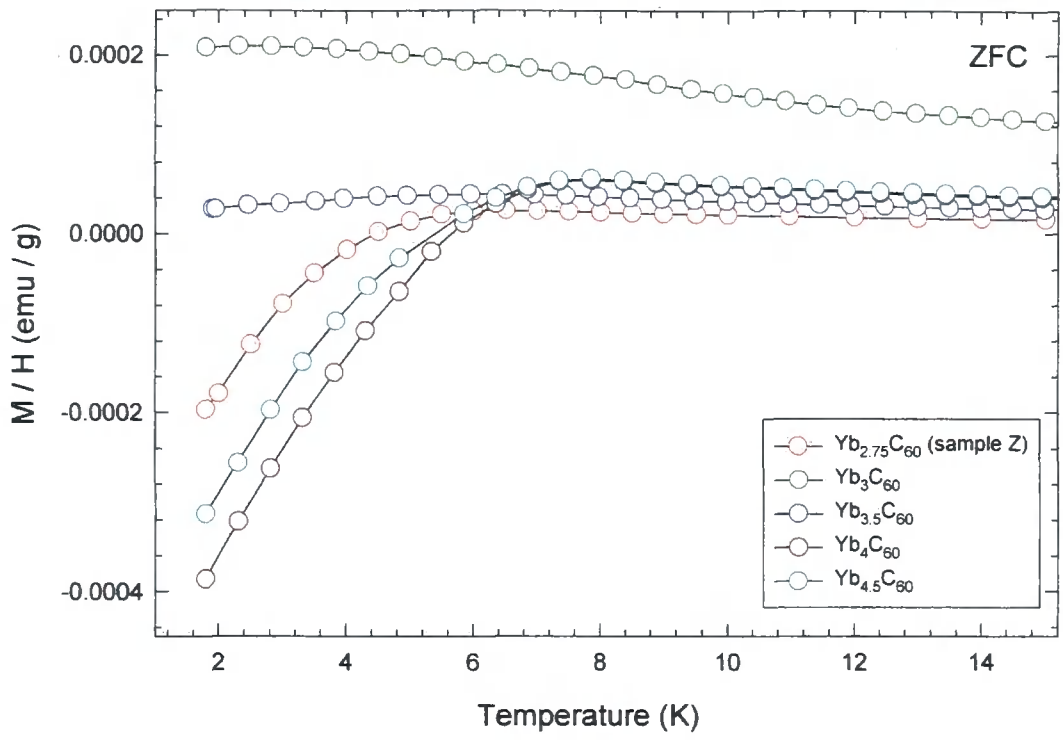

Fig. 3.3. Temperature dependence of the ZFC magnetisation for Yb_xC_{60} samples with nominal *x* content of 2.75 (5.0 Oe), 3 (50 Oe), 3.5 (20 Oe), 4 (20 Oe), and 4.5 (20 Oe). The maximum superconducting fraction was obtained for "Yb_4C_{60}" at ~2.0%.

The magnetic susceptibility for $Yb_{2.75}C_{60}$ (sample Z) was measured in the temperature range of 2-300 K (Fig. 3.4). The Curie- Weiss law was obeyed only in the restricted temperature regions. The average valence of Yb at room temperature was estimated after correcting for the diamagnetic core contributions (corrections were made using Pascal's constants of -20×10^{-6} emu/mol for Yb^{3+} and -5.91×10^{-4} emu/mol for C_{60}^{6-}). The temperature dependence of calculated average magnetic susceptibility at was also included in Fig. 3.4a assuming a linear combination of the Yb^{2+} (diamagnetic) and Yb^{3+} (paramagnetic) contributions, where the paramagnetic susceptibility for Yb^{3+} is given by following equation [26]:

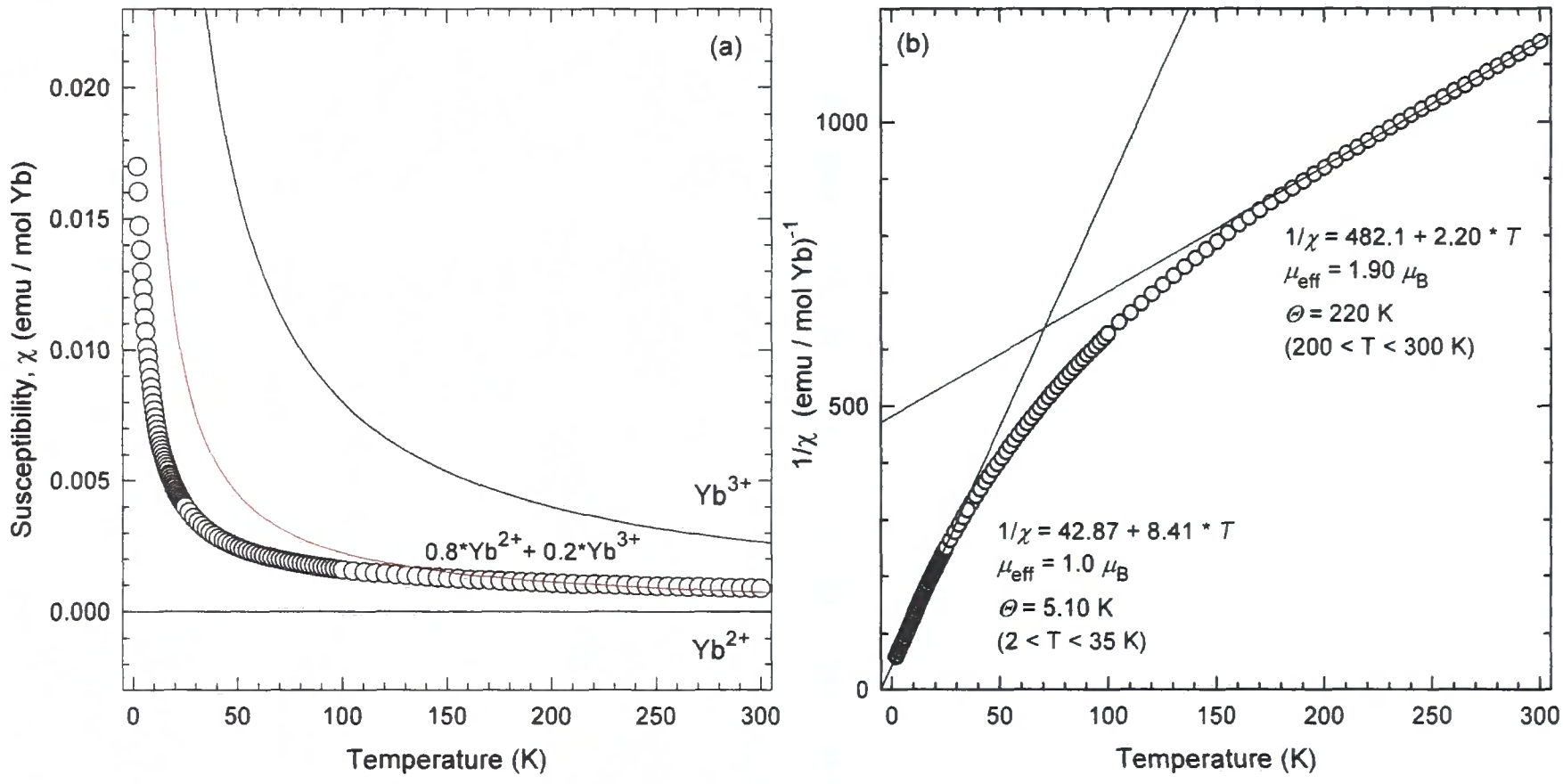

Fig. 3.4. Temperature dependence of (a) the magnetic susceptibility, χ, and (b) its reciprocal, $1/\chi$ in a field, $H = 1$ T for $Yb_{2.75}C_{60}$. In plot (a), the calculated magnetic susceptibilities of the free Yb^{2+} and Yb^{3+} ions are shown by black solid lines, (continued)

Fig. 3.4. (continued) and the weighted average of the susceptibility calculated from the contributions of both Yb^{2+} and Yb^{3+} is represented by a red solid line. In plot (b), the Curie-Weiss fits of the data in the ranges 200-300 K and 2-35 K are shown.

$$\chi(Yb^{3+}) = \frac{\chi_{C7/2}}{378(1+2Z+Y)}\left(98+260Z+162Y+\frac{432k_BT}{\Delta_{68}-\Delta_{67}}(Y-Z)+\frac{560k_BT}{\Delta_{68}}(1-Z)\right)$$

$$\chi_{C7/2} = \frac{N_A g_J^2 \mu_B^2 J(J+1)}{3k_BT}, Y = \exp\left(\frac{-\Delta_{67}}{k_BT}\right), Z = \exp\left(\frac{-\Delta_{68}}{k_BT}\right) \qquad \text{(Eqn. 3.2)}$$

where Δ_{67} and Δ_{68} are the energy difference between the ground state and excited states, g_J is the Lande splitting factor, μ_B the Bohr magneton, k_B the Boltzmann constant, T the temperature, and J the total angular momentum. The calculated free-ion effective magnetic moment of the Yb^{3+} ion from the equation above was 4.54 μ_B, which agrees with the theoretical value given by $g_J[J(J+1)]^{1/2}$, and thus, the estimated average valence state of $Yb_{2.75}C_{60}$ at room temperature was approximately equal to ~+2.18. Below 200 K, the inverse susceptibility plots deviate from the Curie-Weiss behaviour (Fig. 3.4b), as the influence of the crystal field set in, associated with the splitting of the eightfold degenerate $^2F_{7/2}$ octet ground state of the Yb^{3+} ions. Thus, the magnetic susceptibility can no longer be expressed as a linear combination of the Yb^{2+} and Yb^{3+}. At low temperature range (T < 35 K), the population of the highest levels decrease significantly (the first excited level of the free Yb^{3+} ion lies at about 10300 cm^{-1} [27]) so that the influence of the ligand field to the susceptibility decreases, and the paramagnetic susceptibilities can be fitted to Curie-Weiss law, with a reduced magnetic moment of 1.0 μ_B per Yb ion. The reduced average Yb valence was approximated to be +2.05.

3.2.3 Structural Analysis

i) $Yb_{2.75}C_{60}$ (sample C, warming-up)

Fig. 3.5 shows the high-resolution synchrotron powder X-ray diffraction profiles of $Yb_{2.75}C_{60}$, sample C, at 5 and 295 K in the 2θ range 3.0° - 35°. The obtained profiles show that there is no observable change in crystal symmetry on cooling. Furthermore, both diffraction profiles display additional peaks that are not expected in the *fcc* structure – these can only be indexed by assuming an orthorhombic structure after doubling all three lattice parameters of the original fcc unit cell (i.e. $Yb_{2.75}C_{60}$ adopts an orthorhombic superstructure, space group *Pcab*, option 2). Thus, the refinements of the structure of $Yb_{2.75}C_{60}$ were initiated by using the same structure model employed in the $Sm_{2.75}C_{60}$ analysis [20] at all temperatures. However, as seen in the inset of the following figure (Fig. 3.5a and b), the diffraction peaks of sample C observed at both 5 and 295 K are not as symmetric as those of $Sm_{2.75}C_{60}$, and similar asymmetric shape was apparent for all diffraction peaks at all temperatures (indicated by red arrows). The asymmetricity in the peak profiles of sample C most likely reflect somewhat inferior quality of the sample (a slightly lower annealing temperature than that for sample Z was used in order to avoid formation of Yb carbides, see Fig. 3.8). As a result, structural analysis of sample C becomes less straightforward than that of sample Z. After introducing a second phase in the course of the structural analysis, refinements of the diffraction dataset at 295 K proceeded smoothly. The diffraction profile shown in Fig. 3.5a also reveals the existence of phase separation at 5 K (indicated by blue arrow).

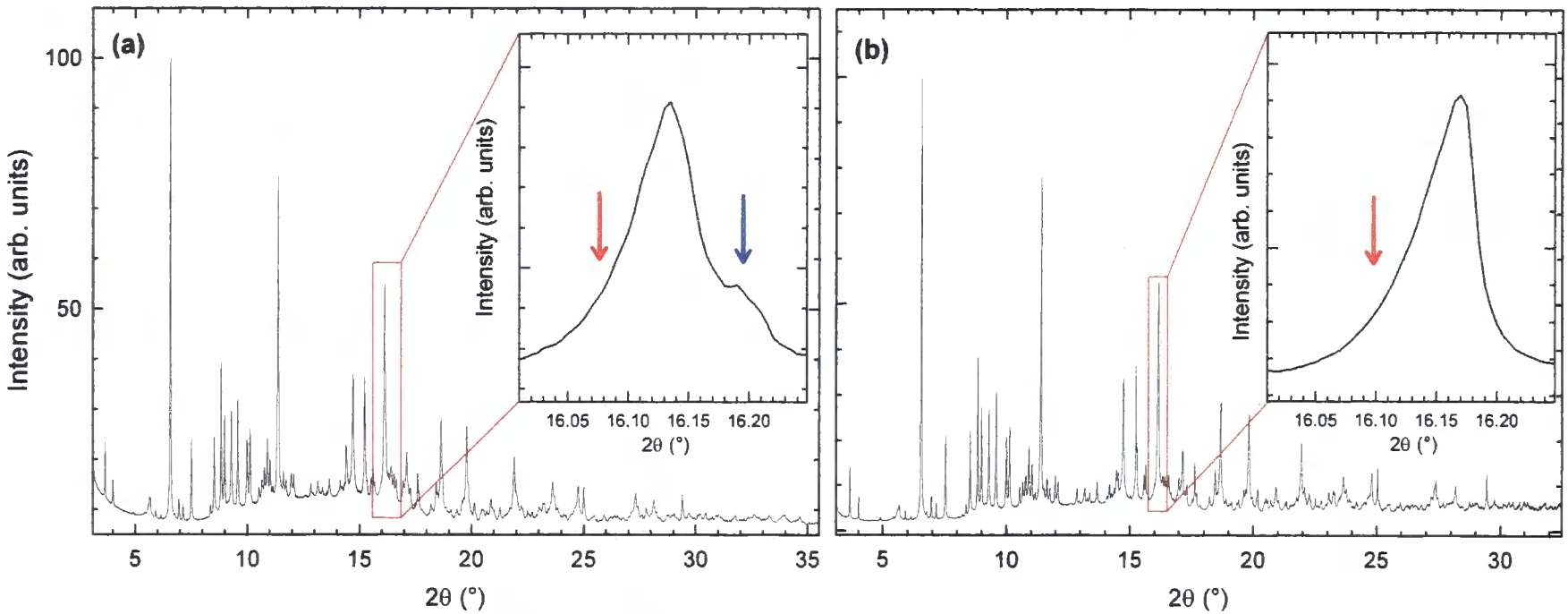

Fig. 3.5. Synchrotron X-ray powder diffraction profiles of $Yb_{2.75}C_{60}$ (λ = 0.799985 Å) of sample C at (a) 5 K and (b) 295 K. The insets in both figures show an expanded view of a selected region of the (844) Bragg peaks, where the red arrows indicate that the peak profile is asymmetric and the blue arrow indicates the existence of phase separation.

Extraction of the lattice constants from the diffraction pattern of sample C at 295 K was carried out using the LeBail pattern decomposition technique. The values of the major phase are: a = 27.8703 (3) Å, b = 27.9066 (3) Å, c = 27.8313 (3) Å, V = 21646.2 (6) Å^3 (minor phase: a = 27.9333 (6) Å, b = 27.9695 (6) Å, c = 27.8943 (6) Å, V = 21793.2 (11) Å^3), and the agreement factors $\chi^2 = 6.199$, $R_{wp} = 6.04\%$, $R_{exp} = 2.43\%$. The lattice constants obtained here are substantially smaller compared to those obtained for $Sm_{2.75}C_{60}$ at the same temperature (a = 28.1871 (2) Å, b = 28.2237 (2) Å, c = 28.1476 (2) Å, V = 22395.0 (5) Å^3). These values reflect the effect of the ionic radii of the intercalated metals on the lattice metrics ($r(Yb^{2+}) < r(Sm^{2+})$).

Refinement of the structure of $Yb_{2.75}C_{60}$ was then initiated by Rietveld analysis of an extended Q-range diffraction dataset (2θ range 3.2° - 28.6°) at 295 K assuming that both phases adopt the same structural model. As in $Sm_{2.75}C_{60}$, the observed superstructure in $Yb_{2.75}C_{60}$ arises from long-range ordering of tetrahedral (T_d) Yb defects, namely one out of every eight T_d sites is only partially occupied (~15% in the present refinement) (Fig. 3.6).

The structural model was constructed by firstly constraining the shape of the C_{60} units to icosahedral symmetry with a cage diameter of 7.01 Å and fixing all C-C bond lengths to 1.44 Å. There are 32 C_{60} molecules present in the unit cell of $Yb_{2.75}C_{60}$; therefore, 240 independent C atoms are required. Secondly, the orientation of five symmetry-inequivalent C_{60} molecules present in the unit cell, $C_{60}(1)$ at (000), $C_{60}(21)$ at (0¼¼), $C_{60}(22)$ at (¼0¼), $C_{60}(23)$ at (¼¼0), and $C_{60}(3)$ at (½½½), were rotated anticlockwise by 37.5° about their local [111], [1 $\bar{1}$ $\bar{1}$], [$\bar{1}$ 1 $\bar{1}$], [$\bar{1}$ $\bar{1}$ 1], and [111] symmetry axes, respectively.

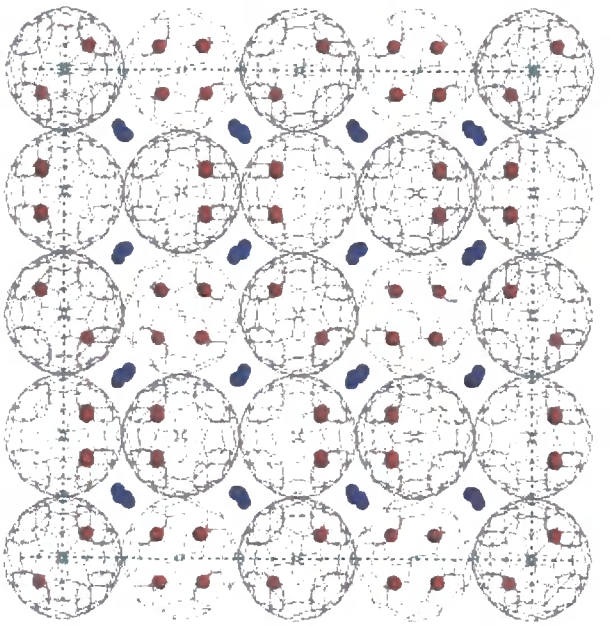

Fig. 3.6. Basal plane projection of the orthorhombic superstructure of $Yb_{2.75}C_{60}$ based on the doubling the *fcc* A_3C_{60} unit cell along all three lattice directions. Yb cations in distorted octahedral and tetrahedral sites are represented by red and blue spheres, respectively. The C_{60} units are optimally rotated about local three-fold symmetry axes.

Finally, every C atom coordinate was scaled with respect to the lattice constant obtained via the LeBail technique for $Yb_{2.75}C_{60}$ using the following expression:

$$x'=\frac{ax}{a'},\ y'=\frac{by}{b'},\ \text{and}\ z'=\frac{cz}{c'} \qquad \text{(Eqn. 3.4)}$$

where a, b, and c are the lattice constants and x, y, and z are atomic coordinates of C atoms of $Sm_{2.75}C_{60}$ and a', b', and c' are the lattice constants and x', y', and z' are the atomic coordinates of C atoms of $Yb_{2.75}C_{60}$, respectively. The resultant structure model, which is different from that proposed in ref. [24], leads to both improved agreement factors for the

Table 3.2a. Refined parameters of $Yb_{2.75}C_{60}$ (sample C, major phase) obtained from the Rietveld refinement of the diffraction data at 5 K.

	Site	x/a	y/b	z/c	Occupancy	B(Å^2)
C_{60} (1)	4a	0	0	0	1.0	2.8 (1)
C_{60} (21)	8c	0	¼	¼	1.0	2.8 (1)
C_{60} (22)	8c	¼	0	¼	1.0	2.8 (1)
C_{60} (23)	8c	¼	¼	0	1.0	2.8 (1)
C_{60} (3)	4b	½	½	½	1.0	2.8 (1)
Yb (11)	8c	0.1380 (4)	0.1148 (5)	0.3610 (4)	0.978 (1)	4.3 (2)
Yb (12)	8c	0.3610 (4)	0.1380 (4)	0.1148 (5)	0.978 (1)	4.3 (2)
Yb (13)	8c	0.1148 (5)	0.3610 (4)	0.1380 (4)	0.978 (1)	4.3 (2)
Yb (21)	8c	0.1337 (4)	0.3689 (5)	0.3779 (6)	0.978 (1)	4.3 (2)
Yb (22)	8c	0.3779 (6)	0.1337 (4)	0.3689 (5)	0.978 (1)	4.3 (2)
Yb (23)	8c	0.3689 (5)	0.3779 (6)	0.1337 (4)	0.978 (1)	4.3 (2)
Yb (3)	8c	0.384 (2)	0.373 (2)	0.376 (2)	0.978 (1)	4.3 (2)
Yb (4) (vacancy)	8c	0.116 (2)	0.127 (3)	0.127 (2)	0.155 (9)	4.3 (2)
Yb (51)	8c	0.1998 (1)	0.1998 (1)	0.1998 (1)	0.939 (4)	1.7 (3)
Yb (52)	8c	0.0501 (1)	0.0501 (1)	0.1998 (1)	0.939 (4)	1.7 (3)
Yb (53)	8c	0.1998 (1)	0.0501 (1)	0.0501 (1)	0.939 (4)	1.7 (3)
Yb (54)	8c	0.0501 (1)	0.1998 (1)	0.0501 (1)	0.939 (4)	1.7 (3)
Yb (61)	8c	0.1998 (1)	0.323 (3)	0.323 (3)	0.061 (4)	1.7 (3)
Yb (62)	8c	0.0501 (1)	-0.073(3)	0.323 (3)	0.061 (4)	1.7 (3)
Yb (63)	8c	0.323 (3)	-0.073(3)	0.0501 (1)	0.123 (7)	1.7 (3)

Table 3.2b. Nearest Yb-C contacts for the T_d sites in sample C at 5 K in Å.

Yb(11)-C	2.608 (7)	Yb(21)-C	2.672 (9)
	2.621 (7)		2.830 (9)
Yb(12)-C	2.605 (6)	Yb(22)-C	2.692 (8)
	2.618 (6)		2.798 (8)
Yb(13)-C	2.592 (8)	Yb(23)-C	2.693 (9)
	2.635 (8)		2.801 (9)
Yb(3)-C	2.72 (1)	Yb(4)-C	2.91 (2)
	2.77 (1)		2.92 (2)

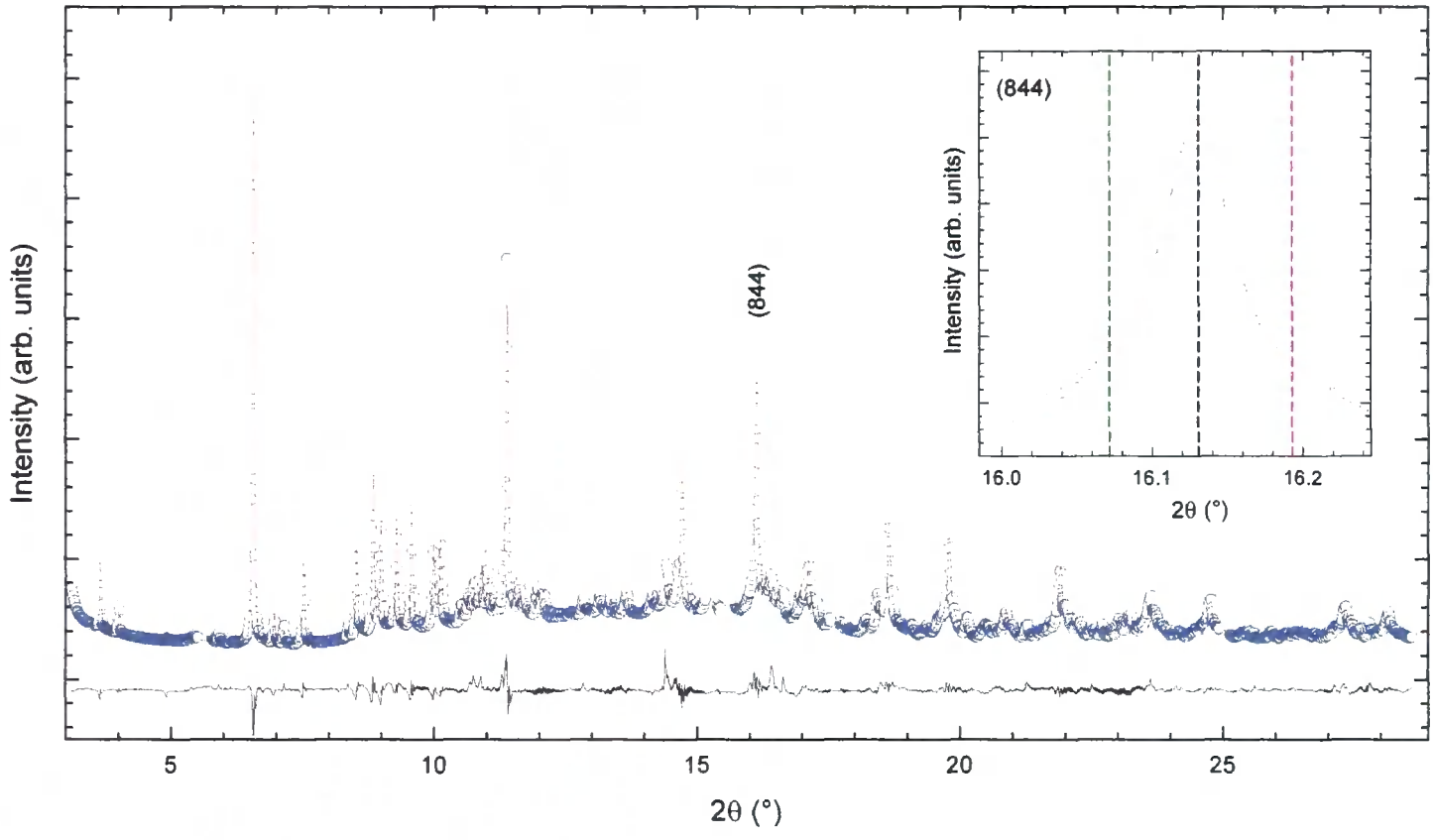

Fig. 3.7. Synchrotron X-ray powder diffraction profile of $Yb_{2.75}C_{60}$ (sample C) at 5 K (λ = 0.799985 Å). Intensities of observed and calculated peaks are shown as blue circles and solid red line, respectively. The solid black line at the bottom indicates the difference of observed and calculated peaks. [*Inset:* Refinement results of the (844) Bragg peak (green, black, and pink dashed lines indicate the position of phase 3, phase 1, and phase 2, respectively).]

Rietveld refinement and avoids the presence of unphysically short Yb-C_{60} contacts. In the refined structural model, the Yb cations are displaced from the centres of the O_h sites by ~2.4 Å and from the centres of the T_d sites by ~0.3 Å with a shortest Yb(3)-C_{60} contact of 2.78(3) Å.

Based on this model, the refinement of the diffraction profile at 5 K was also carried out and the results of the final refinement are shown in Table 3.2 and Fig. 3.7. For the major phase (phase 1), a = 27.9262(9) Å, b = 27.9458(9) Å, c = 27.9067(9) Å, and V = 21779.0(20) Å^3 (agreement factors: χ^2 = 2.914, R_{wp} = 3.89%, R_{exp} = 2.28%). The second phase introduced to account for the features at higher angles has lattice parameters: a = 27.8197(29) Å, b = 27.8391(30) Å, c = 27.8002(30) Å, V = 21530.6(6.8) Å^3. Finally, a third phase was added to compensate for the asymmetry of the diffraction peaks (a = 28.0287(22) Å, b = 28.0481(23) Å, c = 28.0092(22) Å, V = 22019.5(5.3) Å^3). The weight fractions of these three phases converged to 74.8(1)% (phase 1, major phase), 13.0(3)% (phase 2, minor phase), and 12.2(2)% (phase 3, asymmetry). In the course of the refinements, some weak impurity peaks were excluded.

ii) $Yb_{2.75}C_{60}$ (sample Z, cooling protocol)

The diffraction profile of $Yb_{2.75}C_{60}$ (sample Z) at 4 K (λ = 0.80098 Å), obtained on stepwise cooling from 295 K down to 4 K, is shown in Fig. 3.8. As seen in the inset, the diffraction peaks are significantly more symmetric, implying that sample Z is clearly single-phase at all temperatures.

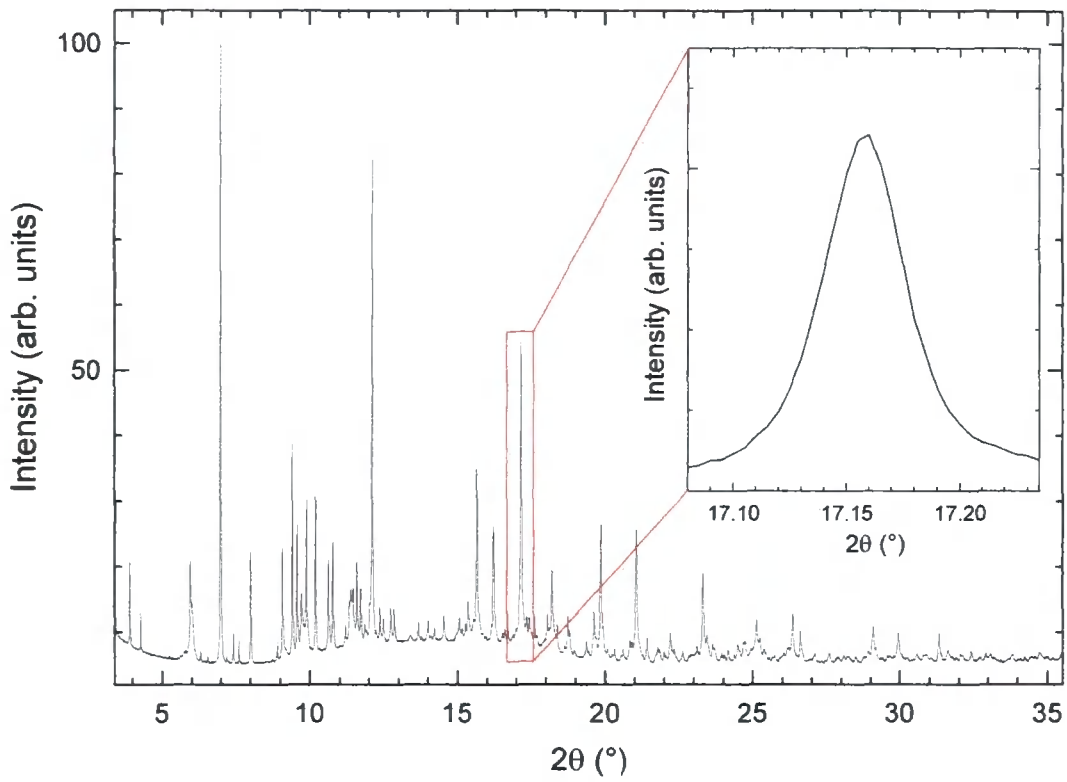

Fig. 3.8. Synchrotron X-ray powder diffraction profile of $Yb_{2.75}C_{60}$ (λ = 0.80098 Å, sample Z) at 4 K obtained on stepwise cooling. [*Inset:* the expanded view of the selected region of the (844) Bragg peaks.]

The structure model employed for the Rietveld refinement of $Yb_{2.75}C_{60}$ (sample Z) [23] was used to carry out the refinement of the same sample obtained using the stepwise cooling protocol at 4 K. The Rietveld refinements were carried out in the 2θ range of 3.2° - 35.0°, while, some of weak impurity peaks were excluded. The final refinement yields: a = 27.9069(3) Å, b = 27.9265(3) Å, c = 27.8874(3) Å, V = 21733.8(6) Å^3 with agreement factors χ^2 = 6.436, R_{wp} = 6.05%, R_{exp} = 2.38% (Table 3.3, Fig. 3.9).

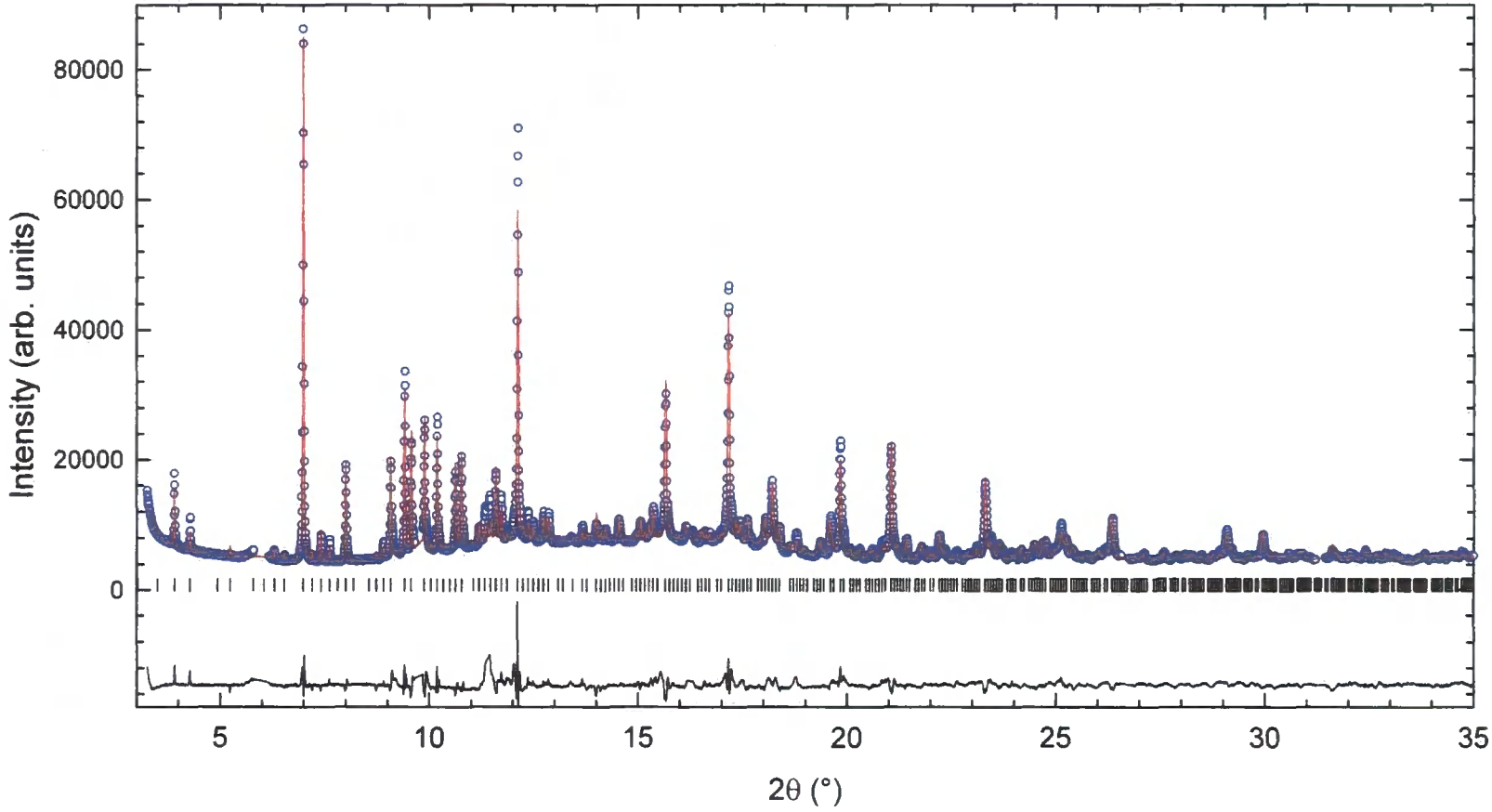

Fig. 3.9. The final result of the Rietveld refinement of the synchrotron X-ray powder diffraction profile of $Yb_{2.75}C_{60}$ (sample Z) at 4 K (λ = 0.80098 Å). Intensities of observed and calculated peaks are shown as blue circles and solid red line, respectively. The ticks represent the positions of diffraction peaks and the solid black line indicates the difference profile.

Table 3.3a. Refined parameters of $Yb_{2.75}C_{60}$ (sample Z, on cooling) obtained from the Rietveld refinement of the diffraction data at 4 K.

	Site	x/a	y/b	z/c	Occupancy	B(Å^2)
C_{60} (1)	4a	0	0	0	1.0	2.3 (1)
C_{60} (21)	8c	0	¼	¼	1.0	2.3 (1)
C_{60} (22)	8c	¼	0	¼	1.0	2.3 (1)
C_{60} (23)	8c	¼	¼	0	1.0	2.3 (1)
C_{60} (3)	4b	½	½	½	1.0	2.3 (1)
Yb (11)	8c	0.1372 (5)	0.1170 (6)	0.3842 (5)	0.979 (2)	4.2 (3)
Yb (12)	8c	0.3842 (5)	0.1372 (5)	0.1170 (6)	0.979 (2)	4.2 (3)
Yb (13)	8c	0.1170 (6)	0.3842 (5)	0.1372 (5)	0.979 (2)	4.2 (3)
Yb (21)	8c	0.1339 (4)	0.3672 (5)	0.3769 (6)	0.979 (2)	4.2 (3)
Yb (22)	8c	0.3769 (6)	0.1339 (4)	0.3672 (5)	0.979 (2)	4.2 (3)
Yb (23)	8c	0.3672 (5)	0.3769 (6)	0.1339 (4)	0.979 (2)	4.2 (3)
Yb (3)	8c	0.378 (3)	0.380 (3)	0.378 (3)	0.979 (2)	4.2 (3)
Yb (4) (vacancy)	8c	0.122 (3)	0.120 (3)	0.122 (2)	0.148 (14)	4.2 (3)
Yb (51)	8c	0.2010 (2)	0.2010 (2)	0.2010 (2)	0.938 (5)	2.0 (3)
Yb (52)	8c	0.0490 (2)	0.0490 (2)	0.2010 (2)	0.938 (5)	2.0 (3)
Yb (53)	8c	0.2010 (2)	0.0490 (2)	0.0490 (2)	0.938 (5)	2.0 (3)
Yb (54)	8c	0.0490 (2)	0.2010 (2)	0.0490 (2)	0.938 (5)	2.0 (3)
Yb (61)	8c	0.2010 (2)	0.304 (4)	0.304 (4)	0.062 (5)	2.0 (3)
Yb (62)	8c	0.0490 (2)	-0.054 (4)	0.304 (4)	0.062 (5)	2.0 (3)
Yb (63)	8c	0.304 (4)	-0.054 (4)	0.0490 (2)	0.125 (9)	2.0 (3)

Table 3.3b. Nearest Yb-C contacts for the T_d sites in sample Z at 4 K in Å.

Yb(11)-C	2.621 (10)	Yb(21)-C	2.723 (10)
	2.638 (10)		2.773 (11)
Yb(12)-C	2.619 (12)	Yb(22)-C	2.744 (10)
	2.635 (14)		2.797 (11)
Yb(13)-C	2.593 (17)	Yb(23)-C	2.744 (12)
	2.641 (14)		2.772 (12)
Yb(3)-C	2.69 (4)	Yb(4)-C	2.94 (6)
	2.78 (4)		2.95 (6)

Table 3.4 shows that the unit cell volume of $Yb_{2.75}C_{60}$ at 5 K is substantially larger than that at 295 K. Thus, an anomalous response of the lattice dimensions with change in temperature is expected.

Table 3.4. The extracted values for the unit cell volume of $Yb_{2.75}C_{60}$ at 5 and 295 K.

Sample	Volume 5 K (Å^3)	Volume 295 K (Å^3)
$Yb_{2.75}C_{60}$ (C_heating)	21779.0 (20)	21647.5 (4)
$Yb_{2.75}C_{60}$ (Z_heating)	21806.0 (8)	21655.0 (6)
$Yb_{2.75}C_{60}$ (Z_cooling)	21733.8 (6)	21625.3 (5)

3.2.4 Temperature Evolution

i) $Yb_{2.75}C_{60}$ (sample C, warming-up)

The evolution of the diffraction profiles collected on sample C shows no apparent changes in relative peak intensities throughout the whole temperature range, implying that there is no sign of a phase transition to a structure with different crystal symmetry detectable. However, careful inspection of each Bragg reflection at various temperatures reveals two interesting features of the present data. Firstly, the diffraction peaks in the low temperature region continuously shift to higher angles on heating (Fig. 3.10a), implying that the lattice dimensions contract as the temperature increases above 5 K; this behaviour is referred to as negative thermal expansion (NTE). This trend continues up to 50 K and is reversed above this temperature, where normal behaviour is restored with the lattice smoothly expanding on heating to 295 K (Fig. 3.10b).

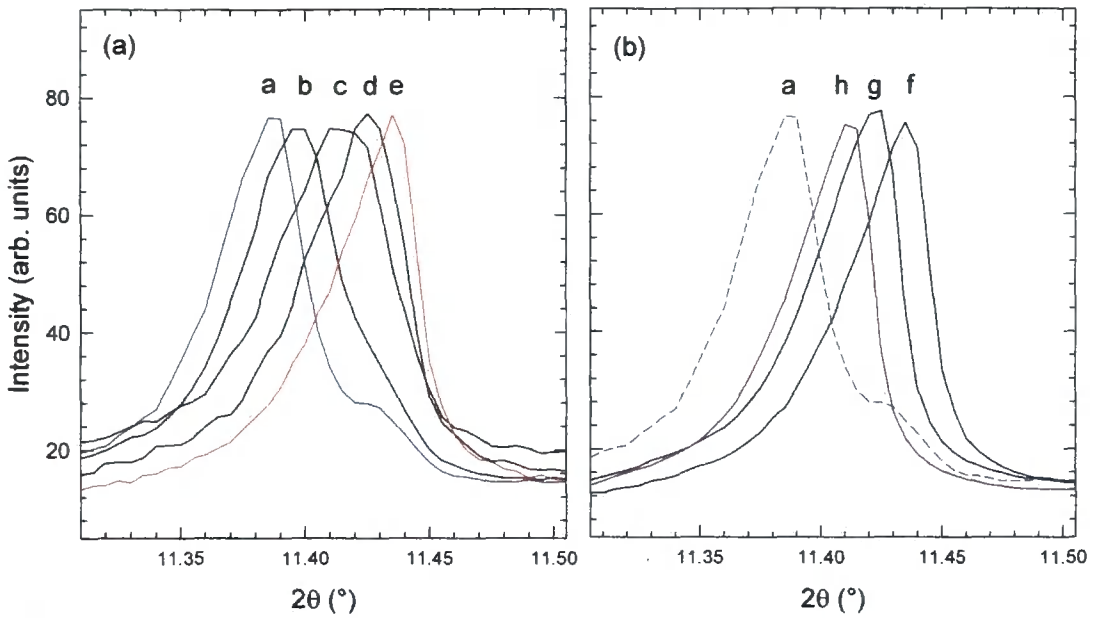

Fig. 3.10. Temperature evolution of the (444) Bragg reflection (λ = 0.799985 Å) in $Yb_{2.75}C_{60}$ (sample C) on heating from (a) 5 to 50 K (low temperature range): a, 5 K; b, 20 K; c, 23 K; d, 28 K; and e, 50 K. The peak shifts to higher angles (lattice contraction) on heating from 5 to 50 K. In the high temperature range (b) of 60 to 295 K, where f, 60 K; g, 180 K; and h, 295 K, the peak shifts to lower angles (lattice expansion) on further heating to room temperature. A change in peak shape is clearly seen between the high and low temperature ranges, where in the high temperature range, the peak shapes are asymmetric, while in the temperature range in which NTE is observed, the peak shapes are less asymmetric but phase separation is evident.

Secondly, the diffraction profile at room temperature, obtained prior to cooling down to 5 K, shows slightly asymmetric peak shape towards the lower angle side (Fig. 3.5b). On the other hand, the diffraction profiles obtained in the low temperature region, where the NTE behaviour is observed, clear phase separation is evident. The lattice dimensions of the second phase increase on heating, unlike the contraction observed for the major phase. The phase separation is suppressed as the temperature increases to 50 K where the NTE behaviour also disappears, and the original peak shape of the high temperature region is recovered. Such behaviour could reflect the

presence of local structural inhomogeneities accompanying the transformation, where a part of the sample experiences anomalous NTE and the other part shows a normal thermal response. It should be noted here that the asymmetry in the peak shape does not completely disappear in the low temperature region, although it is not as apparent as in the high temperature region.

Refinement of the structure at low temperatures was attempted by 3-phase Rietveld analysis initiated by assuming that all phases adopt the orthorhombic space group *Pcab*. Above 50 K, the Rietveld refinements were carried out using a 2-phase structural model, as phase separation no longer exists. The extracted temperature evolution of the unit cell volume, weight fractions, and calculated thermal expansivitiy are shown in Fig. 3.11.

The NTE behaviour observed in the major phase in $Yb_{2.75}C_{60}$ (sample C) is found below a characteristic critical temperature, T_v~ 50 K, which is comparable to that established for sample Z (~60 K) [23]. As the temperature slowly increases above 5 K, the lattice parameters contract steeply until the temperature reaches 28 K with maximum thermal expansivity, α_V (= $d\ln V/dT$), of −1055 ppm/K (Fig. 3.11c), leading to an overall decrease in unit cell size of 1.33%. The unit cell volume of the second phase, on the other hand, slowly expands at a rate of ~14 ppm/K on heating towards 28 K, where the phase separation disappears. At the same temperature, not only the phase separation disappears, but also the high-temperature peak shape is recovered. This is clearly seen in Fig. 3.10a where the diffraction peaks change shape and the weight fraction of the third phase suddenly increases (Fig. 3.11b). The anomalous lattice response disappears above 50 K and the lattice constants increase on heating to 295 K, resulting in an overall volume

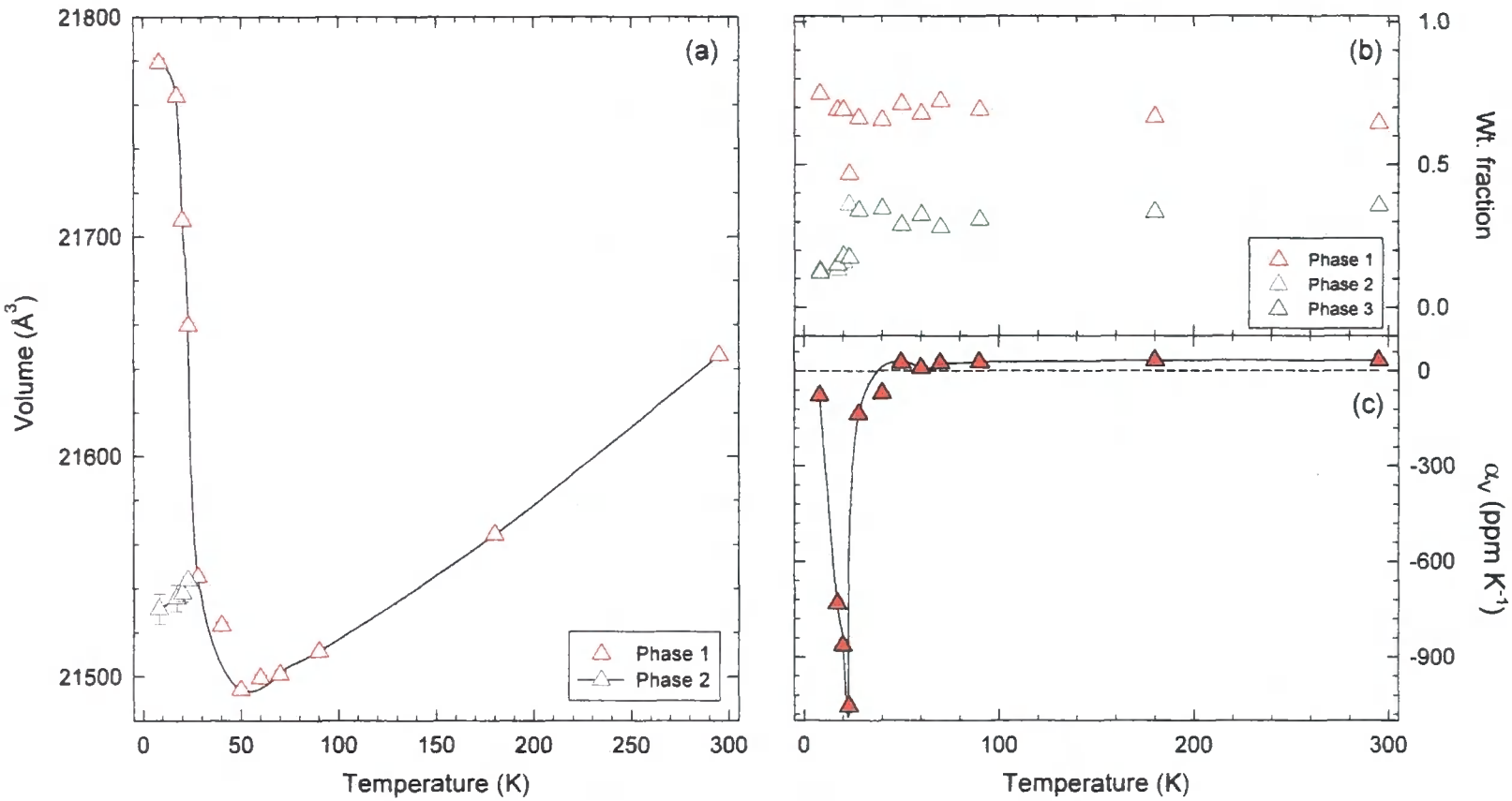

Fig. 3.11. Temperature evolution of (a) the unit cell volume of $Yb_{2.75}C_{60}$ (sample C) on heating; phase 1 (white) and phase 2 (grey), (b) weight fraction of the three phases (phase 3 in green), and (c) the coefficient of thermal expansion, $\alpha_V = d\ln V/dT$ of phase 1.

expansion at a rate of ~28 ppm/K, without showing further change in the peak shape, comparable to what is normally encountered for alkali metal fullerides. However, the lattice expansion in the high temperature region is still not large enough to produce a cell volume at ambient temperature comparable to that at 5 K.

ii) $Yb_{2.75}C_{60}$ (sample Z, warming-up and cooling-down thermal protocols)

The diffraction profiles obtained for $Yb_{2.75}C_{60}$ (sample Z) at various temperatures between 4 and 295 K on heating [23] and 295 and 4 K on stepwise cooling shows no changes in relative peak intensities throughout the whole temperature range (Fig. 3.12), implying once more the absence of a phase transition to a structure with different crystal symmetry.

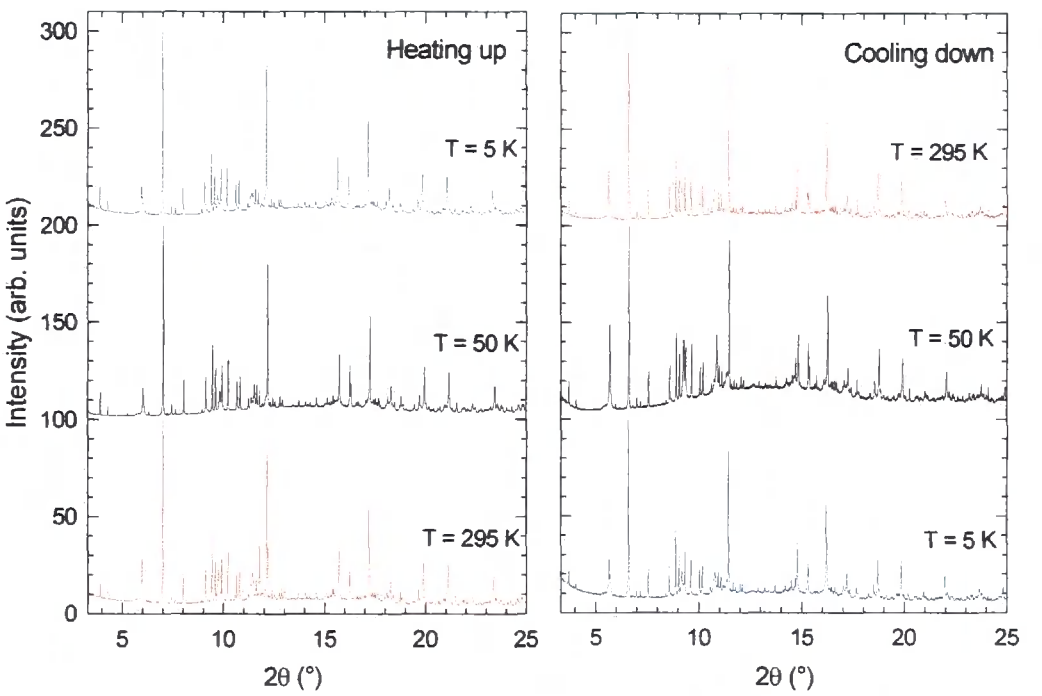

Fig. 3.12. Synchrotron X-ray powder diffraction profiles of $Yb_{2.75}C_{60}$ at selected temperatures as obtained on heating (left, λ = 0.8507 Å) and on cooling (right, λ = 0.8010 Å).

However, inspection of the temperature dependence of the data reveals that the angular position of the diffraction peaks at low temperatures shifts to higher angles on heating and lower angles on cooling (Fig. 3.13a and b).

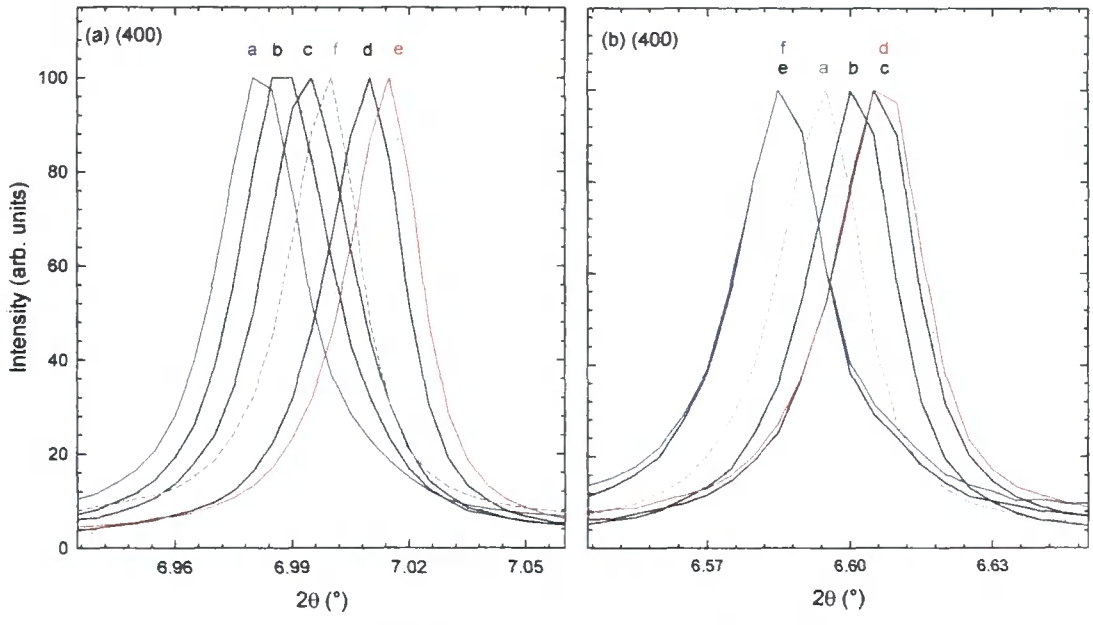

Fig. 3.13. Selected region of the synchrotron X-ray powder diffraction profiles of $Yb_{2.75}C_{60}$ (sample Z), showing the temperature evolution of the (400) Bragg reflection (a) on heating (λ = 0.8507 Å); trace a, 4 K; b, 20 K; c, 25 K; d, 35 K; e, 60 K; f, 295 K, [23] and (b) on cooling (λ = 0.8010 Å); trace a, 295 K; b, 190 K; c, 100 K; d, 40 K; e, 7 K; f, 4 K.

The temperature evolution of the (400) Bragg reflection on heating (Fig. 3.10a) reveals that as temperature increases above 4 K, the peak shifts quasi-continuously to higher angle (lattice contraction) until the temperature reaches 60 K, and then the direction of shift changes to lower angles (lattice expansion) on further heating to room temperature. This trend, similar to that observed in $Sm_{2.75}C_{60}$ [20], implies the material contracts as the temperature increases above 4 K (NTE). A characteristic temperature, T_v,

where the direction of peak shift changes (thus NTE behaviour disappears), for $Yb_{2.75}C_{60}$ is found at substantially higher temperature (~60 K) than in $Sm_{2.75}C_{60}$ (~32 K) and normal behaviour is restored above 60 K with the lattice smoothly expanding on heating to 295 K.

On the other hand, the diffraction profiles collected using the stepwise cooling protocol (Fig. 3.13b) show, starting from 295 K, that the peaks shift monotonically to higher angles on cooling down to 100 K. The rate of shifting towards higher angle decreases significantly on further cooling down to 20 K. Then, a sudden jump to lower angles is observed at 12 K. Here, the transition is more abrupt than the almost continuous shift observed on heating and the onset temperature of NTE is considerably lower.

Extraction of reliable lattice constants of $Yb_{2.75}C_{60}$ (sample Z) on cooling, and thus of the unit cell volume, was performed with the LeBail technique using the same orthorhombic (space group *Pcab*) at all temperatures. The temperature evolution of the extracted unit cell volume is shown in Fig. 3.14a together with that on heating, thereby revealing a strong hysteretic behaviour associated with the transition.

The existence of hysteretic effects is clearly seen in Fig. 3.14a, where the critical temperature is lower than those extracted on heating experiments and the lattice dimensions derived from the analysis of the diffraction data with the stepwise cooling protocol are smaller. Fig. 3.14b shows the calculated thermal expansivity, α_V (= $d\ln V/dT$), on heating plotted against temperature, which is negative throughout the region where NTE is observed. Initially, in absolute value, it increases continuously on heating until it goes through a maximum of -580 ppm/K at 30 K and then

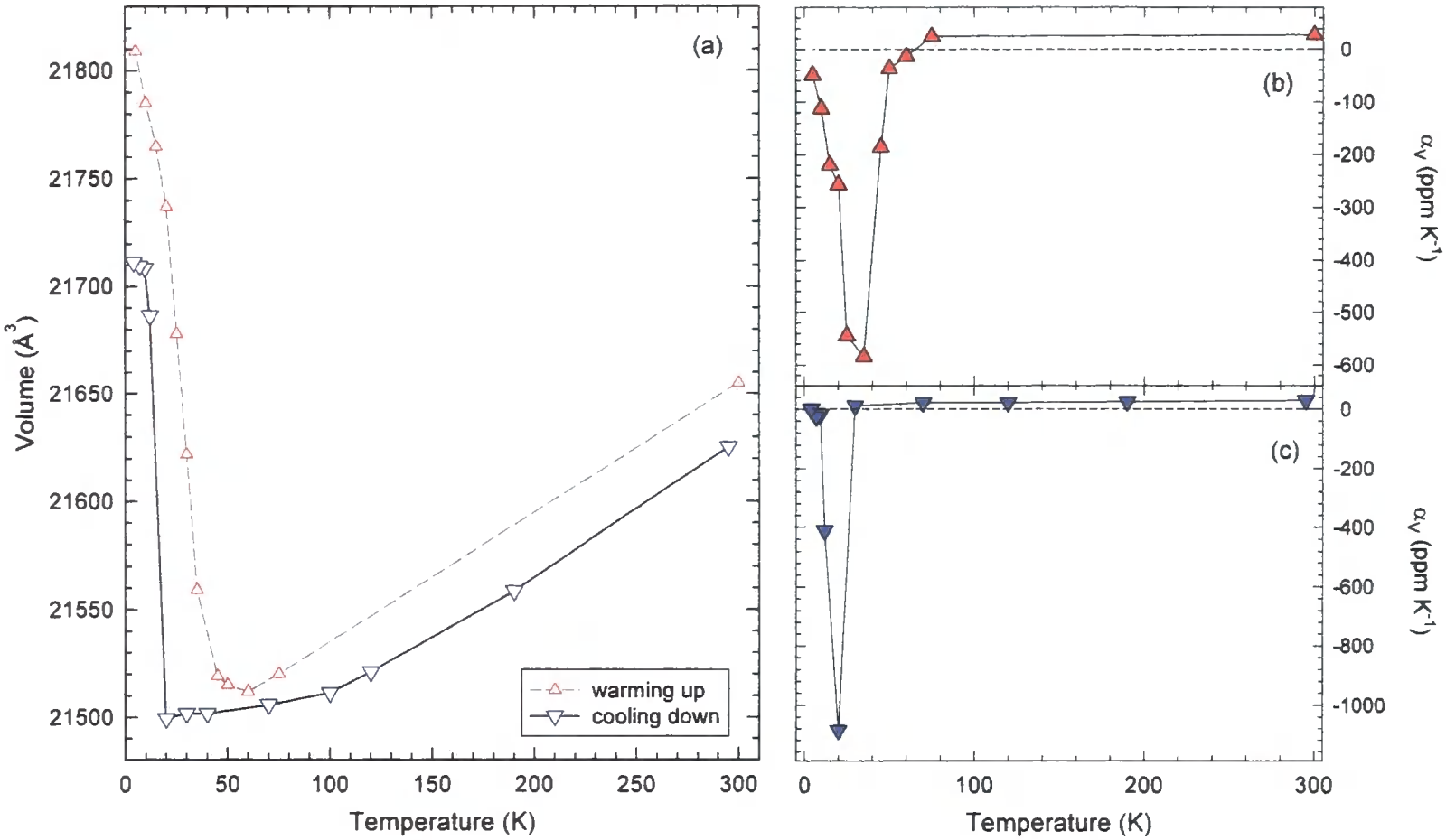

Fig. 3.14. Temperature evolution of (a) unit cell volume of $Yb_{2.75}C_{60}$ (sample Z) on cooling (blue downwards triangle) and on heating (red upwards triangle) and the coefficient of thermal expansion, $\alpha_V = d\ln V/dT$ of (b) heating and (c) cooling.

rapidly decreases to zero at ~60 K. This results in an overall volume contraction of 1.4% on heating from 4 to 60 K without showing any observable change in crystal symmetry. The anomalous lattice response disappears above 60 K, the sign of the thermal expansivity changes and the lattice expands on heating to 295 K at a rate of approximately +28 ppm/K. This value is comparable to that typically encountered in other metal fulleride salts, for example, $d\ln V/dT \approx +30$ ppm/K for $K_3Ba_3C_{60}$ [28]. The lattice expansion above 60 K results in a cell volume at room temperature remarkably smaller compared to that at 4 K.

The thermal expansivity for the stepwise cooling experiment (Fig. 3.14c) in the high temperature region is approximately +25 ppm/K and as the temperature decreases towards 100 K, the rate of contraction also decreases to ~+20 ppm/K; then on further cooling, the value becomes ~+10 ppm/K at 30 K, and approaches zero around 20 K. The sign of the thermal expansivity then changes and increases suddenly, reaching maximum of -1086 ppm/K, as the lattice expands abruptly with an overall increment of 0.99% between 20 and 4 K.

3.2.5 Discussion

The determination of the temperature evolution of the lattice parameters can be a direct indicator to reveal what is happening in these materials at the microscopic level. As already mentioned earlier, in pristine C_{60}, there exist two types of interstitial holes with different hole radii, namely, smaller T_d sites (1.12 Å) and larger O_h sites (2.06 Å). The size of the ions occupying the T_d site can sensitively control the unit cell size of the fullerides.

When ions with ionic radius larger than the hole radius of the T_d site are introduced, the fullerides display a substantial expansion of the lattice. Noting that in $Yb_{2.75}C_{60}$, the size of the T_d hole radius straddles the values of the ionic radii of Yb^{2+} (1.16 Å) and Yb^{3+} (1.01 Å), changes in the valence states can be expected to have a profound effect on lattice size. With this in mind, the anomalous response of the $Yb_{2.75}C_{60}$ lattice size at low temperature without an accompanying change in crystal symmetry can be rationalised in the same manner as for $Sm_{2.75}C_{60}$ in terms of the valence fluctuation model, driven by $Yb^{2+} \leftrightarrow Yb^{3+}$ conversion.

The existence of a mixed valence state in $Yb_{2.75}C_{60}$ may be expected both by the tendency of Yb to exhibit intermediate valence and the availability of the narrow C_{60} t_{1u} band allowing strong coupling with the $4f$ band of Yb to occur. Furthermore, on the basis of a charge transfer model, that is, if all cations are in the same oxidation state, the charge states for the C_{60}^{n-} molecular ions cannot retain integer values for the stoichiometry $Yb_{2.75}C_{60}$. On the other hand, supposing that the creation of a vacancy results in removing Yb^{2+} cations from the unit cell, in order to recover charge balance, the partial introduction of Yb^{3+} cations has to be considered, leading to a mixed valent Yb^{2+}/Yb^{3+} state with an average valence of $+(2+\varepsilon)$. The C_{60} t_{1u} band becomes full with $n = 6$, and thus ε can be estimated to be *ca.* 0.18.

The first evidence to support this hypothesis was obtained from the results of variable-temperature magnetic susceptibility measurements at 1 T (Fig. 3.15). The results showed that the Curie-Weiss law was obeyed over a restricted temperature range of ~200 to 300 K with $\mu_{eff} = 2.18\ \mu_B$ per Yb ion and $\Theta = 197$ K. Considering the magnetic susceptibilities of free Yb^{2+} and

Yb^{3+} ions, Yb^{2+} is diamagnetic and Yb^{3+} is paramagnetic with a calculated free-ion effective magnetic moment of 4.54 μ_B. The average Yb valence, at least in the high temperature range, can therefore be approximated as +2.20, assuming that the measured susceptibility of $Yb_{2.75}C_{60}$ is the weighted sum of the Yb^{2+} and Yb^{3+} susceptibilities. The calculated value obtained here is consistent with an average charge state per C_{60} equal to -6.

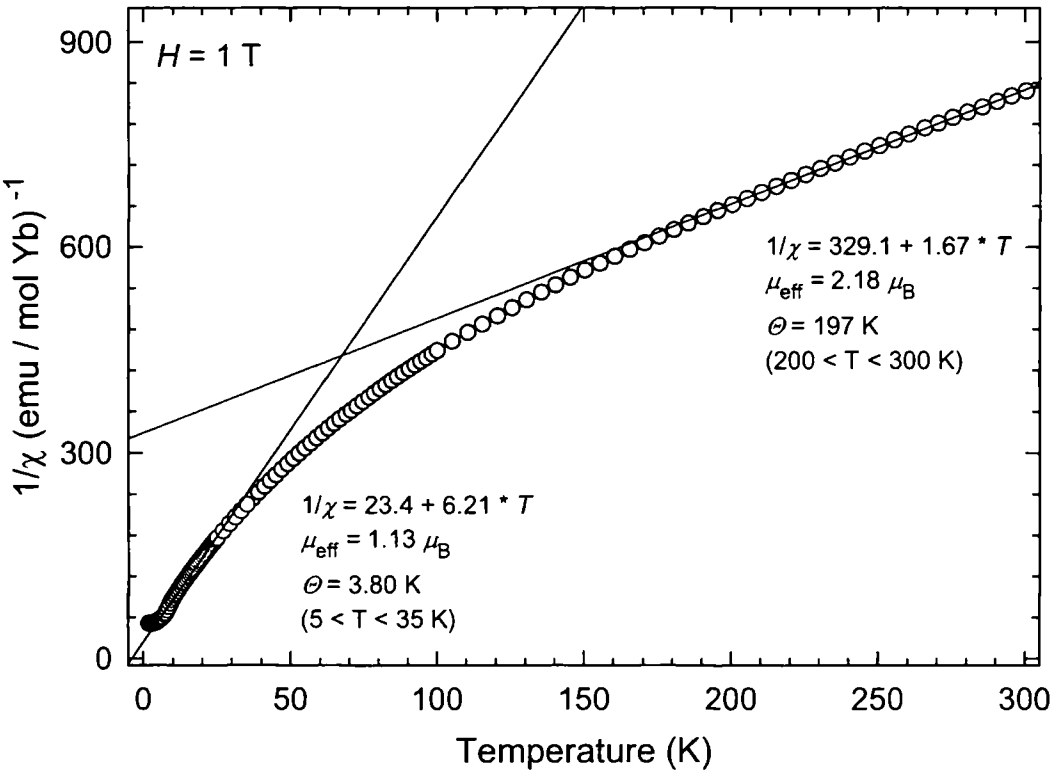

Fig. 3.15. Temperature dependence of the reciprocal of the magnetic susceptibility, $1/\chi$ for $Yb_{2.75}C_{60}$ (sample C). The straight lines depict Curie-Weiss fits of the inverse susceptibility data in the ranges 200-300 K and 5-35 K.

The definition of an average valence below 200 K becomes more complicated due to the effect of the crystal field associated with the splitting of the $^2F_{7/2}$ octet ground state term of Yb^{3+}. Thus, the magnetic susceptibility

can no longer be expressed as a linear combination of the Yb^{2+} and Yb^{3+} contributions. Having said this, very rough estimation of the average Yb valence can be obtained for the data below 35 K where Curie-Weiss behaviour is observed with a reduced magnetic moment of 1.13 μ_B per Yb ion, which is much lower than that expected from crystal field effects alone. The estimate of the reduced average Yb valence gives the value of +2.06 at low temperature, which is consistent with a picture, where the fragility of the valence states of Yb [29] can result in a valence transition of Yb from nearly +2 valence state at 5 K towards mixed state of $+(2+\varepsilon)$ induced by changing temperature, leading to an anomalous isosymmetric lattice response (NTE).

The NTE behaviour and phase separation observed at low temperatures for $Yb_{2.75}C_{60}$ (sample C) can be explained by a partial valence transition of Yb within the compound. The anomalous thermal expansion is driven by the part which undergoes a valence transition from +2 valence state towards +3 state on heating resulting in increase of the average valence from ~+2 to ~+2.2. Some fraction of Yb ions does not experience the valence transition and this is reflected in the observed phase separation.

The results of the temperature evolution of the unit cell volume of $Yb_{2.75}C_{60}$ (sample Z) on heating and on cooling clearly show a hysteretic effect associated with valence transition. The NTE behaviour on heating is quasi-continuous over a broad temperature range of 4 to 60 K, while on cooling, the volume expansion is very abrupt and the onset temperature of NTE is at a much lower temperature of 20 K. The extracted unit cell parameters from the analysis of the diffraction data on cooling at each temperature are smaller than those extracted at the same temperature on heating. The unit cell volume at 4 K obtained on cooling, for example, is

smaller by 0.45% compared to that obtained on heating. Furthermore, overall lattice expansion (or contraction) is smaller for the case of stepwise cooling protocol. These results clearly indicate that the temperature-induced valence transitions of the Yb ions are sensitively affected by the rate of change of temperature.

Our current interpretation of the driving force of the valence transition is in terms of electron transfer and the coupling of the Yb 4*f* band to the electronically active t_{1u} band of C_{60}. As shown schematically in Fig 3.16, at high temperatures, 4*f* electrons can be thermally excited from the narrow 4*f* band into the C_{60} t_{1u} band, making the t_{1u} band fully occupied with 6 electrons, while the average valence of Yb approaches +2.20.

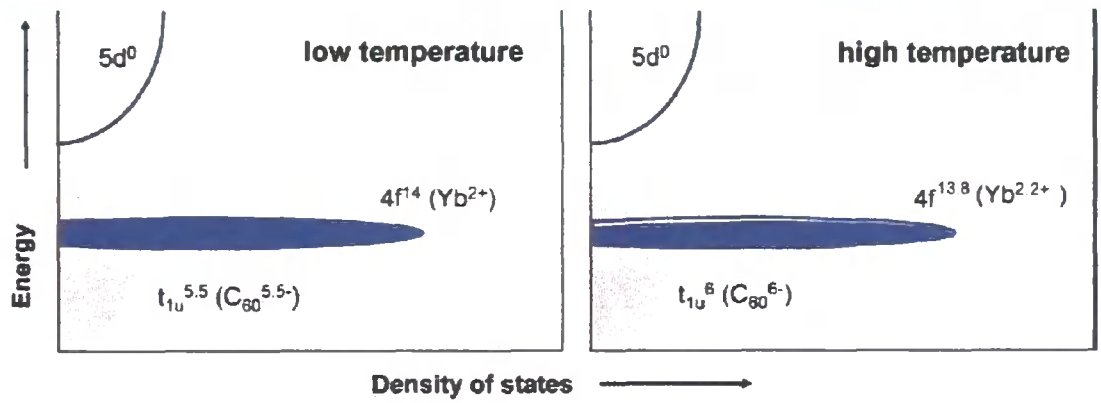

Fig. 3.16. Schematic diagram of the electron density-of-states in $Yb_{2.75}C_{60}$ at low and high temperatures, showing the spilling over of electron density from the Yb 4*f* band to the t_{1u} band of C_{60} on heating.

At low temperatures, these electrons are taken back into the 4*f* band, thus, the valence state of Yb ions approaches +2 and as a result, expansion of the ionic radius is obtained. This implies that no lattice anomalies will be

observed for other isostructural fullerides, which lack an electronically active $4f$ sublattice. A good example to investigate this point comes from the results obtained by similar measurements using the synchrotron X-ray powder diffraction technique at various temperatures for the isoelectronic and isostructural $Ca_{2.75}C_{60}$ fulleride (see Chapter 5). The structural study of $Ca_{2.75}C_{60}$ reveals that the structure of this material is also characterised by cation vacancy ordering as in $Yb_{2.75}C_{60}$ [22], but has no $4f$ sublattice. As expected, the temperature evolution of the unit cell volume of $Ca_{2.75}C_{60}$ shows no anomalous expansion behaviour; instead, its lattice contracts continuously by ~0.4% between 295 and 5 K.

3.3 Pressure-induced valence transitions

$Sm_{2.75}C_{60}$ displayed an abrupt hysteretic phase transition, accompanied by a dramatic volume decrease ($\Delta V/V$ ~ 6.8%) and an insulator-to-metal transition at ~4 GPa induced by a sudden Sm valence transition from +2.2 towards +3 [21]. Here, the results of the study of the compression behaviour of $Yb_{2.75}C_{60}$ (sample C) in the pressure range 0-6.50 GPa, obtained using the synchrotron X-ray powder diffraction technique at ambient temperature are presented. The purpose of this study is to investigate the effect of pressure on the transition as Sm is replaced by Yb.

3.3.1 Experimental Details

The pressure-dependent X-ray powder diffraction experiments at ambient temperature were performed on beamline ID09 at the ESRF, Grenoble. The $Yb_{2.75}C_{60}$ powder was prepared in the same way as for the temperature-dependent experiments, and it was loaded in a diamond anvil cell (DAC) inside an anaerobic glovebox. The DAC is used for high-pressure generation and is equipped with an aluminium gasket. The diameters of two faces of the diamond culet were 600×600 μm^2 and 80 μm deep and 250 μm wide hole is made in the gasket for the sample space. The sample powder was introduced in this hole together with a pressure transmitting medium (helium) and two small rubies placed near the centre of one diamond face. The pressure inside the DAC was increased at room temperature and was measured accurately by the ruby fluorescence method at each measurement.

The diffraction patterns were obtained by using Si(111) monochromised X-ray beam (λ = 0.41746 Å) with a beam size of 30×40 μm^2. The diffracted beam was collected using an image plate detector up to a maximum pressure of 6.50 GPa with typical exposure times of 15 min at a beam current of ~70 mA. The pressure was then gradually released down to the minimum possible pressure without opening the DAC; in this way, the diffraction data were collected down to 3.20 GPa upon depressurisation. The two-dimensional diffraction images were integrated, after masking of the strong Bragg reflections of the ruby crystal, using the local ESRF FIT2D software [30]. The data analysis was performed with the LeBail pattern decomposition technique within the GSAS programme.

3.3.2 Structural Analysis

Synchrotron X-ray powder diffraction profiles of $Yb_{2.75}C_{60}$ were collected at pressures between ambient and 6.50 GPa. The quality of patterns obtained in high-pressure experiments, compared to that obtained in temperature dependent patterns on ID31, is too low to attempt detailed Rietveld refinements for this complex structural model. However, even with these lower quality data, every reflection peak observed was consistent with the same orthorhombic structural model (space group *Pcab*) that was employed in the LeBail technique (Fig. 3.17).

Reliable lattice constants were extracted from the diffraction pattern at ambient temperature and pressure using the LeBail pattern decomposition technique, resulting in values of a = 27.8972(5) Å, b = 27.9530(5) Å, c = 27.8414(5) Å, V = 21711.0(1.1) Å^3, and agreement factors R_{wp} = 2.70%, R_{exp} = 2.50%, and χ^2 = 1.04. The background of the synchrotron data was described by a shifted Chebycshev polynomial function with 20 coefficients, which were refined originally and then kept fixed at the final stages of the refinements in order to reduce the total number of refined parameters. The peak shape was described at all pressures by the asymmetry function of Finger *et al.* [31] (function type 3) implemented in GSAS. These values obtained are comparable to those obtained from Rietveld refinements on the same sample on ID31 at ambient temperature and pressure. The refined parameters and agreement factors at ambient pressure and at 6.50 GPa are summarised in Table 3.5.

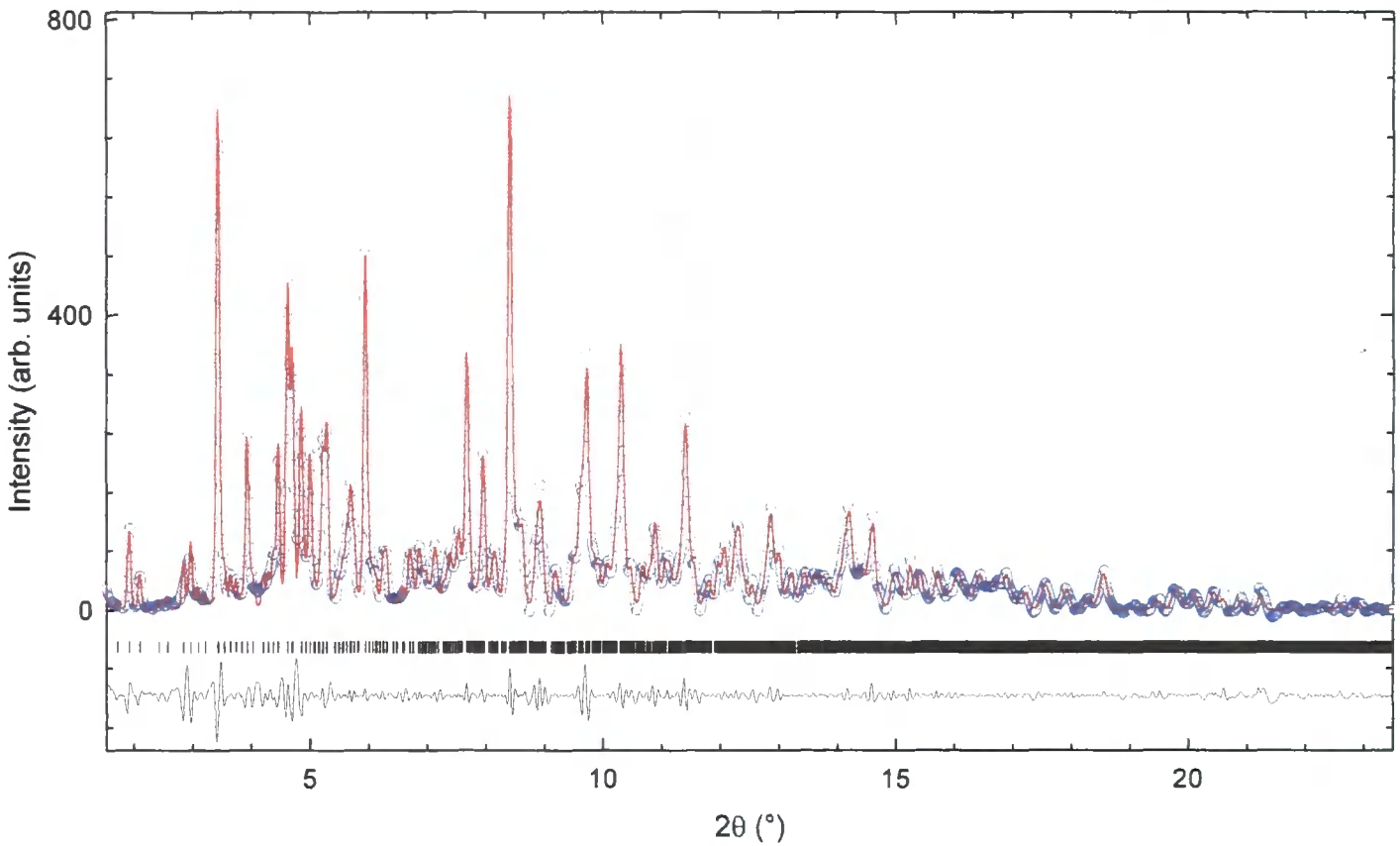

Fig. 3.17. Results of the LeBail analysis of the synchrotron X-ray powder diffraction profile of $Yb_{2.75}C_{60}$ at ambient pressure (P= 1 atm). Observed (blue circles), calculated (solid red line), and difference (solid black line) profiles.

Table 3.5. Summary of the refined parameters of $Yb_{2.75}C_{60}$ (sample C) at ambient pressure and 6.50 GPa.

Pressure (GPa)	0.05	6.50
Instrumental parameters:		
λ (Å)	0.41746	0.41746
Δ2θ (×100, °)	-1.064	-1.064
2θ range (°)	1.5 - 24	1.5 - 24
Step size (°)	0.014	0.014
Lattice parameters:		
a (Å)	27.8972 (5)	26.9144 (5)
b (Å)	27.9530 (5)	26.9682 (5)
c (Å)	27.8414 (5)	26.8606 (5)
V (Å^3)	21711.0 (1.1)	19496.3 (1.5)
Peak profile coefficient:	Type 3	Type 3
GU, GV,	120.3 (7), -47.8 (6),	248.4 (5), -17.4 (4),
GW	2.63 (9)	15.6 (2)
Lx, Ly	0.114 (6), 21.3 (2)	0.754 (5), 1.55 (8)
S/L, H/L	0.005, 0.0005	0.005, 0.0005
Agreement factors:		
Rwp (%), Rexp (%), χ^2	2.70, 2.50, 1.04	4.30, 2.63, 2.68

3.3.3 Pressure Evolution

Figure 3.18 shows the diffraction profiles obtained at selected elevated pressures. There is an excellent correspondence of the reflection intensities in these profiles with those observed at ambient pressure. The lattice constants at each pressure were extracted with the LeBail method using same space group *Pcab*, option 2, at all pressures. Inspection of the diffraction data indicates that as the applied pressure increases, the diffraction peaks continuously shift to higher angles, which is consistent with the expected contraction of the material.

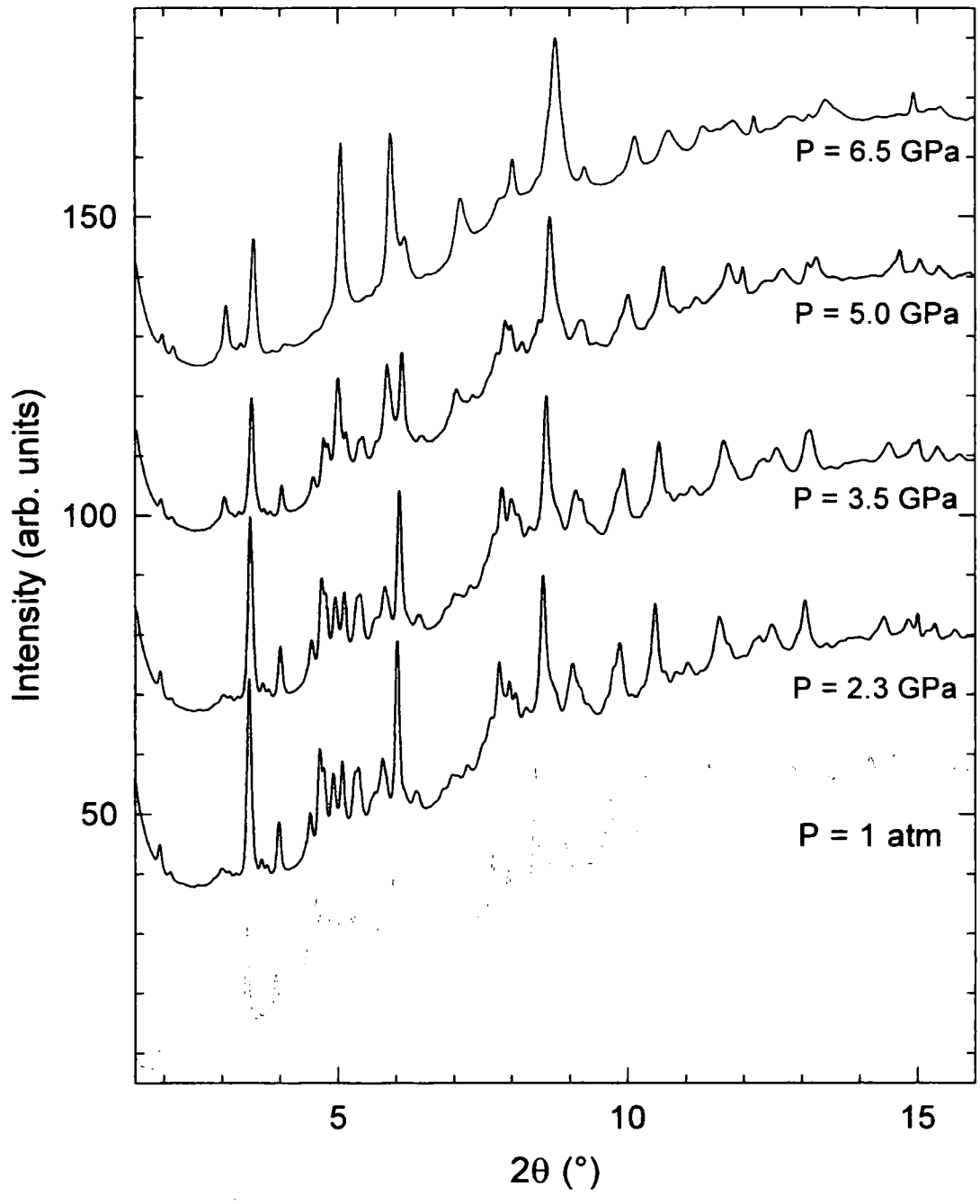

Fig. 3.18. Synchrotron X-ray (λ = 0.41746 Å) powder diffraction profiles for $Yb_{2.75}C_{60}$ collected at elevated pressures between ambient and 6.50 GPa.

However, above 4.30 GPa the peak shift abruptly increases implying the onset of a phase transformation to a structure associated with a drastic reduction of lattice dimensions ($\Delta V/V \sim$ 2.1%). This trend continues up to

5.10 GPa whereupon the peak shifts become much smaller, while the transformation continues with further increase in pressure. The extracted pressure evolutions of the orthorhombic lattice parameters and of the unit cell volume are shown in Fig. 3.19.

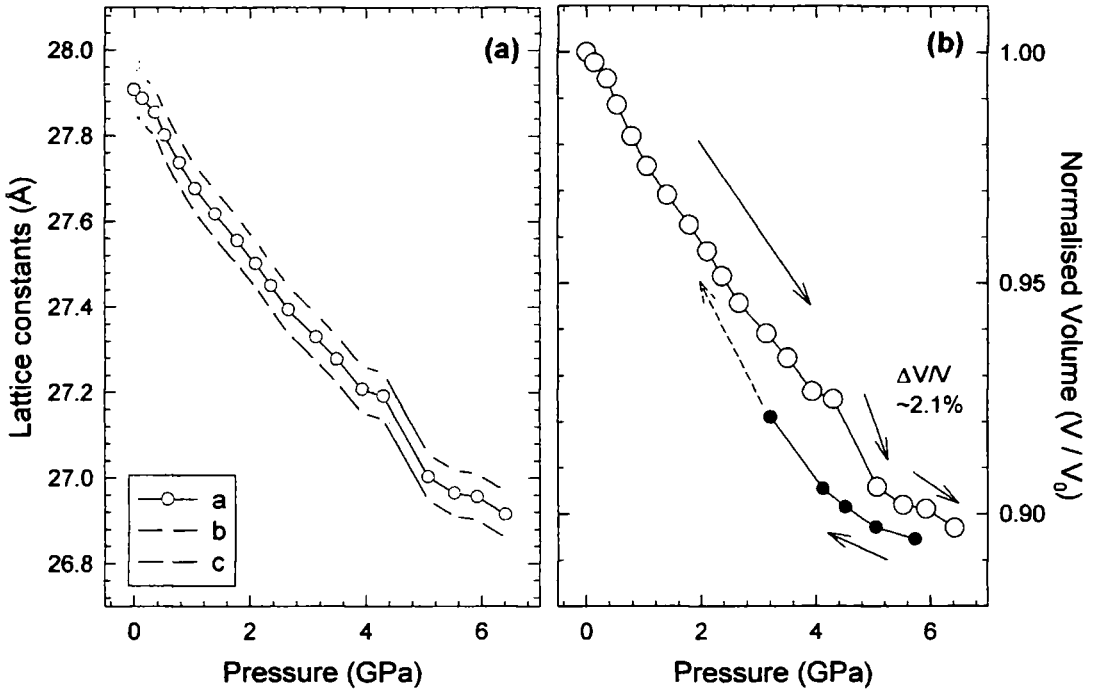

Fig. 3.19. Pressure evolution of (a) the lattice constants; a in blue circles, b in red squares, and c in green triangles and (b) the normalised unit cell volume for $Yb_{2.75}C_{60}$. Open (filled) circles represent data obtained on increasing (decreasing) pressure. Solid arrows represent the direction of pressure evolution of the unit cell volume, while dashed arrow represents expected direction of evolution.

This transition is also associated with change in optical properties, where a change of colour from black to golden yellow occurs, indicating the occurrence of an insulator-to-metal transition. This can be explained by the spilling of the $4f$ electrons into the $5d$ conduction band caused by the applied pressure reducing the energy separation between the localised $4f$ states and

the 5*d* bands. However, the inferior quality of the high pressure diffraction data makes it difficult to discuss in further detail the occurrence of this transition. After release of pressure from 6.50 GPa, the diffraction peaks shift slowly towards lower angles. The diffraction data with releasing pressure were collected down to 3.20 GPa, where it was found that the original low-pressure phase was recovered. The reverse transition is also associated with a reverse colour change from golden yellow to black. These trends imply that the transformation is reversible and is characterised by a hysteretic behaviour as it was observed in the case of $Sm_{2.75}C_{60}$ [21] and SmS [32].

3.3.4 Discussion

In the previous section, the anomalous lattice response of $Yb_{2.75}C_{60}$ at low temperatures (without externally applied pressure) was described and was ascribed to the strong coupling between the Yb and C_{60} electronic structures. The observed effects are related to the fragility of the +2 and +3 valence states of Yb and its tendency to exhibit intermediate valence characteristics. The abrupt phase transformation observed for $Yb_{2.75}C_{60}$ under high pressure at room temperature can be rationalised along the same lines, namely a discontinuous valence change of the rare-earth element from ~+2.2 towards +3 state having a smaller ionic radius and leading to the collapse of the unit cell metrics. Similar pressure-induced valence transitions have been observed for the rare-earth monochalcogenide families and were also rationalised in terms of the valence fluctuation model of two nearly-degenerate electronic configurations, $4f^n5d^0$ and $4f^{n-1}5d^1$ [33]. For instance, YbS also shows a pressure-induced semiconductor-metal transition

associated with the collapse in its lattice constants [34]. The transition is accompanied by a reduction in the lattice constants. The ionic radius of the $4f^{13}$ configuration is ~13% less than that of the $4f^{14}$ state, which results in a first-order isosymmetric lattice collapse at around 20 GPa. Until recently, precise determination of the pressure evolution of the $4f$ occupation, thus the average valence state, has not been achieved, because the XAS spectra at the Yb L_3 edge of YbS under pressure are broadened by the short $2p_{3/2}$ lifetime. Direct information on the electronic configuration of YbS under pressure has recently been obtained by using high-resolution XAS and resonant inelastic X-ray scattering (RIXS) at a third-generation synchrotron source, which provided clear evidence of the valence variation with increasing pressure [35].

Such a pressure derived discontinuous $4f \rightarrow 5d$ electron delocalization can also be expected in $Yb_{2.75}C_{60}$, providing an excellent explanation of the drastic lattice collapse. As pressure increases, the lattice metrics decrease continuously, leading to a reduced gap between the t_{1u} band of C_{60} and the Yb 5d conduction band until a critical pressure of 4.30 GPa is reached, where the first-order transition is triggered. When the gap reaches zero, the $4f$ electron density starts to spill over into the 5d band, as illustrated schematically in Fig. 3.20. This leads to an increase in the average Yb valence towards +3, a decrease in the size of the ionic radius, and thus a decrease in the unit cell size. At sufficiently high pressure, the complete valence change of Yb to +3 state is expected. As pressure is released, the electron density is transferred back into the $4f$ states and the low pressure phase is recovered.

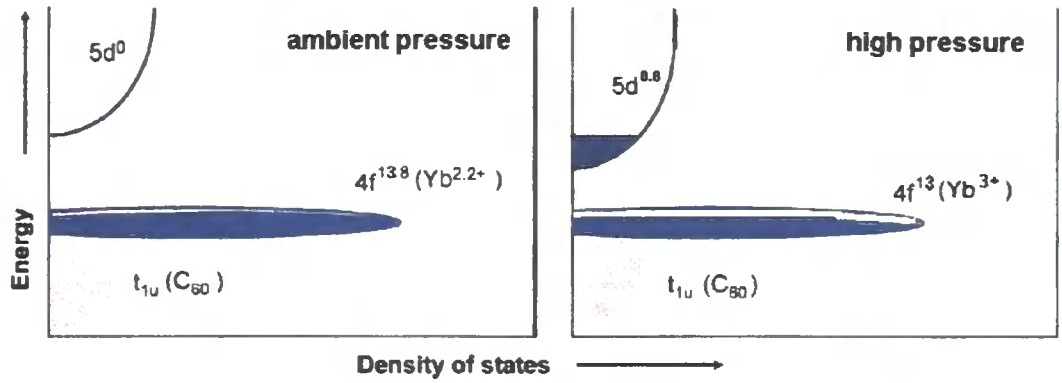

Fig. 3.20. Schematic diagram of the electron density of states in $Yb_{2.75}C_{60}$ at ambient and high pressure, showing the spilling over of electron density from the Yb 4*f* band to the 5*d* band of Yb with increasing pressure that results in the observed unit cell volume collapse.

When the results from high pressure experiments for both $Sm_{2.75}C_{60}$ and $Yb_{2.75}C_{60}$ are compared, the trends observed are very similar to each other. The onset pressure of the phase transformation in $Yb_{2.75}C_{60}$ (4.30 GPa) is found to be slightly higher than that observed for $Sm_{2.75}C_{60}$ (3.95 GPa). This is the good evidence for the influence of substitution of Sm by the Yb atom. As it can be seen in the figure 3.1, the energy difference between the divalent and the trivalent valence states of both Sm and Yb is very close to zero, but while the energy difference of Sm is just above zero, the energy difference for Yb is just below zero, i.e. negative [22]. This suggests that the divalent state for Yb is more favoured and thus requires more energy for the valence transformation to occur, which results in higher onset pressure. It should be noted that this is consistent with the observations on the temperature-induced valence transitions where the onset temperature of NTE for $Yb_{2.75}C_{60}$ (~60 K) is higher than that observed for $Sm_{2.75}C_{60}$ (~32 K).

3.4 Conclusion

The investigation of the effect of Yb substitution for Sm in fulleride salts with stoichiometry $RE_{2.75}C_{60}$ and the understanding of their properties are crucial in order to generalise the mixed valence phenomena in the family of rare-earth fullerides. The temperature and pressure evolution of the structural properties of mixed valence $Yb_{2.75}C_{60}$ has been studied by synchrotron X-ray powder diffraction techniques. The temperature dependent studies reveal the abrupt onset of large lattice expansion (NTE) on cooling below a critical temperature, resulting from the temperature-induced $Yb^{3+} \rightarrow Yb^{2+}$ valence transitions of the Yb ions. The critical temperature is found to be sensitively controlled by changing the intercalating metal (32 K for Sm and 60 K for Yb) and changing the rate of change of temperature (20 K for stepwise slow cooling and 60 K for fast cooling). The transformations are of electronic origin and are driven by the coupling of the Yb $4f$ band and the t_{1u} band of C_{60}. As expected, they are absent when the electronically active $4f$ sublattice is missing in the related alkaline-earth fulleride, $Ca_{2.75}C_{60}$.

Pressure-induced first-order $Yb^{2+} \rightarrow Yb^{3+}$ valence transitions of the Yb ions have also observed in the same material, accompanied by a lattice collapse. The abrupt transition was observed as pressure reached a critical value where the band gap between the Yb $4f$ and $5d$ band approaches zero or start to overlap allowing electrons from the $4f$ band to be spilled into the 5d band. The effect of substitution was evident on the onset pressure of the transition in Yb intercalated fulleride where it was found to be slightly higher than that found in the Sm analogue (3.95 GPa for Sm and 4.30 GPa for Yb).

With the use of synchrotron powder X-ray diffraction technique, the temperature and pressure evolution of the lattice parameters have been precisely investigated. The average valence change with temperature was extracted by the results of temperature dependent magnetic measurements at 1 T, giving estimated values of +2.20 at room temperature and +2.06 below 35 K [23]. However, precise knowledge of the temperature and pressure evolution of the $4f$ occupation is still lacking due to the technical problems in obtaining direct experimental information about the valence states of the extremely air and moisture sensitive materials using XAS experiments. Recent developments of X-ray spectroscopic techniques at third-generation synchrotron facility have opened new opportunities to test the theoretical predictions. Indeed high-resolution XAS and RIXS at the Yb L_3 absorption edges has been successfully employed to measure both the temperature and pressure dependence of the valence for various Yb based Kondo insulators [36, 37]. It is expected that these techniques can also be employed to obtain very precise and direct information on the electronic configuration of $Yb_{2.75}C_{60}$ and to provide quantitative spectroscopic evidence of the valence transition.

3.5 References

[1] Stephens, P. W., Mihaly, L., Lee, P. L., Whetten, R. L., Huang, S., Kaner, R., Deiderich, F., Holczer, K., *Nature* **351**, 632 (1991).

[2] Zhou, O., Fischer, J. E., Coustel, N., Kycia, S., Zhu, Q., McGhie, A. R., Romanow, W. J., McCauley Jr, J. P., Smith III, A. B., Cox, D. E., *Nature*

351, 462 (1991).

[3] Margadonna, S., Prassides, K., Fitch, A. N., Kosaka, M., Tanigaki, K., *J. Am. Chem. Soc.* **121**, 6319 (1999).

[4] Hebard, A. F., Rosseinsky, M. J., Haddon, R. C., Murphy, D. W., Glarum, S. H., Palstra, T. T. M., Ramirez, A. P., Kortan, A. R., *Nature* **350**, 600 (1991).

[5] Tanigaki, K., Ebbesen, T. W., Saito, S., Mizuki, J., Tsai, J. S., Kubo, Y., Kuroshima, S., *Nature* **352**, 222 (1991).

[6] Ganin, A. Y., Takabayashi, Y., Khimyak, Y. Z., Margadonna, S., Tamai, A., Rosseinsky, M. J., Prassides, K., *Nat. Mater.* **7**, 367 (2008).

[7] Fleming, R. M., Ramirez, A. P., Rosseinsky, M. J., Murphy, D. W., Haddon, R. C., Zahurak, S. M., Makhija, A. V., *Nature* **352**, 787 (1991).

[8] Kortan, A. R., Kopylov, N., Glarum, S., Gyorgy, E. M., Ramirez, A. P., Fleming, R. M., Thiel, F. A., Haddon, R. C., *Nature* **355**, 529 (1992).

[9] Brown, C. M., Taga, S., Gogia, B., Kordatos, K., Margadonna, S., Prassides, K., Iwasa, Y., Tanigaki, K., Fitch, A. N., Pattison, P., *Phys. Rev. Lett.* **83**, 2258 (1999).

[10] Gogia, B., Kordatos, K., Suematsu, H., Tanigaki, K., Prassides, K., *Phys. Rev. B.* **58**, 1077 (1998).

[11] Jayaraman, A., Narayanamurti, V., Bucher, E., Maines, R. G., *Phys. Rev. Lett.* **25**, 1430 (1970).

[12] Cooley, J. C., Aronson, M. C., Fisk, Z., Canfield, P. C., *Phys. Rev. Lett.* **74**, 1629 (1995).

[13] Kasaya, M., Iga, F., Takigawa, M., Kasuya, T., *J. Magn. Magn. Mater.* **47-48**, 429 (1985).

[14] Maple, M. B., Wohlleben, D., *Phys. Rev. Lett.* **27**, 511 (1971).

[15] Vértes, A., Klencsár, Z., Kuzmann, E., Forró, L., Oszlányi, G., Pekker, S.,

J. Phys. Chem. Solids **61**, 2013 (2000).

[16] Kasaya, M., Iga, F., Negishi, K., Nakai, S., Kasuya, T., *J. Magnetism and Magnetic Mater.* **31-34**, 437 (1983).

[17] Jayaraman, A., Maines, R. G., *Phys. Rev. B* **19**, 4154 (1979).

[18] Salvador, J. R., Guo, F., Hogan, T., Kanatzidis, M. G., *Nature* **425**, 702 (2003).

[19] Margadonna, S., Prassides, K., Fitch, A. N., Salvador, J. R., Kanatzidis, M. G., *J. Am. Chem. Soc.* **126**, 4498 (2004).

[20] Arvanitidis, J., Papagelis, K., Margadonna, S., Prassides, K., Fitch, A. N., *Nature* **425**, 599 (2003).

[21] Arvanitidis, J., Papagelis, K., Margadonna, S., Prassides, K., *Dalton Trans.* **19**, 3144 (2004).

[22] Strange, P., Scane, A., Temmerman, W. M., Szotek, Z., Winter, H., *Nature* **399**, 756 (1999).

[23] Margadonna, S., Arvanitidis, J., Papagelis, K., Prassides, K., *Chem. Mater.* **17**, 4474 (2005).

[24] Özdas, E., Kortan, A. R., Kopylov, N., Ramirez, A. P., Siegrist, T., Rabe, K. M., Bair, H. E., Schuppler, S., Citrin, P. H., *Nature* **375**, 126 (1995).

[25] Takeuchi, J., Tanigaki, K., Gogia, B., In *Nanonetwork Materials*; AIP conference proceedings **590**, 361 (2001).

[26] Wakeshima, M., Harada, D., Hinatsu, Y., *J. Solid State Chem.* **147**, 618 (1999).

[27] Mitric, M., Antic, B., Balanda, M., Rodic, D., Napijalo, M. Lj., *J. Phys. Condens. Matter* **9**, 4103 (1997).

[28] Margadonna, S., Aslanis, e., Li, W.Z., Prassides, K., Fitch, A.N., Hansen, T.C., *Chem. Mater.* **12**, 2736, (2000)

[29] Sun, Z., Chen, X. H., Takenobu, T., Iwasa, Y., *J. Phys. Condens. Matter* **12**, 8919 (2000).

[30] A. Hammersley program: FIT2D, E.S.R.F., Grenoble, France.

[31] Finger, L. W., Cox, D. E., Jephcoat, A. P., *J. Appl. Cryst.* **27**, 892 (1994)

[32] Claridge, J. B., Kubozono, Y., Rosseinsky, M. J., *Chem. Mater.* **15**, 1830 (2003).

[33] Chatterjee, A., Singh, A. K., Jayaraman, A., *Phys. Rev. B.* **6**, 2285 (1972).

[34] Jayaraman, A., Singh, A. K., Chatterjee, A., Devi, S. U., *Phys. Rev. B.* **9**, 2513 (1974).

[35] Annese, E., Rueff, J-P., Vankó, G., Grioni, M., Braicovich, L., Degiorgi, L., Gusmeroli, R., Dallera, C., *Phys. Rev. B.* **70**, 075117 (2004).

[36] Dallera, C., Grioni, M., Shukla, A., Sarrao, J. L., Rueff, J-P., Cox, D. L., *Phys. Rev. Lett.* **88**, 196403-1 (2002).

[37] Dallera, C., Annese, E., Rueff, J-P., Palenzona, A., Vankó, G., Braicovich, L., Shukla, A., Grioni, M., *Phys. Rev. B.* **68**, 245114 (2003).

CHAPTER 4

Mixed Valence transitions in Samarium and Europium co-intercalated Fullerides

4.1 Introduction

Since the discovery of fullerenes, studies on the intercalation of a wide variety of atoms or molecules in the fullerene lattice have attracted considerable interest. Such an intense effort has led to the preparation of rare-earth based fullerides with composition, RE_xC_{60} (x = 1 - 6) [1, 2]. So far, phases containing Sm, Eu, and Yb dopants are known [3-7] with varied properties such as superconductivity [8, 9], ferromagnetism [10], giant magnetoresistance [11], negative thermal expansion [12, 13] and first-order lattice collapse [14].

For Eu-doped C_{60}, two different phases of nominal composition $Eu_{2.75}C_{60}$ and Eu_6C_{60} have been reported. The former adopts a vacancy-ordered *fcc* superstructure [15] and is paramagnetic, while the latter is isostructural with *bcc* A_6C_{60} (A = alkali metal) displaying a transition to a ferromagnetic state near 14 K which is accompanied by a very large negative magnetoresistance [11]. Their magnetic behaviour can be understood by considering the valence state of Eu ions since the magnetic moment of Eu^{2+} ($^8S_{7/2}$) is 7.94 μ_B, while Eu^{3+} ($^7F_0$) is nonmagnetic. In the case of Eu_6C_{60}, the experimentally determined magnetic moments suggest that the Eu ions are in the divalent state [1,10] consistent with that was derived from X-ray photoelectron spectroscopy measurements [16]. The ferromagnetic exchange interactions between the $4f$ electrons are modulated by the $\pi(C_{60})$ orbitals due to hybridization between the $5d$ and $6s$ orbitals of Eu and the t_{1g} orbitals of C_{60}. The valence state of Eu in $Eu_{2.75}C_{60}$ has been reported to be in the mixed valence state. Ksari-Habiles *et al.* [6] have predicted the presence of Eu^{3+} ions from the magnetic saturation moment, which varied between 4.5

and 5 μ_B, instead of 7 μ_B that would be expected if all the Eu ions were divalent. In the same report, ^{151}Eu Mössbauer spectroscopy measurements were also performed on powdered $Eu_{\sim 3}C_{60}$ samples, where the average valence state was calculated to be ~+2.33. This was followed by detailed ^{151}Eu Mössbauer spectroscopy measurements as a function of temperature, which indicated the slight change in their Eu^{2+}/Eu^{3+} ratio as they were cooled down [17].

Our focus has been directed towards the structural study of the mixed valence phenomena associated with the rare-earth intercalated C_{60} with stoichiometry, $RE_{2.75}C_{60}$ (RE = Sm, Eu, and Yb). So far, we have seen a remarkable sensitivity of the rare-earth valency to external stimuli (temperature, pressure) in Sm- and $Yb_{2.75}C_{60}$ [12-14, and chapter 3]. Here in this chapter, the results from the studies on the structural and magnetic properties of the related rare-earth fulleride, $Eu_{2.75}C_{60}$ and of polycrystalline samples of $(Sm_{1-x}Eu_x)_{2.75}C_{60}$ (x = 1/3 and 2/3) will be presented. The study of Eu-substituted $Sm_{2.75}C_{60}$ compounds as a function of temperature and pressure can provide further information on clarifying the roles of the size and electronic structure in inducing the valence transition in $RE_{2.75}C_{60}$. The lattice constants of EuS and SmS are comparable [18], and therefore the lattice size of $Eu_{2.75}C_{60}$ and $Sm_{2.75}C_{60}$ is expected to be also similar. These samples were measured by the high-resolution synchrotron X-ray powder diffraction technique on beamline ID31 to obtain temperature dependent diffraction data and on beamline ID09 to obtain the pressure evolution of the structure.

4.2 Temperature-induced valence transition

So far, NTE has been successfully observed in $RE_{2.75}C_{60}$ (RE = Sm, Yb). In order to explore the occurrence of a temperature-dependent valence transition in Eu intercalated fullerides, synchrotron X-ray powder diffraction measurements were performed on $Eu_{2.75}C_{60}$ and the co-intercalated Sm-Eu compounds, $(Sm_{1-x}Eu_x)_{2.75}C_{60}$ as a function of temperature. $Eu_{2.75}C_{60}$ and $Sm_{2.75}C_{60}$ are isostructural and isoelectronic rare-earth fullerides but changing the nature of the rare-earth cation sublattice from Sm to Eu could affect the NTE behaviour.

4.2.1 Experimental Details

$Eu_{2.75}C_{60}$ and $(Sm_{1-x}Eu_x)_{2.75}C_{60}$ samples were prepared inside an atmosphere controlled glove-box by reaction of stoichiometric quantities of degassed C_{60}, Sm and Eu powder (Table 4.1). These powders were first mixed well and pressed into pellets. Then they were placed in a tantalum tube and sealed inside a quartz tube filled with helium gas at 300 mbar. The annealing process used for $Sm_{2.75}C_{60}$ was also applied for these compounds, and the tube was placed in a pre-heated furnace at 575°C for 3 days with one intermediate grinding after the second day. After completing the annealing, few milligrams of the samples were sealed in thin-wall glass capillaries of diameter 0.5 mm for the powder X-ray diffraction measurements. Prior to the synchrotron X-ray measurements, the samples were checked using a laboratory X-ray diffractometer (Fig. 4.1).

Table 4.1. Quantities of reactants used for synthesising the $(Sm_{1-x}Eu_x)_{2.75}C_{60}$ samples and the final mass of the product following the annealing protocols. The error of the balance was ±1 mg.

$(Sm_{1-x}Eu_x)_{2.75}C_{60}$ Nominal x	Sm (150.36 g/mol)	Eu (151.96 g/mol)	C_{60} (720.66g/mol)	Product
$Eu_{2.75}C_{60}$ (x = 1)	n/a	58.0 mg 3.817×10^{-4}mol	100 mg 1.388×10^{-4}mol	154 mg
$(Sm_{1/3}Eu_{2/3})_{2.75}C_{60}$ (x = 2/3)	19.1 mg 1.272×10^{-4}mol	38.7 mg 2.544×10^{-4}mol	100 mg 1.388×10^{-4}mol	153 mg
$(Sm_{2/3}Eu_{1/3})_{2.75}C_{60}$ (x = 1/3)	38.0 mg 2.544×10^{-4}mol	19.0 mg 1.272×10^{-4}mol	100 mg 1.388×10^{-4}mol	154mg
$Sm_{2.75}C_{60}$ (x = 0)	57.4 mg 3.817×10^{-4}mol	n/a	100 mg 1.388×10^{-4}mol	152 mg

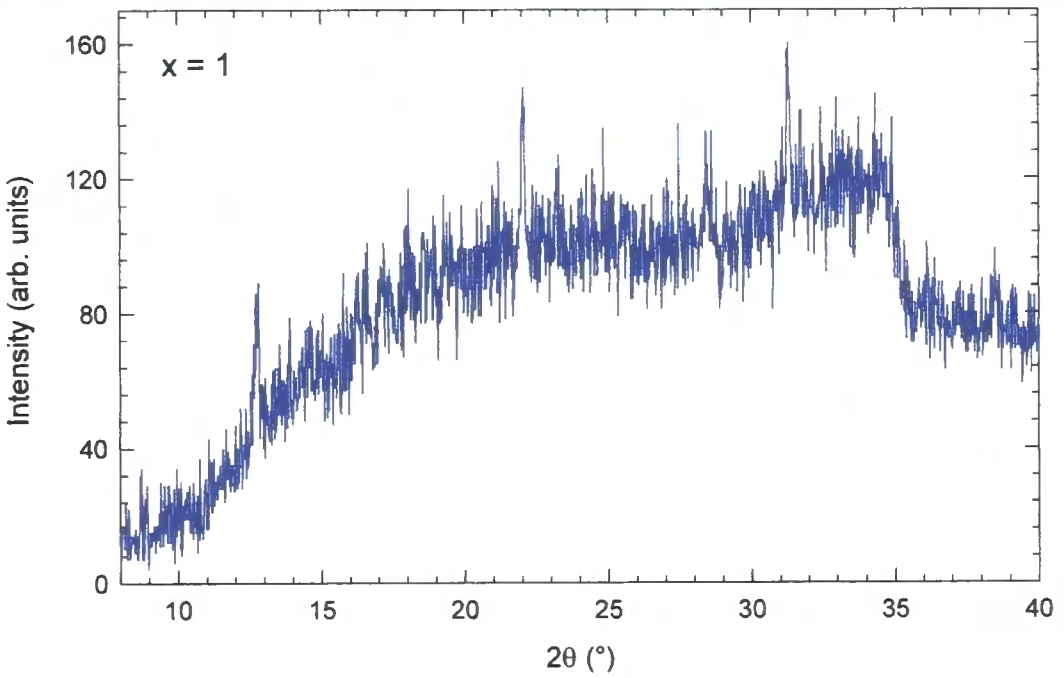

Fig. 4.1. X-ray diffraction profile of $Eu_{2.75}C_{60}$ collected with the Siemens D5000 powder diffractometer (Cu-K_α radiation) at room temperature.

However, the obtained diffraction patterns using Cu-K_α radiation were very poor in intensities, as they suffered from severe absorption problems. More than ever, these samples require the use of synchrotron radiation for further analysis. The magnetic properties were determined by SQUID magnetisation measurements on about 10 mg from each sample that were sealed in quartz SQUID tubes.

Synchrotron X-ray diffraction profiles for $Eu_{2.75}C_{60}$ were collected on heating between 4 and 295 K using a liquid-helium cryostat in continuous scanning mode with the high-resolution powder diffractometer on beamline ID31 at the ESRF. The sample was first cooled down to 4 K at a cooling rate of 4 K/min. The data were collected at various temperatures while the sample was heated slowly (at a rate of 0.5 K/min in the low temperature region) up to room temperature. A monochromatic X-ray wavelength, λ = 0.42977 Å was used and the collected data were rebinned to a step of 0.002° in the 2θ range 1.8° - 25°. The diffraction data of two samples prepared from Sm-Eu co-intercalation with nominal composition, $(Sm_{1-x}Eu_x)_{2.75}C_{60}$ (x = 1/3, 2/3) were also collected at the same beamline. For $(Sm_{2/3}Eu_{1/3})_{2.75}C_{60}$, the data were collected on both heating from 5 to 290 K and slow cooling from 300 to 5 K using X-ray wavelengths, λ = 0.85045 Å and 0.8010 Å, respectively. For $(Sm_{1/3}Eu_{2/3})_{2.75}C_{60}$, the data were collected using X-ray wavelength, λ = 0.42977 Å on heating between 4 and 295 K. Data analysis was performed with the GSAS suite of Rietveld analysis programs.

4.2.2 Magnetisation Measurements

Figure 4.2 shows the magnetic susceptibility and the inverse magnetic

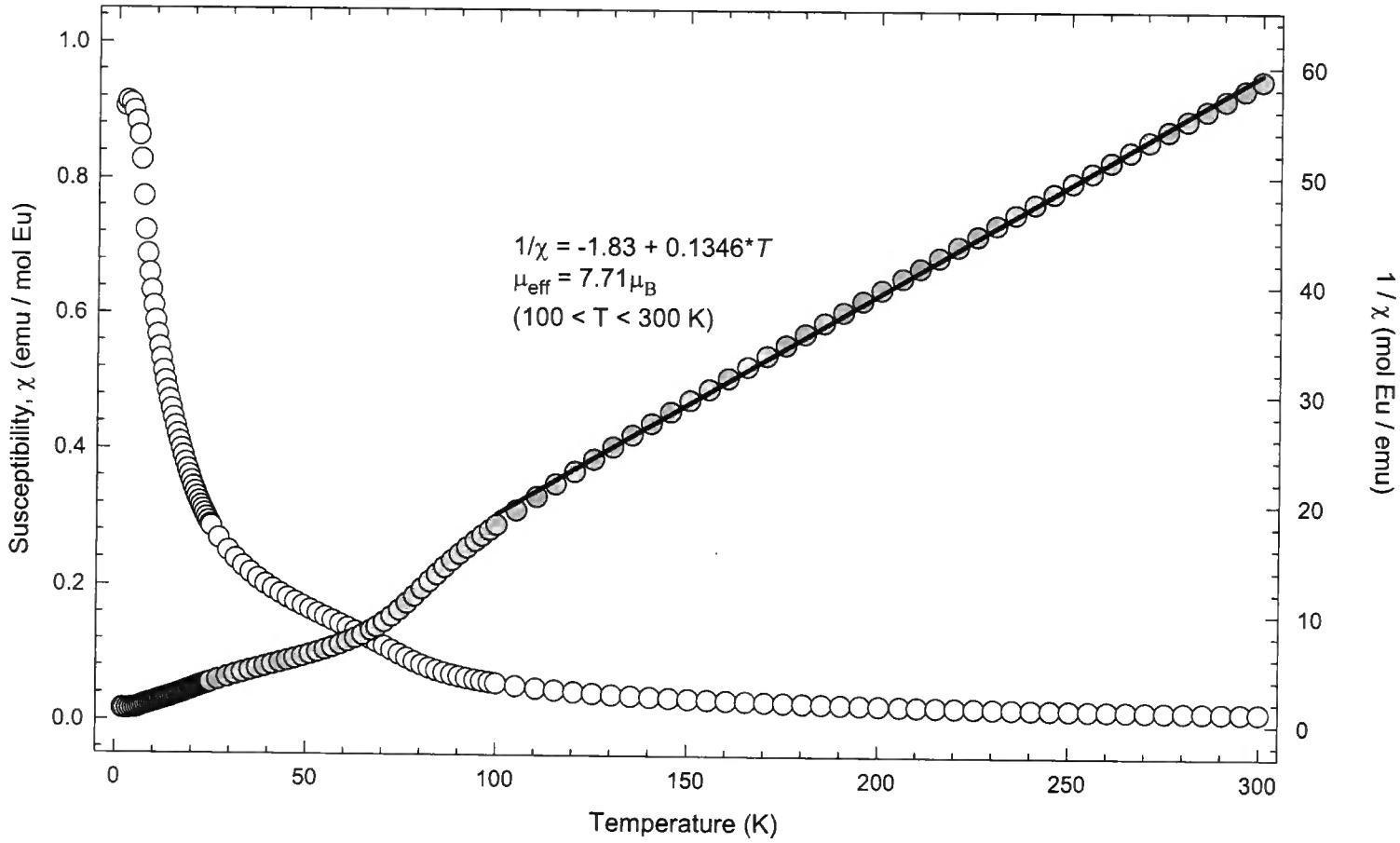

Fig. 4.2. Temperature dependence of the magnetic susceptibility, χ (open, left scale) and its reciprocal, $1/\chi$ (grey, right scale) at H = 1 T for $Eu_{2.75}C_{60}$.

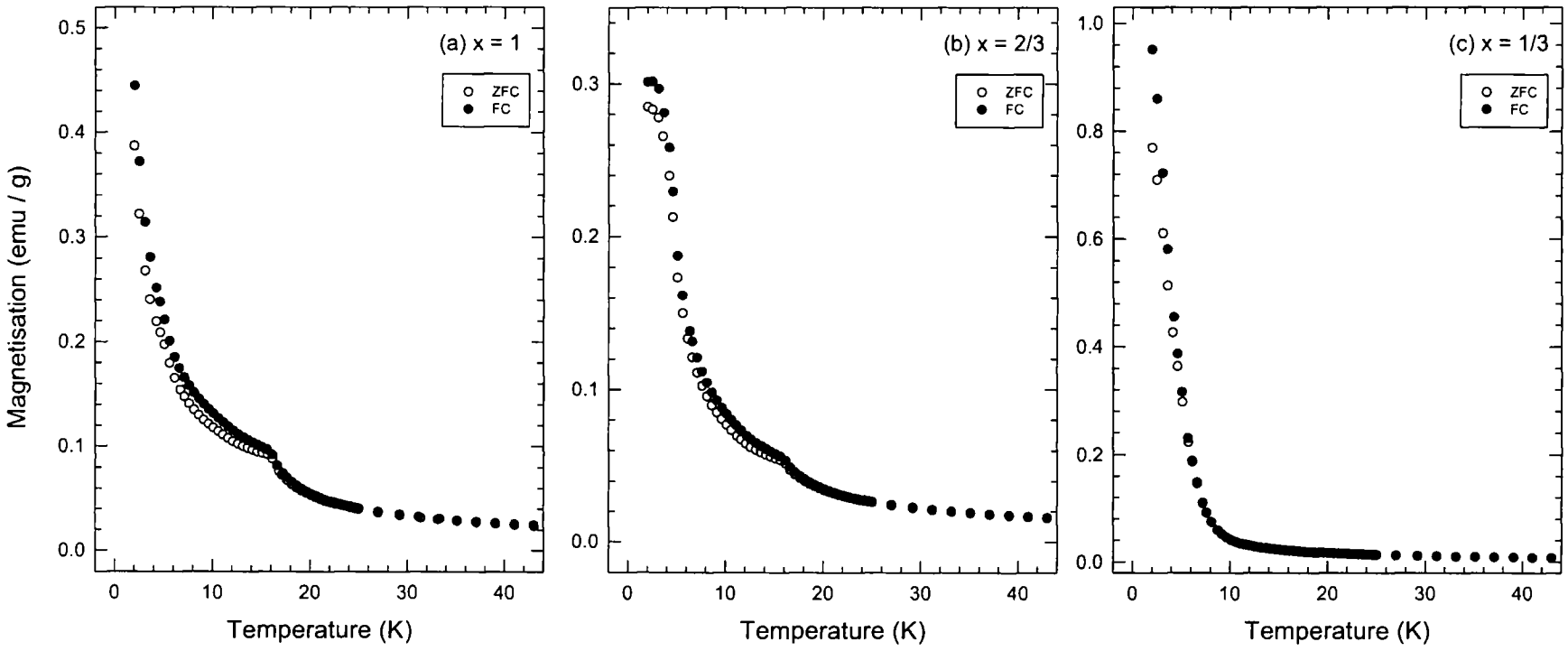

Fig. 4.3. The temperature dependence of the ZFC (open circle) and FC (full circle) magnetisation in a field of 50 Oe for: a) $Eu_{2.75}C_{60}$ ($x = 1$); b) $(Sm_{1/3}Eu_{2/3})_{2.75}C_{60}$ ($x = 2/3$); c) $(Sm_{2/3}Eu_{1/3})_{2.75}C_{60}$ ($x = 1/3$).

susceptibility obtained at 1 T plotted against temperature for $Eu_{2.75}C_{60}$. It is clear that a small ferromagnetic impurity with T_C near 70 K is present. Similar behaviour was observed for Eu_xC_{60}, x = 4-6 [1] and attributed to the presence of EuO (T_C=70 K) [19]. The data in the range 100-300 K were fitted with a Curie-Weiss law, providing an effective magnetic moment, μ_{eff} = 7.71 μ_B per Eu ion (Fig 4.2) and implying that Eu is present as essentially Eu^{2+}. Temperature dependence of magnetisation in a weak field of 50 Oe for $(Sm_{1-x}Eu_x)_{2.75}C_{60}$ (x = 1-1/3) (Fig. 4.3) which also shows a steep increase of magnetisation below 20 K, indicating a ferromagnetic transition.

4.2.3 Structure Analysis

Fig. 4.4 shows the synchrotron X-ray powder diffraction profiles obtained for different concentration of Sm at room temperature (λ = 0.80161 Å) in order to check the phase purity of the samples before carrying out detailed temperature-dependent experiments. The concentration of the Sm was carefully controlled by changing the relative ratio of Eu and Sm mass during preparation of the samples, starting from x = 1 for $Eu_{2.75}C_{60}$, x = 2/3 for $(Sm_{1/3}Eu_{2/3})_{2.75}C_{60}$, x = 1/3 for $(Sm_{2/3}Eu_{1/3})_{2.75}C_{60}$, and x = 0 for $Sm_{2.75}C_{60}$. Inspection of the diffraction profiles of $(Sm_{1-x}Eu_x)_{2.75}C_{60}$ shows no significant changes with variation of Sm concentration, indicating that they are isostructural and that all adopt the orthorhombic superstructure (space group *Pcab*, option 2). As in $Sm_{2.75}C_{60}$, the observed superstructure in arises from long-range ordering of tetrahedral (T_d) Eu/Sm defects.

A selected region of the normalised diffraction profiles of the same data sets is shown in Fig. 4.5a, displaying the evolution of the (444) Bragg

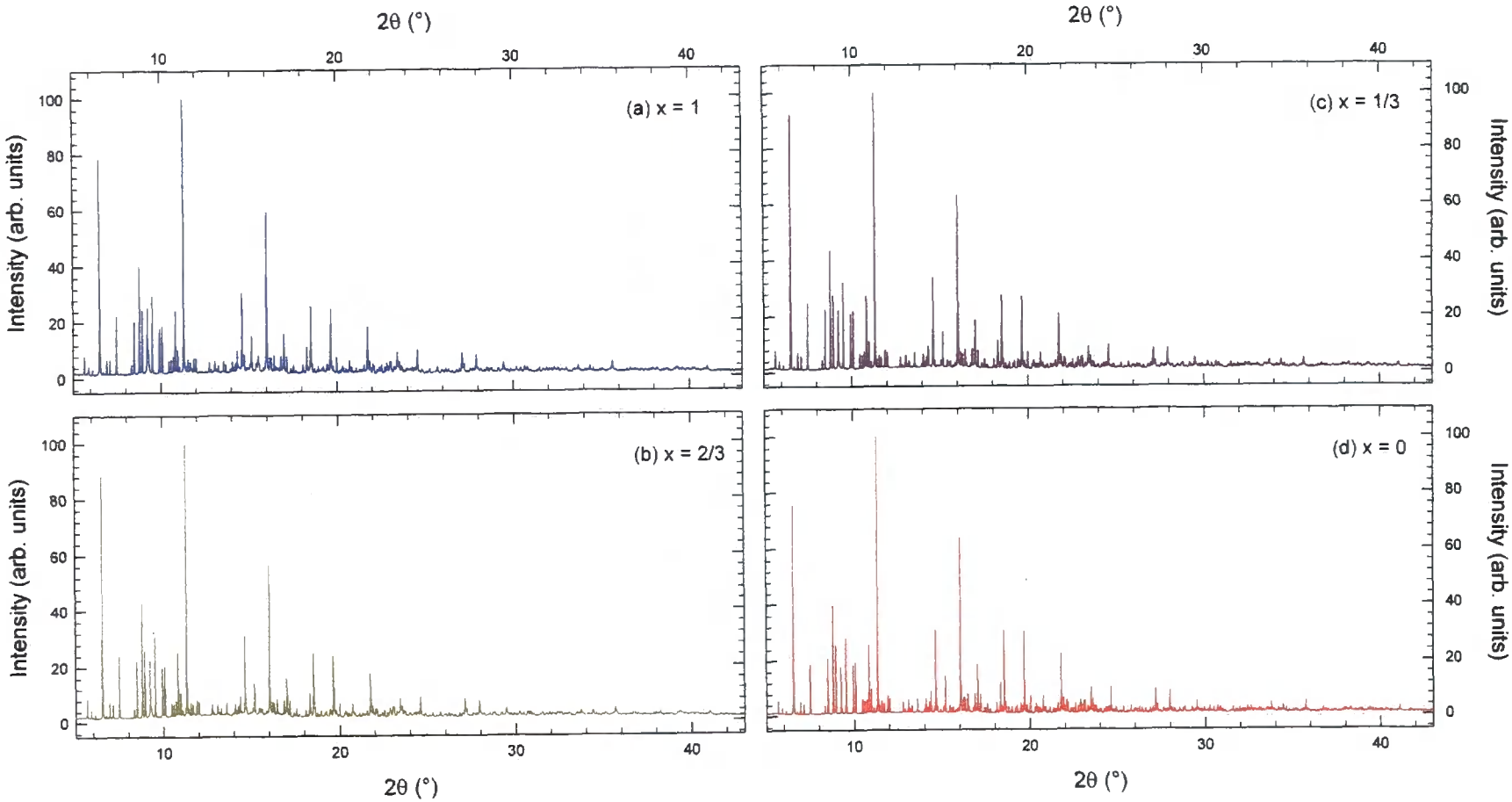

Fig. 4.4. Synchrotron X-ray powder diffraction profiles of $(Sm_{1-x}Eu_x)_{2.75}C_{60}$ at 295 K (λ = 0.8016 Å); a) $Eu_{2.75}C_{60}$ (x = 1); b) $(Sm_{1/3}Eu_{2/3})_{2.75}C_{60}$ (x = 2/3); c) $(Sm_{2/3}Eu_{1/3})_{2.75}C_{60}$ (x = 1/3); and d) $Sm_{2.75}C_{60}$ (x = 0).

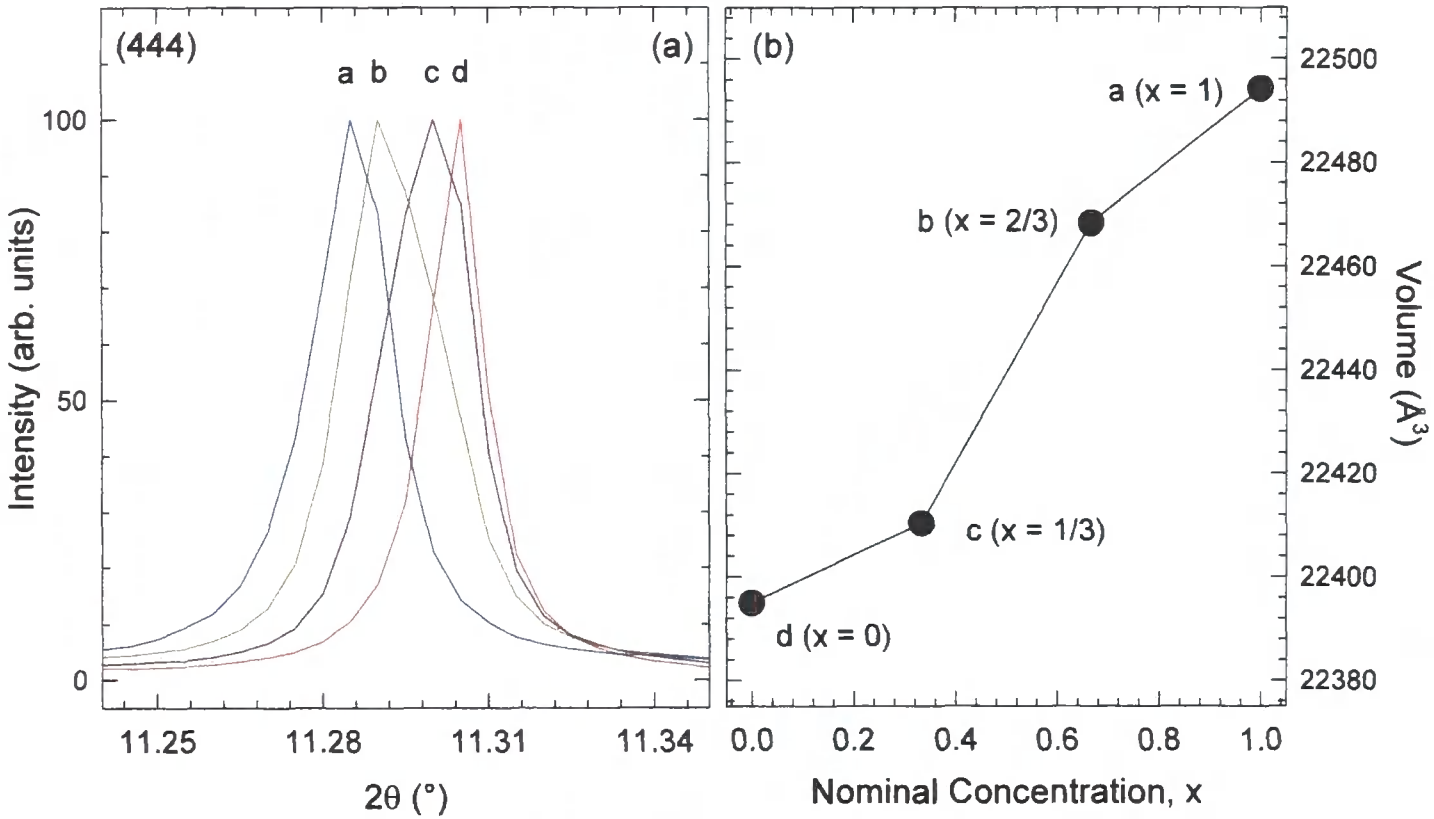

Fig. 4.5. (a) Selected region of the synchrotron X-ray powder diffraction profiles of $(Sm_{1-x}Eu_x)_{2.75}C_{60}$ showing the evolution of the (444) Bragg reflection with *x*. (b) The unit cell volume *vs* nominal concentration, *x* of Eu. The volume changes quasi-linearly with *x*, following Vegard's law.

reflection with change in concentration of Sm. However, an unexpected feature of the data is that the diffraction peaks shift to higher angles as the concentration of Sm increases, thus resulting in small lattice parameters despite what is expected from the lanthanide contraction expectations.

The lattice constants from each diffraction profile were extracted with the Lebail pattern decomposition technique (Table 4.2), and the obtained unit cell volume evolution against the nominal Eu concentration is plotted in Fig. 4.5b. The plot shows that the unit cell volume changes quasi-linearly with the change in the Eu-Sm ratio (Vegard's law), confirming the formation of solid solutions at $x = 2/3$ and 1/3.

Table 4.2. The extracted values for the unit cell volume and the lattice constants for $(Sm_{1-x}Eu_x)_{2.75}C_{60}$.

Sample	Volume (Å^3)	a (Å)	b (Å)	c (Å)
a: $Eu_{2.75}C_{60}$	22494.3(5)	28.2296(2)	28.2664(2)	28.1901(2)
b: $(Sm_{1/3}Eu_{2/3})_{2.75}C_{60}$	22468.3(5)	28.2187(2)	28.2556(2)	28.1791(2)
c: $(Sm_{2/3}Eu_{1/3})_{2.75}C_{60}$	22410.4(5)	28.1945(2)	28.2312(2)	28.1550(2)
d: $Sm_{2.75}C_{60}$	22395.0(5)	28.1871(2)	28.2243(2)	28.1509(2)

These results also imply that the effective ionic radii of Sm and Eu are similar. Some slight broadening in the widths of the diffraction peaks for the mixed compositions possibly reflects the presence of small inhomogeneities.

Rietveld refinement of the structure of $Eu_{2.75}C_{60}$ at room temperature was carried out using the same structural model employed for both $Sm_{2.75}C_{60}$ and $Yb_{2.75}C_{60}$. The results of the final refinement at room temperature with fitted parameters are summarised in Table 4.3. In the case of the mixed composition, $(Sm_{1-x}Eu_x)_{2.75}C_{60}$, the Rietveld refinement was initiated by using the same structural model, but assuming that the Sm and Eu ions are fully disordered in the T_d and O_h-sites of the lattice.

Table 4.3a. Refined parameters of $Eu_{2.75}C_{60}$ obtained from the Rietveld refinement of the synchrotron X-ray diffraction data at room temperature. Estimated errors in the last digit are given in parentheses. The space group is *Pcab* (No.61, option 2). The X-ray wavelength is 0.80161 Å. The values of the lattice constants are a = 28.2296(2) Å, b = 28.2664(2) Å, c = 28.1901(2) Å, V = 22494.3(5) Å^3; agreement factors, χ^2 = 7.83, R_{wp} = 9.27% and R_{exp}=3.31%. The shape of the C_{60} molecules was constrained to icosahedral symmetry with a cage diameter of 7.01 Å and all C-C bond length fixed to a value of 1.44 Å. 240 independent C atoms are needed to define the 32 C_{60} molecules present in the unit cell. The five symmetry-inequivalent C_{60} molecules in the unit cell, C_{60}(1) at (000), C_{60}(21) at (0¼¼), C_{60}(22) at (¼0¼), C_{60}(23) at (¼¼0), and C_{60}(3) at (½½½), were rotated anticlockwise by 37.5° about their local [111], [1$\bar{1}\bar{1}$], [$\bar{1}$1$\bar{1}$], [$\bar{1}\bar{1}$1], and [111] symmetry axes, respectively. The fractional occupancy of the C atoms was fixed to 1. Refinement of the fractional occupancies of the Eu atoms resulted in a nominal stoichiometry of $Eu_{2.751(1)}C_{60}$.

	Site	x/a	y/b	z/c	Occupancy	*B*(Å^2)
Eu(11)	8c	0.1371 (4)	0.1170 (5)	0.3870 (5)	0.975 (2)	4.43 (3)
Eu (12)	8c	0.3870 (5)	0.1371 (4)	0.1170 (5)	0.975 (2)	4.43 (3)
Eu (13)	8c	0.1170 (5)	0.3870 (5)	0.1371 (4)	0.975 (2)	4.43 (3)
Eu (21)	8c	0.1339 (5)	0.3704 (5)	0.3800(5)	0.975 (2)	4.43 (3)
Eu (22)	8c	0.3800(5)	0.1339 (5)	0.3704 (5)	0.975 (2)	4.43 (3)
Eu (23)	8c	0.3704 (5)	0.3800(5)	0.1339 (5)	0.975 (2)	4.43 (3)
Eu (3)	8c	0.378 (3)	0.377 (3)	0.377 (3)	0.975 (2)	4.43 (3)
Eu (4) (vacancy)	8c	0.122 (3)	0.123 (3)	0.123 (3)	0.17 (1)	4.43 (3)
Eu (51)	8c	0.2027 (1)	0.2027 (1)	0.2027 (1)	0.948 (4)	2.75 (4)
Eu (52)	8c	0.0473 (1)	0.0473 (1)	0.2027 (1)	0.948 (4)	2.75 (4)
Eu (53)	8c	0.2027 (1)	0.0473 (1)	0.0473 (1)	0.948 (4)	2.75 (4)
Eu (54)	8c	0.0473 (1)	0.2027 (1)	0.0473 (1)	0.948 (4)	2.75 (4)
Eu (61)	8c	0.2027 (1)	0.315 (4)	0.315 (4)	0.052 (4)	2.74 (4)
Eu (62)	8c	0.0473 (1)	-0.065 (4)	0.315 (4)	0.052 (4)	2.74 (4)
Eu (63)	8c	0.315 (4)	-0.065 (4)	0.0473 (1)	0.105 (9)	2.74 (4)

Table 4.3b. Nearest Eu-C contacts for the T_d sites at 295 K in Å.

Eu(11)-C	2.672 (5)	Eu (21)-C	2.717 (3)
	2.677 (5)		2.871 (4)
Eu (12)-C	2.672 (5)	Eu (22)-C	2.738 (3)
	2.676 (5)		2.841 (4)
Eu (13)-C	2.646 (5)	Eu (23)-C	2.841 (4)
	2.704 (5)		2.906 (5)
Eu (3)-C	2.74 (5)	Eu (4)-C	2.94 (2)
	2.83 (8)		2.95 (3)

4.2.4 Temperature Evolution

i) $Eu_{2.75}C_{60}$

Inspection of the diffraction profiles obtained using stepwise heating protocol for $Eu_{2.75}C_{60}$ at various temperatures between 4 and 295 K revealed that they show no changes in relative peak intensities throughout the whole temperature range (Fig. 4.6a). The temperature dependence of the data reveals that the angular position of the diffraction peaks at low temperatures shifts to higher angles in a quasi-continuous fashion on heating, which implies the material contracts as the temperature increases above 4 K. This trend continues until T reaches 90 K, where the diffraction peak shift changes towards lower angle implying that normal behaviour is restored above 90 K with the lattice smoothly expanding on heating to 295 K (Fig. 4.6b). The NTE behaviour in $Eu_{2.75}C_{60}$ is found at substantially higher temperature (~90 K) than in $Sm_{2.75}C_{60}$ (32 K) and $Yb_{2.75}C_{60}$ (60 K). Careful inspection of these diffraction profiles revealed that there were two features which were not observed for the case of $Sm_{2.75}C_{60}$.

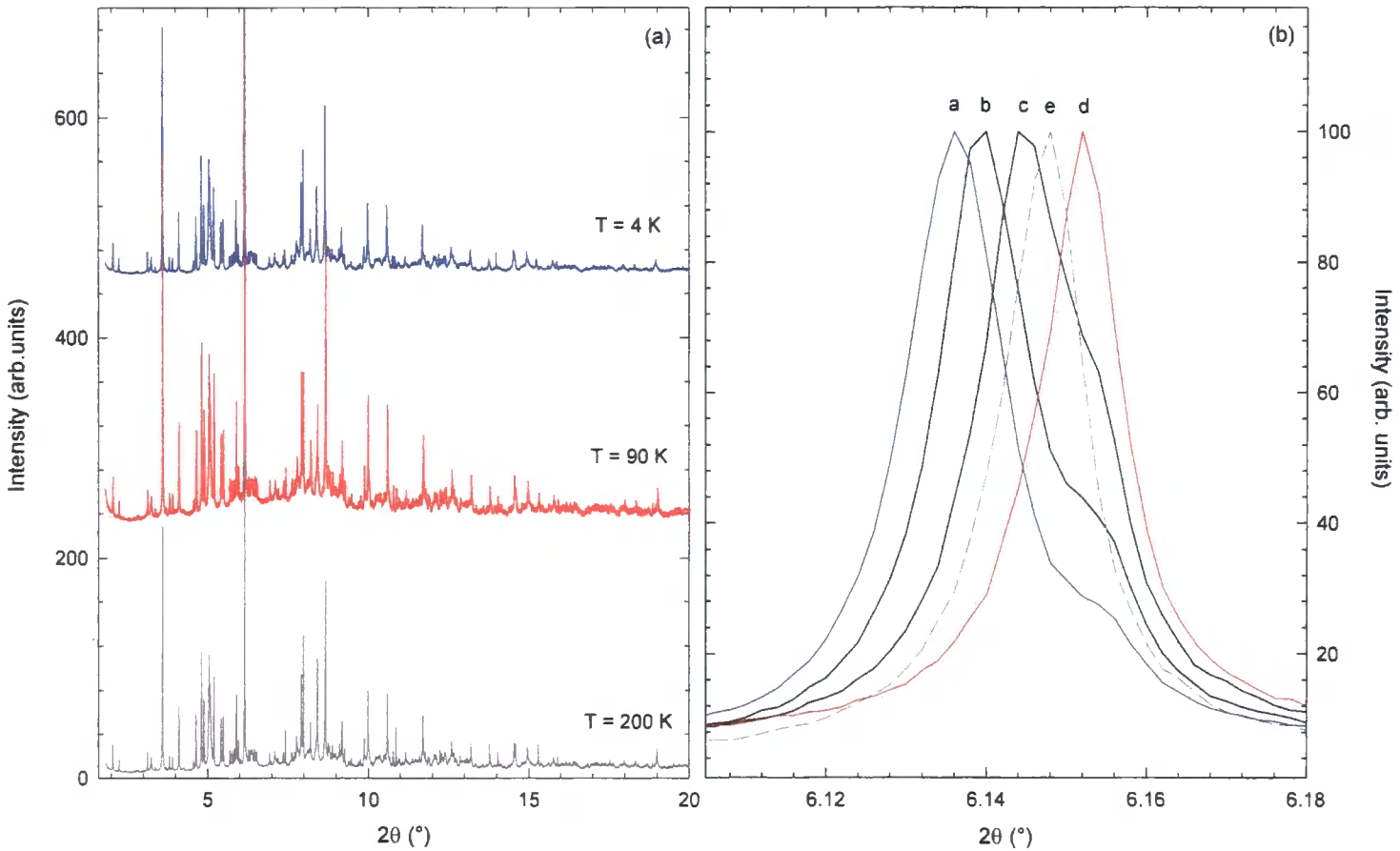

Fig. 4.6. Synchrotron X-ray ($\lambda = 0.4298$ Å) powder diffraction profiles of $Eu_{2.75}C_{60}$; a) at 4, 90 and 200 K, and b) selected region of the diffraction profiles showing the temperature evolution of the (444) Bragg reflection as obtained on heating (continued)

Fig. 4.6. (continued) from 4 to 300 K. Trace a) 4 K (blue); b) 32 K; c) 40 K; d) 90 K (red); e) 200 K (grey dashed). The peak shifts to higher angle (lattice contraction) on heating from 4 to 90 K and then to lower angles (lattice expansion) on further heating to room temperature. The apparent shoulders are observed for traces a, b, and c, but disappear for traces d and e.

They are: a) the apparent phase separation in the temperature region where NTE is observed, where the major phase contracts and the minor phase expands on heating – this phase separation is not apparent above 90 K, where no NTE is observed, and b) two distinct steps in lattice contraction including zero expansion between 44 and 60 K.

Refinement of the structure at low temperatures was attempted by 2-phase Rietveld analysis initiated by assuming that both phases are in the orthorhombic space group *Pcab* with Eu cations occupying off-centred T_d and O_h interstitial sites. Fig. 4.7 shows the result for $Eu_{2.75}C_{60}$ at 4 K. The lattice parameters of the major phase determined by the Rietveld refinements at 4 K are: a = 28.2596 (2) Å, b = 28.2963 (2) Å, c = 28.2200 (2) Å, V = 22565.9 (5) Å^3, weight fractions are 0.891(2) for major phase and 0.109(3) for minor phase, and agreement factors, χ^2 = 6.61, R_{wp} = 7.88%, R_{exp} = 1.82%. The Rietveld refinements were carried out using the 2-phase structural model up to 90 K and the 1-phase model was employed above 90 K in order to extract the lattice constants and weight fraction as a function of temperature. The refined parameters obtained at 4 and 300 K are tabulated and compared in Table 4.4.

Table 4.4. Lattice dimensions and profile parameters for $Eu_{2.75}C_{60}$ at 4 and 300 K.

Temperature:	4 K	300 K
Instrumental parameters:		
λ (Å)	0.4298	0.4298
Δ2θ (×100, °)	9.674 (4)	0.13 (2)
2θ range (°)	3.1 - 21	3.1 - 21
Step size (°)	0.002	0.002
Lattice parameters:		
a (Å)	28.2596 (2)	28.2296 (2)
b (Å)	28.2963 (2)	28.2664 (2)
c (Å)	28.2200 (2)	28.1901 (2)
V (Å^3)	22565.9 (5)	22494.3 (5)
Wt. Fraction (%):	0.9003 (3)	- (-)
Peak profile coefficient:	Type 3	Type 3
GU, GV,	111.6 (8), -8.58 (8),	40.0 (5), -6.11 (2),
GW	0.125 (5)	0.378 (2)
Lx, Ly	0.94 (1), 13.6 (2)	1.40(2), 13.8 (2)
S/L, H/L	0.002, 0.0005	0.002, 0.0005
L11,	0.55×10^{-2},	-0.12×10^{-1},
L22, L33	0.19×10^{-2},-0.35×10^{-3}	0.14×10^{-1}, 0.51×10^{-2}
L12,	-0.37×10^{-2},	0.43×10^{-2},
L13, L23	-0.11×10^{-2}, 0.35×10^{-3}	-0.16×10^{-3}, -0.84×10^{-2}
Agreement factors:		
R_{wp} (%), R_{exp} (%), χ^2	2.70, 2.50, 1.04	9.27, 3.31, 7.38

The temperature evolution of the unit cell volume and of the weight fraction of both major and minor phases is shown in Fig. 4.8a and the calculated thermal expansivity, α_V (= $d\ln V/dT$) is plotted in Fig. 4.8b. The lattice constants of the major phase contract in two distinct steps, where first they decrease quasi-continuously with the rate of contraction gradually increasing, in absolute value, on heating to a maximum of -335 ppm/K at 44 K. Then this rapidly approaches zero at 48 K.

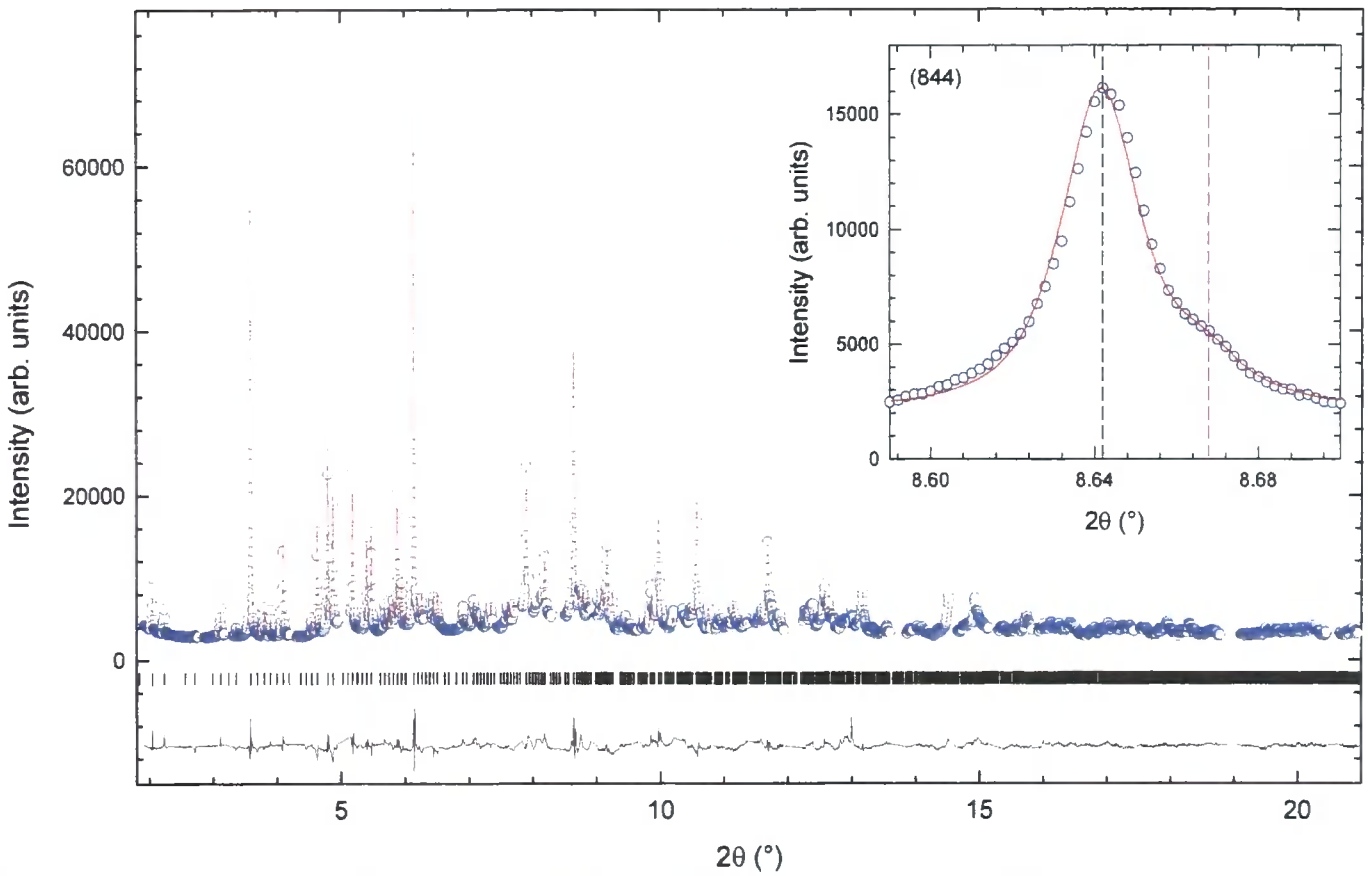

Fig. 4.7. Observed (o) and calculated (solid line) synchrotron X-ray powder diffraction profiles of $Eu_{2.75}C_{60}$ ($\lambda = 0.4298$ Å, $T = 4$ K). The lower solid line shows the difference profile and the tick marks show the reflection positions. Some weak impurity peaks were excluded. [*inset:* Blow-up of the (844) Bragg reflection, showing the two sets of peaks, where the reflection position of major (minor) phase is indicated by black (pink) dashed line.]

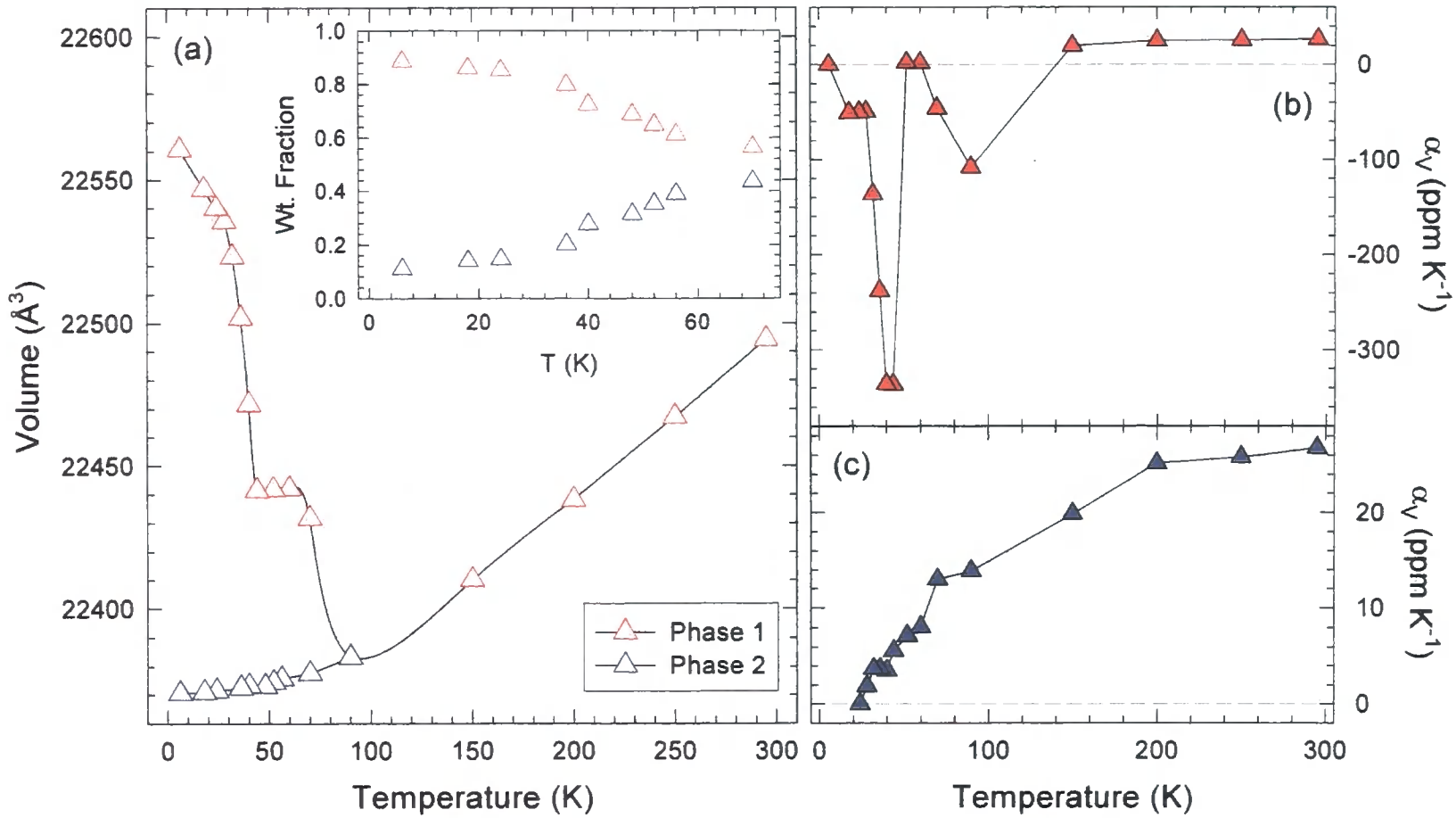

Fig. 4.8. Temperature evolution of (a) unit cell volume of $Eu_{2.75}C_{60}$, where major phase (phase 1) is represented by red triangles and minor phase (phase 2) by blue triangles [*inset:* weight fractions of the two phases at temperatures between (continued)

Fig. 4.8. (continued) 4 and 90 K], (b) the coefficient of thermal expansion, $\alpha_V = d\ln V/dT$, for phase 1 and (c) for phase 2.

The thermal expansivity remains zero up to 60 K, then it increase again at 70 K up to second maximum of -110 ppm/K, which then changes its sign to positive above 90 K (Fig 4.8b). This behaviour leads to an overall decrease in lattice size of 0.82% in two distinct steps between 4 and 90 K (0.55% in first step and 0.27% in second step). On the other hand, the unit cell volume of the minor phase increases slowly on heating at a rate of ~+10 ppm/K towards 90 K, comparable to that typically encountered in other metal fullerides salts in this temperature range [20] (Fig. 4.8c). Above 90 K, the phase separation is no longer apparent and the lattice size increases on heating to 295 K at a rate of approximately +25 ppm/K.

ii) $(Sm_{1/3}Eu_{2/3})_{2.75}C_{60}$

The temperature evolution of the diffraction profiles for $(Sm_{1/3}Eu_{2/3})_{2.75}C_{60}$ were followed on ID31 (λ = 0.42977 Å) on heating between 4 and 295 K. The data were re-binned to a step of 0.002° in the range 1.7° - 15.1° for further analysis.

The diffraction profile at 4 K was similar to that measured for $Eu_{2.75}C_{60}$, implying that this compound also adopts the cation-vacancy ordered superstructure. Phase separation was also observed at low temperatures. The initial model used for the Rietveld refinements were directly imported from the structural model of $Eu_{2.75}C_{60}$ at 4 K, assuming that both Sm and Eu atoms are randomly distributed in the T_d and O_h interstitial sites with the

fractional occupancy of Eu atoms twice as large as that of Sm atoms. The result of the refinement at 4 K is shown in Fig. 4.9.

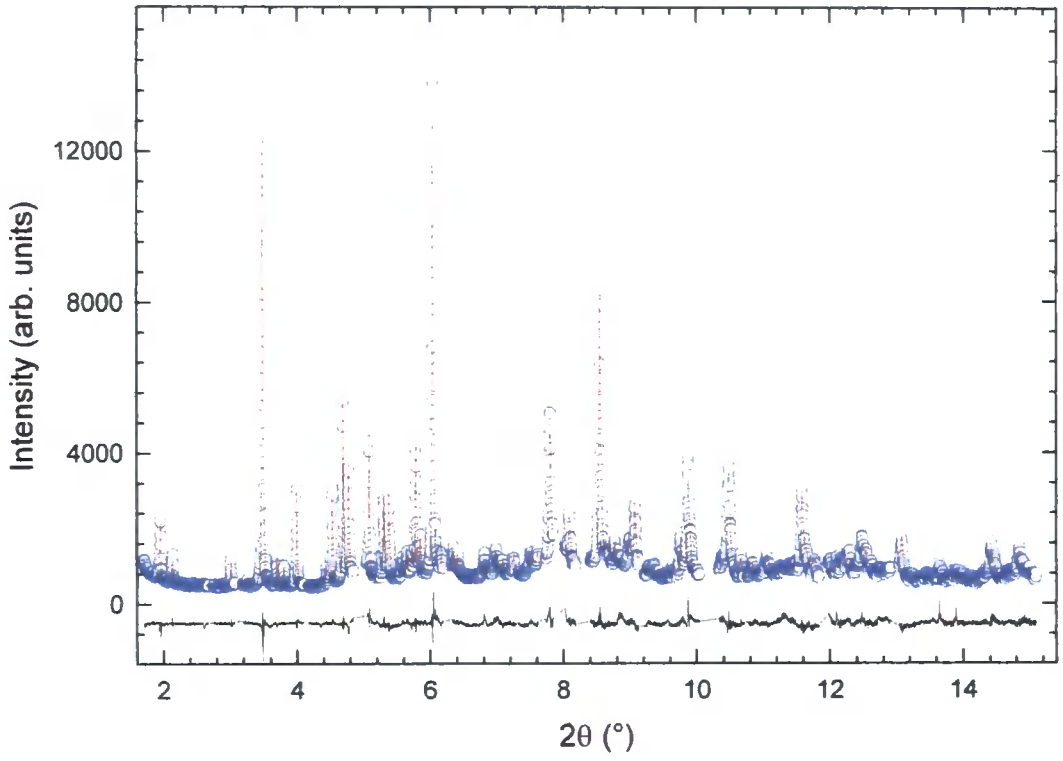

Fig. 4.9. Synchrotron X-ray powder diffraction profile of $(Sm_{1/3}Eu_{2/3})_{2.75}C_{60}$ at 4 K. Intensities of observed and calculated peaks are shown in blue circle and red solid line, and the difference profile is shown as a black solid line, respectively. Some impurity peaks were removed in the course of refinement.

The final refinement yielded the following lattice parameter values: major phase (phase 1) a = 28.2362(2) Å, b = 28.2729(2) Å, c = 28.1968(2) Å, V = 22510.0(5) Å^3, and minor phase (phase 2) a = 28.1612(13) Å, b = 28.1978(13) Å, c = 28.1218(13) Å, V = 22331.0(3.1) Å^3, with weight fractions for major phase of 0.8764(4) and minor phase 0.1236(31), and agreement factors, χ^2 = 3.013, R_{wp} = 7.21%, R_{exp} = 4.15%.

As seen in Fig. 4.10, the diffraction profiles obtained at various temperatures clearly provides evidence for NTE with the angular position of diffracted peaks at low temperatures shifting quasi-continuously to higher angles on heating. This shift continues up to 90 K, where it changes its direction towards lower angles on further heating. The phase separation also disappears at this temperature. The Rietveld refinements were carried out using a 2-phase structural model up to 90 K and a 1-phase model above 90 K.

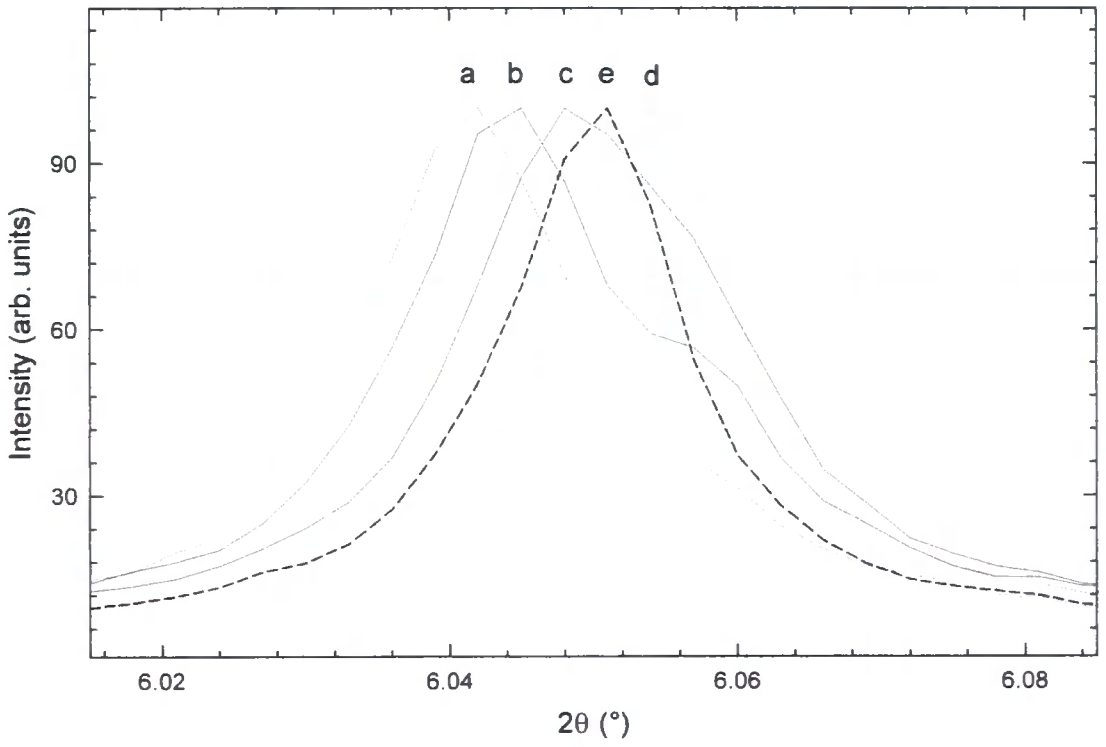

Fig. 4.10. Selected region of the synchrotron X-ray (λ = 0.4298 Å) powder diffraction profiles of $(Sm_{1/3}Eu_{2/3})_{2.75}C_{60}$, showing the temperature evolution of the (444) Bragg reflection. Trace a, 4 K; b, 28 K; c, 32 K; d, 90 K; and e, 200 K. The peak shifts to higher angle (lattice contraction) on heating from 4 to 90 K and then to lower angles (lattice expansion) on further heating to room temperature. Apparent second peaks are observed in traces a, b, and c, but disappear in traces d and e.

The extracted temperature evolution of lattice constants and weight fractions is plotted in Fig. 4.11a. The thermal expansivity for both phases was calculated from the extracted unit cell volume and plotted against temperature in Fig. 4.11b,c.

The NTE behaviour observed in the major phase of $(Sm_{1/3}Eu_{2/3})_{2.75}C_{60}$ shows two step lattice responses with near- zero thermal expansion at around 40 and 50 K. As the temperature slowly increases above 4 K, the lattice parameters contract steeply until the temperature reaches 40 K with a maximum thermal expansivity of -460 ppm/K. Then this rapidly decreases to zero until the lattice parameters begin to decrease again around 60 K. The contraction rate between 50 and 90 K is very small compared to that for the lower temperature region with the thermal expansivity only going through a second maximum of -30 ppm/K. This behaviour leads to an overall decrease in lattice size of 0.62% in two distinct steps between 4 and 90 K (0.55% in first step and 0.07% in second step). Phase 2, on the other hand, shows very slow expansion towards 90 K with an average thermal expansivity of +3 ppm/K. The phase separation is no longer apparent above 90 K and the unit cell volume continuously expands with increasing temperature.

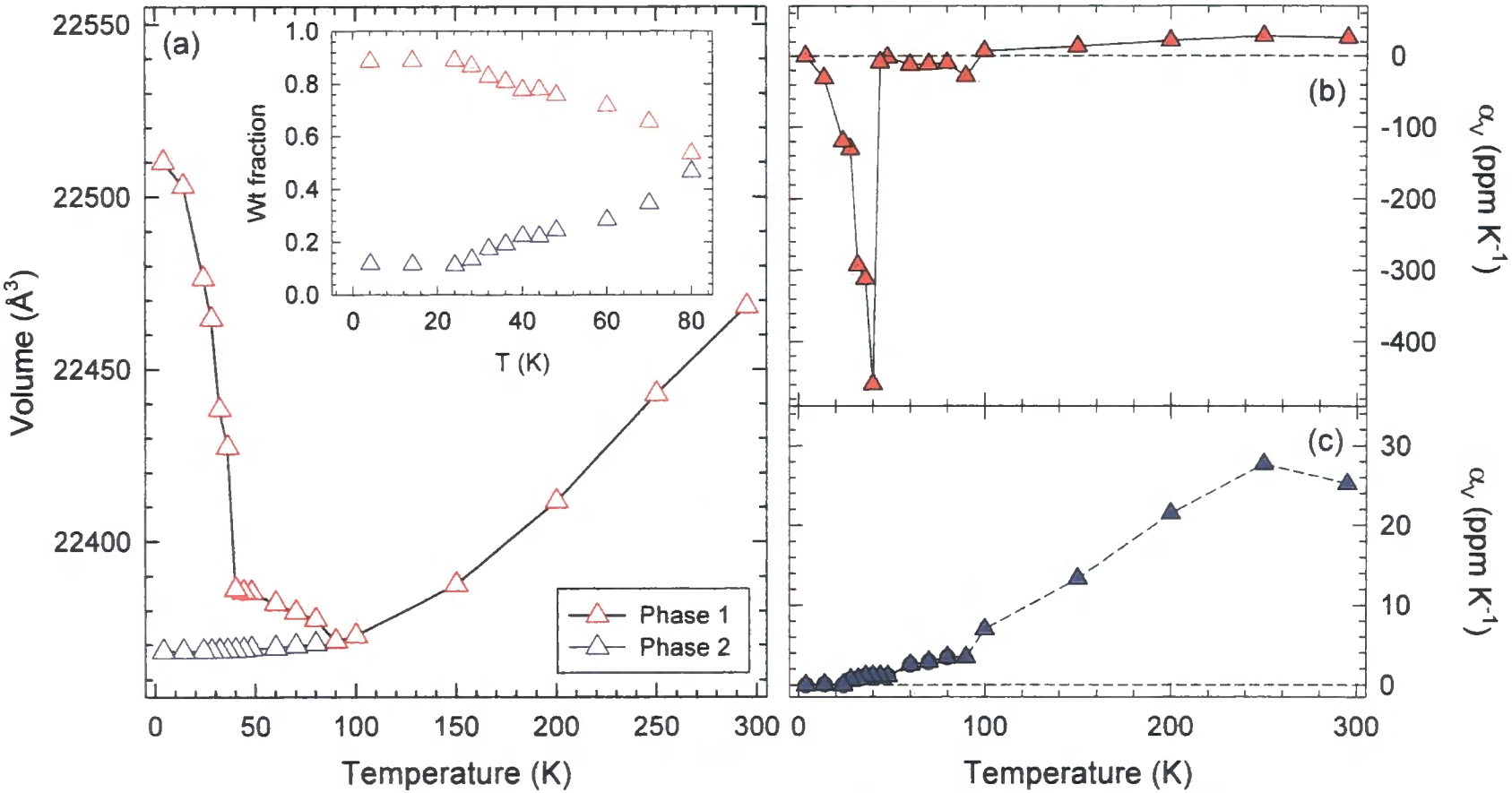

Fig. 4.11. Temperature evolution of (a) unit cell volume of $(Sm_{1/3}Eu_{2/3})_{2.75}C_{60}$, where the major phase (phase 1) is represented by red triangles and the minor phase (phase 2) by blue triangles [*inset:* weight fractions of the two phases at temperatures between 4 and 80 K], the coefficient of thermal expansion, $\alpha_V = d\ln V/dT$, of (b) phase 1 and (c) phase 2.

iii) $(Sm_{2/3}Eu_{1/3})_{2.75}C_{60}$

The synchrotron X-ray powder diffraction profiles of $(Sm_{2/3}Eu_{1/3})_{2.75}C_{60}$ were collected on ID31 (λ = 0.85045 Å) first on heating from 5 to 295 K. The same sample was cooled down slowly with a stepwise cooling protocol from 299 to 5 K (λ = 0.8010 Å). All data obtained were rebinned to a step of 0.003° in the range 3.0° - 30.1°. The temperature evolution of the Bragg (444) reflection at selected temperature is shown in Fig. 4.12 for both heating and cooling measurements.

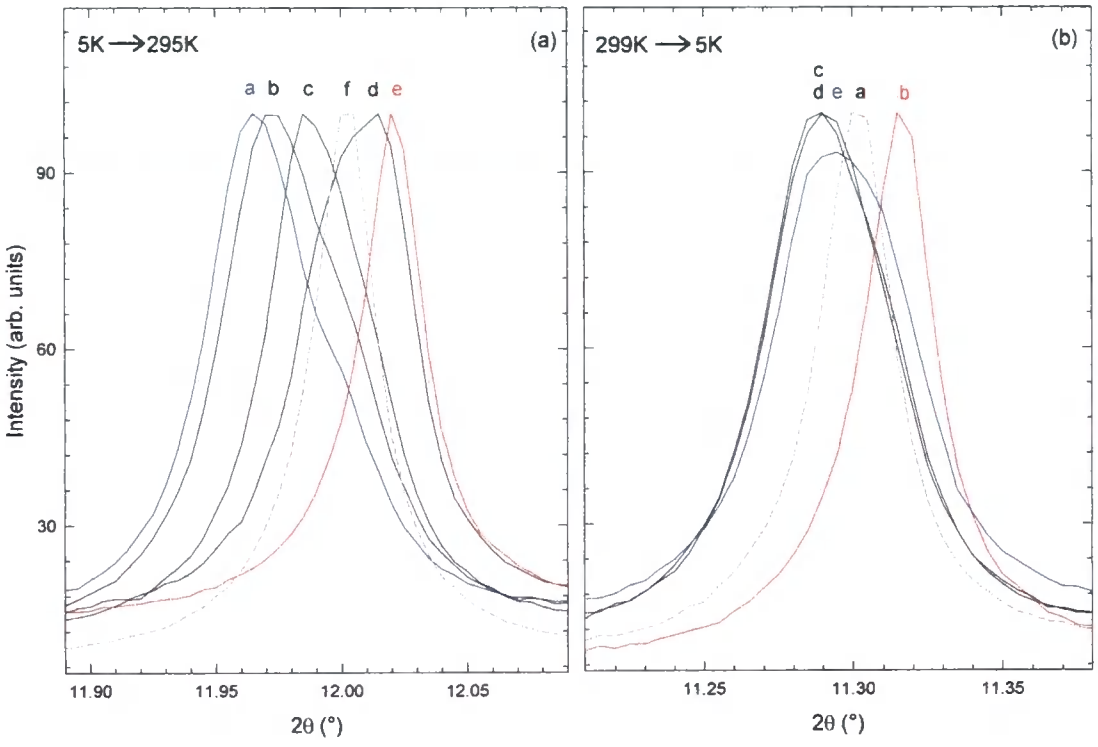

Fig. 4.12. Selected region of the synchrotron X-ray powder diffraction profiles of $(Sm_{2/3}Eu_{1/3})_{2.75}C_{60}$, showing the temperature evolution of the (444) Bragg reflection (a) on heating from 5 to 295 K and (b) on cooling from 299 to 5 K. Plot (a) shows the trace obtained while heating from 5 to 290 K (continued)

Fig. 4.12. (continued) (λ = 0.85045 Å), a) 5 K; b) 20 K; c) 30 K; d) 50 K; e) 80 K; and f) 290 K. The peak shifts to higher angle (lattice contraction) on heating from 4 to 80 K and then to lower angles (lattice expansion) on further heating to room temperature. Apparent second peaks are observed in traces a, b, c, and d but disappear in traces e and f. The plot (b) shows the trace obtained on stepwise cooling from 299 to 5 K (λ = 0.8010 Å), a) 299 K; b) 120 K; c) 60 K; d) 40 K; and e) 5 K. Here, the peak shifts to higher angle on cooling from 299 K to 120 K (lattice contraction), then to lower angles on further cooling down to 60 K (lattice expansion), and again shifts to higher angle down to 5 K (lattice contraction). The width of the peak at very low temperature broadens and may represent the occurrence of phase separation, but it is not broad enough to resolve the existence of a second phase.

Fig. 4.12a shows clear sign of phase separation at low temperatures (between 5 and 60 K). However, inspection of the diffraction data shows that the angular position of both phases shifts to higher angles on heating, implying that both phase experiences NTE in this temperature region. The diffraction peak sharpens at around 70 K and phase separation disappears at 80 K, where normal behaviour is observed on further heating. The temperature evolution of the unit cell volume was extracted from the diffraction profile by Rietveld refinement at all temperature (Fig. 4.13a). The refinements were performed using the same structural model of $(Sm_{1/3}Eu_{2/3})_{2.75}C_{60}$ with the assumption that the fractional occupancy of the Sm is always twice as large as that of Eu in the same interstitial sites.

The extracted lattice parameters for phase 1 at 5 K are a = 28.2787(2) Å, b = 28.3154(2) Å, c = 28.2392(2) Å, V = 22613.6(6) Å^3, while for phase 2 they are a = 28.1987(10) Å, b = 28.2353(10) Å, c = 28.1594(10) Å, V = 22425.8(2.2) Å^3, the weight fractions of the two phases are 0.800(1) for phase 1 and

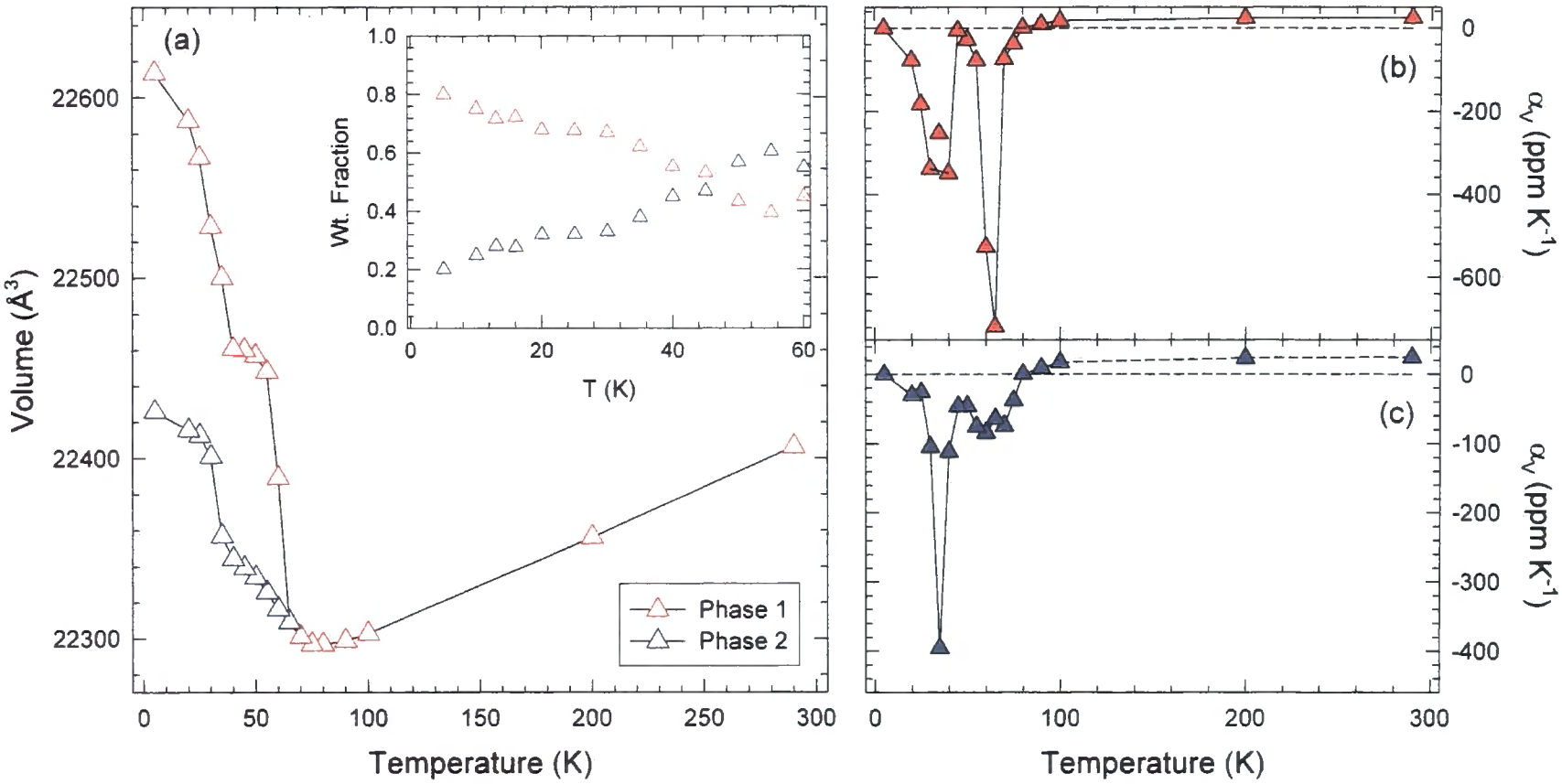

Fig. 4.13. Temperature evolution of (a) unit cell volume of $(Sm_{2/3}Eu_{1/3})_{2.75}C_{60}$ on heating, where phase 1 (phase 2) is represented by red (blue) upward triangles [*inset:* weight fractions of the two phases between 5 and 60 K]. Phase 1 is major phase between 5 and 45 K, but becomes minor phase above 45 K until phase separation disappears. The coefficient of thermal expansion, $\alpha_V = d\ln V/dT$, for (b) phase 1 and (c) phase 2.

0.200 (3) for phase 2, and the agreement factors $\chi^2 = 7.301$, $R_{wp} = 4.45\%$, $R_{exp} = 1.65\%$. As temperature increases above 5 K, both phases show anomalous lattice responses which continue up to 80 K. Phase 1 experiences NTE with two distinct steps, as it initially contracts slowly above 4 K then the rate of contraction increases, in absolute value, towards -350 ppm/K until it rapidly decreases to zero at 40 K, and remains close to zero up to 60 K. Above 60 K, the thermal expansivity shows an abrupt jump towards a maximum of -720 ppm/K and once again it decreases towards zero at around 80 K, where it reaches the minimum unit cell volume (Fig. 4.13b). This behaviour leads to an overall decrease in lattice size of 1.41% (0.68% in first step and 0.75% in second step). The unit cell volume of phase 2 also contracts continuously with increasing temperature and goes through a maximum thermal expansivity of -395 ppm/K at 35 K and then rapidly approaches zero at 80 K (Fig. 4.13c). The overall decrease in lattice size for phase 2 is much smaller compared to that for phase 1, resulting in a decrease of 0.58% done in a single step. As seen in the inset of Fig. 4.12a, phase 1 is the major phase at temperatures between 5 and 45 K, but above this temperature, phase 2 becomes the major phase. Above 80 K, the sign of thermal expansivity changes to positive and the unit cell volume continuously expands with increasing temperature up to 295 K.

Diffraction data were also collected using a stepwise cooling protocol on the same batch of sample in order to find out any hysteretic behaviour associated with the transition. Starting from room temperature, the sample was cooled down inside the cryostat, where the diffraction profiles were collected at each temperature step. The temperature dependence of the angular position of the diffraction peaks at selected region and temperatures

is shown in Fig. 4.12b. Initially, starting from 299 K, the peak shifts to higher angles, implying lattice contraction on cooling down to 120 K, where the diffraction peaks clearly start to shift to lower angles on further cooling. This implies that the onset temperature of NTE behaviour in $(Sm_{2/3}Eu_{1/3})_{2.75}C_{60}$ when slowly cooled is seen at the substantially higher temperature of 120 K (80 K for heating). The NTE behaviour continues until the temperature reaches 60 K, then it shows no further change (ZTE) on cooling to 40 K. On further cooling, surprisingly, the diffraction peaks start to shift to higher angle, which implies that the anomalous lattice responses disappears and normal contraction on cooling is retrieved below 40 K.

The Rietveld refinement of the structure of $(Sm_{2/3}Eu_{1/3})_{2.75}C_{60}$ at 5 K was carried out using the same structural model that was employed for the earlier data analysis, but without phase 2. The values of the lattice parameters obtained from the Rietveld refinement of the diffraction data at 5 K are: a = 28.2029(3) Å, b = 28.2114(3) Å, c = 28.1944(3) Å, V = 22432.8(6) Å^3, and agreement factors $\chi^2 = 4.60$, $R_{wp} = 5.35\%$, $R_{exp} = 2.49\%$. The results of the final refinement are shown in Fig. 4.14.

Extraction of lattice constants was performed with the LeBail pattern decomposition technique using the space group *Pcab* at all temperatures and the obtained temperature evolution of the unit cell volume on cooling is plotted in Fig. 4.15. A surprising feature of the cooling data is that they show three distinct steps in the temperature evolution of the unit cell volume. The first step is NTE (maximum thermal expansivity reaching -120 ppm/K and overall volume increase of 0.60%), followed by ZTE, and then positive thermal expansion (maximum contraction rate of +90 ppm/K and overall volume decrease of 0.13%).

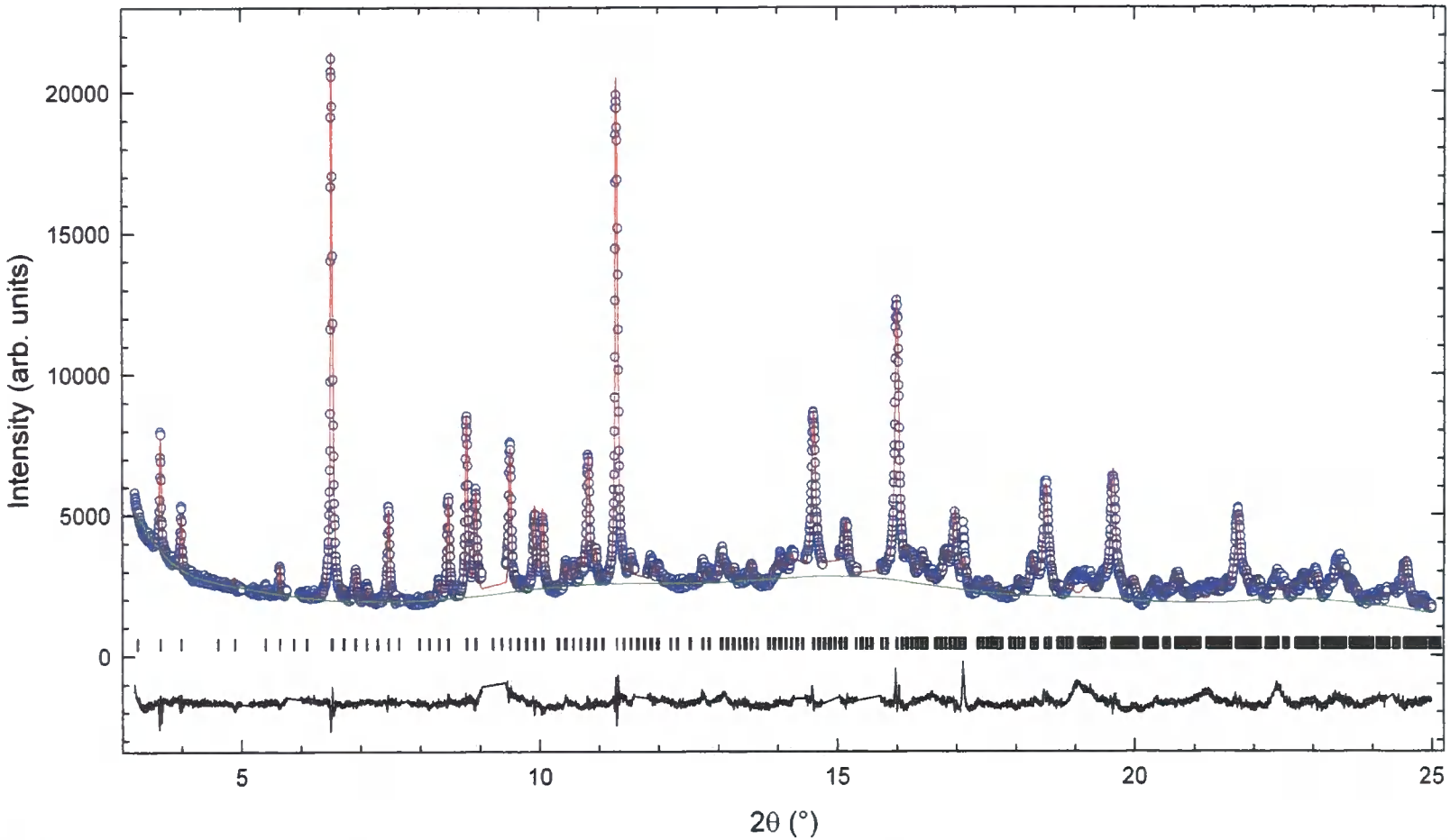

Fig. 4.14. Observed (o) and calculated (solid line) synchrotron X-ray powder diffraction profiles for $(Sm_{2/3}Eu_{1/3})_{2.75}C_{60}$ (λ = 0.8010 Å, T= 5 K) on cooling. The lower solid line shows the difference profile and the tick marks show the reflection positions. Some impurity peaks were excluded from the refinement.

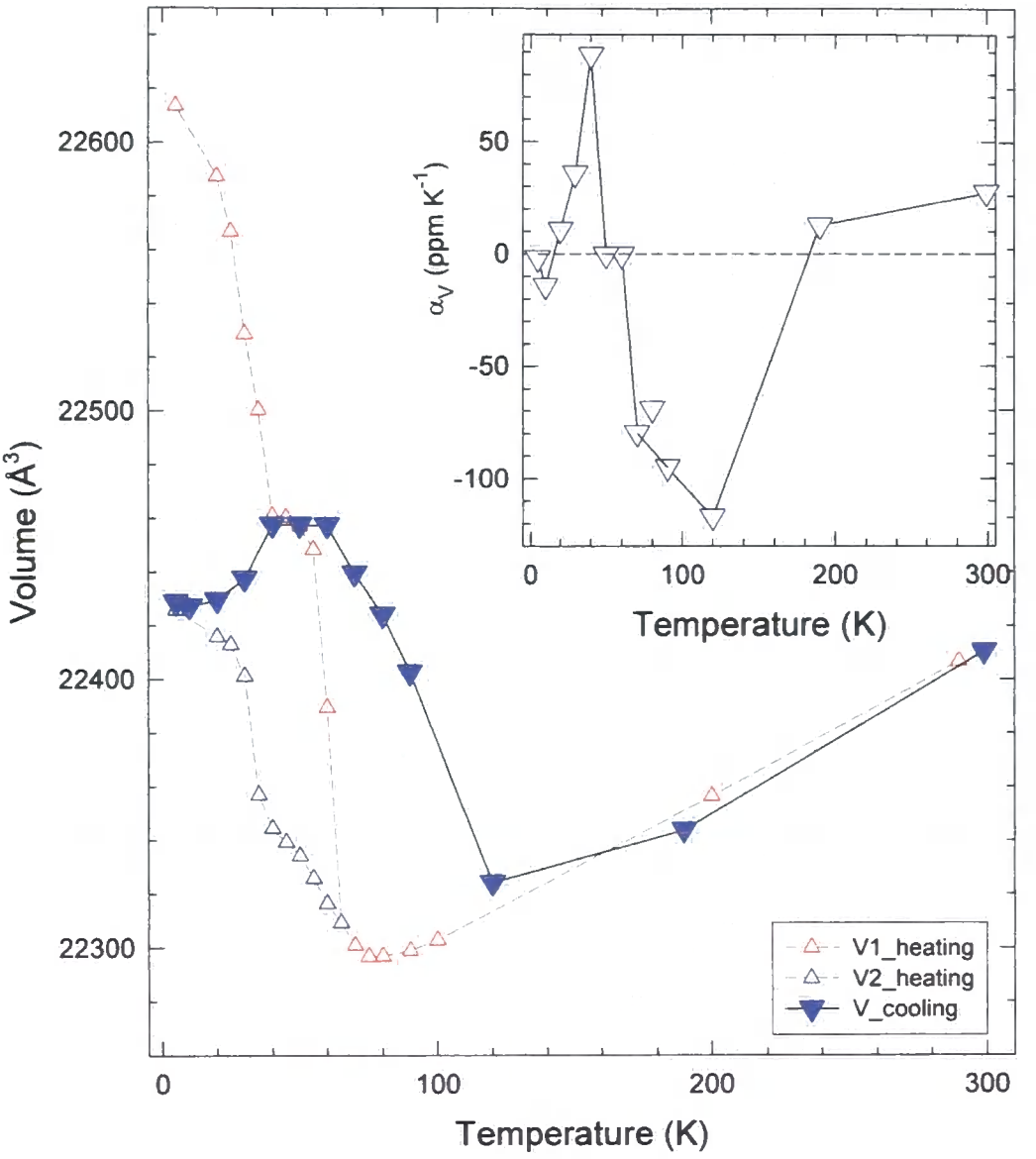

Fig. 4.15. Temperature evolution of the unit cell volume of $(Sm_{2/3}Eu_{1/3})_{2.75}C_{60}$ on cooling (downward blue tringles) and on heating in upward triangles (red for phase 1 and blue for phase 2) [*inset:* the coefficient of thermal expansion, $\alpha_V = d\ln V/dT$].

The refined parameters at 5 K for both warming and cooling measurements are tabulated and compared in Table 4.5.

Table 4.5a. Refined structural parameters for $(Sm_{2/3}Eu_{1/3})_{2.75}C_{60}$ at 5 K obtained from the Rietveld refinement of the synchrotron X-ray diffraction data using slow cooling protocol.

	Site	x/a	y/b	z/c	Occupancy	B(Å²)
Sm(11)	8c	0.1363 (5)	0.1184 (7)	0.3853 (5)	0.629 (1)	2.3 (1)
Sm(12)	8c	0.3853 (5)	0.1358 (4)	0.1184 (7)	0.629 (1)	2.3 (1)
Sm(13)	8c	0.1184 (7)	0.3853 (5)	0.1358 (4)	0.629 (1)	2.3 (1)
Sm(21)	8c	0.1332 (5)	0.3700 (5)	0.3772(6)	0.629 (1)	2.3 (1)
Sm(22)	8c	0.3772(6)	0.1332 (5)	0.3700 (5)	0.629 (1)	2.3 (1)
Sm(23)	8c	0.3700 (5)	0.3772(6)	0.1332 (5)	0.629 (1)	2.3 (1)
Sm(3)	8c	0.376 (2)	0.387 (1)	0.374 (2)	0.629 (1)	2.3 (1)
Sm(4) (vacancy)	8c	0.124(2)	0.113(1)	0.126(2)	0.261 (5)	2.3 (1)
Sm(51)	8c	0.2045 (1)	0.2045 (1)	0.2045 (1)	0.609 (2)	1.8 (2)
Sm(52)	8c	0.0455 (1)	0.0455 (1)	0.2045 (1)	0.609 (2)	1.8 (2)
Sm(53)	8c	0.2045 (1)	0.0455 (1)	0.0455 (1)	0.609 (2)	1.8 (2)
Sm(54)	8c	0.0455 (1)	0.2045 (1)	0.0455 (1)	0.609 (2)	1.8 (2)
Sm(61)	8c	0.2045 (1)	0.304 (2)	0.304 (2)	0.057 (2)	1.8 (2)
Sm(62)	8c	0.0455 (1)	-0.054(2)	0.304 (2)	0.057 (2)	1.8 (2)
Sm(63)	8c	0.304 (2)	-0.054(2)	0.0455 (1)	0.115 (4)	1.8 (2)
Eu(11)	8c	0.1363 (5)	0.1184 (7)	0.3853 (5)	0.314 (1)	2.2 (1)
Eu (12)	8c	0.3853 (5)	0.1358 (4)	0.1184 (7)	0.314 (1)	2.2 (1)
Eu (13)	8c	0.1184 (7)	0.3853 (5)	0.1358 (4)	0.314 (1)	2.2 (1)
Eu (21)	8c	0.1332 (5)	0.3700 (5)	0.3772(6)	0.314 (1)	2.2 (1)
Eu (22)	8c	0.3772(6)	0.1332 (5)	0.3700 (5)	0.314 (1)	2.2 (1)
Eu (23)	8c	0.3700 (5)	0.3772(6)	0.1332 (5)	0.314 (1)	2.2 (1)
Eu (3)	8c	0.376 (2)	0.387 (1)	0.374 (2)	0.314 (1)	2.2 (1)
Eu (4) (vacancy)	8c	0.124(2)	0.113(1)	0.126(2)	0.136 (2)	2.2 (1)
Eu (51)	8c	0.2045 (1)	0.2045 (1)	0.2045 (1)	0.308 (1)	1.8 (2)
Eu (52)	8c	0.0455 (1)	0.0455 (1)	0.2045 (1)	0.308 (1)	1.8 (2)
Eu (53)	8c	0.2045 (1)	0.0455 (1)	0.0455 (1)	0.308 (1)	1.8 (2)
Eu (54)	8c	0.0455 (1)	0.2045 (1)	0.0455 (1)	0.308 (1)	1.8 (2)
Eu (61)	8c	0.2045 (1)	0.304 (2)	0.304 (2)	0.025 (1)	1.8 (2)
Eu (62)	8c	0.0455 (1)	-0.054(2)	0.304 (2)	0.025 (1)	1.8 (2)
Eu (63)	8c	0.304 (2)	-0.054(2)	0.0455 (1)	0.050 (2)	1.8 (2)

Table 4.5b. The extracted results for the lattice dimensions and profile parameters from the diffraction profile of $(Sm_{2/3}Eu_{1/3})_{2.75}C_{60}$ at 5 K both warming up and cooling down measurements.

T= 5 K	Warming up measurements Major phase	Minor phase	Cooling down measurements
Instrumental parameters:			
λ (Å)	0.85045		0. 8010
Δ2θ (×100, °)	0.50 (2)		0.64 (2)
2θ range (°)	3.0 - 30.1		3.0 - 30.1
Step size (°)	0.003		0.003
Lattice parameters:	28.2762 (4)	28.1992 (11)	28.2029 (2)
a (Å)	28.2847 (4)	28.2078 (11)	28.2114 (2)
b (Å)	28.2677 (4)	28.1908 (11)	28.1944 (2)
c (Å)	22608.0 (9)	22424.1 (2.6)	22432.8 (5)
V (Å^3)			
Wt. Fraction:	0.798 (1)	0.209 (2)	- (-)
Peak profile coefficient:	Type 3	Type 3	Type 3
GU	102.3 (8)	138.9 (35)	295.5 (3.8)
GV	-6.26 (10)	-26.0 (5)	-19.5 (4),
GW	0.447 (9)	0.48 (7)	1.30 (3)
Lx, Ly	1.64 (8), 23.5 (9)	2.18 (3), 25.0 (3)	1.84(2), 18.0 (2)
S/L, H/L	0.005, 0.0005	0.005, 0.0005	0.005, 0.0005
L11	-0.12×10^{-2}	0.50×10^{-2}	0.13×10^{-1}
L22	0.33×10^{-2}	0.13×10^{-2}	0.26×10^{-2}
L33	-0.26×10^{-2}	-0.13×10^{-2}	-0.42×10^{-4}
L12	-0.95×10^{-2}	-0.11e-1	-0.88×10^{-2}
L13	-0.19×10^{-2}	-0.14×10^{-2}	-0.40×10^{-3}
L23	0.74×10^{-3}	0.26×10^{-3}	0.76×10^{-3}
Agreement factors: Rwp(%), Rexp(%), χ^2	4.45, 1.65, 7.301		5.35, 2.49, 4.60

4.2.5 Discussion

The synchrotron X-ray powder diffraction technique was employed to characterize the temperature-dependent structural properties of the series of rare-earth-metal intercalated fullerides with stoichiometry, $RE_{2.75}C_{60}$ (RE = Sm, Eu, and Yb). So far, we have shown that, in addition to $Sm_{2.75}C_{60}$ and $Yb_{2.75}C_{60}$, $Eu_{2.75}C_{60}$ and the mixed compositions $(Sm_{1-x}Eu_x)_{2.75}C_{60}$ (x = 2/3, 1/3) display NTE below a certain critical temperature, T_v.

Fig. 4.16 and Table 4.6 compare the results for the present family. The unit cell volume of $(Sm_{1-x}Eu_x)_{2.75}C_{60}$ at room temperature shows an anomalous behaviour; as x increases, the unit cell volume decreases, contrary to what is expected from the lanthanide contraction. This is due to the presence of varying rare-earth mixed valence that leads to deviation from the corresponding lanthanide contraction in the case of trivalent ions. Similar behaviour has been observed in the evolution of the unit cell volume of *RE*CuGa (*RE* = rare-earth) compounds as a function of the rare-earth metal reported by Adroja *et al.* [21], where the unit cell volume of EuCuGa is anomalous; indicating that Eu ions may be in a divalent or mixed valent state.

As described for both $Sm_{2.75}C_{60}$ and $Yb_{2.75}C_{60}$, the NTE behaviour observed at low temperature without change in crystal symmetry for the $(Sm_{1-x}Eu_x)_{2.75}C_{60}$ can also be rationalised along the same line, where the average Eu oxidation state approaches +2 upon cooling below critical temperature.

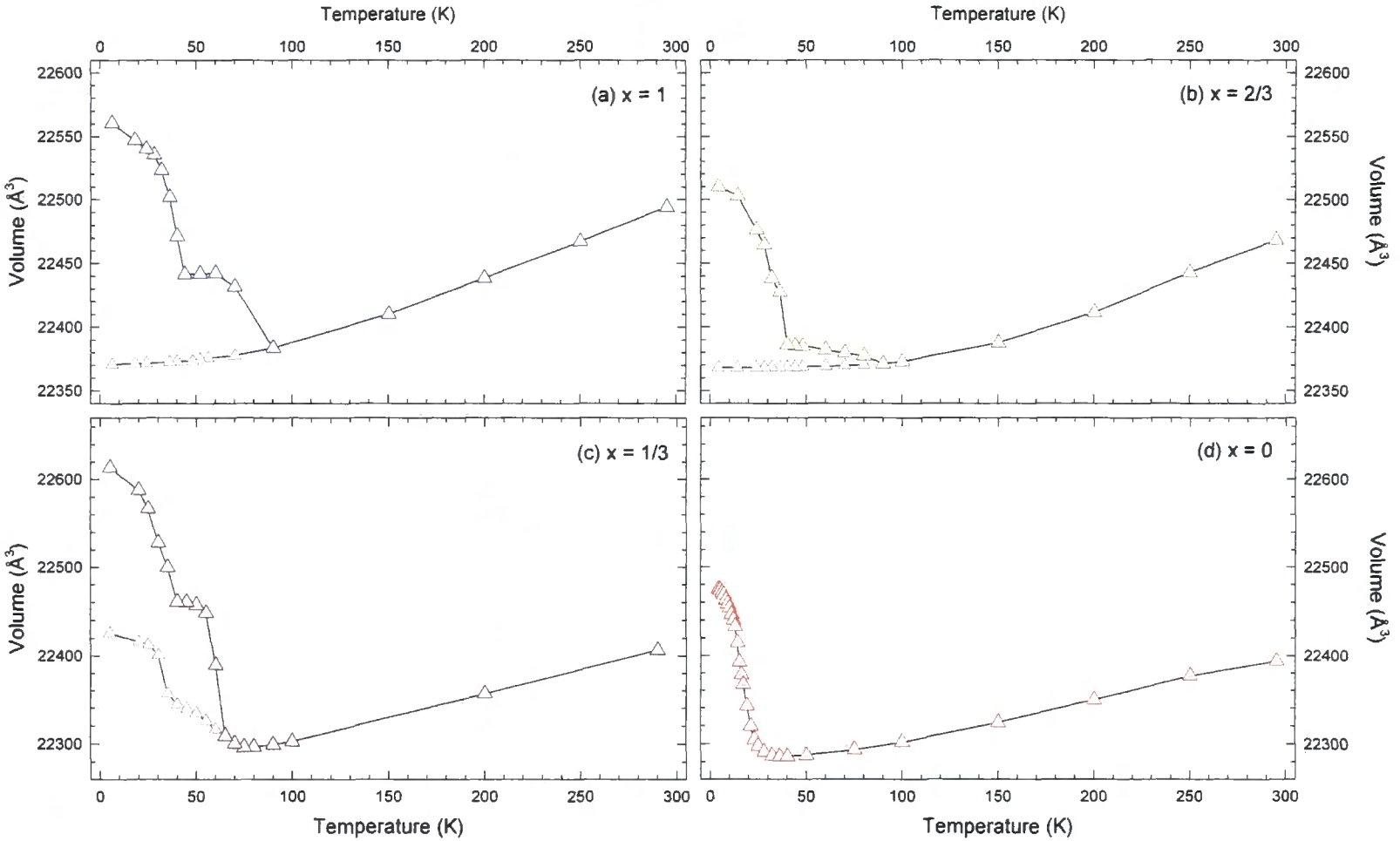

Fig. 4.16. Temperature evolution of the unit cell volume of; a) $Eu_{2.75}C_{60}$ ($x = 1$); b) $(Sm_{1/3}Eu_{2/3})_{2.75}C_{60}$ ($x = 2/3$); (continued)

Fig. 4.16. (continued) c) $(Sm_{2/3}Eu_{1/3})_{2.75}C_{60}$ (x = 1/3) and d) $Sm_{2.75}C_{60}$ (x = 0) obtained on heating from 5 K to room temperature. Second phases for each compound are shown as grey triangles.

Table 4.6. The extracted values of the unit cell volume at room temperature and 5 K and characteristic critical temperatures for each rare-earth fulleride.

Sample	Volume_RT (Å^3)	Volume_5 K (Å^3)	T_v (K)
$Eu_{2.75}C_{60}$	22494.3 (5)	22565.9 (5)	90
$(Sm_{1/3}Eu_{2/3})_{2.75}C_{60}$	22468.3 (5)	22510.0 (5)	90
$(Sm_{2/3}Eu_{1/3})_{2.75}C_{60}$	22410.4 (5)	22608.0 (9)	75
$Sm_{2.75}C_{60}$	22395.0 (5)	22474.9 (5)	36
$Yb_{2.75}C_{60}$	21655.0 (6)	21806.0 (8)	60

The average Eu valence at high temperature is ~+2.2, where the 4f electrons of Eu are thermally excited into the t_{1u} band of C_{60} which becomes fully occupied with 6 electrons [17]. We recall here that the two interstitial holes have radii of 1.12 Å (smaller T_d site) and 2.06 Å (larger O_h site), and thus the ionic radius of the cation occupying the T_d site plays an important role in defining the unit cell size of the fullerides. The ionic radius of RE^{2+} and RE^{3+} (RE = Sm, Eu, and Yb) for the case of six coordination are given in Table 4.7.

Table 4.7. The ionic radii of RE^{2+} and RE^{3+} (RE = Sm, Eu, and Yb) for the case of six-fold coordination [22].

Ion	radius (Å)	Ion	radius (Å)
Sm^{2+}	1.41	Sm^{3+}	1.10
Eu^{2+}	1.31	Eu^{3+}	1.09
Yb^{2+}	1.16	Yb^{3+}	1.01

It is also clear from the figure above that the lattice parameters of Eu-doped C_{60} are larger compared to those of $Sm_{2.75}C_{60}$ at all temperatures. Such behaviour most likely reflects the fact that the Eu^{2+} state should be highly preferred to the Eu^{3+} state [23], thus resulting in larger unit cell volume at all temperatures. The fact that the divalent state of Eu ion is more stable implies that the energy difference between the divalent and trivalent state is negative and larger, in absolute value, than those for Sm and Yb ions [24]. Thus, it is expected that more thermal energy is required for the temperature-induced valence transition to occur and this results in the $(Sm_{1-x}Eu_x)_{2.75}C_{60}$ compounds having higher critical temperatures, T_v.

The data presented here also show apparent phase separation observed below the characteristic critical temperature. As seen in Fig. 4.16a and b, the majority phases of the Eu-rich compositions (x = 1, 2/3) experience NTE, while the minority phases contract on cooling. On the other hand, both majority and minority phases for Sm-rich composition (x = 1/3) experience NTE on cooling (Fig. 4.16c), while no phase separation was observed for the $Sm_{2.75}C_{60}$ case. Such behaviour can be explained by the existence of local structural inhomogeneities accompanying the abrupt transformations of the materials. For Eu-rich compounds below 90 K, phase separation seems to occur into Eu^{2+}-rich and Eu^{3+}-rich phases with the Eu^{2+}-rich phase undergoing NTE behaviour and the Eu^{3+}-rich phase contracting with no anomalous lattice responses. For the case of the Sm-rich compound below 75 K, phase separation occurs into Eu^{2+}-rich and Sm^{2+}-rich phases with both of them experiencing NTE.

Another notable feature of the temperature dependence of the diffraction data collected on $(Sm_{2/3}Eu_{1/3})_{2.75}C_{60}$ is the hysteretic behaviour

observed on heating and cooling experiments. The onset temperature of the NTE extracted from slow cooling measurements is seen at around 120 K (Fig. 4.14), which is substantially higher than that in heating measurements (~75 K). The lattice dimension expands below 120 K which continues down to 60 K, and the rate of expansion becomes zero at 40 K. Surprisingly, the unit cell volume extracted in this temperature region where ZTE is observed on cooling is identical to that obtained on heating. Then, the sign of the thermal expansivity changes to positive below 40 K and the volume contracts on further cooling. The driving force of this intriguing lattice response observed for this compound is unknown. However, it can be conjectured that the nature of the NTE is hugely affected by not only the nature of the rare-earth dopants, but also by the rate of change in temperature. It would be interesting to explore what will happen to the temperature evolution of the unit cell volume on re-heating the same material for a third time.

Finally, it should also be mentioned that the unit cell volume extracted for $(Sm_{2/3}Eu_{1/3})_{2.75}C_{60}$ at 5 K is the largest among the $(Sm_{1-x}Eu_x)_{2.75}C_{60}$ systems (Table 4.6). This is most likely due to the fact that obtaining single-phase material becomes more difficult as the content of Eu increases, as the probability of getting more Eu carbide by-products also increases. Existence of impurity phases are thought to be preventing further lattice expansion at low temperature region, which are also apparent in the low field magnetisation measurements where $(Sm_{2/3}Eu_{1/3})_{2.75}C_{60}$ shows steepest increase in magnetisation in the low temperature region (Fig. 4.3c).

4.3 Pressure-induced valence transitions

The temperature-dependent quasi-continuous valence change accompanied by large NTE behaviour below the characteristic critical temperature, T_v, at ambient pressure was observed in $RE_{2.75}C_{60}$ (RE = Sm, Eu, Yb, and Sm-Eu-mixture). Soon after, the study of compression behaviour of $Sm_{2.75}C_{60}$ and $Yb_{2.75}C_{60}$ in the pressure range 1 atm - 6.50 GPa also revealed an abrupt hysteretic phase transition, resulting in a sudden volume collapse above the transition pressure, P_v. Here, I present the results from synchrotron X-ray powder diffraction measurements at ambient temperature and elevated pressures on $Eu_{2.75}C_{60}$ and $(Sm_{2/3}Eu_{1/3})_{2.75}C_{60}$ in the pressure range 0 - 8.55 GPa.

4.3.1 Experimental Details

The high-pressure X-ray powder diffraction measurements on $Eu_{2.75}C_{60}$ and $(Sm_{2/3}Eu_{1/3})_{2.75}C_{60}$ at ambient temperature were performed at various pressures on the ID09 beamlines at ESRF, Grenoble. The samples used here were taken from the same batches as those used in the temperature-dependent experiments. The powder samples were loaded into a DAC cell (600 × 600 μm^2 diameter faces) with a stainless steel gasket indented to 80 μm with a 250 μm diameter hole inside the glove-box as they are sensitive to air and moisture. The two small rubies, which are used as probes for the measurement of the pressure, were loaded together with the sample powder. Pressure inside the DAC was increased, using helium gas as a pressure medium, at room temperature and accurate values of pressure were

measured by the ruby fluorescence method.

Two-dimensional diffraction patterns (λ = 0. 4174 Å) were collected using an image plate detector with typical exposure time of 15 min. The diffraction profiles for $Eu_{2.75}C_{60}$ and $(Sm_{2/3}Eu_{1/3})_{2.75}C_{60}$ were collected with increasing pressure, starting from ambient pressure, up to a maximum pressure of 7.28 GPa and 8.55 GPa, respectively. After the pressure reached its maximum, it was then gradually released, but in both cases, the diffraction data could only be collected down to ~3.50 GPa. The two-dimensional diffraction images were integrated with local ESRF FIT2D software, after careful masking of single crystal ruby peaks. The data analysis was performed with the LeBail pattern decomposition technique within the GSAS program.

4.3.2 Pressure Evolution

i) $Eu_{2.75}C_{60}$

The structural analysis of the synchrotron X-ray diffraction patterns of $Eu_{2.75}C_{60}$ collected at ambient pressure has been discussed in detail in the previous section (Table 4.3). Rietveld analysis was performed with an orthorhombic superstructure (space group *Pcab*) with the Eu cations occupying off-centred T_d and O_h interstitial sites. One out of every eight T_d sites is partially occupied (~11%) and long-range ordering of these T_d defects results in a unit cell with dimensions twice as large as those of the commonly encountered *fcc* alkali fulleride structures (Fig. 4.17).

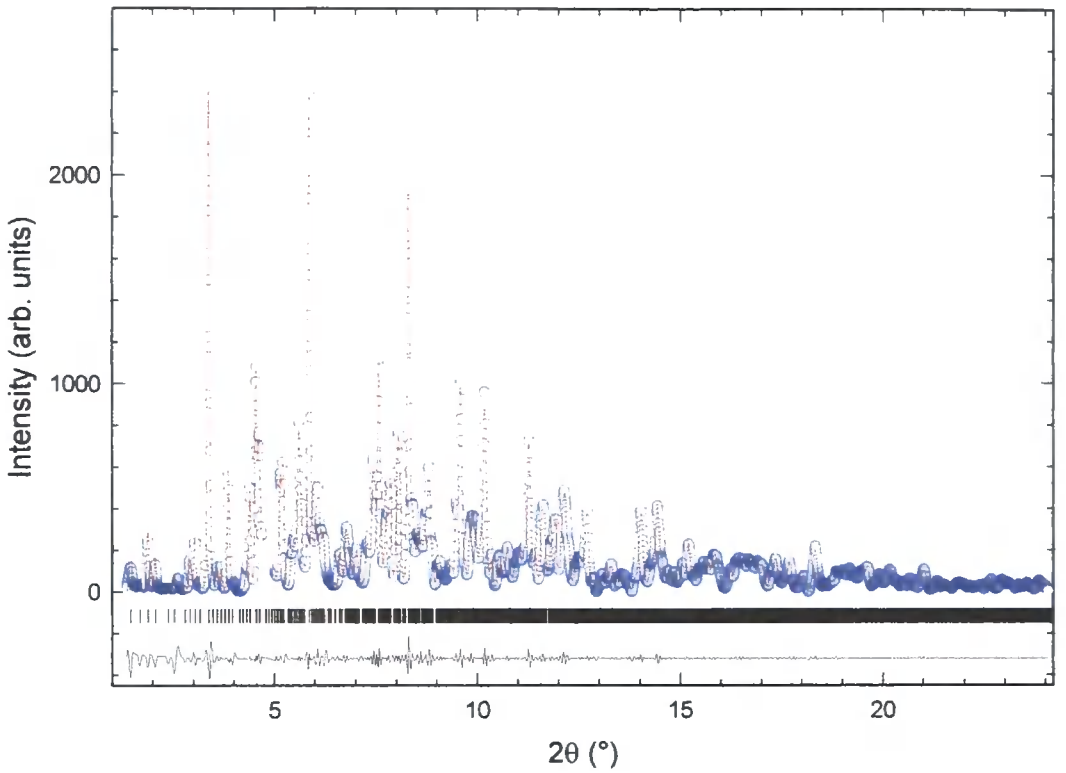

Fig. 4.17. Synchrotron X-ray powder diffraction profile of $Eu_{2.75}C_{60}$ at ambient pressure (P = 1 atm) and temperature (T = 295 K) collected on the ID09 beamline (λ = 0. 4174 Å). Open circles are the experimental data, red line is the calculated pattern, bars represent the Bragg reflections corresponding to the orthorhombic space group *Pcab*, and the black solid line at the bottom is the difference profile. Some impurity peaks were removed in the course of the refinement.

However, as in the case of $Sm_{2.75}C_{60}$ and $Yb_{2.75}C_{60}$, the quality of diffraction data at high pressure obtained on ID09 is not high enough to allow detailed Rietveld refinements for this complex structural model. For this reason, extraction of the lattice constants was carried out by the LeBail pattern decomposition technique at all pressures. The fitted parameters are collected in Table 4.8. The diffraction profiles were then collected as pressure gradually increased in small steps, while the values of the pressure were recorded before and after each measurement.

Table 4.8. Details of the instrumental and lattice parameters derived by the LeBail refinement of the diffraction data of $Eu_{2.75}C_{60}$ at 295 K and 1 atm.

Temperature: 295 K	Pressure: 1 atm
Instrumental parameters:	
λ (Å)	0. 4174
Δ2θ (×100, °)	-1.05 (6)
2θ range (°)	1.3 - 24.1
Step size (°)	0.007
Lattice parameters:	
a (Å)	28.2300 (6)
b (Å)	28.2860 (6)
c (Å)	28.1740 (6)
V (Å^3)	22497.4 (1.4)
Peak profile coefficient:	Type 3
GU	24.0 (3)
GV	-4.30 (2)
GW	0.55 (3)
Lx, Ly	1.05 (2), 11.3 (2)
S/L, H/L	0.005, 0.0005
Agreement factors:	
Rwp(%), Rexp(%), χ^2	2.91, 2.58, 1.273

Selected diffraction patterns obtained for $Eu_{2.75}C_{60}$ during increasing and releasing pressure are shown in Fig. 4.18. Inspection of these profiles indicates that there is an excellent correspondence of the reflection intensities in the diffraction profiles at elevated pressures below 4.80 GPa with those at ambient pressure. As pressure was increased towards 4.80 GPa, the peaks shifts to higher angles monotonically; however, above 4.80 GPa, the peaks abruptly shift to higher angle, implying the occurrence of a phase transformation to a structure with drastically reduced lattice parameters. This trend continues up to 5.30 GPa where the transformation is complete and the peaks shift to higher angles as before with further increase in pressure (Fig. 4.17a). This anomalous lattice collapse is also accompanied by a change in the optical properties of the black crystalline $Eu_{2.75}C_{60}$ powder

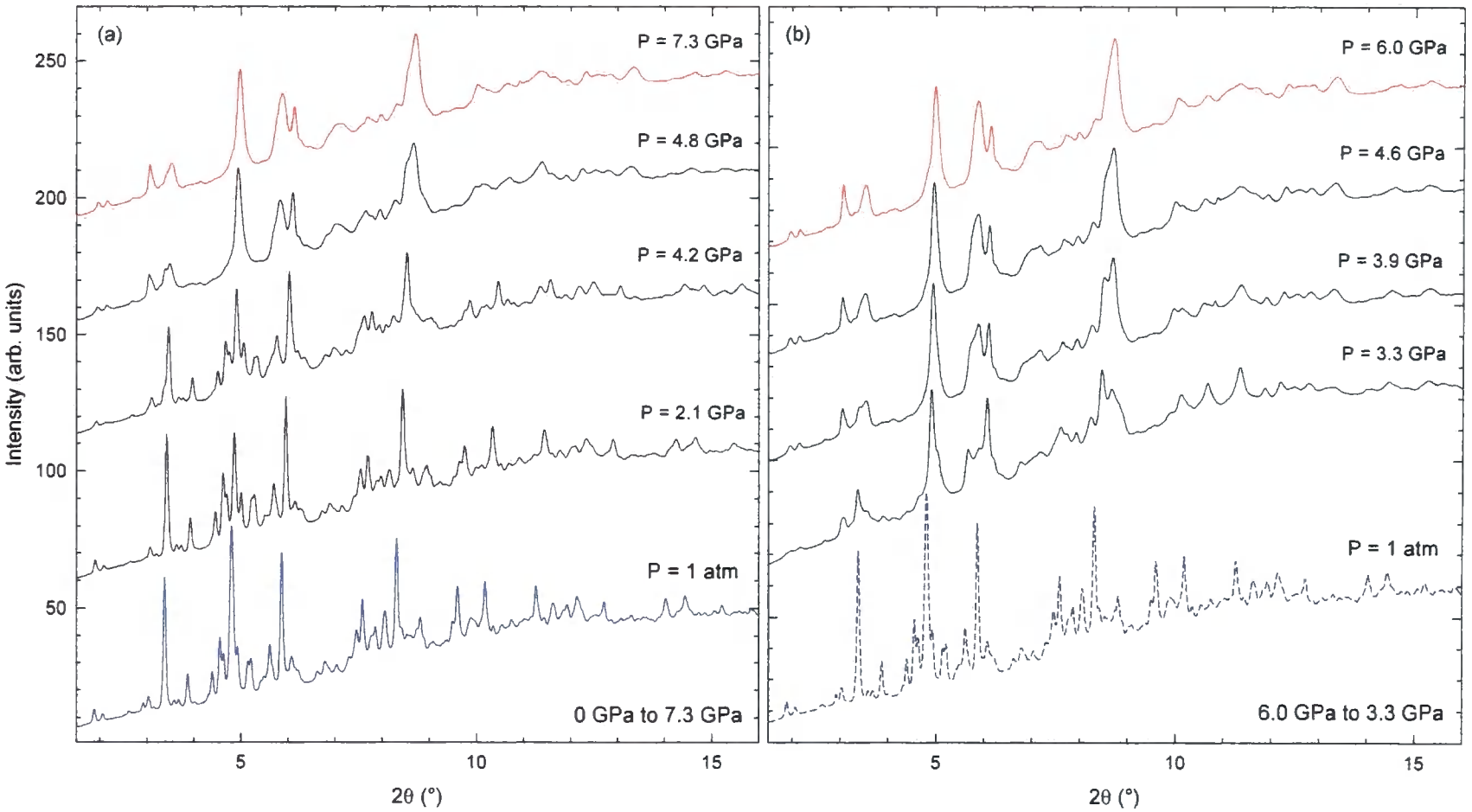

Fig. 4.18. Pressure evolution of the X-ray diffraction profiles of $Eu_{2.75}C_{60}$ ($\lambda = 0.4174$ Å) at room temperature (a) with increasing pressure from 1 atm to 7.3 GPa and (b) with releasing pressure from 6.0 to 3.3 GPa.

which acquires a golden colour, signifying a pressure-induced insulator-to-metal transition.

After the pressure reaches 7.28 GPa, it is slowly released and the diffraction data were collected down to 3.37 GPa. On examination of the diffraction data, it was revealed that the peaks shift slowly to lower angles and a gradual change in the peak shape towards that of the original low-pressure phase occurs. This suggests that the phase transformation is both reversible and characterised by a large hysteretic behaviour as the original low-pressure phase does not fully recover even though the pressure is well below 4.80 GPa (Fig. 4.18b). The reverse phase change is also accompanied by a recovery of the black colour of the material.

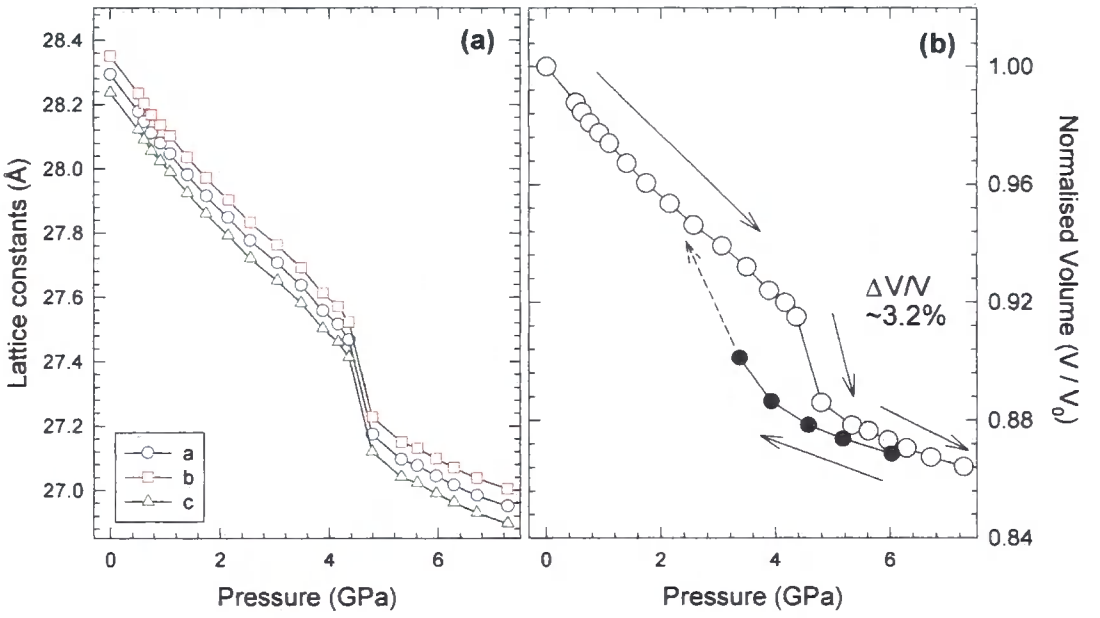

Fig. 4.19. Pressure evolution of (a) the orthorhombic lattice constants (circles: a, squares: b, triangles: c) and (b) the normalised unit cell volume in $Eu_{2.75}C_{60}$. Open symbols represent data obtained on increasing pressure, while full symbols represents data obtained on releasing pressure.

The extracted evolution of the orthorhombic lattice parameters and unit cell volume with pressure are shown in Fig. 4.19. As pressure is increased above 4.80 GPa, an abrupt decrease in the lattice dimensions is observed. As the sample pressurised between 1 atm and 4.40 GPa, the lattice dimension contracts at almost constant rate with the calculated volume compressibility, $\kappa = -d\ln V/dP = 0.022(2)$ GPa^{-1}.

The sudden decrease in lattice dimension observed at 4.80 GPa results in a collapse of the unit cell volume, $\Delta V/V \sim 3.2\%$. The lattice contraction continues on further increase in pressure with a substantially smaller value for the volume compressibility, $\kappa = -d\ln V/dP = 0.007(3)$ GPa^{-1}. After pressure release at 7.28 GPa, the volume of the high-pressure phase slowly expands in the pressure range 7.28 to 3.37 GPa.

ii) $(Sm_{2/3}Eu_{1/3})_{2.75}C_{60}$

Investigation of the sensitivity of the $(Sm_{2/3}Eu_{1/3})_{2.75}C_{60}$ structure to the application of pressure and the structure analysis was carried out in the same manner as in the case of $Eu_{2.75}C_{60}$. The synchrotron X-ray powder diffraction profiles for pressures between 1 atm and 8.65 GPa at ambient temperature were collected on the ID09 beamline at the ESRF (see §4.3.1 for experimental description).

Extraction of the lattice constants was again carried out by the LeBail method at all pressures. The results of the LeBail pattern decomposition technique at 1 atm is presented in Fig. 4.20 and the fitted parameters are collected in Table 4.9. The values of the lattice parameters at 295 K and 1 atm are: a = 28.1953(5) Å, b = 28.2319(5) Å, c = 28.1558(5) Å, V = 22414.5(1.3)

Å^3, and agreement factors $\chi^2 = 1.02$, $R_{wp} = 7.22\%$, $R_{exp} = 7.15\%$. These values are comparable to the results obtained by ultra-high resolution synchrotron X-ray diffraction on ID31.

Selected diffraction profiles obtained on increasing P between 1 atm and 8.65 GPa (Fig. 4.21a) and on releasing pressure down to 3.76 GPa are shown in Fig. 4.21b. As seen in these figures, the diffraction profiles show an excellent correspondence with those obtained for $Eu_{2.75}C_{60}$. Upon reaching a pressure of 4.79 GPa, a sudden change in the reflection intensities is observed, implying a phase transformation sets in to a structure accompanied by drastic reduction in lattice parameters. This trend continues up to 6.00 GPa where the transformation is complete and the peak continues to shift to higher angles with further increase in pressure (Fig. 4.21a). After the pressure reaches 8.65 GPa, it was slowly released and the diffraction data were collected down to 3.75 GPa. Upon releasing, the peaks shift slowly towards lower angles and showed sign of a reverse phase transformation at 3.75 GPa. This implies that the phase transformation is both reversible and characterised by a large hysteretic behaviour as the original low-pressure phase does not fully recover even though P is well below 4.80 GPa (Fig. 4.21b).

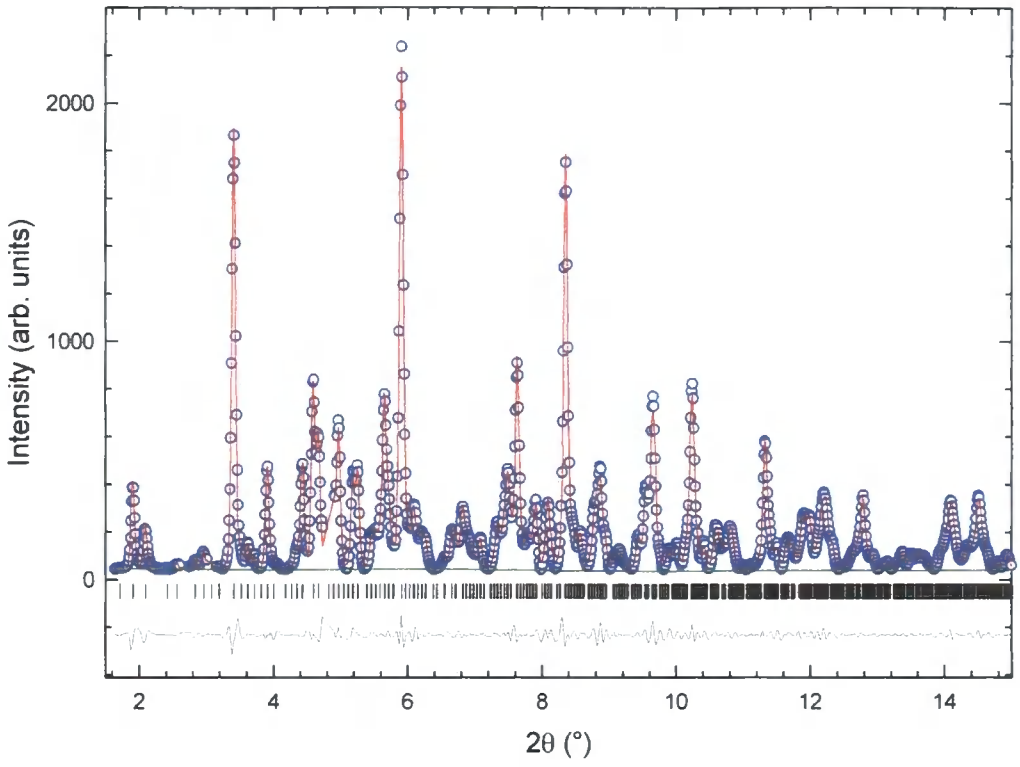

Fig. 4.20. Synchrotron X-ray powder diffraction profile of $(Sm_{2/3}Eu_{1/3})_{2.75}C_{60}$ (P= 1 atm, T = 295 K) collected on ID09 (λ = 0. 4174 Å). Open circles are the experimental data, red line is the calculated pattern, bars represent the Bragg reflections, and the black solid line is the difference profile.

Table 4.9. Details of the instrumental and lattice parameters derived by the LeBail refinement of $(Sm_{2/3}Eu_{1/3})_{2.75}C_{60}$ at 1 atm.

Instrumental Parameters:		Lattice parameters:	
λ (Å)	0.4174	a (Å)	28.1953 (5)
Δ2θ(×100) (°)	0.64 (3)	b (Å)	28.2319 (5)
2θ range (°)	1.64-15.06	c (Å)	28.1558 (5)
Excluded region (%)	3.33	Volume (Å^3)	22414.5 (1.3)
Agreement factors:		profile coefficient:	
R_{wp} (%)	7.22	GU, GV	15.0(7), -5.7(8)
R_{exp} (%)	7.15	GW	0.66 (5)
χ^2	1.02	Lx, Ly	1.12(2),11.4(3)
		S/L, H/L	0.005, 0.0005

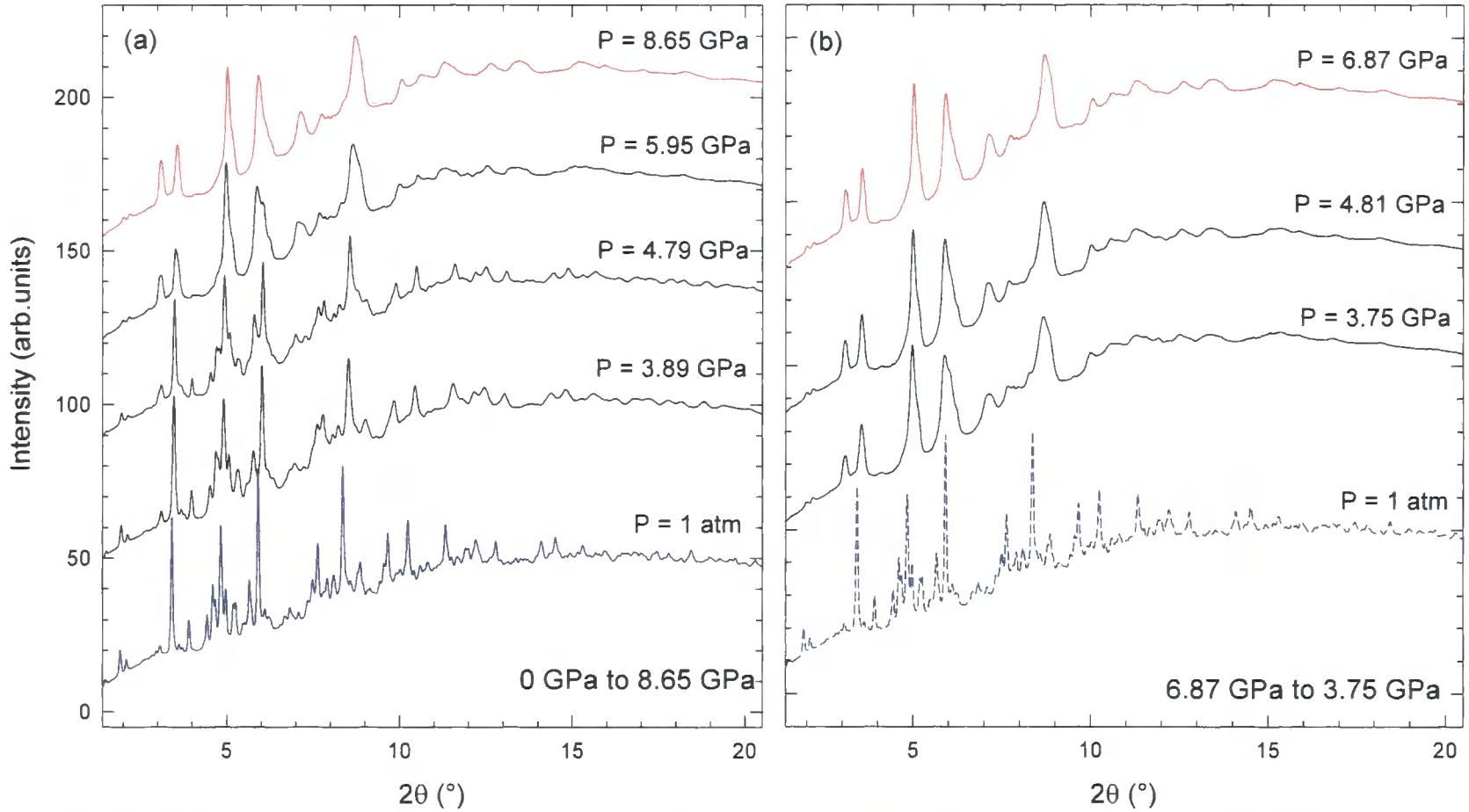

Fig. 4.21. Pressure evolution of the X-ray diffraction profiles of $(Sm_{2/3}Eu_{1/3})_{2.75}C_{60}$ (λ = 0.4174 Å) at room temperature (a) with increasing pressure from 1 atm to 8.65 GPa and (b) with releasing pressure from 8.65 to 3.76 GPa.

The extracted evolution of the orthorhombic lattice parameters and unit cell volume with pressure is shown in Fig. 4.22. As the sample is pressurised from 1 atm to 4.53 GPa, the lattice dimensions contract continuously at a constant rate with an average volume compressibility of $\kappa = 0.017(2)$ GPa^{-1} until it reaches the critical pressure, P_V of ~4.5 GPa.

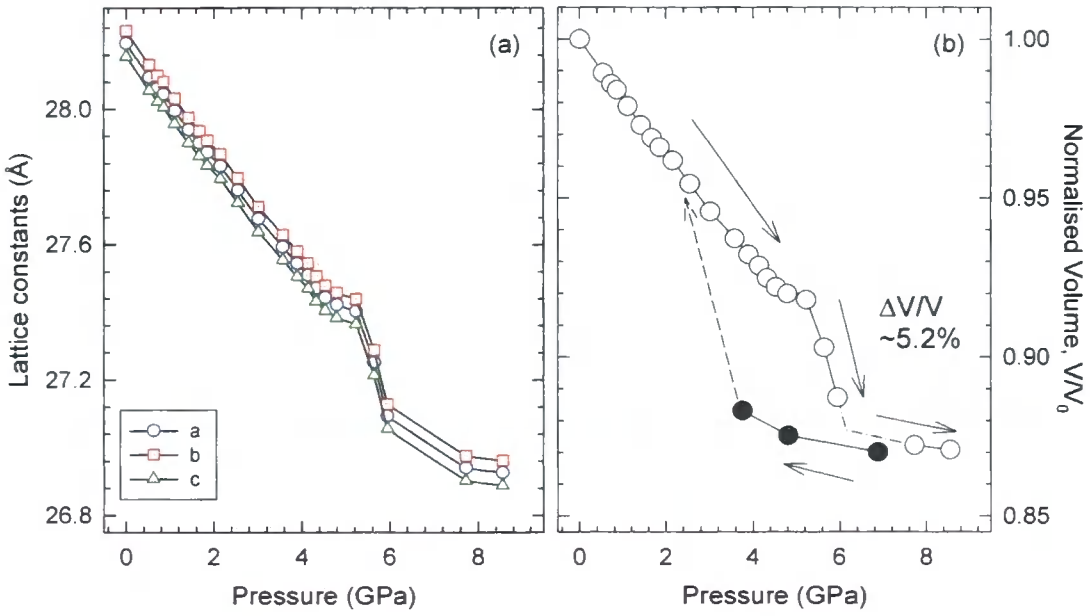

Fig. 4.22. Pressure evolution of (a) the orthorhombic lattice constants (circles: a, squares: b, triangles: c) and (b) the normalised unit cell volume in $(Sm_{2/3}Eu_{1/3})_{2.75}C_{60}$. Open symbols represent data obtained on increasing pressure, while full symbols represent data obtained on releasing pressure.

Above this critical pressure, the large lattice collapse occurs resulting in an abrupt decrease in unit cell volume of $\Delta V/V \sim 5.2\%$ and the phase transformation is complete at ~6.0 GPa. This high-pressure phase continues to contract with further increase in P up to 8.65 GPa, resulting in a considerably smaller value for the linear volume compressibility, $\kappa = -d\ln V/dP = 0.006(2)$ GPa^{-1}. After pressure release, the high-pressure phase

expands initially with a similar value of the compressibility, $\kappa \sim 0.007$ GPa^{-1}, then the compressibility become almost twice as large below 4.80 GPa giving value of $\kappa \sim 0.015$ GPa^{-1} at 3.75 GPa.

4.3.3 Discussion

In the previous chapter we interpreted the abrupt phase transformation of $Yb_{2.75}C_{60}$ above a critical pressure at ambient temperature as a discontinuous valence change of Yb from ~+2.3 towards +3 state. A similar phenomenology is observed in the high-pressure experiments of both $Eu_{2.75}C_{60}$ and $(Sm_{2/3}Eu_{1/3})_{2.75}C_{60}$ and it can be also rationalised along the same lines, namely pressure-induced valence transitions of Eu and Sm from +2.3 state to nearly +3 resulting in a collapse of the unit cell metrics. The obtained results from each of the high pressure experiments on the samples $RE_{2.75}C_{60}$ (RE = Sm, Eu, and Yb) are collected in Table 4.10.

Table 4.10. The extracted values of the unit cell volume at ambient pressure and temperature, critical pressure, and the change in the volume during the phase transitions.

Sample	Volume_0 GPa (Å^3)	P_V (GPa)	$\Delta V/V$(%)
$Eu_{2.75}C_{60}$	22497.4(1.4)	4.40	3.2
$(Eu_{1/3}Sm_{2/3})_{2.75}C_{60}$	22414.5(1.3)	4.53	5.1
$Sm_{2.75}C_{60}$	22395.0(5)	3.95	6.0
$Yb_{2.75}C_{60}$	21711.0(1.1)	4.30	2.1

From Table 4.10 it is clear that Eu and Yb substitution for Sm in $Sm_{2.75}C_{60}$ affects the behaviour of the pressure-induced lattice collapse. For instance, substitution of Eu and Yb results in substantial increase in the

transition pressure and decrease in the percentage of lattice collapse during the transition. In order to explain this, we recall the similar behaviour observed on Eu and Yb substitution in SmS compounds under high pressure [18]. The results from the studies of Eu and Yb substituted SmS compounds under high pressure are tabulated in Table 4.11.

Table 4.11. The data presented in the report by Jayaraman *et al.* [18].

Sample	a (Å)	P_V (kbar)	$4f$ -$5d$ gap (eV)
SmS	5.97	6.5	0.1
$Sm_{0.75}Eu_{0.25}S$	5.97	15	0.18
EuS	5.96	continuous	1.64
YbS	5.68	continuous	1.0

It has been suggested that the $4f$-$5d$ energy gap controls the onset of the first-order transition, which is triggered when the $4f$-$5d$ gap approaches zero. Therefore, the valence transition of the rare-earth metal requires higher pressure for systems in which larger $4f$-$5d$ energy gaps are present. Thus, consistent with the picture for RES (RE = Sm, Eu, Yb), the Eu and Yb substitution for Sm in $Sm_{2.75}C_{60}$ results in substantial increase in the critical pressure due to larger $4f$-$5d$ energy gap observed for both Eu and Yb rare-earth metals.

4.4 Conclusion

Synchrotron X-ray powder diffraction measurements have been used to investigate both the temperature and pressure evolution of the structural properties of mixed-valence rare-earth fullerides, $(Sm_{1-x}Eu_x)_{2.75}C_{60}$. The

diffraction data obtained from temperature-dependent studies reveal that the onset of anomalous lattice expansion (NTE) at low temperatures associated with temperature-induced $RE^{3+} \rightarrow RE^{2+}$ valence transitions of the rare-earth metals. The characteristic temperature, T_v, where NTE sets in can be tuned by changing the concentration of the Eu-substituent (T_v = 32 K for x = 0, 75 K for x = 1/3, and 90 K for x = 2/3, 1).

The pressure-dependent studies have shown that the rare-earth valence states are also found to be fragile upon compression. The diffraction data reveal that the lattice metrics experiences abrupt collapse associated with pressure-induced first-order (reversible) $RE^{2+} \rightarrow RE^{3+}$ valence transition above critical pressure, P_V. Upon introducing Eu as a substituent for $Sm_{2.75}C_{60}$ resulted in an increase of the critical pressure from ~3.95 GPa to ~4.50 GPa.

In both cases, the transformations are closely related to the electronic structure of the intercalated rare-earth metal that plays an important role in controlling both the temperature-induced electron transfer between the $4f$ sublattice and the t_{1u} band of C_{60} and the pressure-induced electron transfer between the $4f$ and $5d$ bands of the rare-earth ions.

4.5 References

[1] Ginwalla, A. S., Balch, A. L., Kauzlarich, S. M., Irons, S. H., Klavins, P., Shelton, R. N., *Chem. Mater.* **9**, 278 (1997).

[2] Cao, X. W., Hao, J. M., Wu, X. S., Wang, Y. F., Wu, Y., Liu, J. J., Hu, S. F.,

Lan, G. X., *Appl. Phys. A* **70**, 223 (2000).

[3] Özdas, E., Kortan, A. R., Kopylov, N., Ramirez, A. P., Siegrist, T., Rabe, K. M., Bair, H. E., Schuppler, S., Citrin, P. H., *Nature* **375**, 126 (1995).

[4] Chen, X. H., Roth, G., *Phys. Rev. B* **52**, 15534 (1995).

[5] Chen, X. H., Liu, Z. S., Li, S. Y., Chi, D. H., Iwasa, Y., *Phys. Rev. B* **60**, 6183 (1999).

[6] Krari, Y., Claves, D., Chouteau, G., Touzain, Ph., Jeandey, C., Oddou, J. L., Stepanov, A., *J. Phys. Chem. Solids* **58**, 1771 (1997).

[7] Rabe, K. M., Citrin, P. H., *Phys. Rev. B* **58**, R551 (1998).

[8] Takeuchi, J., Tanigaki, K., Gogia, B., In *Nanonetwork Materials*; AIP conference proceedings **590**, 361 (2001).

[9] Akada, M., Hirai, T., Takeuchi, J., Yamamoto, T., Kumashiro, R., Tanigaki, K., *Phys. Rev. B* **73**, 094509 (2006).

[10] Margiolaki, I., Margadonna, S., Prassides, K., Hansen, T., Ishii, K., Suematsu, H., *J. Am. Chem. Soc.* **124**, 11288 (2002).

[11] Ishii, K., Fujiwara, A., Suematsu, H., Kubozono, Y., *Phys. Rev. B* **65**, 134431 (2002).

[12] Arvanitidis, J., Papagelis, K., Margadonna, S., Prassides, K., Fitch, A. N., *Nature* **425**, 599 (2003).

[13] Margadonna, S., Arvanitidis, J., Papagelis, K., Prassides, K., *Chem. Mater.* **17**, 4474 (2005).

[14] Arvanitidis, J., Papagelis, K., Margadonna, S., Prassides, K., *Dalton Trans.* 3144 (2004).

[15] Claves, D., Krari, Y., Chouteau, G., Touzain, Ph., *Solid State Commun.* **106**, 431 (1998).

[16] Wang, X. X., Li, H. N., Xu, Y. B., *Solid State Commun.* **147**, 436 (2008).

[17] Vértes, A., Klencsár, Z., Kuzmann, E., Forró, L., Oszlányi, G., Pekker, S., *J. Phys. Chem. Solids* **61**, 2013 (2000).

[18] Jayaraman, A., Maines, R. G., *Phys. Rev. B* **19**, 4154 (1979).

[19] Paparoditis, C., Suryanarayanan, R., Llinares, C., Moteil, E., Bordure, G., *Solid State Commun.* **9**, 1871 (1971).

[20] Margadonna, S., Aslanis, E., Li, W. Z., Prassides, K., *Chem. Mater.* **12**, 2736 (2000).

[21] Adroja, D. T., Malik, S. K., Padalia, B. D., Bhatia, S. N., Walia, R., Vijayaraghavan, R., *Phys. Rev. B* **42**, 2700 (1990).

[22] Shannon, R.D., *Acta Crystallogr. Sect. A*, **32**, 751 (1976).

[23] Claves, D., Touzain, Ph., *Synth. Met.* **80**, 301 (1996).

[24] Strange, P., Svane, A., Temmerman, W. M., Szotek, Z., Winter, H., *Nature* **399**, 756 (1999).

CHAPTER 5

Mixed Valence transitions: Samarium and Calcium co-intercalated Fullerides

5.1 Introduction

As it has been already mentioned, systematic studies on rare-earth fullerides have been limited because of the difficulties in preparation of high-quality single-phase materials. For instance, the early reports on superconductivity with T_c = 8 K for $Sm_{2.75}C_{60}$ [1] have proven to be erroneous [2]. Thus, a main challenge during my project was to establish reliable and reproducible synthetic protocols for synthesizing single-phase rare-earth fulleride materials to allow systematic studies of their structural and electronic properties.

The synthesis of single-phase rare-earth fullerides with stoichiometry $RE_{2.75}C_{60}$ (RE = Sm, Eu, Yb) has been successfully established after intensive effort of various members of Prof. Prassides' group (as described in this thesis). This led to the discovery of mixed valence phenomena associated with the rare-earth valency, which displayed a remarkable sensitivity to external stimuli and resulted in the observation of a variety of temperature- and pressure-induced abrupt or continuous valence transitions [2-4]. The observed anomalous responses were interpreted in terms of electronically driven valence changes caused by electron transfer between the electronically active narrow C_{60} t_{1u} band and the rare-earth 4f and/or 5d bands.

In extending further our systematic studies of the valence change in the rare-earth fullerides, we also took an approach analogous to that followed in binary chalcogenides such as SmS. Systematic investigations of the valence change in SmS solid solutions ($Sm_{1-x}M_xS$) were carried out by Jayaraman *et al.* who explored the effect of Eu, Yb and Ca substitution for Sm in tuning the

pressure-induced valence changes [5]. The studies of the valence transition in the rare-earth fulleride family were initiated with the $Sm_{2.75}C_{60}$ composition by synchrotron X-ray diffraction, where both temperature-induced and pressure-induced valence transitions were described. We then established similar transitions for Yb- and Eu- substituted compounds. The transitions are accompanied by abrupt NTE below a critical temperature, T_v (32 K for Sm, 60 K for Yb, 90 K for Eu) and a lattice collapse above a critical pressure, P_v (3.95 GPa for Sm, 4.30 GPa for Yb, 4.40 GPa for Eu).

In this chapter, I will present continuation studies on the Sm valence transition using Ca- substituted compounds of stoichiometry $(Sm_{1-x}Ca_x)_{2.75}C_{60}$ for values of x ranging between 1 and 0. We note that the ionic radius of Ca^{2+} is significantly smaller than that of Sm^{2+} and more importantly, unlike the rare-earth metals, Ca has no electronically active $4f$ sublattice. Thus, the effect of Ca substitution for Sm may trigger substantially different response compared to that of Yb and Eu substitution already described in the previous chapters.

5.2 Temperature-induced valence transition

The studies of the evolution of the structural and electronic properties of Ca-substituted rare-earth fullerides with stoichiometry $(Sm_{1-x}Ca_x)_{2.75}C_{60}$ were carried out by synchrotron X-ray diffraction and absorption techniques. The temperature-dependent X-ray diffraction measurements are expected to provide the evidence of the effect of Ca-substitution on the critical temperature at which the abrupt onset of large lattice expansion occurs. On the other hand, X-ray absorption and resonant inelastic X-ray scattering

(RIXS) measurements are expected to probe directly the valence states and reveal the origin of the low-temperature first-order valence transition that is the driving force of the NTE.

5.2.1 Experimental Details

The $(Sm_{1-x}Ca_x)_{2.75}C_{60}$ (x = 0, 1/6, 1/3, 1/2, 2/3, 1) samples were synthesised by direct reaction of stoichiometric quantities of C_{60} (super gold grade of purity >99.9%), calcium (99.9% pure), and samarium (99.9% pure) (Table 5.1). Prior to synthesis, C_{60} was degassed overnight at 200°C under dynamic vacuum of 10^{-5} mbar. The annealing protocols followed differ depending on the relative concentration of calcium (Ca) and samarium (Sm) metals.

Table 5.1. Quantities of reactants used for synthesising $(Sm_{1-x}Ca_x)_{2.75}C_{60}$ and the final mass of the product after the annealing protocols. The error of the balance was ±1 mg.

$(Sm_{1-x}Ca_x)_{2.75}C_{60}$ Nominal x	Sm (150.36 g/mol)	Ca (40.078 g/mol)	C_{60} (720.66g/mol)	Product
$Sm_{2.75}C_{60}$ (x = 0)	57.4 mg 3.817×10^{-4}mol	n/a	100 mg 1.388×10^{-4}mol	153 mg
$(Sm_{5/6}Ca_{1/6})_{2.75}C_{60}$ (x = 1/6)	57.0 mg 3.781×10^{-4}mol	3.0 mg 0.756×10^{-4}mol	120 mg 1.665×10^{-4}mol	174 mg
$(Sm_{2/3}Ca_{1/3})_{2.75}C_{60}$ (x = 1/3)	38.0 mg 2.544×10^{-4}mol	5.0 mg 1.272×10^{-4}mol	100 mg 1.388×10^{-4}mol	137 mg
$(Sm_{1/2}Ca_{1/2})_{2.75}C_{60}$ (x = 1/2)	19.0 mg 1.259×10^{-4}mol	5.0 mg 1.259×10^{-4}mol	66 mg 1.259×10^{-4}mol	82 mg
$(Sm_{1/3}Ca_{2/3})_{2.75}C_{60}$ (x = 2/3)	20.0 mg 1.272×10^{-4}mol	10.0 mg 2.544×10^{-4}mol	100 mg 1.388×10^{-4}mol	125 mg
$Ca_{2.75}C_{60}$ (x = 1)	n/a	9.0 mg 2.290×10^{-4}mol	60 mg 0.832×10^{-4}mol	62 mg

$Sm_{2.75}C_{60}$ was prepared by reaction of stoichiometric quantities of C_{60} and Sm, pressed into pellets and contained in a sealed tantalum (Ta) cell inside an evacuated quartz tube at 575°C for 3 days with one intermediate regrinding (2 + 1 days) [2].

The $(Sm_{5/6}Ca_{1/6})_{2.75}C_{60}$, $(Sm_{1/2}Ca_{1/2})_{2.75}C_{60}$, and $(Sm_{1/3}Ca_{2/3})_{2.75}C_{60}$ samples were prepared by reaction of stoichiometric quantities of degassed C_{60}, Ca and Sm powders. The Ca powders were prepared by dissolving Ca metal using liquid ammonia. 50 ml of liquid ammonia was first condensed and dried using a small piece of Na metal in a glass tube, which was then re-condensed over Ca metal placed inside a glass tube with a glass magnetic stirrer at -60°C. It was stirred for 1 hour in order to dissolve all Ca metal while the temperature was kept at -60°C using dry ice in the acetone bath. The ammonia was removed by heating the tube at 150°C on a vacuum line first under low-vacuum of 10^{-3} mbar and then by high vacuum of 10^{-5} mbar. The glass tube was sealed and placed inside the glovebox to remove the product, which can be used as Ca powder. These powders were mixed well with C_{60} and Sm, pressed into pellets and contained in a sealed Ta tube. The Ta tube was then placed inside a quartz tube filled with helium (300 mbar) and sealed. The tubes containing $(Sm_{5/6}Ca_{1/6})_{2.75}C_{60}$ and $(Sm_{1/2}Ca_{1/2})_{2.75}C_{60}$ samples were placed in a pre-heated furnace at a temperature of 575°C for 7 days with two intermediate regrindings (1 + 2 + 4 days), while the tube containing $(Sm_{1/3}Ca_{2/3})_{2.75}C_{60}$ was heated at the same temperature but for a longer annealing period (10 days, 1 + 2 + 3 + 4 days).

$(Sm_{2/3}Ca_{1/3})_{2.75}C_{60}$ and $Ca_{2.75}C_{60}$ samples were synthesised by direct reaction of stoichiometric quantities of degassed C_{60}, Ca and Sm powders pressed into pellets and contained in a sealed Ta tube placed inside a quartz

tube filled with helium (300 mbar). The Ca powders for these samples were prepared by grinding Ca metal using a diamond coated file. The tube was heated at 575°C for 5 days with two intermediate regrindings (1 + 2 + 2 days) for $(Sm_{2/3}Ca_{1/3})_{2.75}C_{60}$ and 12 days with three intermediate regrindinsg (1 + 2 + 3 + 6 days) for $Ca_{2.75}C_{60}$. We found that it was important not to anneal the reactants for more than 2 days in the earlier stages of the reactions in order to avoid the formation of Sm carbides. In addition, the samples containing larger concentrations of Ca required longer annealing times at the later stages to assure phase purity.

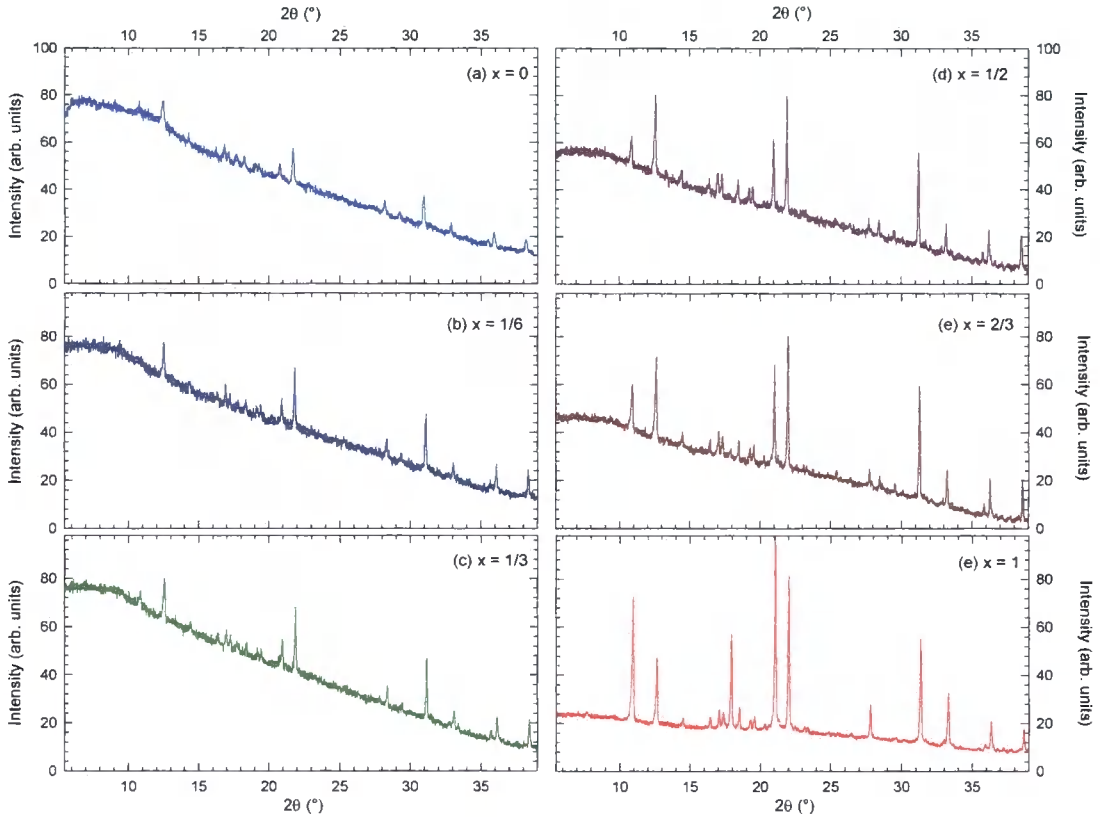

Fig. 5.1. X-ray diffraction profiles of $(Sm_{1-x}Ca_x)_{2.75}C_{60}$ (nominal x = 0, 1/6, 1/3, 1/2, 2/3, 1) at 295 K collected with the Siemens D5000 powder diffractometer (Cu-K_α radiation).

Few milligrams of the samples were sealed in thin-wall glass capillaries of diameter 0.5 mm for powder X-ray diffraction measurements. These were employed to monitor phase purity at each intermediate grinding stage using our laboratory X-ray diffractometer prior to the synchrotron X-ray measurements (Fig. 5.1).

The effect of the annealing procedure is clearly seen in Fig. 5.2, which shows the two diffraction profiles obtained on ID31 for the $(Sm_{1/3}Ca_{2/3})_{2.75}C_{60}$ sample after 6 days of annealing and after further 4 days of annealing. As the wavelength used for the two measurements was different, the profiles are plotted as a function of Q, where Q is defined as [6]:

$$Q = 4\pi \frac{\sin\theta}{\lambda} = \frac{2\pi}{d} \qquad \text{(Eqn. 5.1)}$$

The obtained profile after 6 days shows asymmetric peak shapes with larger widths compared to the profile obtained after an additional 4 days of annealing of the same batch of sample.

Although every necessary precaution was taken during sample handling in order to obtain the targeted samples, the nominal stoichiometry may not exactly correspond to the final stoichiometry. Thus, we attempted to extract the sample stoichiometry by analytical techniques such as Rutherford Backscattering Spectrometry (RBS). This technique is particularly useful in determining the Ca:Sm ratio in the $(Sm_{1-x}Ca_x)_{2.75}C_{60}$ compounds because of the large mass difference between the two elements.

The samples were also characterised by SQUID magnetisation measurements for which about 20 mg of the sample was sealed in a quartz SQUID tube.

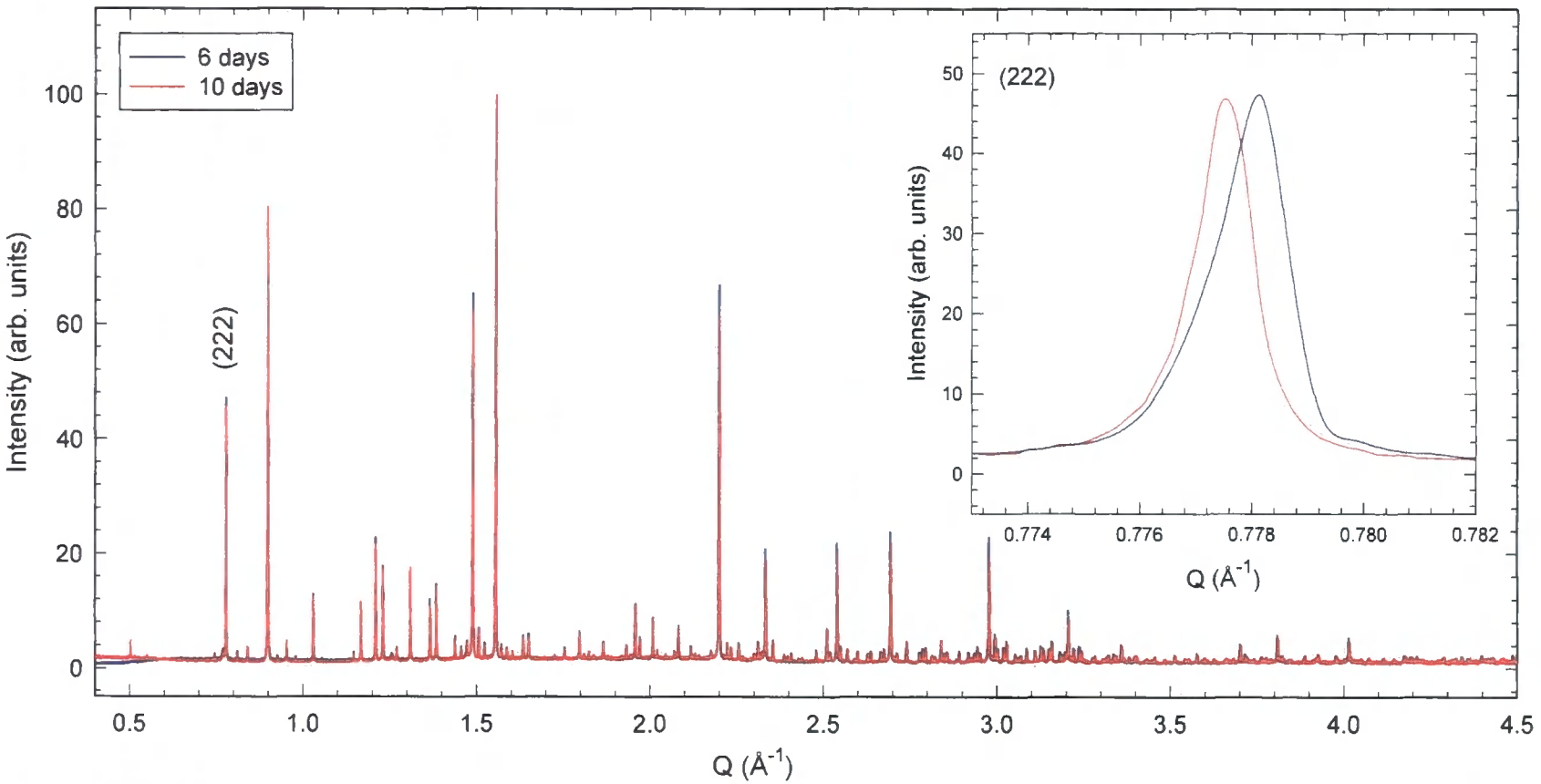

Fig. 5.2. Synchrotron powder X-ray diffraction profiles of $(Sm_{1/3}Ca_{2/3})_{2.75}C_{60}$ at 295 K (plotted *vs* Q range, Å^{-1}), where the blue (red) solid line shows the diffraction profile after 6 (10) days of annealing. *Inset:* Blow up of the (222) Bragg peak.

Low-field measurements in a field of 20 Oe were carried out under ZFC and FC conditions to search for bulk superconductivity and total susceptibilities were obtained in the temperature range 2 to 300 K in a field of 1 T after correcting for the diamagnetic core contributions with a Quantum Design MPMS5 SQUID susceptometer. The obtained magnetic susceptibility data at sufficiently high temperature region were used to derive estimates of the average Sm valence.

High-resolution synchrotron powder X-ray diffraction profiles for these samples were obtained at various temperatures between 5 and 300 K using a liquid-helium-cryostat in continuous scanning mode with the high-resolution powder diffractometer on ID31. Among the present Ca and Sm co-intercalated compounds, the temperature evolution was followed for $(Sm_{5/6}Ca_{1/6})_{2.75}C_{60}$, $(Sm_{2/3}Ca_{1/3})_{2.75}C_{60}$, $(Sm_{1/2}Ca_{1/2})_{2.75}C_{60}$ and $Ca_{2.75}C_{60}$. For the $(Sm_{1/3}Ca_{2/3})_{2.75}C_{60}$ sample, the diffraction profiles were collected only at 5 and 300 K.

Temperature dependent diffraction measurements were carried out in two ways: slowly warming up from 5 K while collecting data up to room temperature and slowly cooling down from room temperature while collecting data down to 5 K. In the case of the warming up protocols, the samples were first cooled down to 5 K at a rate of 5 K/min, then they were warmed up to 300 K at an average rate of 0.1 K/min in the low temperature region and 0.5 K/min in the high temperature range. The diffraction data were collected once the temperature was stabilised at each temperature (λ = 0.41274 Å for $(Sm_{5/6}Ca_{1/6})_{2.75}C_{60}$, $(Sm_{1/2}Ca_{1/2})_{2.75}C_{60}$ and $Ca_{2.75}C_{60}$, and λ = 0.8503 Å for $(Sm_{2/3}Ca_{1/3})_{2.75}C_{60}$ and $(Sm_{1/3}Ca_{2/3})_{2.75}C_{60}$). On the other hand, the diffraction measurements in the cooling protocols were carried out while cooling the

sample from 300 to 5 K at an average rate of 1 K/min. Such measurements were performed for $(Sm_{5/6}Ca_{1/6})_{2.75}C_{60}$ and $(Sm_{2/3}Ca_{1/3})_{2.75}C_{60}$ (λ = 0.41274 Å). The collected data were rebinned to a step of 0.003° for further analysis.

The $(Sm_{2/3}Ca_{1/3})_{2.75}C_{60}$ sample was also measured on ID16, an undulator beamline dedicated to high-resolution inelastic X-ray scattering (IXS), for X-ray absorption spectroscopy measurements in total fluorescence yield mode (TFY-XAS) at 300 K and partial fluorescence yield (PFY-XAS) and RIXS measurements as a function of temperature between 4 and 300 K. In TFY mode, the integrated scattered intensity is recorded as a function of incident energy, $h\nu_{in}$ which varies through the L_3 absorption edge of Sm, while in PFY mode, the intensity of a specific radiative transition, in this case the $L_{\alpha 1}$ de-excitation is measured as the incident energy varies through the Sm L_3 edge. These measurements were used to estimate the temperature evolution of the Sm valence state. In the RIXS measurements, specific final states of given $4f$ occupancy can be probed, and thus, the temperature dependence of the Sm $4f$ occupation number can be determined accurately at all temperatures.

5.2.2 Structural Analysis

Fig. 5.3 shows the results from high-resolution synchrotron powder X-ray diffraction profiles of $(Sm_{1-x}Ca_x)_{2.75}C_{60}$ (x = 0 (a), 1/6 (b), 1/3 (c), 1/2 (d), 2/3 (e), 1 (f)) samples at room temperature. Phase purity of each sample was carefully checked prior to the temperature dependent experiments. All samples are isostructural with $Sm_{2.75}C_{60}$.

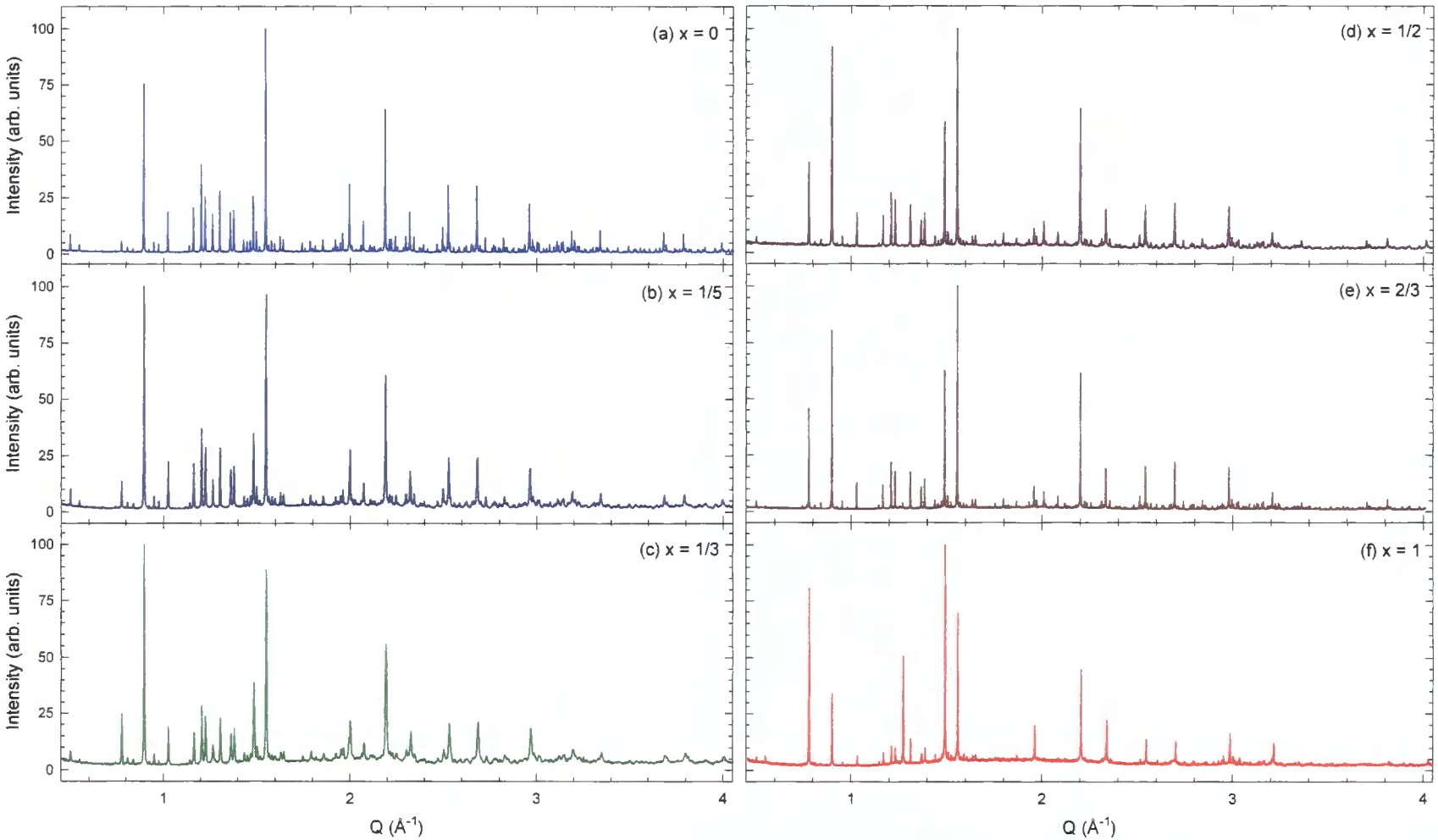

Fig. 5.3. Synchrotron X-ray powder diffraction profiles of $(Sm_{1-x}Ca_x)_{2.75}C_{60}$ at 295 K plotted as a function of Q. (continued)

Fig. 5.3. (continued) Plot a) $Sm_{2.75}C_{60}$ (x = 0, λ = 0.8016 Å); b) $(Sm_{5/6}Ca_{1/6})_{2.75}C_{60}$ (x = 1/6, λ = 0.4127 Å); c) $(Sm_{2/3}Ca_{1/3})_{2.75}C_{60}$ (x = 1/3, λ = 0.4127 Å); d) $(Sm_{1/2}Ca_{1/2})_{2.75}C_{60}$ (x = 1/2, λ = 0.4127 Å); e) $(Sm_{1/3}Ca_{2/3})_{2.75}C_{60}$ (x = 2/3, λ = 0.8502 Å); and f) $Ca_{2.75}C_{60}$ (x = 1, λ = 0.4127 Å).

Both $Sm_{2.75}C_{60}$ [2] and $Ca_{\sim 3}C_{60}$ [7] have crystal structures based on doubling the *fcc* unit cell of the alkali-metal intercalated fullerides, A_3C_{60}. The structural properties of the isostructural Ca-Sm-mixed compounds, $(Sm_{1-x}Ca_x)_{2.75}C_{60}$, can also be treated along the same line, where the observed superstructure is again due to the ordering of the partially occupied T_d sites. The structural model is also characterised by large displacements of the cations from the centres of the O_h sites (~2.3 Å) and smaller displacements from the centres of the T_d sites (~0.4 Å). The shape of the C_{60} molecules was constrained to icosahedral symmetry with a cage diameter of 7.01 Å and all C-C bond length fixed to a value of 1.44 Å. 240 independent C atoms are needed to define the 32 C_{60} molecules present in the unit cell. The five symmetry-inequivalent C_{60} molecules in the unit cell, $C_{60}(1)$ at (000), $C_{60}(21)$ at (0¼¼), $C_{60}(22)$ at (¼0¼), $C_{60}(23)$ at (¼¼0), and $C_{60}(3)$ at (½½½), were rotated anticlockwise by 37.5° about their local [111], $[1\bar{1}\bar{1}]$, $[\bar{1}1\bar{1}]$, $[\bar{1}\bar{1}1]$, and [111] symmetry axes, respectively.

The diffraction profiles also show significant changes in the relative intensities of selected peaks with increasing Ca concentration. The most prominent ones are seen in the change of intensity of, for instance, (222) and (226) Bragg reflections, which increase with increasing Ca concentration. The Rietveld refinements of the profiles of $(Sm_{1-x}Ca_x)_{2.75}C_{60}$ at room temperature were carried out based on the structural model used for $Sm_{2.75}C_{60}$, with Ca homogeneously disordered in the available interstitial

sites. Fig. 5.4 shows the Rietveld refinement results for $(Sm_{2/3}Ca_{1/3})_{2.75}C_{60}$ in which the fractional occupancies of Ca were purposefully varied between 0, 1/3, and 1.

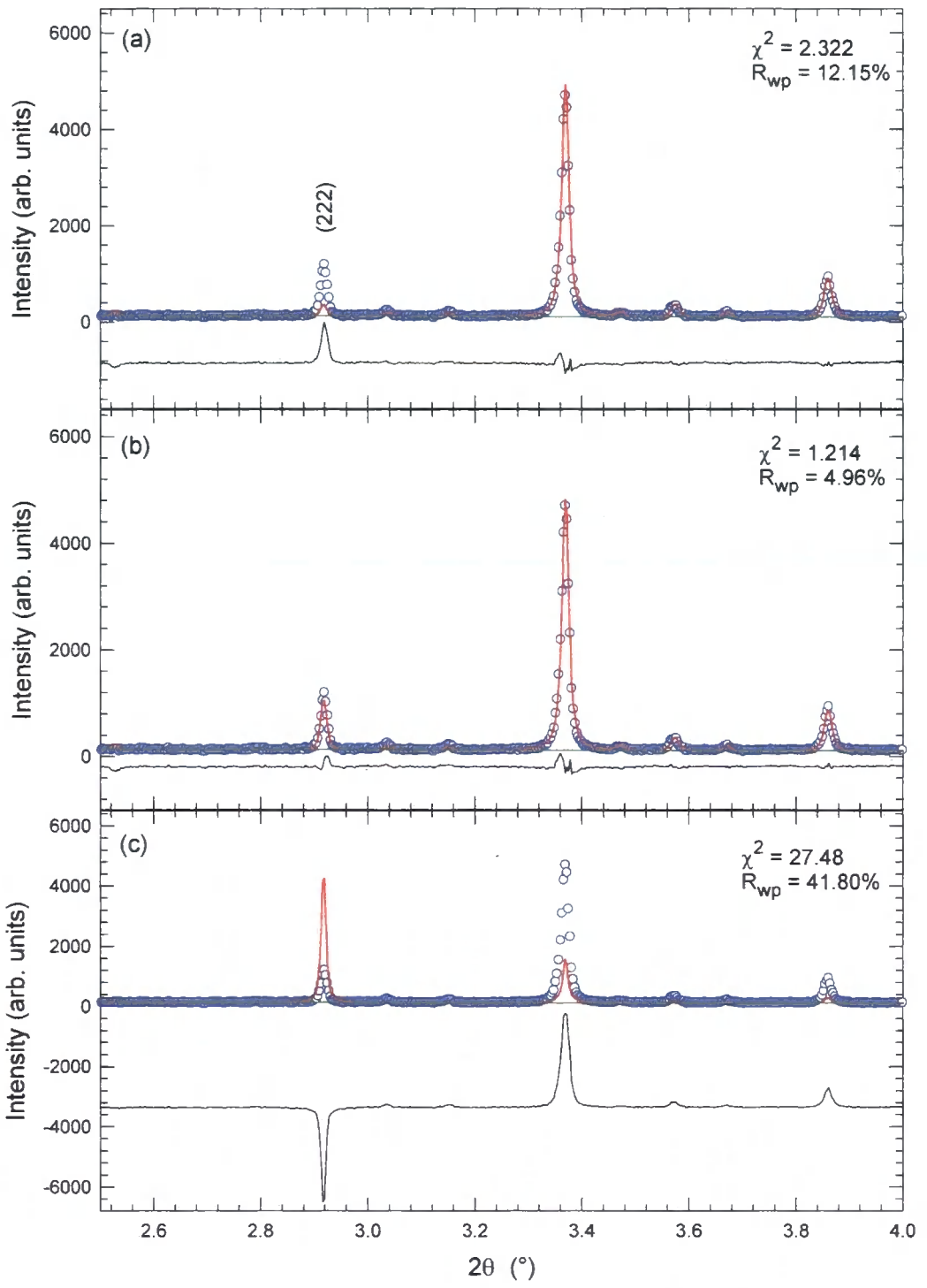

Fig. 5.4. Results (selected region) of the Rietveld refinements of (continued)

Fig. 5.4.(continued) the profile of $(Sm_{2/3}Ca_{1/3})_{2.75}C_{60}$ obtained from synchrotron powder X-ray diffraction at room temperature, varying the ratio of fractional occupancies of Sm and Ca (a) 1 : 0, (b) 2 : 1, and (c) 0 : 1.

It is apparent from this figure that the Rietveld refinement improves significantly when the ratio of the fractional occupancy of Sm and Ca was set as 2 : 1 (Table 5.2), in excellent agreement with the nominal composition of the material. This implies that because of the significant difference in scattering factor between Ca and Sm, the Rietveld refinements can provide reliable estimates of the actual compositions of the $(Sm_{1-x}Ca_x)_{2.75}C_{60}$ family of materials.

Another obvious effect on the diffraction profiles of changing the Ca concentration was seen in the 2θ positions of each Bragg reflection for different sample compositions. As it can be seen in Fig. 5.5, the Bragg reflections (for example, the (844) peaks) of $(Sm_{1-x}Ca_x)_{2.75}C_{60}$ samples shift to higher angles as the nominal Ca concentration increases, which implies that the lattice parameters of the Ca-substituted samples become substantially smaller compared to $Sm_{2.75}C_{60}$, consistent with the ionic radius of Ca^{2+} (0.99 Å) being smaller than that of Sm^{2+} (1.41 Å). Extraction of the lattice constants from each diffraction profile was carried out with Rietveld refinements; here the refinements were initiated using the model introduced before and the ratio of fractional occupancies of Ca and Sm was fixed based on the nominal composition of the sample as a first approximation.

Table 5.2. Refined structural parameters for $(Sm_{2/3}Ca_{1/3})_{2.75}C_{60}$ at 300 K.

	Site	x/a	y/b	z/c	*N*	*B*(Å²)
$C_{60}(1)$	4a	0	0	0	1.0	1.0(1)
$C_{60}(21)$	8c	0	¼	¼	1.0	1.0(1)
$C_{60}(22)$	8c	¼	0	¼	1.0	1.0(1)
$C_{60}(23)$	8c	¼	¼	0	1.0	1.0(1)
$C_{60}(3)$	4b	½	½	½	1.0	1.0(1)
Ca(11)	8c	0.1372 (2)	0.1150 (2)	0.3862 (2)	0.331 (1)	1.34 (5)
Ca(12)	8c	0.3862 (2)	0.1372 (2)	0.1150 (2)	0.331 (1)	1.34 (5)
Ca(13)	8c	0.1150 (2)	0.3862 (2)	0.1372 (2)	0.331 (1)	1.34 (5)
Ca(21)	8c	0.1325 (2)	0.3704 (2)	0.3786(2)	0.331 (1)	1.34 (5)
Ca(22)	8c	0.3786(2)	0.1325 (2)	0.3704 (2)	0.331 (1)	1.34 (5)
Ca(23)	8c	0.3704 (2)	0.3786(2)	0.1325 (2)	0.331 (1)	1.34 (5)
Ca(3)	8c	0.3828 (7)	0.377 (1)	0.377 (1)	0.331 (1)	1.34 (5)
Ca(4) (vacancy)	8c	0.117(1)	0.122(1)	0.123(2)	0.016 (2)	1.34 (5)
Ca(51)	8c	0.2023 (1)	0.2023 (1)	0.2023 (1)	0.298 (1)	3.45 (4)
Ca(52)	8c	0.0477 (1)	0.0477 (1)	0.2023 (1)	0.298 (1)	3.45 (4)
Ca(53)	8c	0.2023 (1)	0.0477 (1)	0.0477 (1)	0.298 (1)	3.45 (4)
Ca(54)	8c	0.0477 (1)	0.2023 (1)	0.0477 (1)	0.298 (1)	3.45 (4)
Ca(61)	8c	0.2023 (1)	0.308 (1)	0.308 (1)	0.035 (2)	3.45 (4)
Ca(62)	8c	0.0477 (1)	-0.058(1)	0.308 (1)	0.035 (2)	3.45 (4)
Ca(63)	8c	0.308 (1)	-0.058(1)	0.0477 (1)	0.070 (1)	3.45 (4)
Sm(11)	8c	0.1372 (2)	0.1150 (2)	0.3862 (2)	0.662 (1)	1.34 (5)
Sm(12)	8c	0.3862 (2)	0.1372 (2)	0.1150 (2)	0.662 (1)	1.34 (5)
Sm(13)	8c	0.1150 (2)	0.3862 (2)	0.1372 (2)	0.662 (1)	1.34 (5)
Sm(21)	8c	0.1325 (2)	0.3704 (2)	0.3786(2)	0.662 (1)	1.34 (5)
Sm(22)	8c	0.3786(2)	0.1325 (2)	0.3704 (2)	0.662 (1)	1.34 (5)
Sm(23)	8c	0.3704 (2)	0.3786(2)	0.1325 (2)	0.662 (1)	1.34 (5)
Sm(3)	8c	0.3828 (7)	0.377 (1)	0.377 (1)	0.662 (1)	1.34 (5)
Sm(4) (vacancy)	8c	0.117(1)	0.122(1)	0.123(2)	0.033 (3)	1.34 (5)
Sm(51)	8c	0.2023 (1)	0.2023 (1)	0.2023 (1)	0.597 (1)	3.45 (4)
Sm(52)	8c	0.0477 (1)	0.0477 (1)	0.2023 (1)	0.597 (1)	3.45 (4)
Sm(53)	8c	0.2023 (1)	0.0477 (1)	0.0477 (1)	0.597 (1)	3.45 (4)
Sm(54)	8c	0.0477 (1)	0.2023 (1)	0.0477 (1)	0.597 (1)	3.45 (4)
Sm(61)	8c	0.2023 (1)	0.308 (1)	0.308 (1)	0.070 (1)	3.45 (4)
Sm(62)	8c	0.0477 (1)	-0.058(1)	0.308 (1)	0.070 (1)	3.45 (4)
Sm(63)	8c	0.308 (1)	-0.058(1)	0.0477 (1)	0.140 (3)	3.45 (4)

The obtained lattice constants and unit cell volumes are tabulated in Table 5.3 and the unit cell volumes are plotted against nominal concentration, *x*, in Fig. 5.6.

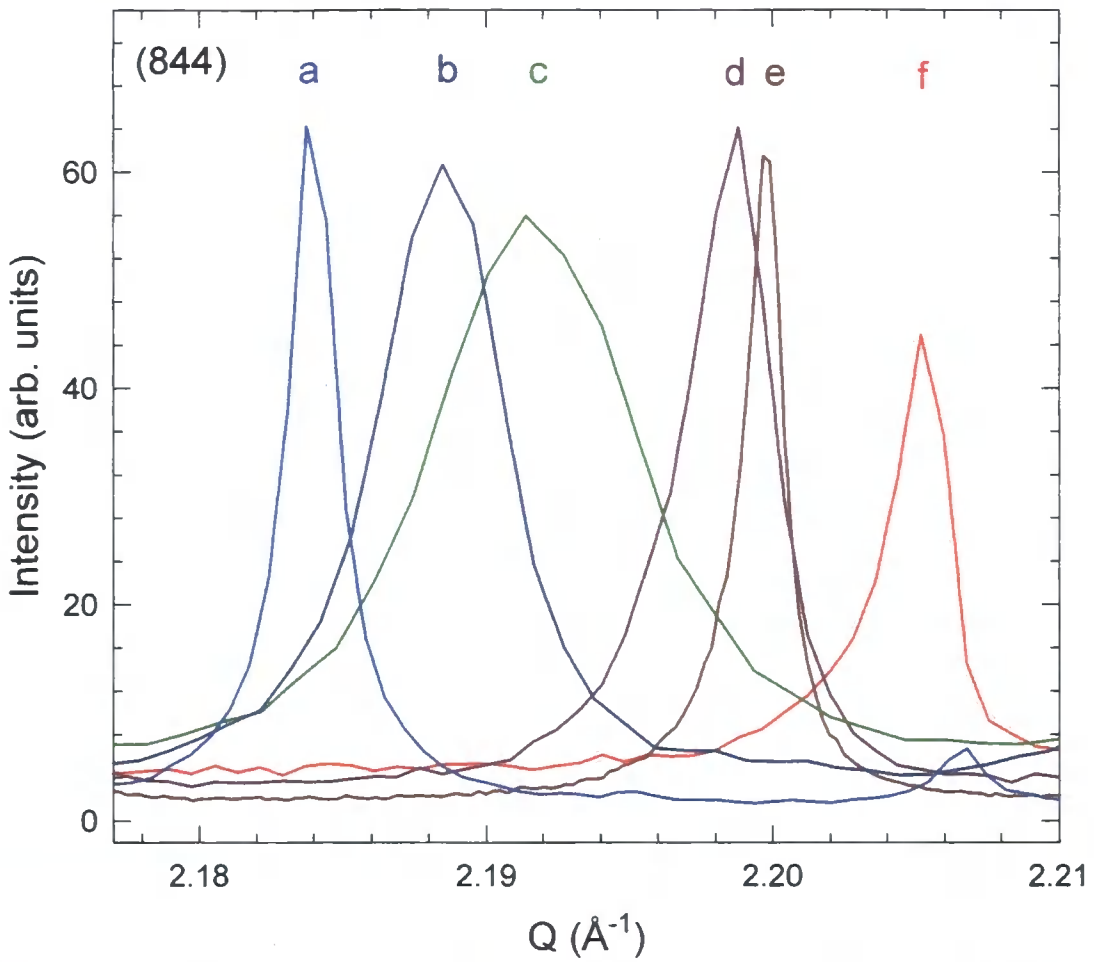

Fig. 5.5. Selected region of the normalised diffraction profiles of $(Sm_{1-x}Ca_x)_{2.75}C_{60}$, showing the evolution of the (844) Bragg reflection with change in the sample composition, where x = (a) 0, (b) 1/6, (c) 1/3, (d) 1/2, (e) 2/3, and (f) 1.

Table 5.3. The extracted values of the unit cell volume and lattice constants for $(Sm_{1-x}Ca_x)_{2.75}C_{60}$.

Sample	Volume (Å^3)	a (Å)	b (Å)	c (Å)
a: $Sm_{2.75}C_{60}$	22395.0 (4)	28.1871 (2)	28.2243 (2)	28.1509 (2)
b: $(Sm_{5/6}Ca_{1/6})_{2.75}C_{60}$	22291.2 (6)	28.1460 (3)	28.1545 (3)	28.1348 (3)
c: $(Sm_{2/3}Ca_{1/3})_{2.75}C_{60}$	22177.4 (3)	28.0955 (3)	28.1152 (3)	28.0759 (3)
d: $(Sm_{1/2}Ca_{1/2})_{2.75}C_{60}$	21997.8 (3)	28.0206 (1)	28.0290 (1)	28.0093 (1)
e: $(Sm_{1/3}Ca_{2/3})_{2.75}C_{60}$	21926.5 (4)	27.9912 (2)	27.9996 (2)	27.9800 (2)
f: $Ca_{2.75}C_{60}$	21775.3 (3)	27.9259 (1)	27.9288 (1)	27.9194 (1)

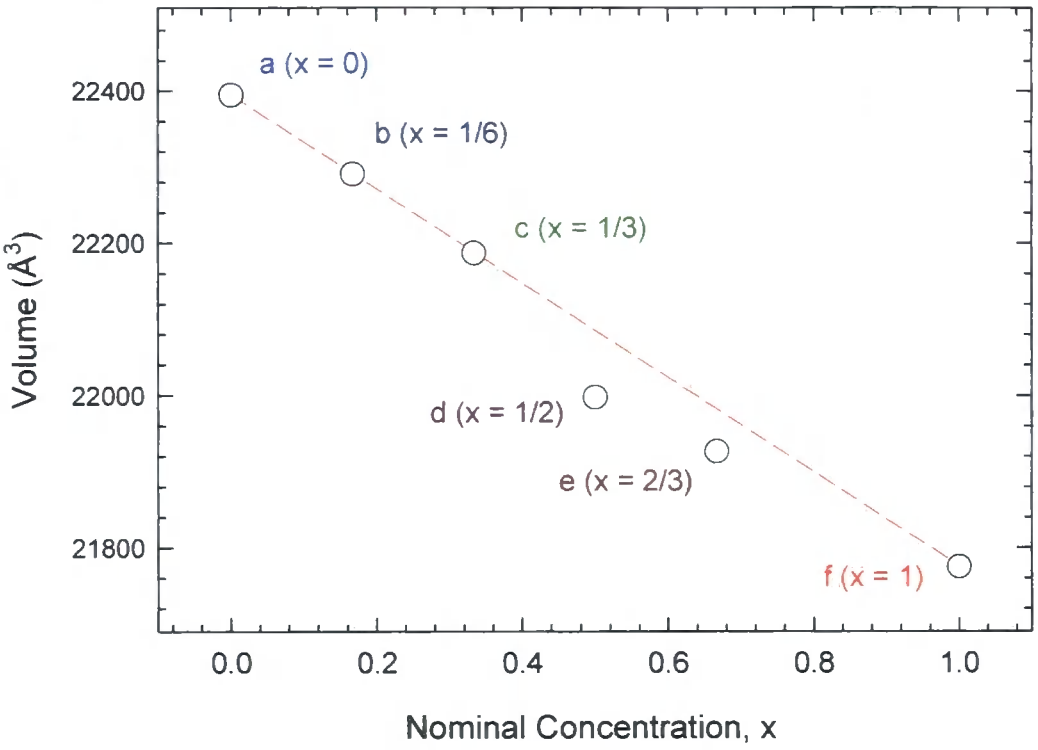

Fig. 5.6. The evolution of unit cell volume against nominal concentration varied x in $(Sm_{1-x}Ca_x)_{2.75}C_{60}$.

From the plot of the evolution of the unit cell volume against the nominal Ca concentration, it is clear that there is a quasi-linear decrease with Ca substitution, implying the validity of Vegard's law and solid solution formation. However the unit cell volume of the samples with x = 1/2 and 2/3 are slightly off the linear behaviour. Rietveld refinements on these samples were repeated by allowing the variation of the ratio of the fractional occupancies of Ca and Sm. The preliminary results indicated that for both these samples the fractional occupancy of Sm was slightly smaller than the nominal value.

In order to probe further the stoichiometry of these samples, the samples with Ca concentration of x = 1/3, 1/2, and 2/3 were analysed by

high-energy ion scattering spectroscopy (also known as RBS). These measurements were carried out using 3.0 MeV protons as incident ions and data were collected by a high-resolution solid state detector, composed of two Si detectors (see also Chapter 2, section 4 for detail). The yield, dN(in counts per second), obtained for a Ca was 1538.39 (57.6) Yield/ppm and for Sm was 3140.51 (55.5) Yield/ppm, for x = 1/3, giving ratio of 1 : 2, which is in agreement with the nominal values. Fig. 5.7 and 5.8 show the results obtained from the RBS measurements with the normalised yield, dN, plotted against energy for both $(Sm_{1/2}Ca_{1/2})_{2.75}C_{60}$ and $(Sm_{1/3}Ca_{2/3})_{2.75}C_{60}$ samples.

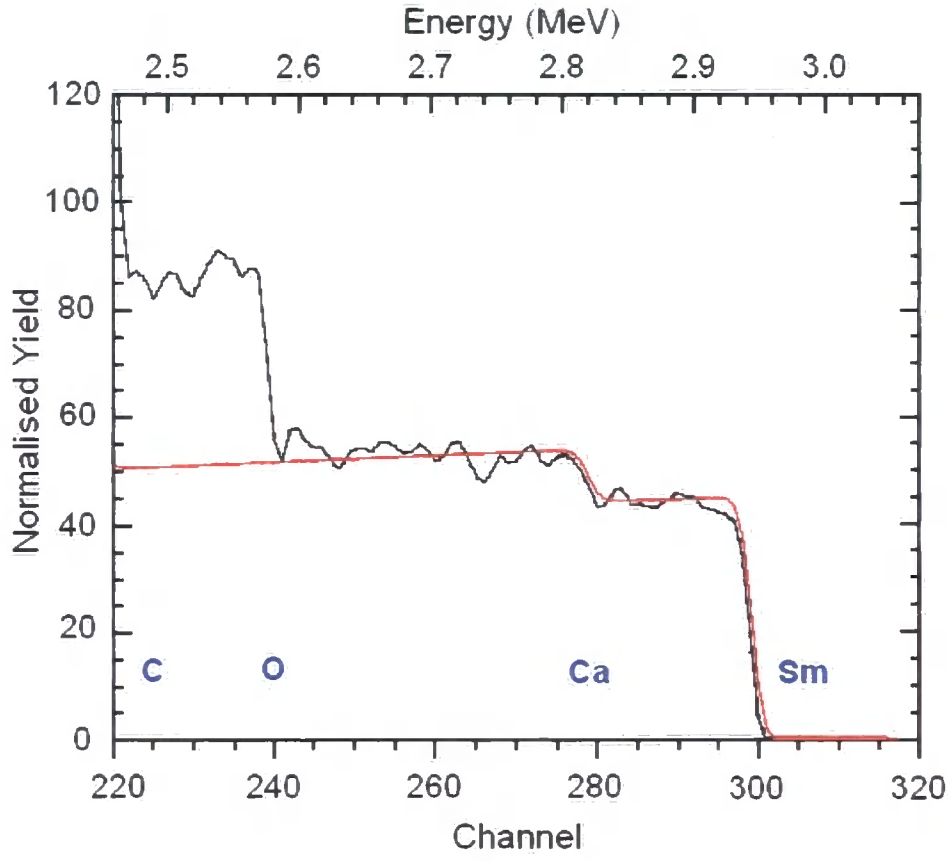

Fig. 5.7. 3.0 MeV proton backscattering spectrum of the $(Sm_{1/2}Ca_{1/2})_{2.75}C_{60}$ sample. The stoichiometry was determined from the step heights, where the solid black line is the observed and red line is the simulation spectrum. The Sm : Ca ratio was calculated as 1 : 2.05.

The results obtained for both $x = 1/2$ and 1/3 revealed slightly lower Sm concentration than the nominal values. For $x = 1/2$, dN for Ca was 2953.4 (27.3) Yield/ppm and for Sm was 1440.6 (28.0) Yield/ppm (2.05 : 1), and for $x = 1/3$, dN for Ca was 3581.09 (58.7) Yield/ppm and for Sm was 1179.20 (40.3) Yield/ppm (3.03 : 1).

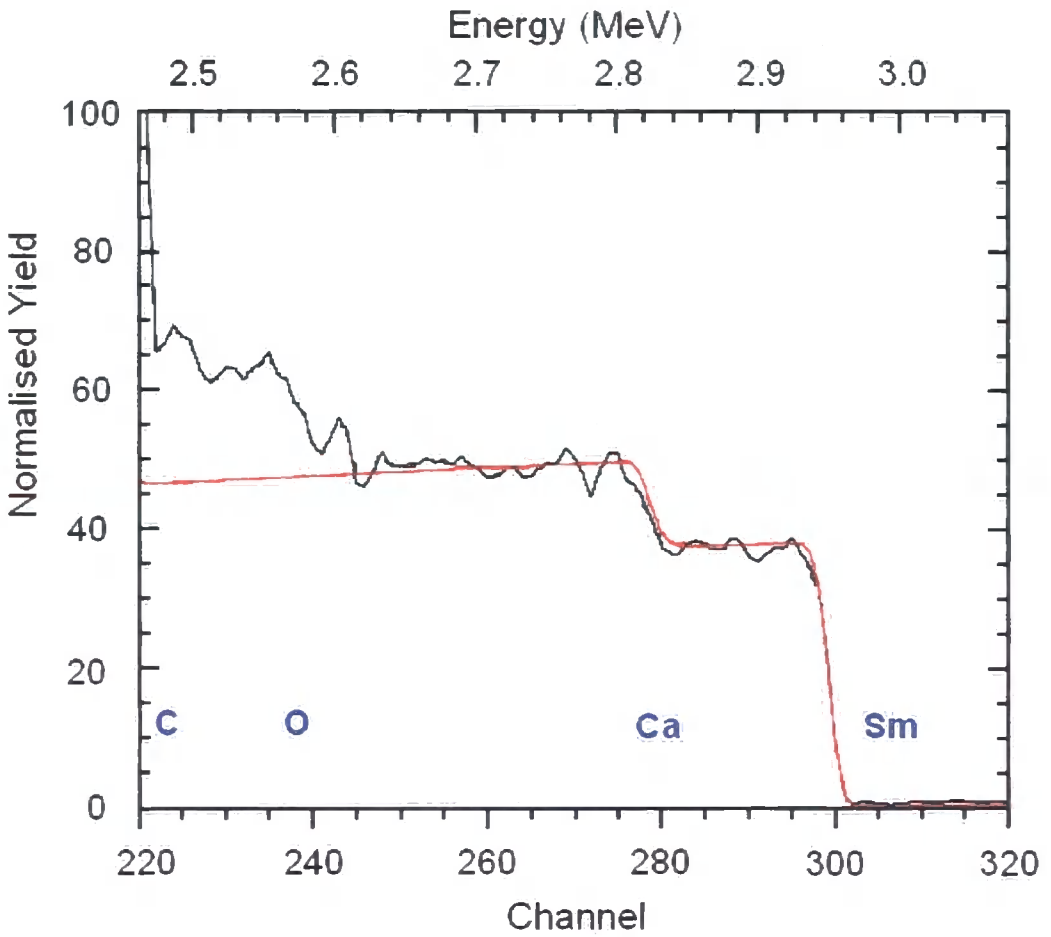

Fig. 5.8. 3.0 MeV proton backscattering spectrum of the $(Sm_{1/3}Ca_{2/3})_{2.75}C_{60}$ sample. The stoichiometry was determined from the step heights, where the solid black line is the observed and red line is the simulation spectrum. The Sm : Ca ratio was calculated as 1 : 3.03.

The Ca and Sm-related step heights obtained in the spectrum allow the determination of the stoichiometries of the samples as $(Sm_{1/3}Ca_{2/3})_{2.75}C_{60}$ (Sm : Ca = 1 : 2) instead of $(Sm_{1/2}Ca_{1/2})_{2.75}C_{60}$ and $(Sm_{1/4}Ca_{3/4})_{2.75}C_{60}$ (Sm : Ca =

1 : 3) instead of $(Sm_{1/3}Ca_{2/3})_{2.75}C_{60}$. Re-evaluation of the lattice constants, employing the RBS Sm/Ca ratios was then carried out. The unit cell volumes are plotted against the RBS-derived Sm and Ca concentrations in Fig. 5.9. This shows that the unit cell volume of the all $(Sm_{1-x}Ca_x)_{2.75}C_{60}$ samples scales in an excellent fashion with the concentration of Ca and Sm, confirming solid solution formation in the Ca/Sm phase field.

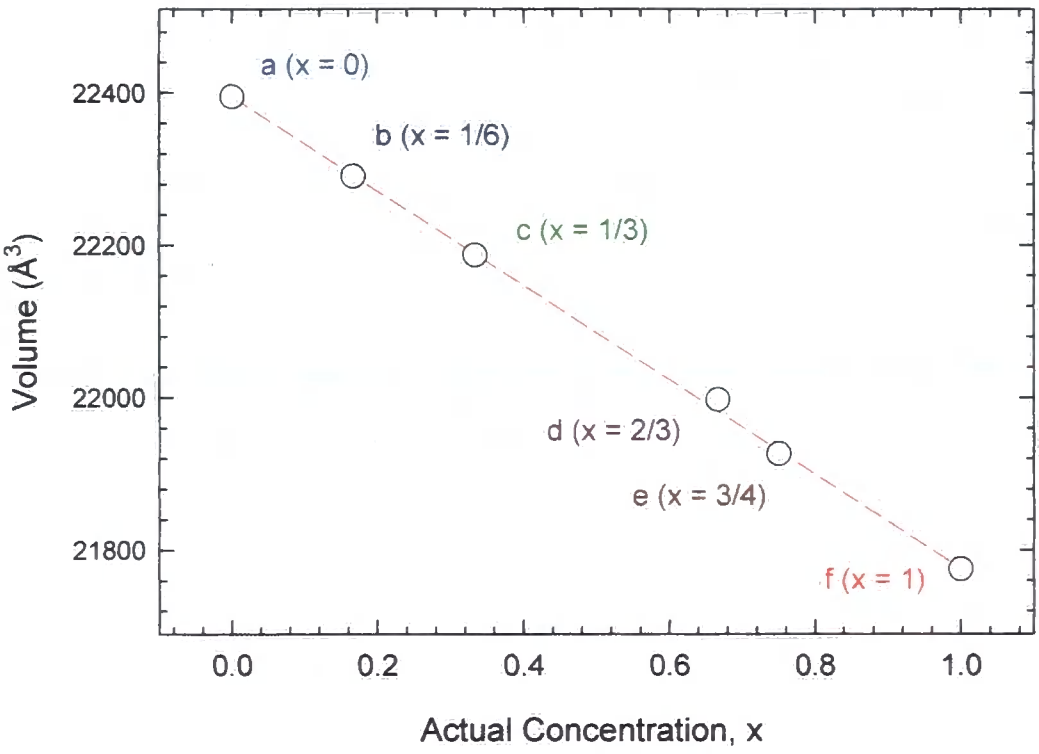

Fig. 5.9. The evolution of unit cell volume against concentration of Ca (x) obtained from RBS measurements.

5.2.3 High-Field Magnetisation Measurements

Temperature-dependent magnetic measurements for $(Sm_{1-x}Ca_x)_{2.75}C_{60}$ samples in high magnetic field were employed to extract estimates of the average Sm valence at room temperature. Magnetisation measurements were performed on samples of mass ~20 mg sealed in quartz tubes in the

temperature range 2 to 300 K in fields of 1, 2, and 4 T with a Quantum Design MPMS5 SQUID susceptometer. The total susceptibilities were obtained after correcting for the diamagnetic core contributions from the difference of the values measured at 4 and 2 T. This methodology was chosen in order to remove the contributions from ferromagnetic impurities present. The diamagnetic core contributions for $(Sm_{1-x}Ca_x)_{2.75}C_{60}$ can be estimated by employing the values of χ_{core} of the intercalants, Sm^{2+} (χ_{core} = -21.5×10^{-6} emu/mol), and Ca^{2+} (χ_{core} = -10.4×10^{-6} emu/mol) [8], and of C_{60}^{6-}, which is estimated to be -5.91×10^{-4} emu/mol [9] (cf. the diamagnetic core susceptibility of neutral C_{60} is -2.43×10^{-4} emu/mol [10]).

In the intermediate valence compounds, the average Sm valence can be derived from total susceptibility data at sufficiently high temperatures with the magnetic susceptibility expressed as a linear combination of the free-ion Sm^{2+} and Sm^{3+} contributions [2]:

$$\chi = (1-\varepsilon)\chi(Sm^{2+}) + \varepsilon\chi(Sm^{3+}) \qquad \text{(Eqn. 5.2)}$$

where $(2+\varepsilon)$ is approximately the average Sm valence. This relationship only holds for the data above some characteristic temperature, T_{sf}, where the measuring scale ($k_B T$) is faster than the fluctuation frequency (ω_{sf}) of the magnetic moment between the values of the two valence configurations [11]. Fig. 5.10 shows the results of temperature-dependent magnetic measurements for $(Sm_{1-x}Ca_x)_{2.75}C_{60}$ (x = 1/3, 2/3, 3/4). The diagrams also include the calculated magnetic susceptibilities of the Sm^{2+} and Sm^{3+} ions and the temperature dependence of the average susceptibility calculated from the contributions from both Sm^{2+} and Sm^{3+}.

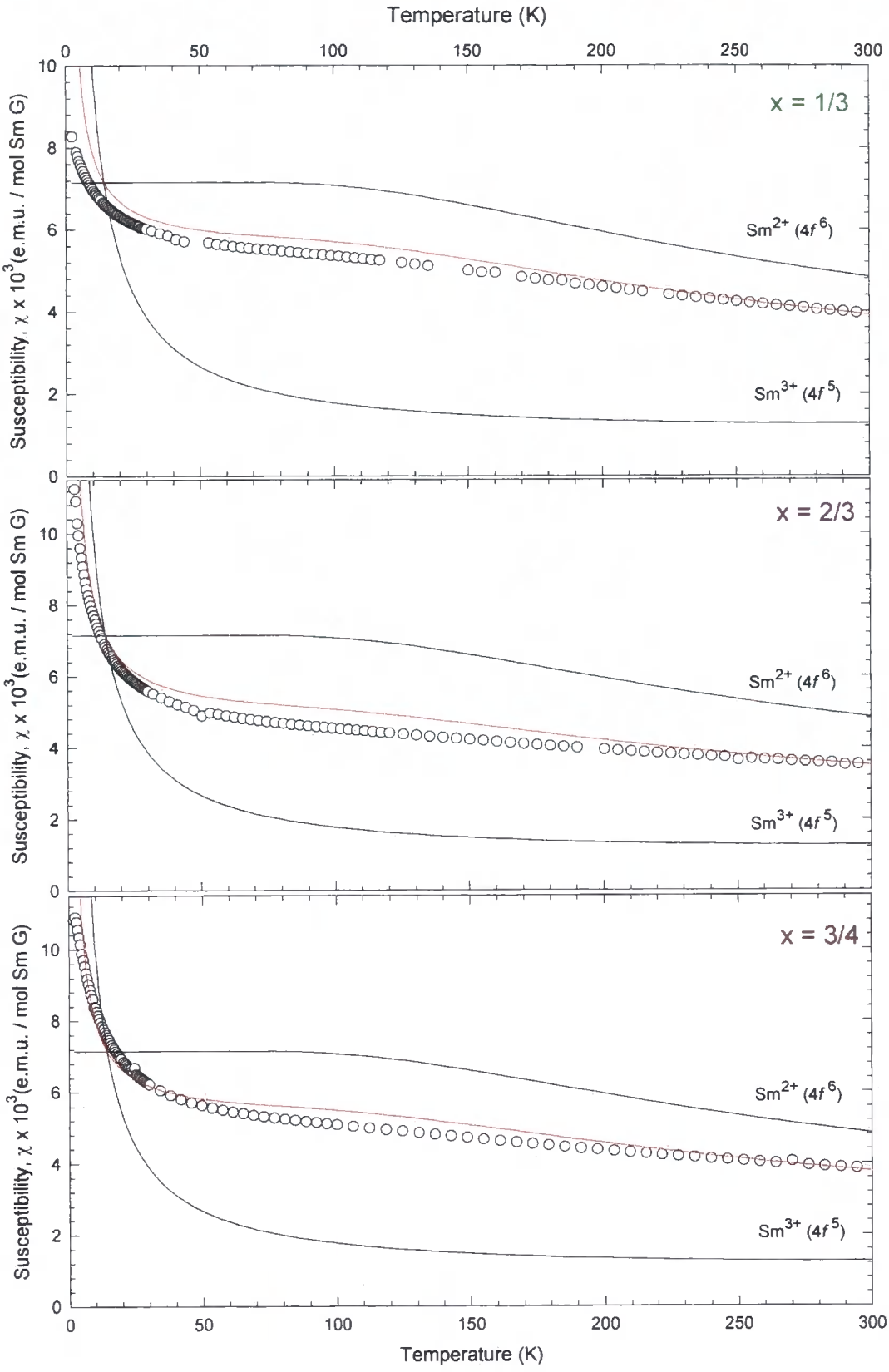

Fig. 5.10. Temperature dependence of magnetic susceptibilities of $(Sm_{1-x}Ca_x)_{2.75}C_{60}$ (x = 1/3, 2/3, 3/4). Open circles represent the (continued)

Fig. 5.10. (continued) measured magnetic susceptibilities of each sample obtained by taking the difference of the values measured in fields of 4 and 2 T. The calculated magnetic susceptibilities of the free Sm^{2+} and Sm^{3+} ions are shown by black solid lines, and the weighted average of the susceptibility calculated from the contributions of Sm^{2+} and Sm^{3+} are represented by the red solid line.

The magnetic susceptibilities of the free Sm^{2+} and Sm^{3+} ions are obtained by summing the corresponding Curie and van Vleck contributions. Sm^{2+} has a nonmagnetic $^7F_0$ ground state with $4f^6$ configuration, where the Curie contribution of the ground state is zero and thus leading to a van Vleck susceptibility of [12]:

$$\chi\left(Sm^{2+}\right)=\frac{8N_a\mu_B^2}{\Delta E_J} \qquad \text{(Eqn. 5.3)}$$

where N_a and μ_B is the Avogadro number and the Bohr magneton, and ΔE_J is the energy difference between the $J = 1$ and $J = 0$ states. Sm^{3+} has a $^6H_{5/2}$ ground state with a $4f^5$ configuration, which approximately follows Curie like behaviour with van Vleck contribution. This is reflecting the splitting of the six-fold degenerate ground state, J_z = ±1/2, ±3/2, and ±5/2. The susceptibility of Sm3+ can be expressed as follows [13-15]:

$$\chi\left(Sm^{3+}\right)=\frac{N_a g^2\mu_B^2}{k_B T}\left(\frac{M_{1eff}^2+M_{2eff}^2 Y+M_{3eff}^2 Z}{1+Y+Z}\right)$$
$$Y=\exp\left(\frac{-\Delta_{78}}{k_B T}\right), Z=\exp\left(\frac{-\Delta_{76}}{k_B T}\right) \qquad \text{(Eqn. 5.4)}$$

where Δ_{78} and Δ_{76} are the energy difference between the ground state and excited states, M_{ieff} is the effective magnetic quantum number of each sublevel, g is the Lande splitting factor, μ_B the Bohr magneton, k_B the

Boltzmann constant, T the temperature.

As it can be seen in the figure above, the room temperature value of the magnetic susceptibilities of $(Sm_{1-x}Ca_x)_{2.75}C_{60}$ straddles those calculated for the free Sm^{2+} and Sm^{3+} ions, providing an estimate of the average Sm valence of 2.26+ (x = 1/3), 2.38+ (x = 2/3), and 2.3+ (x = 3/4). The temperature dependence of the calculated magnetic susceptibilities strongly deviates from the measured values implying that an anomalous response and temperature dependent changes in the Sm valency are likely to occur on cooling.

5.2.4 Structural response and Negative Thermal Expansion

High-resolution synchrotron X-ray powder diffraction techniques were employed to investigate the structural properties of $(Sm_{1-x}Ca_x)_{2.75}C_{60}$ as a function of temperature between 5 and 300 K. Few milligrams of the powder samples were carefully introduced into 0.5 mm diameter glass capillaries and placed inside the liquid-helium-cryostat in the beamline ID31 at ESRF. The collected data were rebinned to a step of 0.003° and data analysis was performed with the GSAS suite of Rietveld analysis program.

i) $(Sm_{5/6}Ca_{1/6})_{2.75}C_{60}$

The sample $(Sm_{5/6}Ca_{1/6})_{2.75}C_{60}$ (x = 1/6) was first cooled down to 5 K inside the cryostat at a rate of 5 K/min and the X-ray diffraction profile was collected when the temperature stabilised at 5 K (λ = 0.41274 Å). The sample was then slowly heated using a stepwise heating protocol with an average rate of 0.1 K/min while the diffraction profiles were collected at each step

until the temperature reached 120 K. Then the rate of heating was increased to 0.81 K/min up to room temperature. A slow cooling protocol was then applied (-1.3 K/min down to 160 K, -0.38 K/min down to 60 K, and -1.0 K/min down to 5 K) in order to investigate if this sample showed any hysteresis behaviour.

Fig. 5.11 shows the temperature evolution of the (444) Bragg reflection for this sample. The diffraction peaks at low temperatures continuously shift to higher angles on heating (Fig. 5.11a), which implies that the lattice dimensions contract as temperature increases to 120 K, while the peaks shift to lower angles on cooling (Fig. 5.11b) below 110 K down to 5 K, which implies the lattice dimensions expand on cooling.

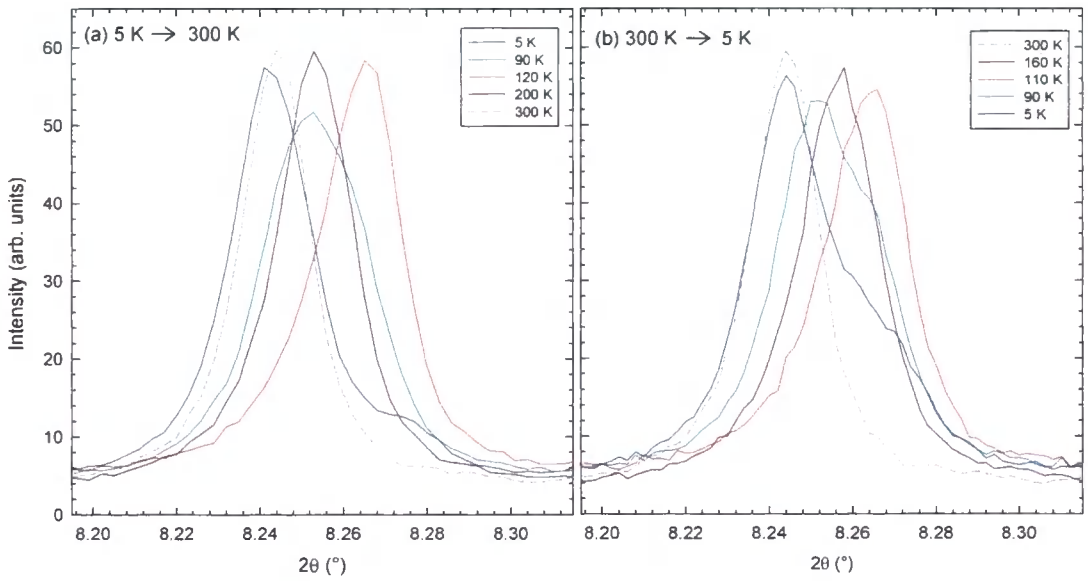

Fig. 5.11. Selected region of the synchrotron X-ray powder diffraction profiles of $(Sm_{5/6}Ca_{1/6})_{2.75}C_{60}$, showing the temperature evolution of the (444) Bragg reflection (a) on heating from 5 to 300 K and (b) on cooling from 300 to 5 K. The peak shifts to higher angle on heating from 5 to 120 K and then to lower angle on further heating to 300 K, while on cooling, the peak shifts to higher angle down to 110 K and changes the direction towards lower angle on further cooling down to 5 K.

In both cases, the NTE behaviour is clearly observed below the critical temperature T_v, where the sample phase separates into two phases below the critical temperature. It should be noted here that broadening of the diffraction peak widths is observed below T_v, going through a maximum (broader by ~55% than at room temperature) at around 90 K, and then phase separation is observed on further cooling. Such behaviour is most likely to reflect the presence of local structural inhomogeneities accompanying the rapid 1st-order transformation of the material.

Rietveld refinements were first carried out on the diffraction profiles at 5 K obtained on both rapid and slow cooling using a 2-phase model (Fig. 5.12). The weight fractions of the major and minor phases were also determined by the Rietveld refinements using the equation below [16]:

$$X_\alpha = \frac{S_\alpha Q_\alpha}{\sum_n S_n Q_n} \qquad \text{(Eqn. 5.5)}$$

where S_α is the scale factor and Q_α is the density of phase α, of which S is the refined parameter and Q is the value calculated from the refined composition and cell parameters of each phase. The values obtained from the analysis are shown in Table 5.4.

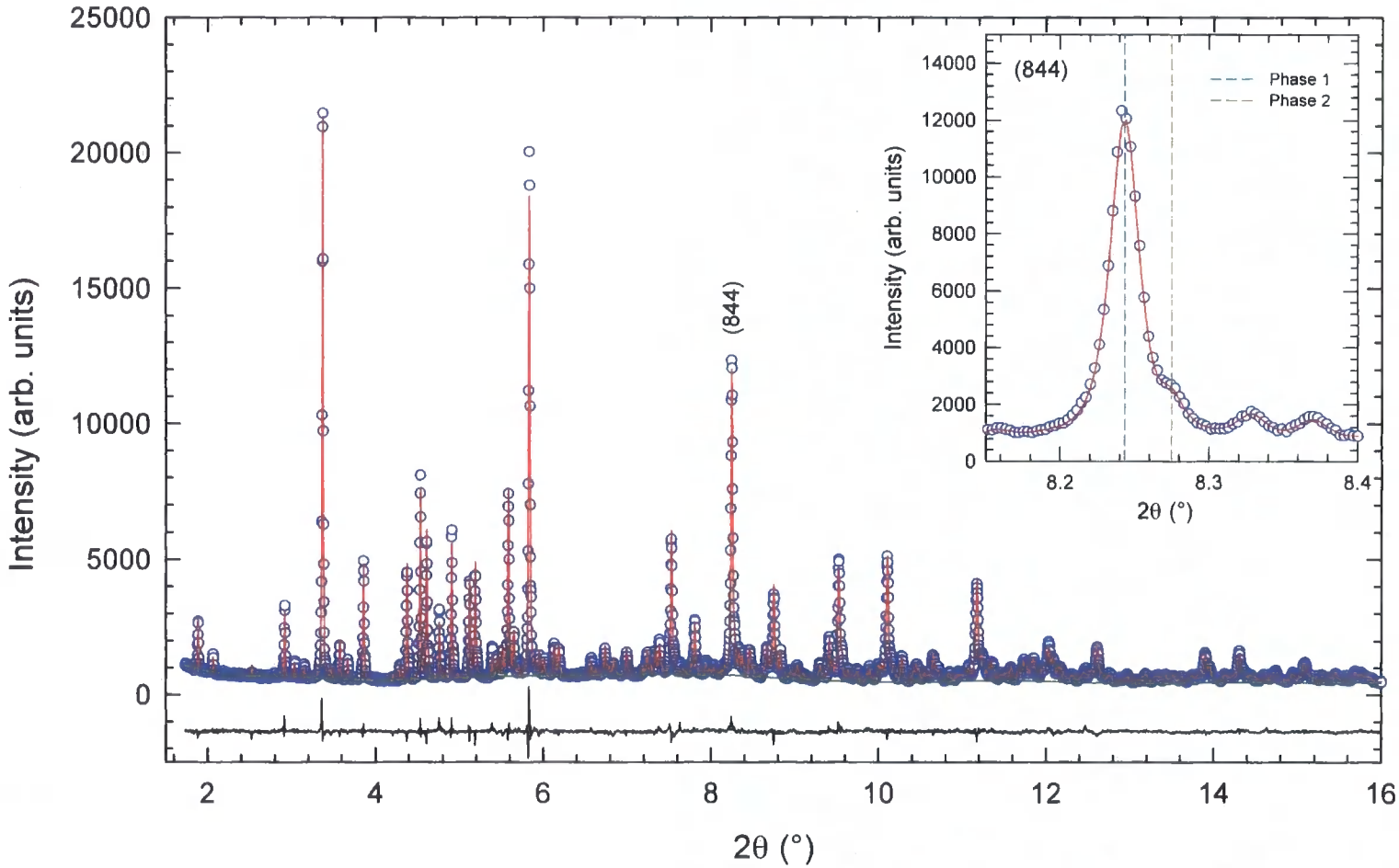

Fig. 5.12. Result of the Rietveld refinement of the profile of $(Sm_{5/6}Ca_{1/6})_{2.75}C_{60}$ at 5 K (quenched) [*inset*: blow up of the (844) Bragg peak fitted using the 2-phase model].

Table 5.4. The extracted values of the lattice constants and unit cell volume for the major phase in $(Sm_{5/6}Ca_{1/6})_{2.75}C_{60}$ (λ = 0.41274 Å, *Pcab* (option 2))

Temperature:	5 K(rapid cooling)	300 K	5 K (slow cooling)
$\Delta 2\theta$ (×100, °)	0.446 (5)	0.430 (5)	0.354 (6)
a (Å)	28.1490 (2)	28.1460 (3)	28.1436 (3)
b (Å)	28.1576 (2)	28.1545 (3)	28.1531 (3)
c (Å)	28.1379 (2)	28.1348 (3)	28.1324 (3)
V (Å^3)	22302.3 (6)	22295.0 (6)	22290.2 (7)
Wt. frac (%)	0.931 (1)	- (-)	0.728 (6)
Sm(3)-C_{60} (Å)	2.650 (5)	2.659 (6)	2.652 (3)
GU, GV	100.4(4), -4.67 (5)	41.1 (8), -2.95 (5)	658.8(4), -4.15 (6)
GW	0.191 (2)	0.082 (2)	0.188 (3)
Lx, Ly	0.060(5), 6.89 (7)	0.568 (5), 13.5 (1)	0.016 (6), 4.95 (3)
L11	0.49×10^{-1}	0.35×10^{-3}	0.31×10^{-1}
L22	0.46×10^{-1}	0.92×10^{-3}	0.39×10^{-1}
L33	0.42×10^{-2}	-0.23×10^{-2}	0.81×10^{-2}
L12,	-0.84×10^{-2}	-0.20×10^{-3}	-0.12×10^{-1}
L13	0.55×10^{-2}	-0.86×10^{-3}	-0.11×10^{-1}
L23	-0.13×10^{-1}	0.36×10^{-3}	0.95×10^{-2}
S/L, H/L	0.002, 0.0005	0.002, 0.0005	0.002, 0.0005
R_{wp}(%),R_{exp} (%)	5.24, 2.93	7.20, 4.77	6.82, 4.89
χ^2	3.201	2.277	1.944

Phase separation was only observed in the lower temperature region below T_v, where NTE occurs. Extraction of the unit cell volume of both phases was performed using the same 2-phase orthorhombic model at all temperatures and plotted in Fig. 5.13, together with the weight fractions calculated for both warming and cooling sequences against temperature (Fig. 5.13 inset). It is apparent from the figure that the phase that undergoes NTE becomes the major phase. The weight fraction of phase 1 obtained at 5 K on warming up measurements (93%) turned out to be higher than that obtained on cooling down measurements (73%).

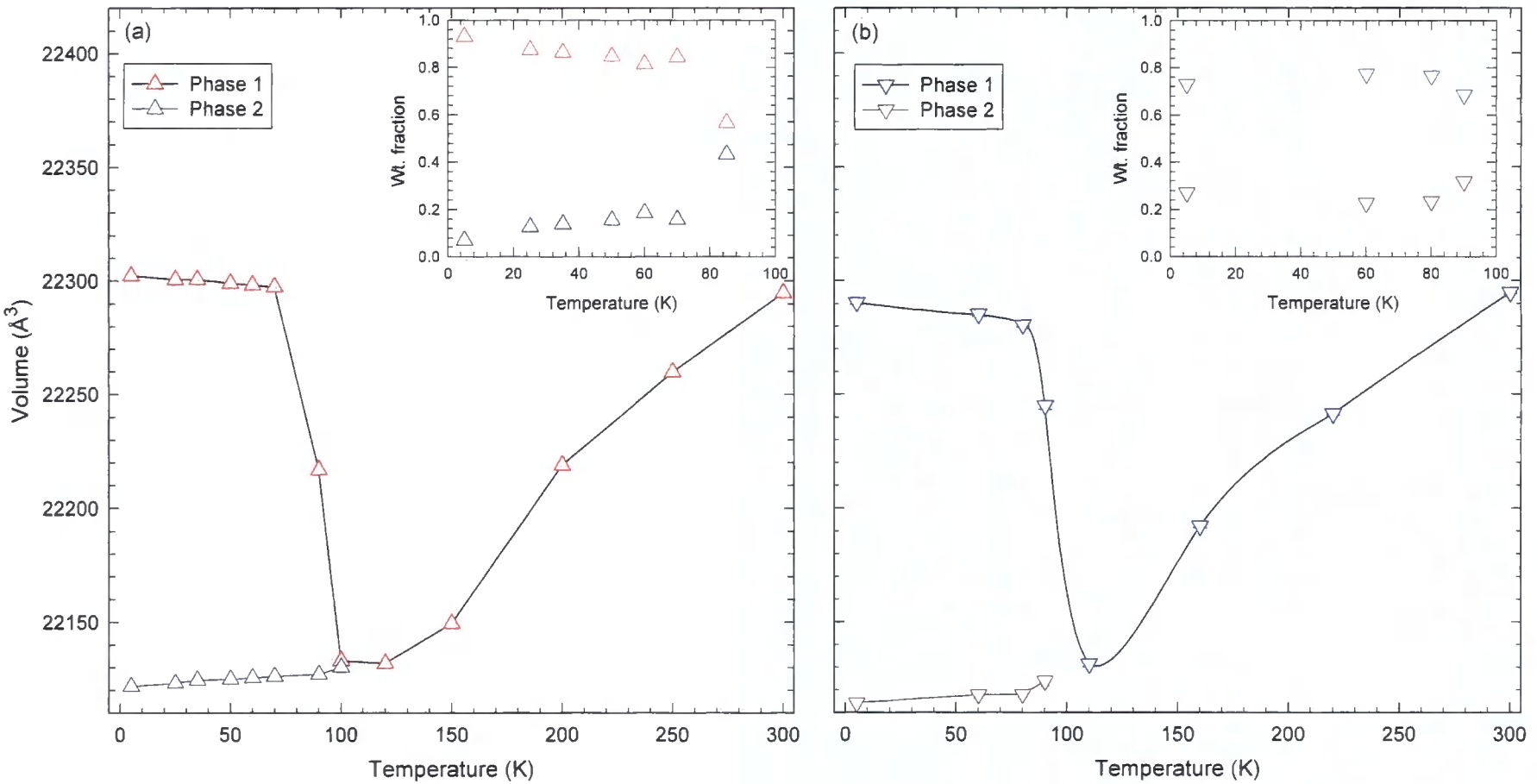

Fig. 5.13. Temperature evolution of the unit cell volume of $(Sm_{5/6}Ca_{1/6})_{2.75}C_{60}$ collected between (a) 5 and 300 K (warming up), and (b) 300 and 5 K (cooling down) [*inset*: calculated weight fractions of the two phases at low temperatures].

The thermal expansivity, α_V (= $\mathrm{d}\ln V/\mathrm{d}T$), of phase 1 for the two measurements is shown in the Fig. 5.14.

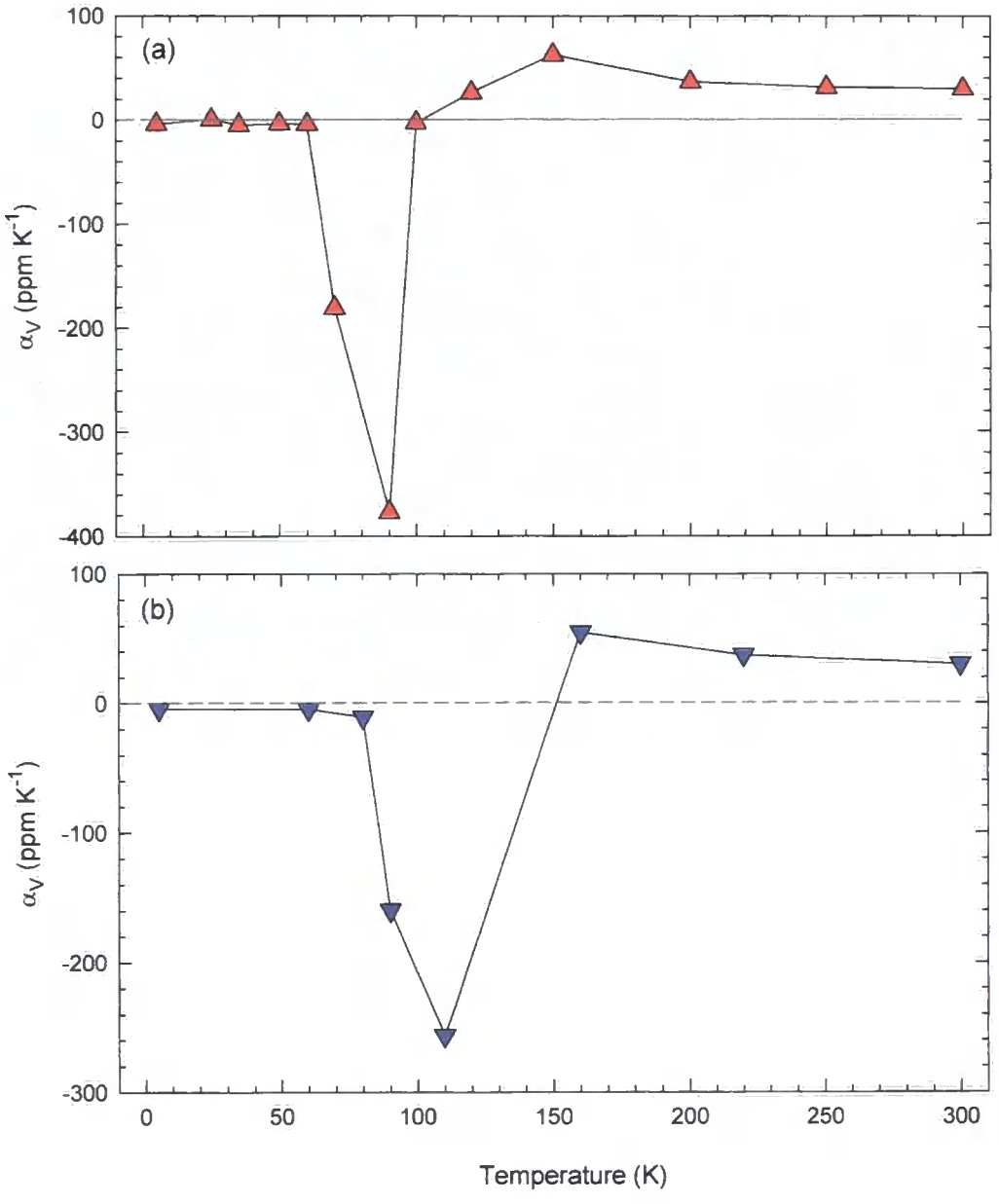

Fig. 5.14. Temperature dependence of the coefficient of thermal expansivity, α_V (= $\mathrm{d}\ln V/\mathrm{d}T$) of (a) warming and (b) cooling measurements.

As can be seen in the figure, an unexpected feature here, compared to $Sm_{2.75}C_{60}$[2], $Yb_{2.75}C_{60}$[4], and $Eu_{2.75}C_{60}$ [Chapter 4], is that the thermal

expansivity in the warming up measurements stays almost zero on heating up to 60 K, and then goes through the maximum value of -380 ppm/K at 120 K. Similarly, in the slowly cooled measurements, α_V is at its maximum value of -260 ppm/K around 110 K and then rapidly approaches zero at 60 K and slowly decrease as it was cool down to 5 K. The overall decrease (increase) in unit cell volume is 0.76% (0.71%) on heating (cooling) from 5 to 120 K (110 to 5 K). The NTE behaviour and phase separation disappear above 110 K and the unit cell volume increases on heating to 300 K at a rate of ~40 ppm/K.

ii) $(Sm_{2/3}Ca_{1/3})_{2.75}C_{60}$

The diffraction profile of $(Sm_{2/3}Ca_{1/3})_{2.75}C_{60}$ (x = 1/3) at room temperature was first measured outside the cryostat, then the sample was cooled down to 5 K inside the cryostat at a rate of 5 K/min (rapid cooling). The X-ray diffraction profile was collected when the temperature stabilised at 5 K (λ = 0.8503 Å). The sample was then slowly heated using a stepwise heating protocol with an average rate of 0.3 K/min while the diffraction profiles were collected at the each step until the temperature reached 110 K. Then the rate was increased to 1.10 K/min up to room temperature. Investigation of the hysteretic response of the temperature evolution of the unit cell parameters was carried out by applying a slow cooling down protocol (average rate of 1.05 K/min down to 130 K, 0.57 K/min down to 60 K, and 0.87 K/min down to 5 K) (λ = 0.41274 Å). These measurements were performed at a different experimental period. The obtained data were rebinned to a step of 0.003° for further analysis.

Fig. 5.15 shows the temperature evolution of the (444) Bragg's reflection of the selected profiles for both warming up (left) and cooling down (right) measurements. As the wavelength used in the two measurements was different, the profiles are plotted as a function of Q. It is immediately apparent that NTE is present in both measurements. More specifically, in the case of warming up, the (444) Bragg reflection continuously shifts to higher angle as temperature increases above 5 K, then the direction of shift changes towards lower angle at 130 K up to room temperature. Similarly, in the case of slow cooling measurements, the peak shifts towards higher angles down to 110 K, then back towards lower angles on further cooling down to 5 K. However, it should be noted that when the sample is at room temperature, the peak shift in the high temperature region is still not large enough to recover the peak position observed at 5 K. NTE is observed in both cases with no observable change in crystal symmetry below critical temperature, T_v, of approximately 130 K. Furthermore, unlike the case of $(Sm_{5/6}Ca_{1/6})_{2.75}C_{60}$, no clear phase separation below the critical temperature was observed in both measurements, while peak broadening was still observed in the same temperature range. The broadening of the peak becomes maximum (larger by ~30% and ~8% for warming up and cooling down measurements, respectively) at 90 K in both measurements. This may imply that the presence of local structural inhomogeneities is less important in $(Sm_{2/3}Ca_{1/3})_{2.75}C_{60}$.

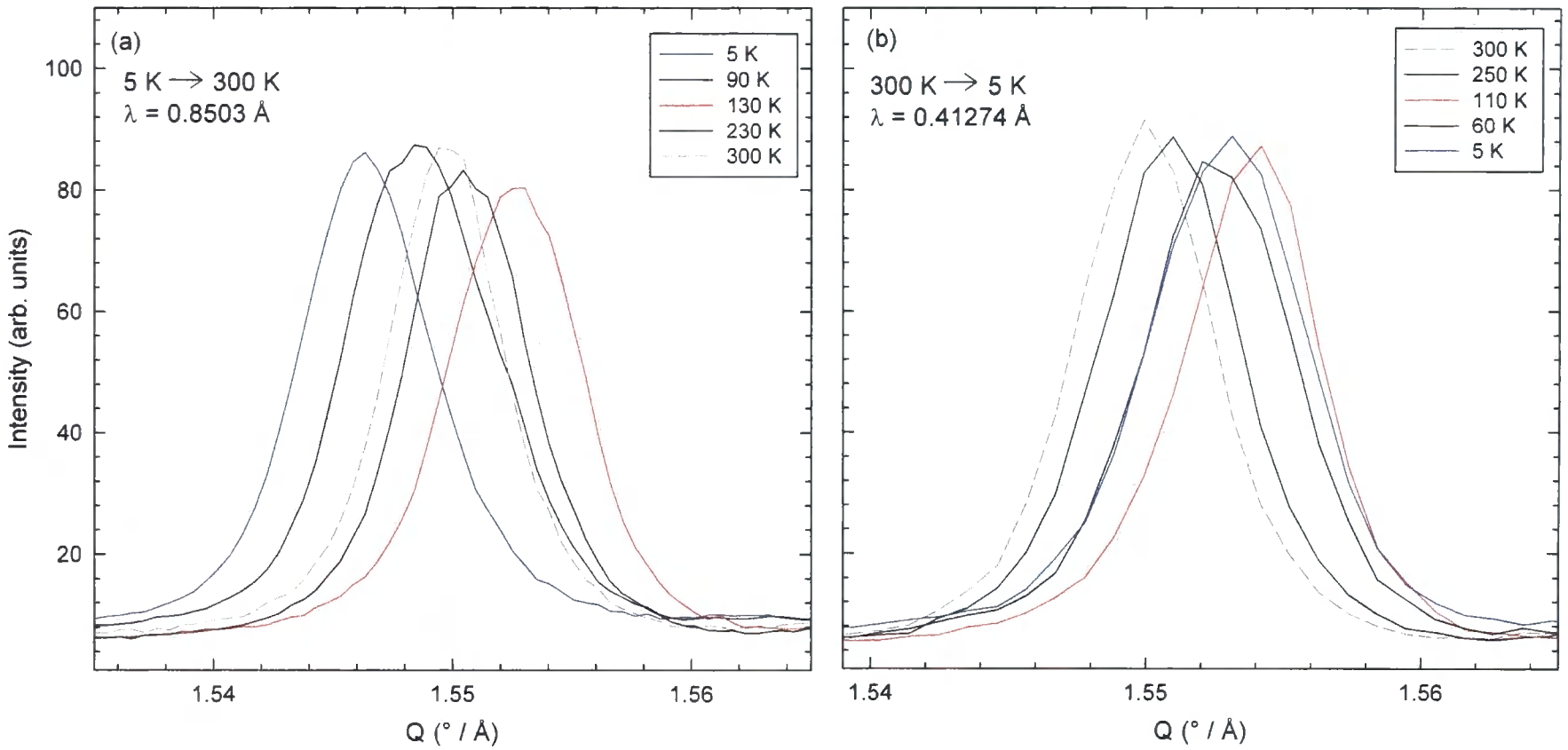

Fig. 5.15. Selected region of the synchrotron X-ray powder diffraction profiles of $(Sm_{2/3}Ca_{1/3})_{2.75}C_{60}$, showing the temperature evolution of the (444) Bragg reflection (a) on heating from 5 to 300 K and (b) on cooling from 300 to 5 K.

Rietveld refinements were first carried out for the diffraction profiles at 5 K obtained on both rapidly and slowly cooled measurements using 2-phase and single-phase model, respectively. The extracted lattice constants from each diffraction profile are given in Table 5.5 together with the unit cell volume and agreement factors.

Table 5.5. The extracted values for the lattice constants and the unit cell volume for $(Sm_{2/3}Ca_{1/3})_{2.75}C_{60}$ at 5 K, obtained for rapidly and slowly cooled protocols, and at room temperature.

Temperature:	(rapid cooling)* 5 K	300 K	(slow cooling) 5 K
Instrumental	parameters:		
λ (Å)	0.8503	0.8503	0.41274
Δ2θ (×100, °)	0.26 (1)	0.45 (1)	0.44 (1)
2θ range (°)	3.5-27	2.5-30	1.7-19
Step size (°)	0.003	0.003	0.003
Lattice	parameters:		
a (Å)	28.1577 (4)	28.0954 (3)	28.0459 (5)
b (Å)	28.1774 (4)	28.1038 (3)	28.0656 (5)
c (Å)	28.1380 (4)	28.0869 (3)	28.0263 (5)
V (Å^3)	22325.0 (9)	22177.1 (7)	22060.2 (1.3)
Wt. Fraction (%):	0.911 (1)	- (-)	- (-)
Peak profile	coefficient:	Type 3	
GU	366.0(2)	308.6(3),	220.3(3)
GV, GW	-15.2(2), 0.34 (1)	-27.3 (4),1.06 (1)	-4.73(2),0.14 (1)
Lx, Ly	1.06 (2), 11.1 (2)	1.18(1), 13.5 (1)	0.43 (1), 17.8 (2)
S/L, H/L	0.005, 0.0005	0.005, 0.0005	0.005, 0.0005
L11	0.37×10^{-3}	-0.16×10^{-1}	0.44×10^{-2}
L22	0.36×10^{-2}	0.51×10^{-3}	0.13×10^{-2}
L33	-0.59×10^{-2}	-0.14×10^{-2}	-0.23×10^{-2}
L12	-0.41×10^{-2}	-0.17×10^{-2}	0.27×10^{-3}
L13	-0.45×10^{-3}	-0.16×10^{-3}	-0.27×10^{-3}
L23	0.15×10^{-3}	0.24×10^{-4}	0.27×10^{-3}
Sm(3)-C_{60} (Å)	2.664 (4)	2.675 (2)	2.65 (1)
Agreement	factors:		
R_{wp}(%),R_{exp}(%),χ^2	5.14, 2.10, 6.01	4.96, 4.50, 1.21	7.84, 6.66, 1.39

*Values shown here are for the major phase only, as the weight fraction of the minor phase was almost negligible (<5%).

The lattice dimensions and unit cell volume at 5 K of the rapidly cooled sample is larger than those at 300 K, while for the slowly cooled sample they were smaller than those at 300 K. Extraction of the lattice constants and the unit cell volume at all other temperatures were carried out using the same method, where the asymmetric peak profiles in the low temperature region due to the local structural inhomogeneities were accounted for by introducing a second-phase (Fig. 5.16, Table 5.6). The temperature evolution of the unit cell volume is shown in Fig. 5.17.

Table 5.6. The extracted results of the lattice dimensions and profile parameters from the diffraction profile of $(Sm_{2/3}Ca_{1/3})_{2.75}C_{60}$ at 50 K for both the major and minor phases.

T= 50 K	*Pcab* (option 2)	
Instrumental parameters:		Agreement factors:
λ (Å)	0.8503	R_{wp}: 5.04%
Δ2θ (×100, °)	0.38 (1)	R_{exp}: 2.28%
2θ range (°)	3.3-27	χ^2 : 4.893
Step size (°)	0.003	
Lattice parameters:	**Major phase**	**Minor phase**
a (Å)	28.1470 (4)	28.0601 (3)
b (Å)	28.1667 (4)	28.1038 (3)
c (Å)	28.1273 (4)	28.0869 (3)
V (Å^3)	22299.6 (9)	22093.8 (2.2)
Wt. Fraction (%):	0.777 (1)	0.223 (3)
Peak profile coefficient:	Type 3	Type 3
GU, GV,	229.8 (7), -10.0 (8),	385.9 (5), -35.2 (2),
GW	0.947 (5)	2.80 (2)
Lx, Ly	0.60 (1), 11.53 (2)	0.26 (2), 9.983 (2)
S/L, H/L	0.005, 0.0005	0.005, 0.0005
L11	0.52×10^{-2}	0.29×10^{-2}
L22, L33	0.23×10^{-2}, -0.25×10^{-2}	0.16×10^{-2}, -0.30×10^{-2}
L12, L13,	-0.26×10^{-2}, -0.21×10^{-3}	-0.88×10^{-3}, -0.92×10^{-3}
L23	0.19×10^{-3}	0.41×10^{-3}
R_{wp} (%), R_{exp} (%), χ^2	2.70, 2.50, 1.04	9.27, 3.31, 7.38

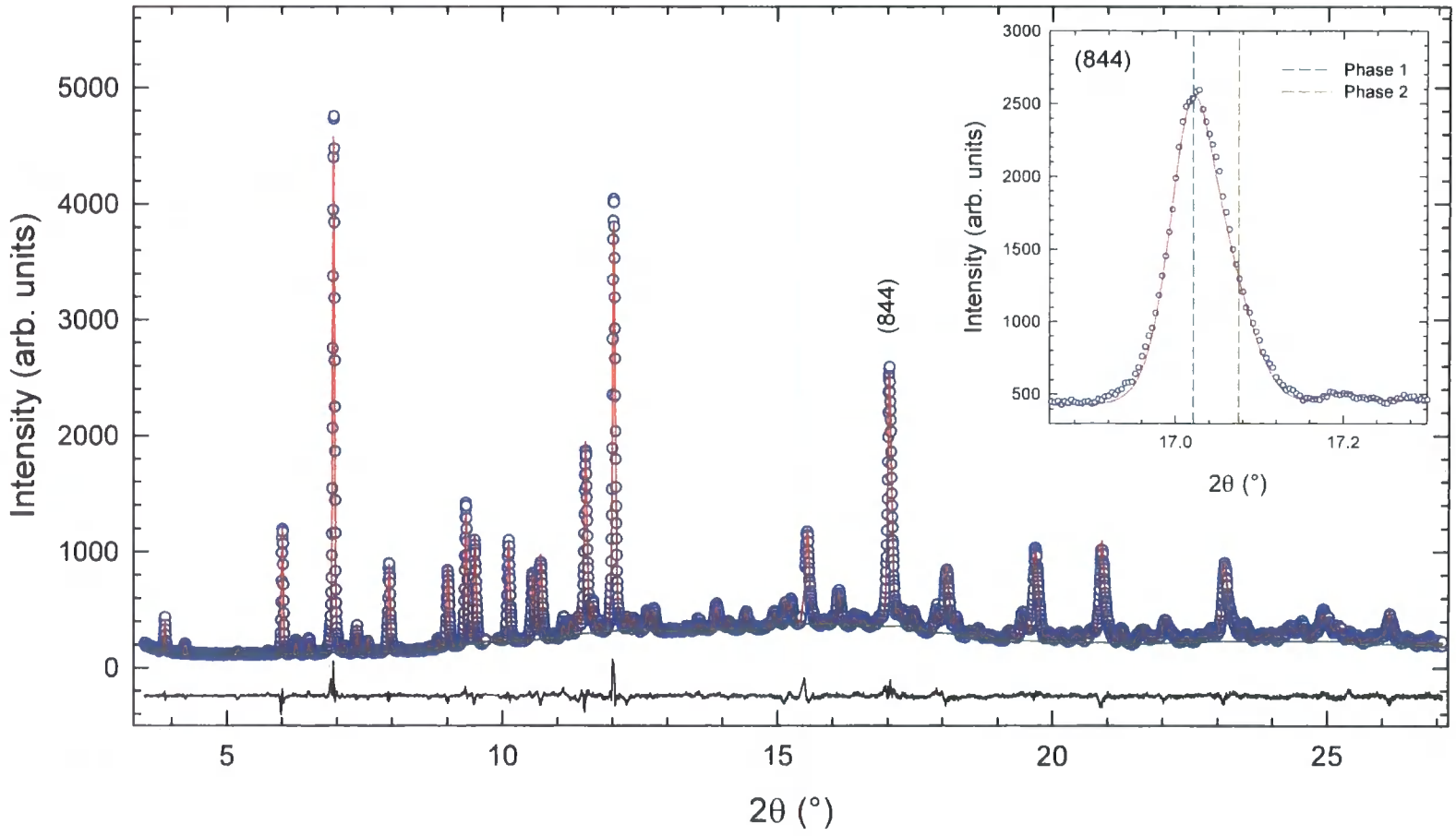

Fig. 5.16. Result of the Rietveld refinements on the profile of $(Sm_{2/3}Ca_{1/3})_{2.75}C_{60}$ at 50 K (warming up from 5 K) [*inset*: blow up of asymmetric (844) Bragg's peak fitted using 2-phase model].

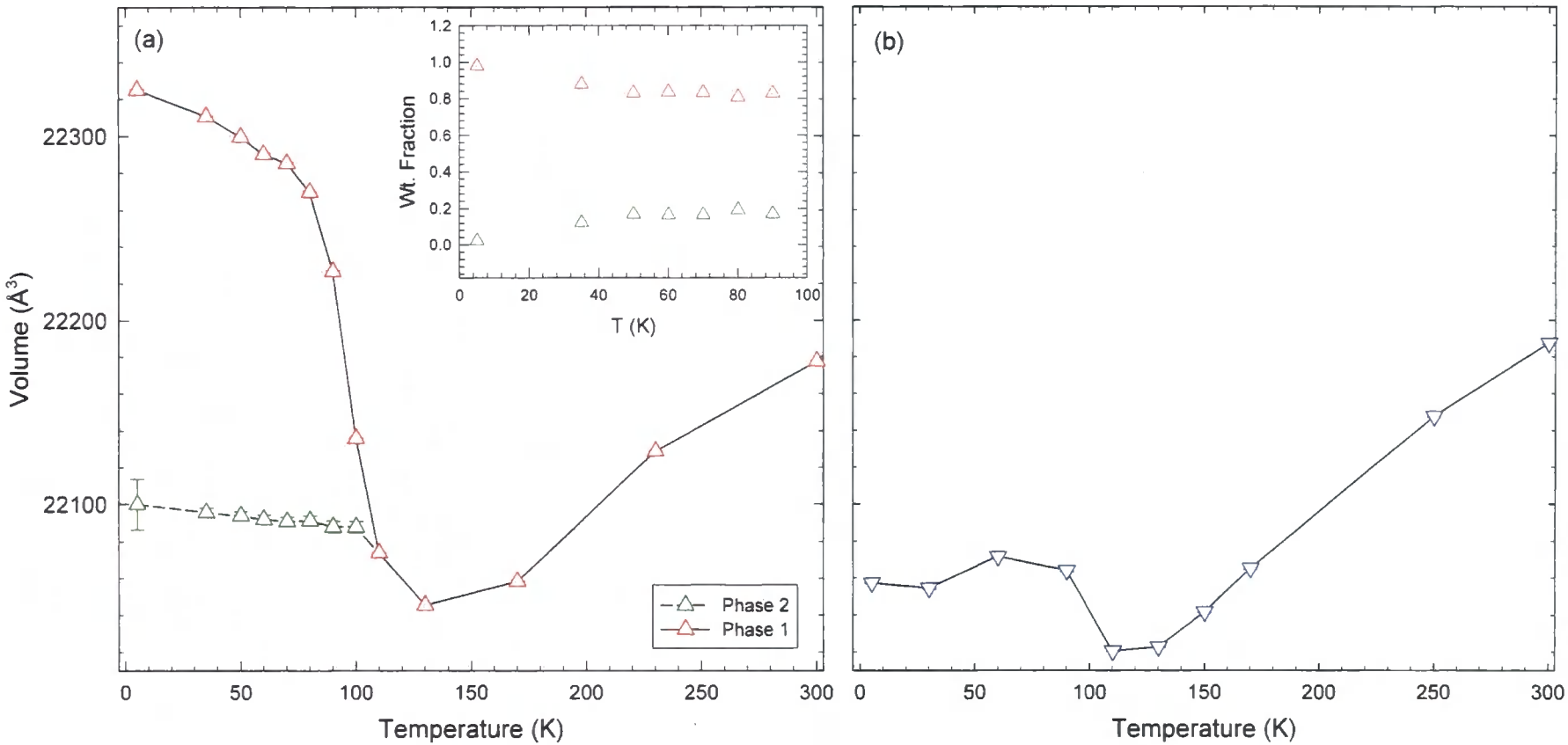

Fig. 5.17. Temperature evolution of unit cell volume of $(Sm_{2/3}Ca_{1/3})_{2.75}C_{60}$ collected between (a) 5 and 300 K (warming up), and (b) 300 and 5 K (cooling down) [*inset*: calculated weight fractions between two phases at low temperature region].

The thermal expansivity, α_V (= dln V/d T), of phase 1 from both measurements are shown in the figure below (Fig. 5.18).

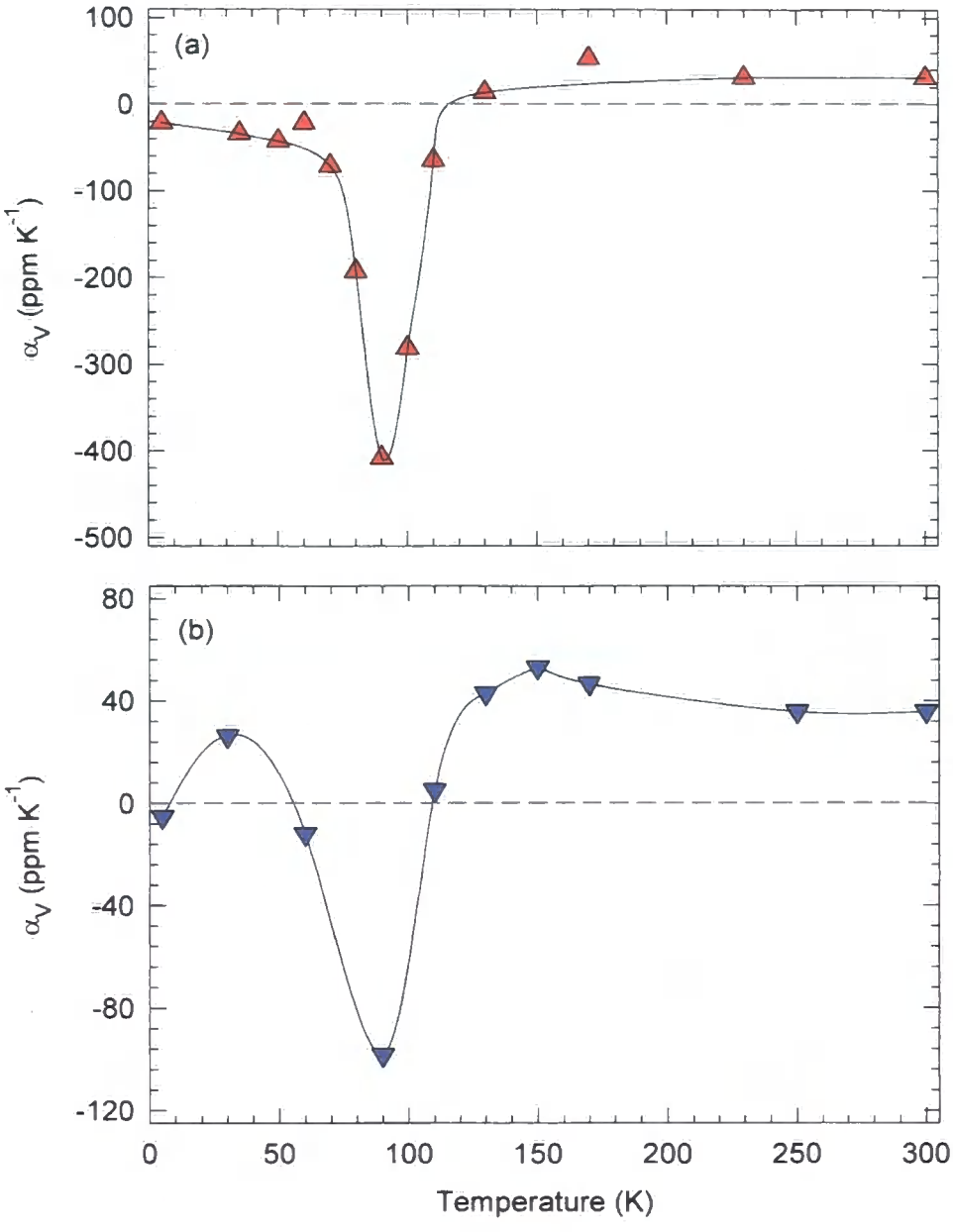

Fig. 5.18. Temperature dependence of the coefficient of thermal expansivity, α_V of (a) warming up measurements and (b) slowly cooled measurements.

The lattice dimensions of the warming up phase first contracts slowly (at an average rate of -23 ppm/K) in a continuous fashion as the sample slowly

warms up (average rate of 0.3 K/min) until 70 K, where the contraction rate rapidly increases until it goes through a maximum of -410 ppm/K at 90 K and then approaches zero at ~130 K. This behaviour leads to an overall decrease in lattice size of 1.25% on heating from 5 to 130 K, where the thermal expansivity is negative throughout this temperature range. The sign of the thermal expansivity changes to positive at 130 K and the lattice constants increase on further heating up to 300 K at an average rate of 30 ppm/K. The peak broadening that was observed below 130 K also disappears and followed by ~30% sharpening compared to the maximum peak width observed at 90 K. On the other hand, the lattice dimensions of the slowly cooled phase (at a rate of 1 K/min) shows that it first contracts at an average rate of 45 ppm/K on cooling from 300 to 100 K, where the rate approaches zero and starts to expand on further cooling (-100 ppm/K) down to 60 K showing an overall increase in lattice size of 0.23%. On further cooling, α_V becomes positive again (25 ppm/K) and the lattice size decreases by 0.07% between 60 and 5 K.

iii) $(Sm_{1/3}Ca_{2/3})_{2.75}C_{60}$

This sample was originally prepared with a target composition, $(Sm_{1/2}Ca_{1/2})_{2.75}C_{60}$ by direct reaction of stoichiometric quantities of degassed C_{60}, Ca and Sm powder. However, the actual composition of the sample was found by RBS measurements to be $(Sm_{1/3}Ca_{2/3})_{2.75}C_{60}$. The agreement factors for the Rietveld refinement of the high-resolution synchrotron X-ray powder diffraction at 300 K was also improved by using the RBS-derived stoichiometry.

The sample was cooled down to 5 K at a rate of 5 K/min (rapid cooling).

The X-ray diffraction profile was collected when the temperature stabilised at 5 K (λ = 0.41274 Å). The sample was then slowly heated using a stepwise heating protocol with an average rate of 0.3 K/min while the diffraction profiles were collected at each step until the temperature reached 110 K, then the rate was increased to 0.83 K/min up to room temperature. The obtained data were rebinned to a step of 0.003° for further analysis.

Fig. 5.19 shows the temperature evolution of the (444) Bragg reflection at selected temperatures.

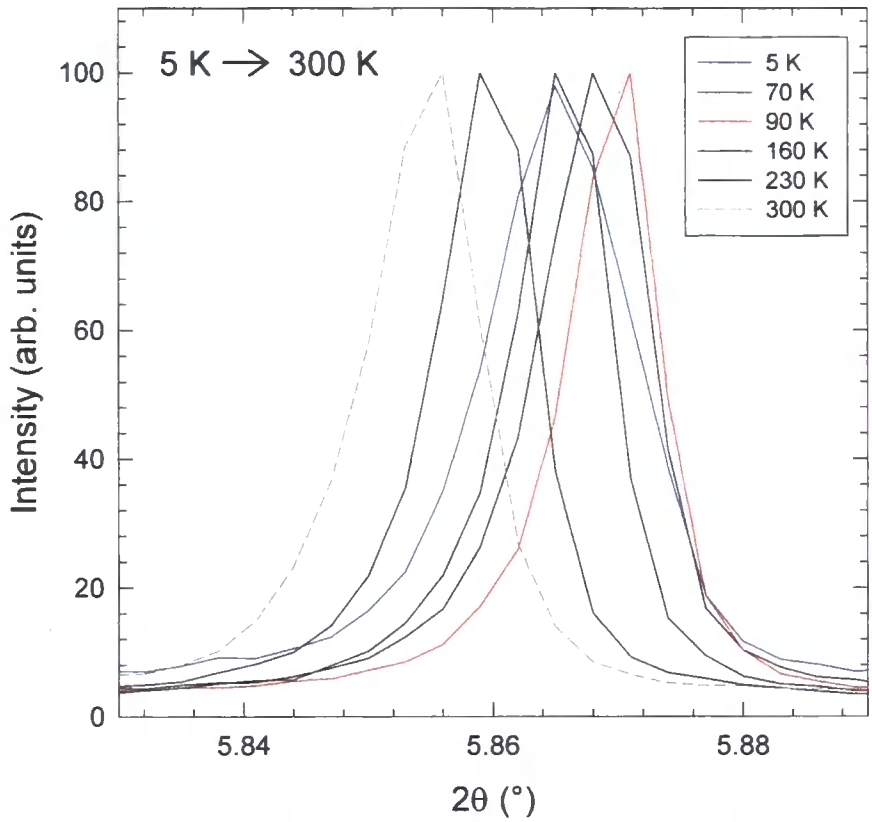

Fig. 5.19. Selected region of the synchrotron X-ray powder diffraction profiles of $(Sm_{1/3}Ca_{2/3})_{2.75}C_{60}$, showing the temperature evolution of the (444) Bragg reflection on heating from 5 to 300 K.

The angular position slightly shift towards lower angles between 5 and 20 K, then shifts continuously towards higher angle as the temperature

increases above 20 K, implying that the unit cell metrics decrease in a continuous fashion. At 100 K, the peak shift changes its direction towards lower angle and the lattice dimensions increase on further heating to room temperature. There was no observable change in the diffraction profiles at all temperature, which indicates that this behaviour is not accompanied by any change in crystal symmetry. However, the widths of the diffraction peaks in the low temperature range where NTE is observed are broader by ~40% compared to the average value at high temperature.

Extraction of the lattice constants (Fig. 5.20a) was performed by Rietveld refinement using a 2-phase orthorhombic model in the low temperature region to account for the broadening (Fig. 5.20 inset). A single phase model was used above the critical temperature. The results indicate the presence of local structural inhomogeneities causing phase separation associated with the rapid transformation of the material, possibly into Sm-rich and Ca-rich phases. The thermal expansivity of phase 1 (major phase) is plotted in Fig. 5.20b. It is positive between 5 and 20 K, it then becomes negative at 40 K, and increases in absolute value continuously on heating until it goes through a maximum of -200 ppm/K at 70 K, then rapidly approaches zero at 100 K. This results in an overall decrease in lattice dimensions of 0.34% on heating from 5 to 100 K. The thermal expansivity of phase 2 (minor phase), on the other hand, is positive throughout this temperature range, with an average rate of 3.7 ppm/K. On further heating above 100 K, phase separation is no longer observable and the lattice dimensions start to expand at a rate of ~40 ppm/K up to 300 K, producing a larger cell volume compared to that at 5 K.

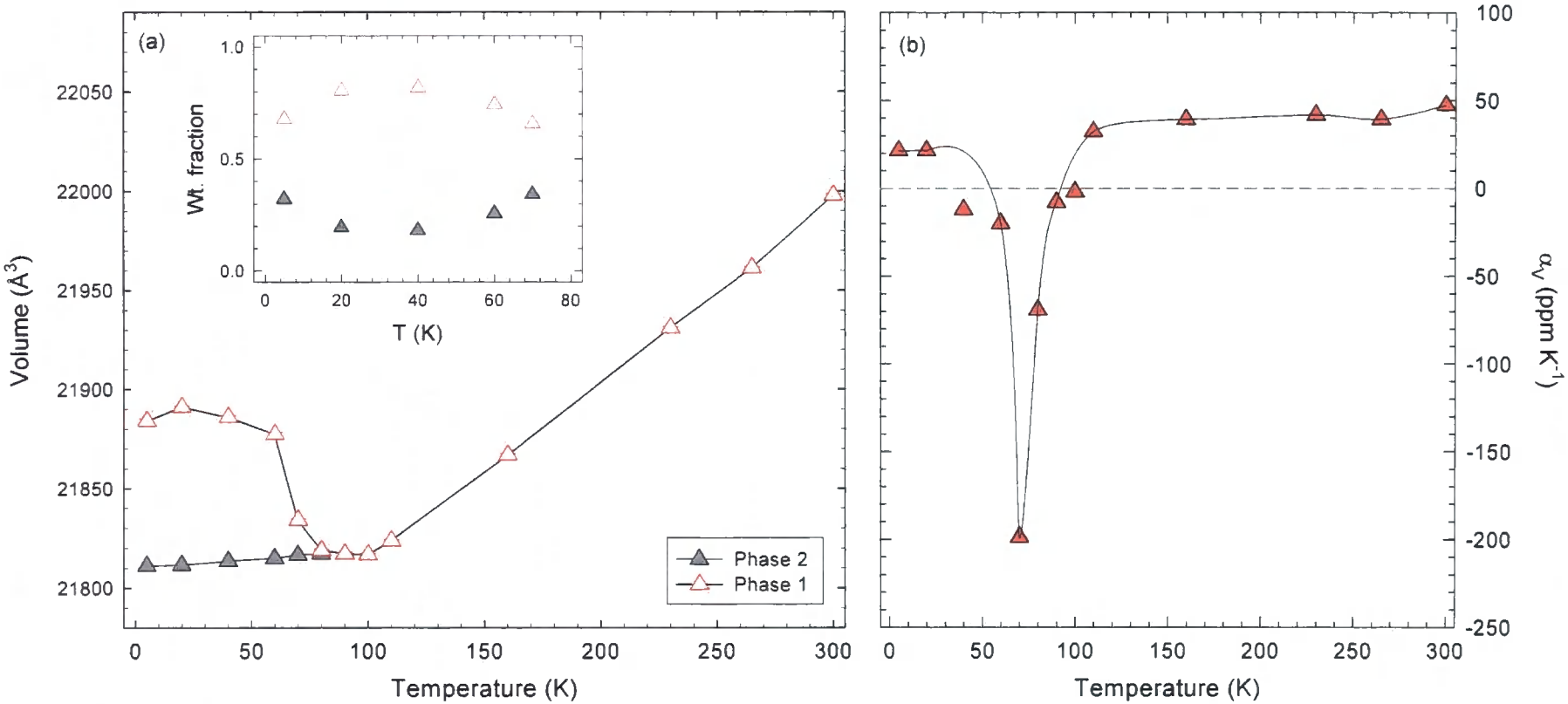

Fig. 5.20. Temperature evolution of (a) unit cell volume of $(Sm_{1/3}Ca_{2/3})_{2.75}C_{60}$ on heating of phase 1 (red triangle) and phase 2 (grey triangle) [*inset*: calculated weight fractions between two phases at low temperature region] and (b) the coefficient of thermal expansion of phase 1.

iv) $Ca_{2.75}C_{60}$

The temperature evolution of the structural properties of the alkaline-earth fulleride, $Ca_{2.75}C_{60}$, was also studied between 5 and 300 K. The sample was cooled down to 5 K at a rate of 5 K/min and the diffraction profile was collected using a wavelength, λ = 0.41274 Å. The sample was then slowly heated by a stepwise heating protocol with an average rate of 0.4 K/min, while the diffraction profiles were collected every 50 K up to 300 K.

The angular positions of the diffraction peaks shift continuously to lower angles as the temperature increases above 5 K, implying the lattice dimensions expand with no anomalous expansion behaviour. Rietveld refinements at all temperatures were carried out in *Pcab* in order to be consistent with other samples. The temperature evolution of the unit cell volume is plotted in Fig. 5.21, while the thermal expansivity exhibits a positive value throughout. The lattice dimensions first slowly increase as temperature increases from 5 to 100 K (5 ppm/K), then the rate of expansion increases to an average rate of 25 ppm/K up to 300 K, resulting in a volume expansion of ~0.55%, which is comparable to that observed in other metal fulleride samples [17].

The occurrence of the lattice anomalies due to the changes in external stimuli (temperature, pressure) reflects the complex electronic response of the 4*f* orbitals. Hence, the absence of the lattice anomalies in $Ca_{2.75}C_{60}$ confirms the importance of the electronically active 4*f* sublattice in driving the complex responses observed.

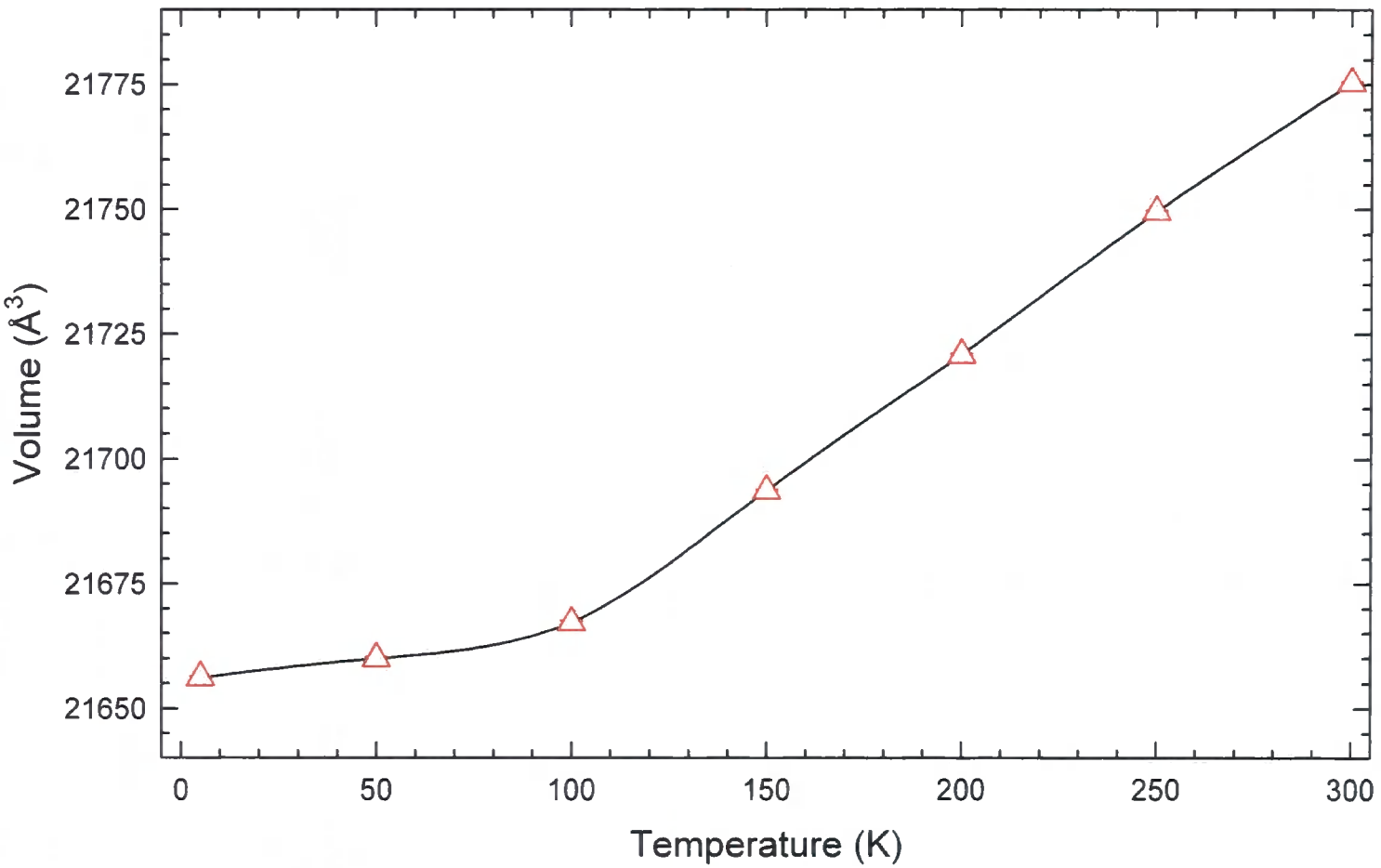

Fig. 5.21. Temperature evolution of unit cell volume of $Ca_{2.75}C_{60}$ between 5 and 300 K, showing no anomalous lattice expansion on heating.

5.2.5 Direct spectroscopic investigation of the rare-earth valence

Investigation of the valence state of the rare-earth fullerides by direct spectroscopic techniques is expected to offer important information for the description of the electronic structure of these materials. In rare-earth based materials, the valence is directly related to the number of $4f$ holes n_h by $\nu = 2 + n_h$, which depends on the $4f/5d$ hybridisation strength, also known as the characteristic Kondo temperature, T_K. The intermediate valence in rare-earth solids reflects the hybridisation of the energetically close RE^{2+} ($4f^n5d^0$) and RE^{3+} ($4f^{n-1}5d^1$) configurations, which can be varied by chemical doping, temperature, and pressure.

Direct or indirect experimental information on the $4f$ population of the rare-earth ions in the fulleride salts can be probed using various spectroscopic techniques. Among them, the temperature and pressure evolution of the valence state for various rare-earth based materials was successfully obtained by X-ray absorption spectroscopy (XAS) at the rare-earth metal L_3 absorption edges with the use of third-generation synchrotron X-ray sources and improved detection systems [18, 19]. In the present work, the high-resolution XAS technique was employed for direct study of intermediate valence and its evolution with change in temperature in $(Sm_{2/3}Ca_{1/3})_{2.75}C_{60}$. The same batch of sample was also examined using the resonant inelastic X-ray scattering (RIXS) technique to obtain information on the $4f$ occupation number. Both experiments were performed on beamline ID16 at ESRF, Grenoble, France and the obtained results were compared for consistency between two different measurements.

i) XAS at the Sm L_3 edge

The XAS measurements at the Sm L_3 absorption edge in the total fluorescence yield (TFY) mode involves the excitation of a Sm $2p_{3/2}$ core electron, which is excited into unoccupied Sm $5d$ states. Those electrons are excited from intermediate valence ground state of the Sm, a hybrid state $|\Psi_g\rangle = \alpha|Sm^{2+}\rangle + \beta|Sm^{3+}\rangle$, to the final $2p^54f^6$ and $2p^54f^5$ states, which are partially split in energy by the strong Coulomb interaction with the $2p$ core hole. The integrated scattered intensity is recorded as the incident energy, $h\nu_{in}$, varies through the L_3 absorption edge, which in turn can yield direct information on the local electronic properties at the Sm site. Fig. 5.22 shows a schematic total energy scheme for the Sm L_3 XAS process and the spectra of $(Sm_{2/3}Ca_{1/3})_{2.75}C_{60}$ at 300 K.

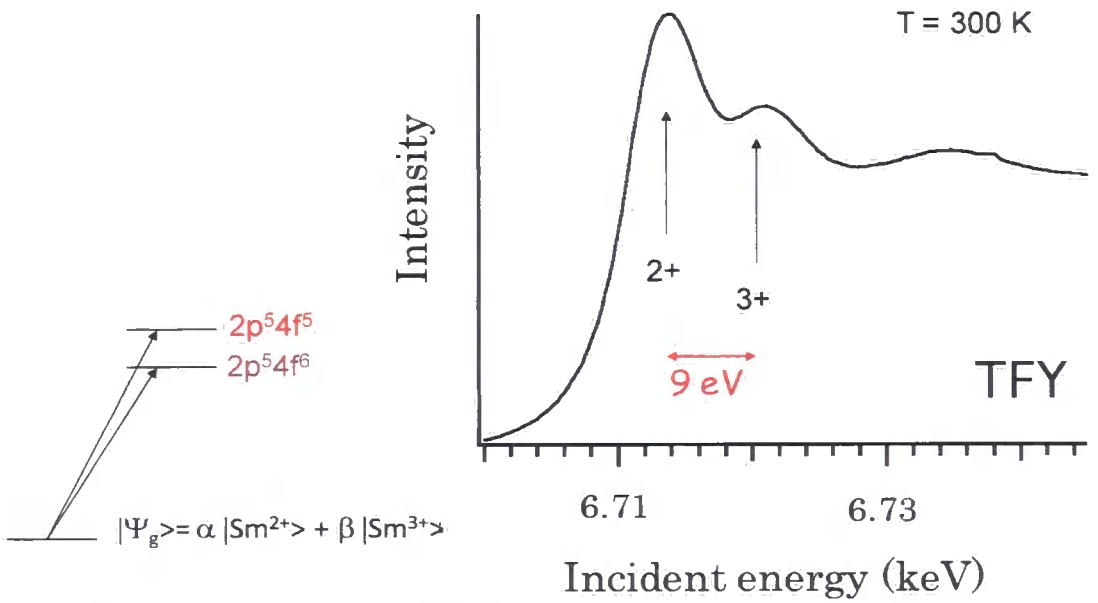

Fig. 5.22. (Left) Energy level scheme for the Sm mixed valence state in $(Sm_{2/3}Ca_{1/3})_{2.75}C_{60}$. The arrows indicate the relavant XAS transitions. (Right) TFY Sm L_3 XAS spectgra of $(Sm_{2/3}Ca_{1/3})_{2.75}C_{60}$ at 300 K.

The spectra were obtained by integrating the scattered intensity as a function of incident energy. Two main structures are observed at around 6713 and 6722 eV, separated by the Coulomb interaction energy ($Q_{pf} \sim 9$ eV) corresponding to the difference in energy of the two final states of $2p^5 4f^5$ and $2p^5 4f^6$ character. The observed values are comparable those obtained for various Sm-based Kondo insulators [20]. The relative intensity of these structures provides a direct measure of the average rare-earth valence in the material. However, due to the short lifetime of the Sm $2p$ hole, the XAS spectra are subject to intrinsic energy broadening. An overall narrowing of the spectral structures can be achieved by detecting the signal from a radiative decay channel with a final state $3d$ core hole, that is the $2p$ hole is filled by a $3d$ core electron, and the intensity of the peak emission is monitored while scanning the incident energy [21]. This is known as high-resolution partial fluorescence yield X-ray absorption spectroscopy (PFY-XAS) mode. In this case, the intensity of the $L_{\alpha 1}$ de-excitation ($2p^5 3d^{10} + h\nu_{in} \rightarrow 2p^6 3d^9 + h\nu_{out}$, $h\nu_{out} = 5636$ eV, Fig. 5.23) fluorescence is measured as the incident energy varies through the Sm L_3 edge. In the PFY spectra, the spectral broadening is determined by the longer lifetime of the shallower 3d hole, rather than by that of the deep $2p$ hole [22], thus providing narrower spectral features and significantly improved resolution.

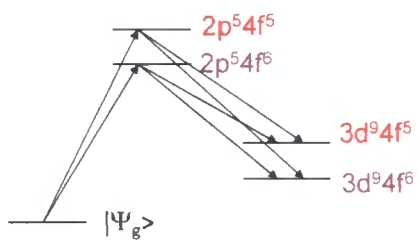

Fig. 5.23. Energy level scheme for Sm ion appropriate for PFY-XAS mode.

The temperature evolution of the PFY spectra of the $(Sm_{2/3}Ca_{1/3})_{2.75}C_{60}$ powder, sealed inside a thin glass capillary, was measured between 4 and 300 K. Consistent with the TFY mode measurements, two main structures from the Sm^{2+} and Sm^{3+} contributions were observed at 6713 eV and 6722 eV, respectively, at all temperature (Fig. 5.24). In the high-resolution PFY spectrum, the spectral contributions of the two features are better resolved and allow preliminary estimation of the Sm valence at each temperature. The estimated valence value from the relative intensity of the Sm^{2+} and Sm^{3+} features at 300 K indicates that the average valence state of the Sm ion is closer to +2 than to +3.

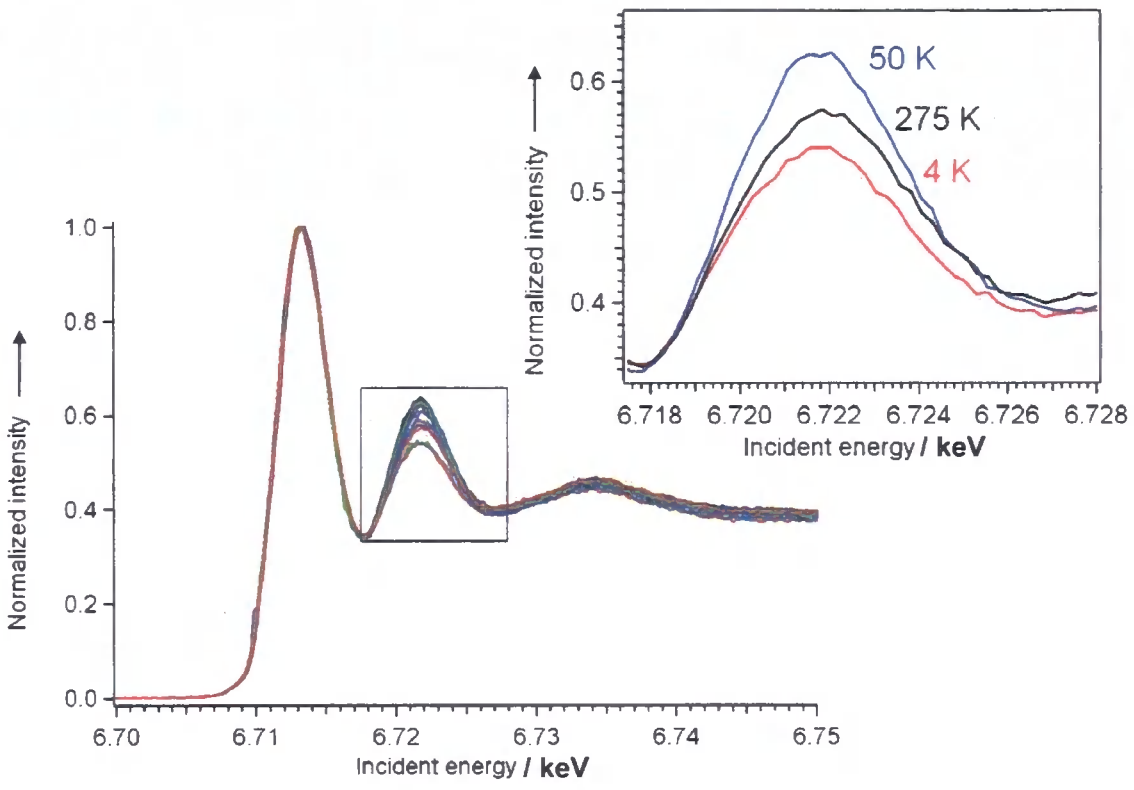

Fig. 5.24. Temperature dependence of the PFY Sm L_3 XAS spectra of $(Sm_{2/3}Ca_{1/3})_{2.75}C_{60}$ recorded between 4 and 300 K, where the spectral intensities are normalised to that of the Sm^{2+} feature (6713 eV). The inset shows a blow-up of the Sm^{3+} (6722 eV) spectral component at 4, 50 and 275 K.

As it can be seen from the inset in Fig. 5.24., the temperature evolution of the relative intensities, $I(Sm^{2+})/I(Sm^{3+})$, decreases in a continuous fashion below 300 K, which implies that the average Sm valence increases monotonically on cooling towards T_v. On further cooling, an abrupt phase transition occurs and the Sm state collapses to valence values even smaller than those at ambient temperature. The spectra of the same sample were collected several time using different cooling protocols. The evolution on the Sm^{3+} intensity as a function of temperature is plotted in Fig. 5.25, where the data were collected using slow cooling (~0.35 K/min) and slow warming protocols (~0.8 K/min).

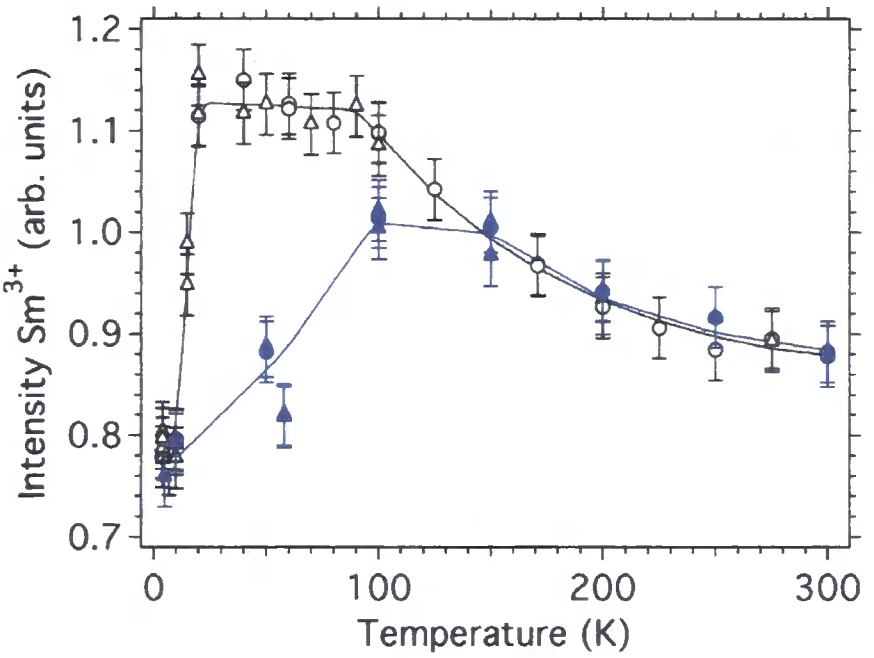

Fig. 5.25. Temperature evolutions of the Sm^{3+} intensity obtained by using slow cooling (~0.35 K/min, open symbols) and slow warming (~0.8 K/min, blue symbols) protocols.

In both cases, the $I(Sm^{2+})/I(Sm^{3+})$ ratio provides quantitative evidence for the occurrence of a first-order valence transition between Sm^{2+} and Sm^{3+} with an

apparent hysteretic behaviour between the two different sets of experimental measurements. The intensities of the Sm^{3+} features obtained on slow warming measurements shows that they increase gradually as temperature increases from 5 K towards 100 K ($Sm^{2+} \rightarrow Sm^{3+}$), which then decrease on further heating towards 300 K ($Sm^{3+} \rightarrow Sm^{2+}$). This behaviour is consistent with what has been observed in the diffraction measurements and the occurrence of NTE. Upon slow cooling from 300 K, the $I(Sm^{3+})$ continuously increases until the temperature approaches 90 K, then the value stays the same until a sharp valence transition occurs at $T_v \approx 20$ K to a state with increased Sm^{2+} character, which corresponds to the abrupt increase in the spectral weight of the Sm^{2+} feature.

ii) RIXS at the Sm L_3 edge

The resonant inelastic X-ray scattering (RIXS) experimental technique involves an incident X-ray photon, of which energies are tuned to excite a core electron, and an emitted X-ray photon of the same energy from de-excitation of the core-excited state. The energy of the incident photon can be tuned by measuring emission spectra at various $h\nu_{in}$ across, in the case of $(Sm_{2/3}Ca_{1/3})_{2.75}C_{60}$, the Sm L_3 absorption edge and plotting them as a function of the transferred energy, $h\nu_T = h\nu_{in} - h\nu_{out}$, that is, the excitation energy transferred from the photon to the solid (Fig. 5.26). The temperature (and/or pressure) dependence RIXS measurements are carried out by recording the $L_{\alpha 1}$ X-ray emission at fixed incident energies along the absorption edge. The temperature evolution of the Sm valence states can also be probed using RIXS technique, where final Sm electronic states of mainly $3d^9 4f^5$ and $3d^9 4f^6$

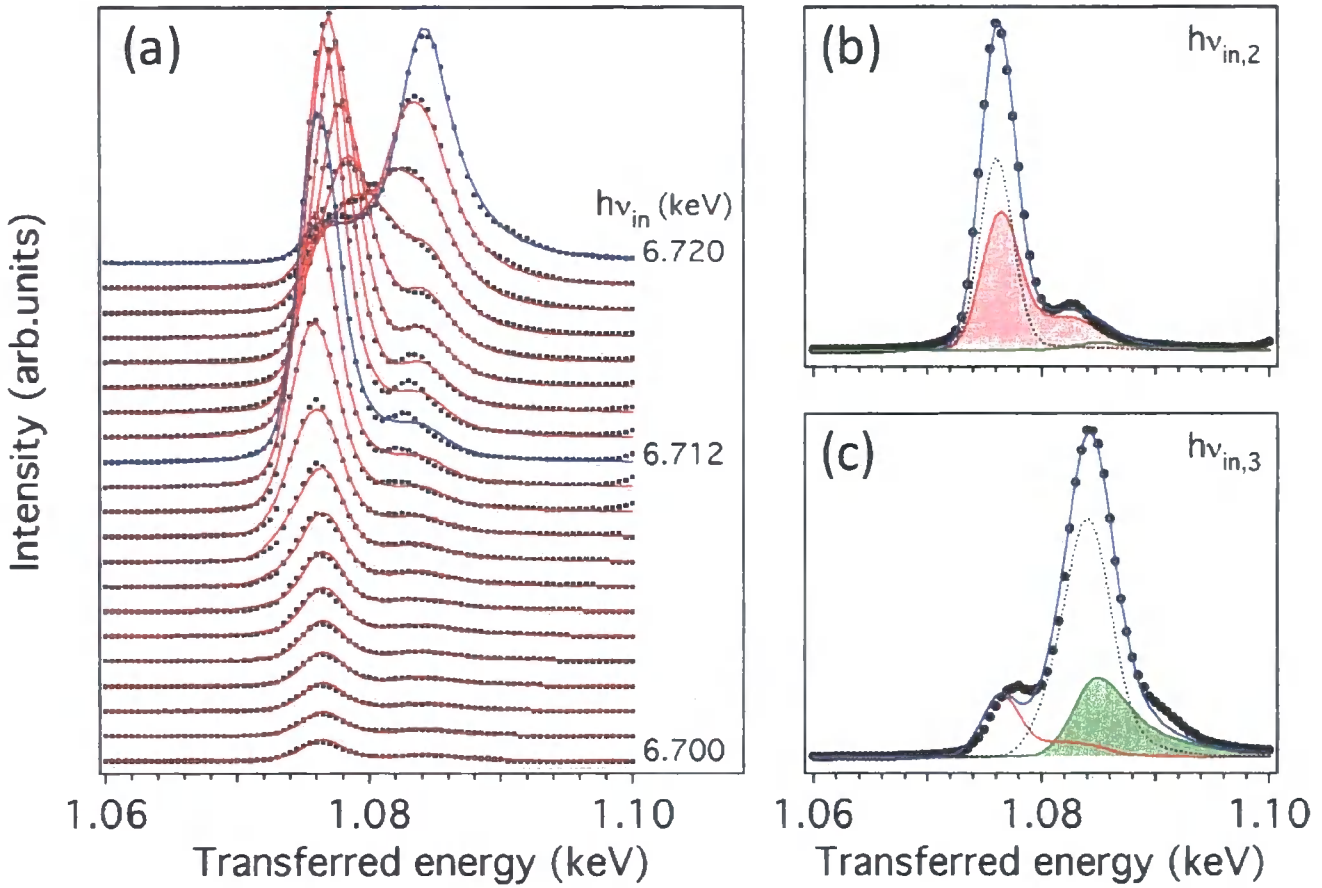

Fig. 5.26. (a) $L_{\alpha 1}$ RIXS spectra of $(Sm_{2/3}Ca_{1/3})_{2.75}C_{60}$ excited at 1 eV intervals along the Sm^{2+} feature. The Sm^{2+} and Sm^{3+} features are strongly and clearly peaked at $h\nu_{in}$ = 6712 eV and 6720 eV, respectively. Fit of RIXS spectrum at (b) 6712 eV and (c) 6720 eV.

character are reached radiatively from the XAS final states. By tuning the excitation energy through the maximum of the corresponding Sm^{2+} and Sm^{3+} features in PFY spectrum, the contributions from each feature are selectively and resonantly enhanced [23]. The obtained results are in excellent agreement with those from the PFY-XAS measurements, where the Sm^{2+} feature is strongly peaked at $h\nu_{in}$ = 6712 eV and Sm^{3+} signal at $h\nu_{in}$ = 6720 eV. The RIXS spectra were measured while cooling the sample from 300 to 4 K using the same slow cooling protocol (~0.35 K/min) and the valence state of Sm at each temperature can be evaluated by:

$$\nu = 2 + \frac{I\left(Sm^{3+}\right)}{I\left(Sm^{2+}\right) + I\left(Sm^{3+}\right)} \qquad \text{(Eqn. 5.6)}$$

where $I(Sm^{2+})$ and $I(Sm^{3+})$ are the intensities at their respective resonance corresponding to the weight of the divalent and trivalent Sm, by assuming that $I(Sm^{2+})$ and $I(Sm^{3+})$ are proportional to the number of atoms in each electronic configuration [24]. At room temperature, the average valence state of Sm is ~+2.20. The $I(Sm^{2+})/I(Sm^{3+})$ ratio of the two features in the RIXS spectra continuously decreases in intensity on cooling implying a decrease in the Sm $4f$ occupation number and an increase in the average valence which approaches a maximum value of ~+2.28 at 20 K. On further cooling below 20 K, a sudden valence change occurs and the Sm $4f$ occupation number abruptly decreases leading to an average valence of ~+2.19 at 4 K (Fig. 5.27). The obtained results are again in excellent agreement with those from the PFY-XAS measurements, confirming the electronic nature of the low temperature first-order valence transition.

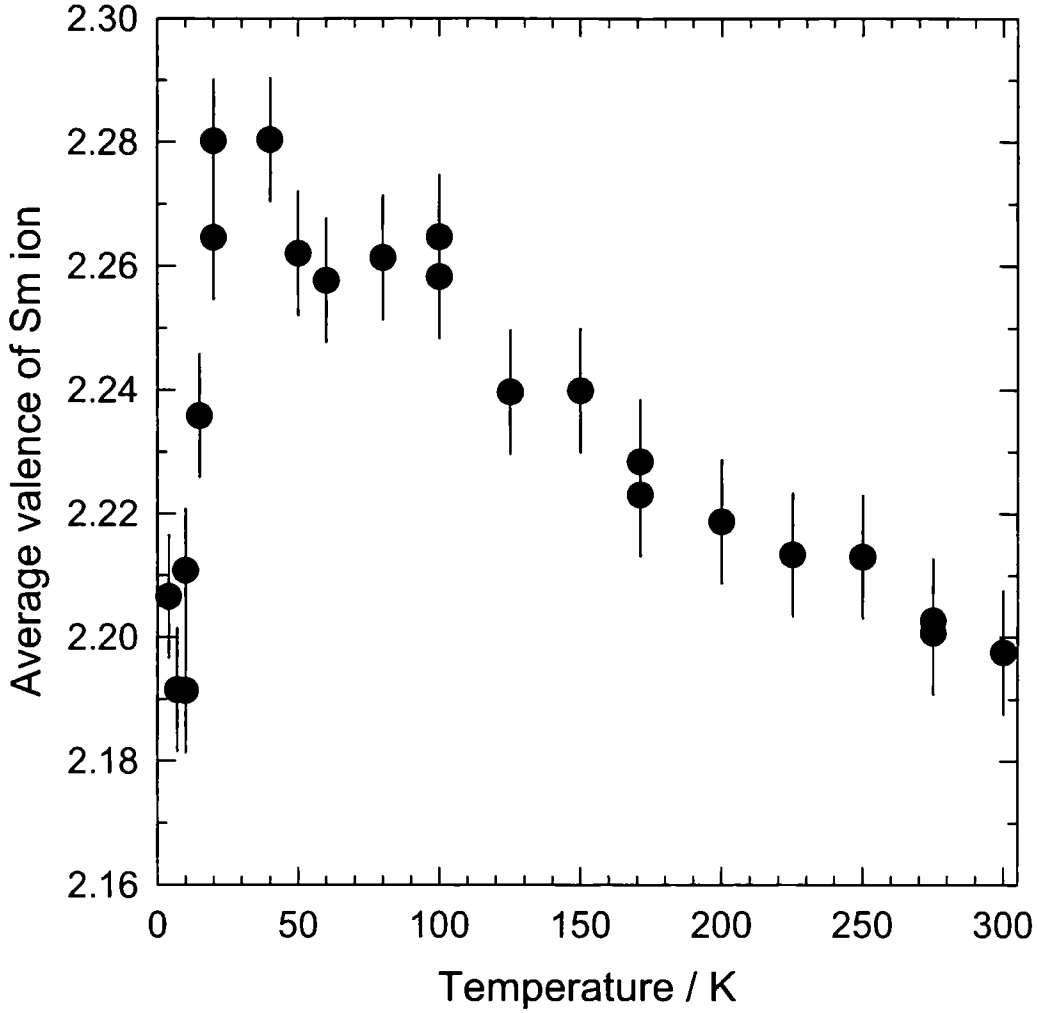

Fig. 5.27. Temperature evolution of the average valence of the Sm ions in $(Sm_{2/3}Ca_{1/3})_{2.75}C_{60}$ extracted from the $L_{\alpha 1}$ RIXS measurements across the Sm L_3 edge.

5.2.6 Discussion and Conclusion

Well-established synthetic techniques enabled systematic studies of the complex evolution of the structural and electronic properties of mixed valence Sm intercalated fullerides with stoichiometry $Sm_{2.75}C_{60}$ and their isostructural Ca substituted, $(Sm_{1-x}Ca_x)_{2.75}C_{60}$ $(0 \leq x \leq 1)$ analogues by using

synchrotron X-ray diffraction and absorption techniques. The temperature dependent structural properties of the $Sm_{2.75}C_{60}$ fulleride by high-resolution X-ray diffraction studies reveal the onset of NTE, a large lattice expansion on cooling, below critical temperature of T_v = 32 K [2]. This anomalous lattice response of the lattice size at low temperature have been rationalised in terms of the change in the average Sm oxidation state induced by a first-order valence transition between Sm^{2+} and Sm^{3+} states. It has been also proposed that the driving force of the valence change is of electronic origin, where electrons are thermally transferred between the Sm 4*f* band and the t_{1u} band of C_{60} by applying external temperature change. As expected, analogous electronic instabilities accompanied by anomalous lattice response were encountered for other isostructural $RE_{2.75}C_{60}$ fullerides, where Sm ions are substituted by Eu and Yb ions. Consistent with this picture, anomalous expansion was not observed for $Ca_{2.75}C_{60}$ fulleride which lacks an electronically active 4*f* sublattice, instead, its lattice contracts between 300 and 5 K by 0.55%.

The NTE behaviour was sensitively affected by changing the nature of the rare-earth cation from Sm to other substituent metal. For instance, the onset temperature of the NTE, the critical temperature T_v, increases significantly from 32 K in $Sm_{2.75}C_{60}$ to a maximum of 130 K for Ca substituted fullerides. Similarly, considerable effect can be seen in the magnitude of the volume inflation, which sensitively depends on the concentration of Ca ions substituted (Table 5.7).

Table 5.7. The extracted values for the unit cell volume at 5 K, the critical temperature, and the change in the volume during NTE. w denotes the data obtained on warming up measurements and c labels the data obtained on cooling down measurements.

Sample	Volume_5 K (Å^3)	T_v (K)	$\Delta V/V$(%)
$Sm_{2.75}C_{60}$	22474.9(5)	32	0.84
$(Sm_{5/6}Ca_{1/6})_{2.75}C_{60}$_w	22302.3(6)	120	0.76
$(Sm_{5/6}Ca_{1/6})_{2.75}C_{60}$_c	22290.2(7)	110	0.71
$(Sm_{2/3}Ca_{1/3})_{2.75}C_{60}$_w	22325.0(9)	130	1.25
$(Sm_{2/3}Ca_{1/3})_{2.75}C_{60}$_c	22060.2(1.3)	100	0.23
$(Sm_{1/2}Ca_{1/2})_{2.75}C_{60}$	21884.1(1.0)	100	0.34
$Ca_{2.75}C_{60}$	21662.8(3)	-	-

Table 5.7 clearly shows that by substituting Sm by Ca results in substantial increase of the onset temperature of NTE. This substitution effect most likely results from the suppression of the thermal excitation of the 4f electrons of Sm upon introduction of Ca ions, which lack an electronically active 4f sublattice.

The volume inflation is closely related to the valence change as a function of temperature. If we recall that the tetrahedral hole in $RE_{2.75}C_{60}$ has a radius of 1.12 Å, straddling the values of the ionic radii of Sm^{2+} (1.41 Å) and Sm^{3+} (1.10 Å) and therefore, changes in the average valence state have a profound effect on lattice size. In Sm-based materials, the Sm valence is directly related to the number of $4f$ holes, thus precise measurement of the changes in $4f$ occupation can provide evidence to confirm the electronic nature of the low temperature first-order valence transition. The temperature dependence of the intermediate Sm valence was directly investigated by PFY-XAS measurements along the Sm L_3 absorption edge of $(Sm_{2/3}Ca_{1/3})_{2.75}C_{60}$, of which showed the maximum volume inflation in the Ca substituted family. The obtained XAS spectra at room temperature showed

two features, representing radiatively reached final state configurations of Sm^{2+} ($3d^94f^6$) and Sm^{3+} ($3d^94f^5$). This two-feature spectrum implies that the sample is in the intermediated state with average valence state of the Sm ion estimated to be closer to +2 than to +3, which is consistent with what was derived by magnetic susceptibility measurements (+2.2~+2.3). Unlike the magnetic susceptibility measurements, the temperature evolution of the PFY-XAS spectra provides a good estimate of the average Sm valence at all temperatures from the relative intensity of the clearly resolved features.

The temperature evolution of the $I(Sm^{2+})/I(Sm^{3+})$ ratio obtained from the PFY spectra reveals a continuous decrease below 300 K, implying that the average Sm valence increases monotonically on cooling towards T_v. However, what was remarkable from these measurements is that the relative intensity suddenly increases below $T_v \sim 20$ K implying a first-order valence transition to a state with increased Sm^{2+} character ($Sm^{3+} \rightarrow Sm^{2+}$). The obtained results provide excellent evidence to confirm the electronic nature of the low temperature first-order valence transition and they are entirely consistent with the structural data and the observation of NTE at low temperatures.

The temperature evolution of the Sm valence state of $(Sm_{2/3}Ca_{1/3})_{2.75}C_{60}$ was also probed by using the RIXS technique. RIXS has developed as an effective technique for probing the mixed valence ground state of rare-earths under pressure [25], and now it has been applied to probe the temperature dependence directly. In contrast to XAS, RIXS is sensitive to even small components of a given electronic configuration, thus it can provide precise information of the Sm^{2+} and Sm^{3+} contributions. The average valence state of Sm at ambient temperature is +2.20. As the sample was slowly cooled down,

the $I(Sm^{2+})/I(Sm^{3+})$ ratio continuously decreases implying a decrease in the Sm $4f$ occupation number and an increase in the average valence which approaches a maximum value of ~+2.28 on cooling down to 20 K. On further cooling, a sudden valence change occurs and the Sm $4f$ electron occupation number abruptly increases leading to an average valence of ~+2.19 at 4 K. This result is entirely consistent with those from PFY-XAS measurements and with those from X-ray diffraction measurements.

5.3 References

[1] Chen, X. H., Roth, G., *Phys. Rev. B,* **52**, 15534 (1995).

[2] Arvanitidis, J., Papagelis, K., Margadonna, S., Prassides, K., Fitch, A. N., *Nature* **425**, 599 (2003).

[3] Arvanitidis, J., Papagelis, K., Margadonna, S., Prassides, K., *Dalton Trans.* **19**, 3144 (2004).

[4] Margadonna, S., Arvanitidis, J., Papagelis, K., Prassides, K., *Chem. Mater.* **17**, 4474 (2005).

[5] Jayaraman, A., Maines, R. G., *Phys. Rev. B* **19**, 4154 (1979).

[6] Roisnel, T., Carvajal, J. R., WinPLOTR manual(2003), P. 28.

[7] Claridge, J. B., Kubozono, Y., Rosseinsky, M. J., *Chem. Mater.* **15**, 1830 (2003).

[8] Martin, D. H., Magnetism in Solids (MIT Press, Cambridge, MA, 1967), P.166.

[9] Gogia, B., Kordatos, K., Suematsu, H., Tanigaki, K., Prassides, K., *Phys.*

Rev. B **58**, 1077 (1998).

[10] Tanigaki, K., Prassides, K., *J. Mater. Chem.* **5**, 1515 (1995).

[11] Maple, M. B., Wohlleben, D., *Phys. Rev. Lett.* **27**, 511 (1971).

[12] Bucher, E., Narayanamurti, V., Jayaraman, A., *J. Appl. Phys.* **42**, 1741 (1971).

[13] Figueroa, E., Gramm, K., Beckman, O., Rao, K.V., *Physica Scripta* **22**, 533 (1980).

[14] Norikiyo, U., *J. Phys. Soc. JPN.* 15, 2041 (1960).

[15] Chinchure, A.D., Mazumdar, C., Marathe, V.R., Nagarajan, R., Gupta, L.C., Shah, S.S., *Phys. Rev. B.* **50**, 609 (1994).

[16] Lifshin, E., X-ray Characterization of Materials (Wiley-VCH, NY, 1999), P. 80.

[17] Margadonna, S., Brown, C. M., Lappas, A., Prassides, K., Tanigaki, K., Knudsen, K. D., Le Bihan, T., Mézouar, M., *J. Solid State Chem.*, **145**, 471 (1999).

[18] Beaurepaire, E., Kappler, J. P., Krill, G., *Phys. Rev. B.* **41**, 6768 (1990).

[19] Lawrence, J. M., Kwei, G. H., Canfield, P. C., de Witt, J. G., Lawson, A. C., *Phys. Rev. B.* **49**, 1627 (1994).

[20] Alekseev, P. A., Chernikov, R. V., Golubkov, A. V., Klementiev, K. V., Menushenkov, A. P., Nemkovsky, K. S., *Nuclear Instruments and Methods in Physics Research A*, **543**, 205 (2005).

[21] Dallera, C., Grioni, M., Shukla, A., Vankó, G., Sarrao, J. L., Rueff, J. P., Cox, D. L., *Phys. Rev. Lett.*, **19**, 6403 (2002).

[22] Hämäläinen, K., Siddons, D. P., Hastings, J. B., Berman, L. E., *Phys. Rev. Lett.*, **67**, 2850 (1991).

[23] Dallera, C., Annese, E., Rueff, J. P., Palenzona, A., Vankó, G., Braicovich,

L., Shukla, A., Grioni, M., *Phys. Rev. B*, **68**, 245114 (2003).

[24] Annese, E., Barla, A., Dallera, C., Lapertot, G., Sanchez, J-P., Vankó, G., *Phys. Rev. B*, **73**, 140409(R) (2006).

[25] Dallera, C., Annese, E., Rueff, J. P., Grioni, M., Vankó, G., Braicovich, L., Barla, A., Sanchez, J-P., Gusmeroli, R., Palenzona, A., Degiorgi, L., Lapertot, G., *J. Phys. Condens. Matter.*, **17**, S849 (2005)

CHAPTER 6

Conclusions

6.1 Overview

The fullerenes were discovered in 1985 by Kroto *et al.* and still attract much research into their fascinating behaviour. Initially, much of the research focused on characterising pristine C_{60}, where it was found that the high electron affinity of C_{60} and the weak intermolecular van der Waals forces in its crystalline form make solid C_{60} an excellent host for electron donors. Soon after the discovery, intensive effort was put on studying intercalated solid C_{60} salts, also known as fullerides, where the electron donors can be alkali, alkaline-earth or rare-earth metals. These fullerides have displayed a variety of interesting properties, such as superconductivity, ferromagnetism, giant magneto-resistance, negative thermal expansion, and first-order lattice collapse. The most well known fullerene derivatives have been those of the alkali metals with stoichiometry A_3C_{60}, which are metallic and become superconducting with maximum transition temperature, T_c, of 38 K with the application of pressure (for Cs_3C_{60}). In A_3C_{60} superconductors, T_c is modulated by the density-of-states at the Fermi level, $N(E_F)$, for which, as the $N(E_F)$ increases, T_c also increases.

The structural and electronic properties of those fullerides salts are sensitively affected by the nature and size of the dopants, and the doping level. For instance, the structures of A_3C_{60} ($A_2A'C_{60}$, A, A' = alkali metal) can be classified into four different types depending on the size of the ionic radii occupying the available tetrahedral and octahedral interstitial sites. They are: a) orientationally ordered primitive cubic (space group $Pa\bar{3}$) structures, adopted by Na_2RbC_{60} and Na_2CsC_{60}, where the smaller T_d holes (~1.12 Å) are occupied by Na^+ (0.95 Å) and the larger O_h holes (~2.06 Å) are occupied by the

larger alkali ions (Rb^+, Cs^+); b) merohedrally disordered fcc (space group $Fm\bar{3}m$) structures, adopted when ions with larger ionic radius than that of the T_d holes (K^+, Rb^+) are intercalated, such as K_3C_{60}, Rb_3C_{60}; c) when T_d holes are occupied by Li^+ ions, Li_2CsC_{60} and Li_2RbC_{60} adopt fcc (space group $Fm\bar{3}m$) structures with quasi-spherical C_{60}^{3-} ions; d) a body-centred-cubic-derived (*bcc*), so-called A-15 type structure is adopted for Cs_3C_{60} (space group $Pm\bar{3}n$). For (a) and (b), superconductivity is observed below T_c at ambient pressure reaching the highest value of T_c = 33 K for $RbCs_2C_{60}$, while for (d), Cs_3C_{60} is an insulator at ambient pressure but becomes a bulk superconductor with $T_c(P)$ passing through a maximum at 38 K, no superconductivity was observed in (c). In any cases, full charge transfer from the metals to C_{60} occurs and the t_{1u} conduction band of C_{60} (LUMO) becomes half filled.

Highly-doped states of C_{60}^{n-} (n > 6) can be achieved when alkaline-earth metals are used as intercalants and the conduction band is derived from the next unoccupied triply degenerate t_{1g}, (LUMO+1), state of C_{60}. This also leads to metallic and superconducting compositions for various levels of band filling. Bulk superconducting phases in the Ba-C_{60} and Sr-C_{60} systems have been established to have stoichiometry Ba_4C_{60} and Sr_4C_{60} with T_c of 6.7 and 4.4 K, respectively, adopting highly anisotropic orthorhombic structures (space group *Immm*). These systems are the first examples of non-cubic fulleride superconductors. High-resolution X-ray diffraction has revealed the existence of strong hybridisation between alkaline-earth metal and carbon orbitals, which contrasts with the alkali fullerides where full charge transfer from the metal to C_{60} occurs.

The rare-earth fulleride chemistry had not been as widely established as that of the alkali and alkaline-earth metals due to the difficulties in devising reliable protocols for preparation of single-phase materials. One of the objectives of my project was to establish reproducible synthetic procedures to obtain single-phase materials to carry out systematic investigations of the structural and electronic properties of various rare-earth fullerides. Prior to my project, our research group had successfully synthesised rare-earth fullerides with stioichiometry $RE_{2.75}C_{60}$ (RE = Sm, Yb) and obtained fascinating results. The former showed both temperature- and pressure-induced valence transitions accompanied by anomalous structural behaviour, namely negative thermal expansion (NTE) and lattice collapse, respectively. These responses were unexpected in fullerene systems and revealed intermediate valence phenomena with remarkable sensitivity of the rare-earth valency to external stimuli.

The observation of mixed valence phenomena in rare-earth fullerides established an unexpected link to the class of strongly correlated Kondo insulators, whose behaviour can be rationalised in terms of the valence fluctuation model. For instance, NTE was observed for $YbGa_{1.05}Ge_{0.95}$, where a large and abrupt volume increase on cooling from 15 K down to 5 K was caused by a sudden change in valence state of the Yb ion from Yb^{3+} towards the larger Yb^{2+}. The valence transition for this composition was controlled by the spilling over of Ga $4p$ electronic density into the Yb $4f$ band. Similarly, SmS has been reported to display a discontinuous $4f \rightarrow 5d$ electron delocalization with increasing pressure accompanied by an abrupt decrease in volume ($\Delta V/V \sim 16\%$) at 6.5 kbar. This first-order pressure-induced valence transition without change in crystal structure was attributed to an

electronic transition of the Sm ion from Sm^{2+} to Sm^{3+} state having different ionic radii, and is also associated with a semiconductor-to-metal transition due the strong hybridisation between the localised $4f$ and the conduction $5d$ electrons.

The anomalous behaviour observed in the rare-earth fullerides was rationalised along the same line, that is in terms of the valence fluctuation model where the average valence state of RE ions changes with changing external stimuli (temperature or pressure). Estimates of the average Sm and Yb valence in $Sm_{2.75}C_{60}$ and $Yb_{2.75}C_{60}$ were derived from magnetic susceptibility measurements as +2.2-2.3. The driving force of the changes in valence is electronic in origin and, in the case of temperature dependence, thermal transfer of electrons occurs between the narrow $4f$ band of RE ions and the C_{60} t_{1u} band, while in the case of pressure dependence, as pressure increases, spilling over of $4f$ electron density into the $5d$ conduction band occurs as a result of band overlap. In both cases, the electronically active $4f$ sublattice of RE ions plays an important role. On the other hand, anomalous behaviour was not observed for the isostructural and isoelectronic $Ca_{2.75}C_{60}$ fulleride, which lacks an electronically active $4f$ sublattice.

6.2 Main Achievements of This Thesis

In chapter 2, details of the synthetic procedures are presented for intercalating C_{60} with different types of metals including alkaline-eartn and rare-earth metals. These techniques have afforded single-phase materials, allowing the systematic characterisation of their structural, electronic, and magnetic properties.

The following three chapters contain results of the experimental investigation on the effect of Yb, Eu, and Ca substitution for Sm in $Sm_{2.75}C_{60}$. The properties of the materials were followed as function of temperature and pressure. Our underlying aim in performing these studies has been to generalise the anomalous behaviour observed in the lattice parameters of $Sm_{2.75}C_{60}$ as a function of both temperature and pressure, and also to clarify the role of the dopant size and of its electronic configuration in inducing the valence transition in $RE_{2.75}C_{60}$. In the course of the structural work, it was found that the $Sm_{2.75}C_{60}$ structure was remarkably robust. All the fullerides prepared here adopt the same orthorhombic superstructure, which arises from the long-range ordering of T_d defects, namely one out of every eight T_d sites is only partially occupied, resulting in doubling of the unit cell metrics of the *fcc* alkali fullerides.

The investigation of the properties of $Yb_{2.75}C_{60}$ was presented in chapter 3. Studies of this compound were initiated in search of bulk superconductivity in the Yb-C_{60} phase field. However, contrary to reports in the literature, the presence of bulk superconductivity was not observed in the many different batches measured (maximum superconducting fraction found was at the trace level of 0.8%), while slightly higher values were observed for samples with nominal composition Yb_4C_{60}. The structural properties of $Yb_{2.75}C_{60}$ were studied both as a function of temperature and pressure by high-resolution synchrotron X-ray powder diffraction. The temperature-dependent measurements were carried out on two different batches (samples C and Z), which exhibited essentially identical diffraction patterns with sample C having slightly more impurity phase. In both cases, the diffraction data revealed that the extracted unit cell volume at 5 K was larger than that

at 300 K and that it decreases continuously with increasing temperature between 5 and 60 K. The volume contracts steeply with the thermal expansivity reaching -1055 ppm/K and leading to an overall decrease in unit cell size of 1.4%. Above 60 K, the anomalous lattice response disappears and the lattice expands on heating to 295 K. On the other hand, on slow cooling we find that the Bragg peaks shift monotonically to higher angles down to 20 K. On further cooling, a sudden jump to lower angles is observed at 12 K, implying the occurrence of an abrupt volume inflation with an overall increment of 0.99%. This is clear evidence of the existence of hysteretic behaviour in valence transition associated with its first-order nature.

The anomalous response of the $Yb_{2.75}C_{60}$ lattice size at low temperature without accompanying change in crystal symmetry can be rationalised in the same manner as for $Sm_{2.75}C_{60}$ in terms of the valence fluctuation model, driven by the $Yb^{2+} \leftrightarrow Yb^{3+}$ conversion. The interpretation of the driving force of the valence transition is electron transfer from the Yb $4f$ band to the electronically active t_{1u} band of C_{60}.

Pressure-dependent powder X-ray diffraction measurements were carried out on sample C in the pressure range 0-6.50 GPa at ambient temperature. In analogy with the case of $Sm_{2.75}C_{60}$, the lattice constants contract monotonically with increasing pressure until a critical pressure is reached and an abrupt valence transition occurs. A sudden drop in unit cell dimensions ($\Delta V/V \sim 2.1\%$) was observed at 4.30 GPa. On releasing pressure, the lattice constants slowly increase until the reverse transition to the low-pressure phase occurs. The reverse transition is characterised by a large hysteretic behaviour as the original phase does not fully recover even at 3.20 GPa. The transition was also accompanied by a reversible insulator-to-metal

transition. The pressure-induced valence transition sets off when the Yb $5d$ and $4f$ bands begin to overlap and the $4f$ electrons begin to spill over into the $5d$ band, resulting in an increase in the average Yb valence towards 3+, a decrease in the size of the rare-earth ion and a transition to a metallic state.

In chapter 4, results obtained from structural studies on $Eu_{2.75}C_{60}$ and the solid solutions, $(Sm_{1-x}Eu_x)_{2.75}C_{60}$ (x = 1/3 and 2/3) are presented. These were studied again both as a function of temperature and pressure by high-resolution synchrotron X-ray powder diffraction. All $(Sm_{1-x}Eu_x)_{2.75}C_{60}$ samples are isostructural and adopt the orthorhombic superstructure. In the temperature dependent measurements, NTE was observed for all samples, with the onset temperature of NTE increasing substantially by introduction of Eu ions (90 K for $Eu_{2.75}C_{60}$). Unexpectedly, the diffraction data in the Eu substituted compounds showed two distinct temperature regions where NTE is observed and separated by each other by a plateau at around 50 K. We recall here that the energy difference between divalent and trivalent states of Sm and Yb is very close to zero, while that for Eu is negative and larger, implying that the divalent state of Eu ion is more stable. Thus, the $RE^{2+} \leftrightarrow RE^{3+}$ conversion for Sm and Yb is more continuous and expected to complete at a lower temperature. The fact that the divalent state of the Eu ion is more stable can result in the average room-temperature valence state to be much closer to 2+ that that of the Sm phase; this is consistent with the larger unit cell volume of Eu substituted compounds found.

Pressure-induced valence transitions were also observed in both $Eu_{2.75}C_{60}$ and $(Sm_{2/3}Eu_{1/3})_{2.75}C_{60}$ with onsets at 4.40 and 4.53 GPa, respectively. Abrupt collapse of the unit cell volume was observed above this pressure resulting in volume change of $\Delta V/V$~3.2 and ~5.1%, respectively. In

these systems, the introduction of Eu leads to an increase in critical pressure (*cf.* 3.95 GPa for $Sm_{2.75}C_{60}$) and a decrease in the volume change accompanying the transition (*cf.* 6.0% in $Sm_{2.75}C_{60}$). Such differences are consistent with the Eu 4*f* band located deep in the energy gap.

Further studies on mixed valence phenomena in rare-earth fullerides are continued in chapter 5. Here, the structural and electronic properties of Ca-substituted compounds with stoichiometry $(Sm_{1-x}Ca_x)_{2.75}C_{60}$ (x = 0, 1/6, 1/3, 2/3, 3/4, 1) are studied as a function of temperature. For the mixed compounds, the stoichiometry was established by a combination of structural analysis and high-energy ion scattering spectroscopy. First of all, the temperature evolution of the unit cell volume of $Ca_{2.75}C_{60}$ showed no anomalous lattice behaviour due to the absence of the electronically active 4*f* sublattice. On the other hand, NTE was successfully observed for all other compounds. The NTE onset temperature of the Ca-substituted materials turned out to be the highest among all samples measured so far, reaching 130 K. The current understanding of this effect is that the smaller Ca^{2+} ions occupy T_d sites resulting in the weakening of the hybridisation between the Sm 4*f* and the C_{60} t_{1u} orbitals.

The complex temperature evolution of the Sm valence states was directly probed by using the high resolution partial fluorescence yield X-ray absorption spectra (PFY-XAS) and resonant inelastic X-ray scattering (RIXS) measurements on the $(Sm_{2/3}Ca_{1/3})_{2.75}C_{60}$ fulleride. Both PFY-XAS and RIXS have revealed the first-order valence transition at low temperature region. As the sample is cooled down from ambient temperature towards a critical temperature, T_v, a continuous decrease in the 4f electron occupation number, thus, $Sm^{2+} \rightarrow Sm^{3+}$ transition, which approaches a maximum value of ~+2.28

was observed. On further cooling below T_v, a sudden valence change occurs and the Sm 4*f* electron occupation number abruptly increases leading to an average valence of ~+2.19 at 4 K. This result, while entirely consistent with that from X-ray diffraction measurements at low temperatures, also reveals that the material is electronically active throughout the whole temperature range investigated.

6.3 Future Directions

The aim of this thesis was the systematic investigation of the structure and electronic properties of selected rare-earth metal fullerides. The work described here has provided results that are useful in rationalising the complex behaviour of these mixed valence materials. However, still more work is required, for instance, precise assignment of superconducting phase in Yb_xC_{60}, if it exists. As seen in the case of Cs_3C_{60}, identification of the phase responsible for superconductivity in this material has been a key target since the discovery of superconductivity, and recent development in the solvent-controlled synthesis has lead to isolation of bulk superconducting Cs_3C_{60}. Thus, if the real superconducting phase in Yb_xC_{60} was identified, it may also results in observing bulk superconductivity in these materials. Moreover, the magnetic behaviour of $Eu_{6-x}Sr_xC_{60}$ systems, which shows the transition to the ferromagnetic state, is still not fully understood. It appears to be affected by the strong interaction between C_{60}-π and Eu-*f* states, however, results obtained from neutron diffraction measurements makes the idea of a direct exchange interaction inappropriate to rationalise the magnetic behaviour of these systems. We also have been trying to synthesise

other rare-earth based materials and alkaline-earth and rare-earth mixed materials, such as $Tm_{2.75}C_{60}$, $(Eu_{1-x}Sr_x)_{2.75}C_{60}$, and $(Yb_{1-x}Ba_x)_{2.75}C_{60}$, which are also expected to show potentially interesting electronic and structural behaviour. However, the protocols for producing single-phase materials have not been successfully established as yet.

An additional avenue opened by this work in the attempt to fully understand the interesting electronic behaviour is to employ the PFY-XAS and RIXS techniques as a function of both T and P to probe the valence of other rare-earth ions. We are expected to carry out these measurements on various rare-earth based fullerides under different conditions near future.